REPORT DOCUMENTATION PAGE

Form Approved
OMB NO. 0704-0188

1. AGENCY USE ONLY (Leave Blank)	2. REPORT DATE	3. REPORT TYPE AND DATES COVERED
	15 APRIL 2003	FINAL REPORT 20 may 98 - 19 Dec 02

4. TITLE AND SUBTITLE

COMPRESSIVE FAILURE OF FIBER REINFORCED COMPOSITES

5. FUNDING NUMBERS

DAAG55-98-1-0317

6. AUTHOR(S)

ANTHONY M. WAAS - (PI)

7. PERFORMING ORGANIZATION NAME(S) AND ADDRESS(ES)

THE UNIVERSITY OF MICHIGAN, DRDA
3003 S. State Street, Ann Arbor, MI 48109-1274

8. PERFORMING ORGANIZATION REPORT NUMBER

9. SPONSORING / MONITORING AGENCY NAME(S) AND ADDRESS(ES)

U. S. Army Research Office
P.O. Box 12211
Research Triangle Park, NC 27709-2211

10. SPONSORING / MONITORING AGENCY REPORT NUMBER

P-38086-EG .1

11. SUPPLEMENTARY NOTES

The views, opinions and/or findings contained in this report are those of the author(s) and should not be construed as an official Department of the Army position, policy or decision, unless so designated by other documentation.

12 a. DISTRIBUTION / AVAILABILITY STATEMENT

Approved for public release; distribution unlimited.

12 b. DISTRIBUTION CODE

13. ABSTRACT (Maximum 200 words)

This final technical report was prepared by the University of Michigan, in Ann Arbor, Michigan, on ARO Grant DAAG55-98-1-0317, for the Army Research Office, Solid Mechanics Branch. The research reported herein was accomplished under the grant title "COMPRESSIVE FAILURE OF FIBER REINFORCED COMPOSITE," under the technical cognizance of Dr. Bruce LaMattina of the Solid Mechanics Branch of ARO.

The authors gratefully acknowledge the able assistance of instrument maker Terry Larrow and Electronics Technician Tom Griffin of the Aerospace Engineering Department workshop. We also thank Masters Students Amit Salvi and Joe Gianetti for their assistance in various stages of the project.

This report consists of the doctoral thesis of Chandra S. Yerramalli, whose research work constituted the project supported through the ARO.

14. SUBJECT TERMS	15. NUMBER OF PAGES
	16. PRICE CODE

17. SECURITY CLASSIFICATION OR REPORT	18. SECURITY CLASSIFICATION ON THIS PAGE	19. SECURITY CLASSIFICATION OF ABSTRACT	20. LIMITATION OF ABSTRACT
UNCLASSIFIED	UNCLASSIFIED	UNCLASSIFIED	UL

NSN 7540-01-280-5500

Standard Form 298 (Rev.2-89)
Prescribed by ANSI Std. 239-18
298-102

Enclosure 1

20030514 051

COMPRESSIVE FAILURE OF FIBER REINFORCED COMPOSITES

Proposal No. 38086-EG

Anthony M. Waas
Aerospace Engineering Department
The University of Michigan, Ann Arbor

Final Technical Report to ARO for work performed under ARO
Grant DAAG55-98-1-0317

April 15, 2003

Composite Structures Laboratory
Department of Aerospace Engineering
College of Engineering
University of Michigan, Ann Arbor, MI 48109-2140

Foreword

This final technical report was prepared by the Univ. of Michigan, Ann Arbor, Michigan, on ARO Grant DAAG55-98-1-0317, for theArmy Research Office, Solid Mechanics Branch. The research reported herein was accomplished under the grant title "COMPRESSIVE FAILURE OF FIBER REINFORCED COMPOSITE", under the technical cognizance of Dr. Bruce LaMattina of the Solid mechanics branch of ARO.

The authors gratefully acknowledge the able assistance of instrument maker Terry Larrow and Electronics Technician Tom Griffin of the Aerospace Engineering Dept. workshop. We also thank Masters Students Amit Salvi and Joe Gianetti for their assistance in various stages of the project..

Abstract

This report consists of the doctoral thesis of Chandra S. Yerramalli, who research work constituted the project supported through the ARO.

A MECHANISM BASED MODELING APPROACH TO FAILURE IN FIBER REINFORCED COMPOSITES

by

Chandra Sekher Yerramalli

A dissertation submitted in partial fulfillment
of the requirements for the degree of
Doctor of Philosophy
(Aerospace Engineering)
in The University of Michigan
2003

Doctoral Committee:

Professor Anthony M. Waas, Chairperson
Associate Professor Carlos E. S. Cesnik
Professor Antoine E. Naaman
Associate Professor Ann Marie Sastry
Dr. Bruce LaMattina, U.S. Army Research Office

To my Parents, Ramamnanna and Ravi

ACKNOWLEDGEMENTS

I would like to thank my advisor Prof. Waas, who has been a source of encouragement and ideas during the course of this thesis work. His ability to understand and explain the physics of the problem has been a great resource to me during my research. I would like to express my gratitude to the US Army Research Office for funding this research work and to Dr. LaMattina, who has always been supportive of our research effort. I would also like to thank him for agreeing to be a part of my doctoral committee. I am grateful to Prof. Cesnik, Prof. Naaman and Prof. Sastry for their useful comments on my thesis. Prof. Naik, at IIT Bombay introduced me to the subject of composite materials and his encouragement and confidence in my abilities is always a source of inspiration to me.

I would also like to thank my friends Biju, Dr.Chung and Suman, who really helped me when the going was tough and I thought Ph.D was not my cup of tea. The composite structures research group of Dr.Ahn, Amit, Ajith, Dr.Shuching, Joe, Rafael, Erik, Basu, Wei and Kristian has been a great group to hang out with and share the joys and pains of research. Thanks also to Sunny for all those informative late night chats and discussions on various technical and non-technical issues. I would also like to thank all my friends in the University of Michigan, for making my graduate school experience a memorable one.

The support of Aerospace engineering technicians, Terry, Dave, Tom, Mike and Chris has been crucial to the completion of my experiments. I will always be grate-

ful to them for accomodating my last minute requests to improvise and fabricate equipment for my experiments. I would also like to thank the department secretaries Margaret and Suzanne, who have been of great help to me and made my stay in the University of Michigan a pleasant one. I am also grateful to Heidi, the Aerospace engineering librarian for allowing me the liberal use of library resources. I am grateful to the Aerospace engineering department for providing me teaching assistanships for two semesters and thus providing me invaluable teaching experience.

TABLE OF CONTENTS

DEDICATION ii

ACKNOWLEDGEMENTS iii

LIST OF FIGURES viii

LIST OF TABLES xiii

LIST OF APPENDICES xiv

CHAPTER

I. INTRODUCTION 1

1.1 Background 1
1.2 Motivation 3
1.3 Literature Review 4
1.3.1 Static Loading 5
1.3.2 Dynamic Loading 11
1.3.3 Summary 13
1.4 Significant Contributions of the Current Thesis 14
1.5 Thesis Outline 16
1.6 Publications Related to this Thesis 17

II. SHEAR RESPONSE OF POLYMER MATRIX COMPOSITES 20

2.1 Introduction 20
2.2 Experiments 23
2.2.1 Materials and Chemicals 23
2.2.2 Test Procedure 24
2.2.3 Shear Stress Analysis 25
2.3 Test Results 26
2.4 Interphase Model 28
2.5 Discussion 32
2.6 Concluding Remarks 35

III. AXIAL COMPRESSIVE RESPONSE OF FRPC; NON-STEADY STATE AXIAL SPLITTING 52

3.1 Introduction 52
3.2 Summary of Experimental Results 54
3.2.1 Glass Fiber Composites 55
3.2.2 Carbon Fiber Composites 56
3.3 Axial Splitting Model - Steady State 57
3.3.1 Strain Energy Release Rate, $\mathcal{G}$ 58
3.3.2 Discussion 64
3.4 Axial Splitting Model - Shear Lag 65
3.4.1 Shear Lag Analysis 67
3.4.2 Splitting Model - Shear Lag Method 70
3.4.3 Strain Energy Release Rate, $\mathcal{G}$ 74
3.4.4 Solution 75
3.4.5 Discussion 77
3.5 Conclusions 79

IV. COMBINED COMPRESSION TORSION RESPONSE OF FRPC 99

4.1 Introduction 99
4.2 Experimental Details 103
4.2.1 Testing Plan 105
4.2.2 Experimental Results 105
4.3 Analysis 107
4.3.1 Kinking Analysis 108
4.3.2 Splitting Analysis 109
4.4 Solution Procedure 117
4.5 Discussion 117
4.6 Conclusions 120

V. RESPONSE OF FRPC TO COMPRESSION, TORSION AND COMBINED COMPRESSION-TORSION LOADING - A FINITE ELEMENT BASED STUDY 140

5.1 Introduction 140
5.2 Modeling 142
5.2.1 Initial Geometric Imperfection 143
5.2.2 Model Implementation 145
5.2.3 Size Effects - Effect of fiber diameter 150
5.3 Conclusions 153

VI. STATIC AND DYNAMIC COMPRESSIVE RESPONSE OF HYBRID (GLASS/CARBON) COMPOSITES 187

6.1 Introduction 187
6.2 Experiments 189
6.2.1 Static Compression 190
6.2.2 Dynamic Compression 191
6.3 Analysis 192
6.4 Conclusions 197

VII. A NON-DIMENSIONAL NUMBER TO CLASSIFY COMPOSITE COMPRESSIVE FAILURE 211

7.1 Introduction 211
7.2 Experimental Work 213
7.3 Failure Mechanisms 214
7.4 Dimensional Analysis 217
7.5 Results and Discussion 221
7.6 Conclusions 223

VIII. CONCLUSIONS AND SUGGESTIONS FOR FUTURE WORK 234

8.1 Conclusions 234
8.2 Suggestions for Future Work 236

APPENDICES 239

BIBLIOGRAPHY 259

LIST OF FIGURES

1.1 Schematic of failure mechanisms in FRPC 19

2.1 Schematic of the 3 cylinder model 38
2.2 Torque (Nm) vs rotation (deg) for a carbon/vinylester composite of $V_f = 60\%$ 39
2.3 Fiber inclination at various cross sections of a torsion specimen . . 40
2.4 Angle of inclination γ as a function of radial distance for a carbon/vinylester composite 41
2.5 Typical shear response curves of glass/vinylester composites 42
2.6 Typical shear response curves of carbon/vinylester composites . . . 43
2.7 A schematic of a solid cylinder under torsion 44
2.8 Comparison of shear stress-strain curve of glass/vinylester composite, pure matrix and in-situ matrix for $V_f = 10\%$ 45
2.9 Comparison of shear stress-strain curve of carbon/vinylester composite, pure matrix and in-situ matrix for $V_f = 10\%$ 46
2.10 Comparison of shear stress-strain curve of glass/vinylester composite, pure matrix and in-situ matrix for $V_f = 60\%$ 47
2.11 Comparison of shear stress-strain curve of carbon/vinylester composite, pure matrix and in-situ matrix for $V_f = 60\%$ 48
2.12 Variation of shear modulus of in-situ matrix with fiber volume fraction 49
2.13 Shear modulus of glass/vinylester composite as a function of V_f . . 50
2.14 Interphase thickness as a function of V_f for G_i=1800MPa 51

3.1 Typical compressive stress-strain curve of glass-fiber specimen . . . 83
3.2 Typical splitting failure mode of glass fiber composite specimen ($V_f = 30\%$) 84
3.3 Kinking/splitting failure mode of glass fiber composite specimen ($V_f = 50\%$) 85
3.4 Typical compressive stress-strain curve of carbon-fiber specimen . . 86
3.5 An optical microscope picture of a kink band in carbon composite . 87
3.6 A high resolution picture of the kink band under SEM 87

3.7 Composite model with initial crack 88

3.8 Variation of compressive strength σ with fiber volume fraction V_f for a glass epoxy composite material with different values of fracture energy γ_f and misalignment angle $\phi = 2^0$ 89

3.9 Variation of compressive strength σ with fiber volume fraction V_f for a glass epoxy composite material with different values of fracture energy γ_f and misalignment angle $\phi = 2^0$ 90

3.10 Variation of compressive strength σ with fiber volume fraction V_f for a glass epoxy composite material with different values of misalignment angle $\phi = 2^0$ and $\gamma_f = 0.1224\ KJ/m^2$ 91

3.11 Variation of compressive strength σ with fiber volume fraction V_f for a glass epoxy composite material with different values of misalignment angle $\phi = 2^0$ and $\gamma_f = 0.119\ KJ/m^2$ 92

3.12 RVE showing the various regions of analysis 93

3.13 Free body diagram of a small segment of fiber and attached matrix 94

3.14 Variation of normalised stress along the length of fiber as a function of increasing ϵ with crack length factor n1 = 7 95

3.15 Curves of compliance as a function of normalized crack length for different values of ϵ and L = $20r_o$ 96

3.16 Normalized compliance with normalized crack length factor, n1 . . . 97

3.17 Curves of rate of change of compliance with crack length $\frac{dc}{dl}$ as a function of crack length with varying ϵ and L = $20r_o$ 98

4.1 Grip cross sections 122

4.2 Pure compression test setup 123

4.3 Different loading paths in a displacement/rotation control test . . . 123

4.4 Axial strain as a function of shear strain for $\Delta/r\theta = 5.23$ and glass/vinlyester composite 124

4.5 Axial stress vs shear stress for $\Delta/r\theta = 5.23$ and glass/vinylester composite. 125

4.6 Axial stress variation with applied shear strain for $\Delta/r\theta = 5.23$ and glass/vinylester composite 126

4.7 Shear stress variation with applied axial strain for $\Delta/r\theta = 5.23$ and glass/vinylester composite 127

4.8 Failure envelope for a carbon/vinylester composite of $V_f = 50\%$ . . 128

4.9 Failure envelope for a glass/vinylester composite of $V_f = 50\%$ 129

4.10 Plot showing the stress reversal in glass composite for high values of $\Delta/r\theta$ 130

4.11 Typical image of a split region in glass composites with extensive brooming of fibers 131

4.12 Image at the cross section A-A of the splitting zone in a glass composite,$V_f = 50\%$ 132
4.13 Kinking failure in glass composites at $\Delta/r\theta = 0.59$ 132
4.14 Kinking failure in carbon composites 133
4.15 Free body diagram of a kinked segment of a cylinder under combined compression and torsion 133
4.16 Composite cylinder under compression-torsion loading 134
4.17 Schematic cross section of fiber-matrix cylinder showing the crack tip details 135
4.18 Combined compression-torsion failure plot for carbon/vinylester composite of $V_f = 50\%$ 136
4.19 Combined compression-torsion failure plot for glass/vinylester composite of $V_f = 50\%$ 137
4.20 Comparison of the new fracture critieria with experimental data for a glass/vinylester composite of $V_f = 50\%$ 138
4.21 Variation of axial and torsional SERR with shear stress, τ for glass/vinylester composite of $V_f = 50\%$ 139

5.1 A 3D finite element micro-mechanical model of a composite cylinder 157
5.2 Peak stress, σ_{max} as a function of initial imperfection, ϕ 158
5.3 Mode-1 displacement of 3D FE model 159
5.4 Mode-3 displacement of 3D FE model 160
5.5 Pure compression response of vinylester matrix used as input for FE modeling 161
5.6 A schematic of the FE model for pure compression and pure torsion 162
5.7 Comparison of the experimental and 3D FE shear stress-strain curve for a carbon/vinylester composite of $V_f = 0.5$ 163
5.8 Compressive response curves of carbon/vinylester composite of $V_f =$ 0.5 for different values of imperfections 164
5.9 Compressive response curve of carbon/vinylester composite of $V_f =$ 0.5 and $\phi_1 = 1^0$ with orthotropic fiber properties 165
5.10 Deformed mesh of carbon/vinylester composite of $V_f = 0.5$ and $\phi_1 =$ 1^0 with orthotropic fiber properties 166
5.11 Deformed mesh of carbon/vinylester composite of $V_f = 0.5$ and $\phi_1 =$ 1^0 with orthotropic fiber properties 167
5.12 Deformed mesh of a slice of the carbon/vinylester composite of $V_f =$ 0.5 and $\phi_1 = 1^0$ with orthotropic fiber properties 168
5.13 Deformed mesh of a slice of the carbon/vinylester composite of $V_f =$ 0.5 and $\phi_1 = 1^0$ with orthotropic fiber properties 169
5.14 Deformed mesh of a slice of the carbon/vinylester composite of $V_f =$ 0.5 and $\phi_1 = 1^0$ with orthotropic fiber properties 170

5.15 Contours of ϵ_{xx} for the carbon/vinylester composite of $V_f = 0.5$ and $\phi_1 = 1^0$ with orthotropic fiber properties 171
5.16 Contours of ϵ_{xx} for the carbon/vinylester composite of $V_f = 0.5$ and $\phi_1 = 1^0$ with orthotropic fiber properties 172
5.17 Contours of ϵ_{xx} for the carbon/vinylester composite of $V_f = 0.5$ and $\phi_1 = 1^0$ with orthotropic fiber properties 173
5.18 Contours of γ_{xz} for the carbon/vinylester composite of $V_f = 0.5$ and $\phi_1 = 1^0$ with orthotropic fiber properties 174
5.19 Contours of γ_{xz} for the carbon/vinylester composite of $V_f = 0.5$ and $\phi_1 = 1^0$ with orthotropic fiber properties 175
5.20 Displacement and rotational control loading of 3D FE model 176
5.21 Load vs displacement reponse of 3D FE model under combined compression-torsion 177
5.22 Load vs torque reponse of 3D FE model under combined compression-torsion 178
5.23 Torque vs theta reponse of 3D FE model under combined compression-torsion 179
5.24 Comparison of combined compression-torsion failure envelope of 3D FE with experimental data 180
5.25 Torsional response of a 3D FE model of a glass composite of $V_f = 0.5$ for micro-mechanically scaled models 181
5.26 Compressive stress response of a 3D FE model of a glass composite of $V_f = 0.5$ for micro-mechanically scaled models 182
5.27 Torsional response of a 3D FE model of a glass composite of $V_f = 0.5$ for structurally scaled models 183
5.28 Compressive stress response of a 3D FE model of a glass composite of $V_f = 0.5$ for structurally scaled models 184
5.29 Compressive stress response of a 3D FE model of a glass composite of $V_f = 0.5$ and $r_f = 12\mu m$ 185
5.30 Compressive stress response of a 3D FE model of a glass composite of $V_f = 0.5$and $r_f = 6.75\mu m$ 186

6.1 Typical compressive response of hybrid composites as a function of the hybrid ratio for a global fiber volume fraction of 30% 199
6.2 Variation of failure strength as a function of the hybrid ratio for a global fiber volume fraction of 30% 200
6.3 Variation of elastic modulus as a function of the hybrid ratio for a global fiber volume fraction of 30% 201
6.4 The compressive stress response of a Aluminum6060 alloy under high strain rate tests. 202

6.5 Variation of strain rate with the applied strain for aluminum6060 alloy specimens 203
6.6 Variation of stress with strain rate for $V_{gc} = 0.5$ 204
6.7 Variation of failure strength with strain rate, for different hybrid ratios 205
6.8 Typical stress strain curves for a composite of hybrid ratio, $V_{gc} = 0.5$ 206
6.9 A typical strain gage signal obtained from the SHPB test on a hybrid composite of g/c ratio 1 207
6.10 Concentric cylinder models 208
6.11 Failure model predictions for hybrid composites (static loading) . . 209
6.12 Variation of failure strength with strain rate, for different hybrid ratios 210

7.1 A cross sectional view of pure compression grips 224
7.2 Kink band in glass composites of fiber diameter 13.5μm and V_f = 10% 225
7.3 Kink bands in glass composites of fiber diameter 13.5μm and $V_f = 60\%$ 225
7.4 Combined splitting and kinking in glass composites of fiber diameter 24μm and $V_f = 50\%$ 226
7.5 Comparison of compressive strengths between glass 24μm and 13.5μm diameter specimens 227
7.6 Comparison of compressive stress of glass and carbon composites as function of V_f 228
7.7 Kink band in glass composite reinforced with 24μm fiber diameter at $\Delta/R\theta = 0.52$ 229
7.8 Variation of the non-dimensional number, η with V_f 230
7.9 Variation of the non-dimensional number with V_f 231
7.10 Variation of non-dimensional number for glass composites as a function of shear modulus at fixed V_f 232
7.11 Variation of the non-dimensional number, η due to uncertainities (10%) associated with the values of γ_f, G_c and r_0 with V_f 233

C.1 Comparison of failure envelopes considering the composite as a deformation theory solid and as a nonlinear elastic solid 246

D.1 256
D.2 Comparison of the measured striker velocity and the predicted velocity 257
D.3 258

LIST OF TABLES

2.1 Ramberg-Osgood parameters for glass and carbon/vinylester composites 36
2.2 Measured values of shear modulus of vinylester matrix composite . . 36
2.3 Measured values of shear modulus of vinylester matrix composite . . 37
2.4 The predicted values of In-situ matrix shear modulus and yield stress values 37
2.5 The predicted In-situ matrix shear modulus and yield stress values . 37

3.1 Maximum stress values of glass-fiber composites, Lee (1998) 81
3.2 Maximum stress values of carbon-fiber composites, Lee (1998) . . . 81
3.3 $\frac{dc}{dl}$ values obtained from splitting and FE models 82
3.4 Compressive stress values obtained from splitting and FE models with $\gamma_f = 1.0546X10^{-}4KJ/m^2$ 82

4.1 Properties of glass fiber and vinylester resin 121
4.2 Ramberg-Osgood fit for shear stress-strain curve of glass/vinylester and pure vinylester specimens 121

5.1 3D finite element model details 155
5.2 Material properties of fiber and matrix 155
5.3 Normalised displacements from buckling analysis of FE model(carbon-1) 155
5.4 Boundary conditions for pure compression 156
5.5 Boundary conditions for pure torsion 156
5.6 Boundary conditions for combined compression-torsion 156
5.7 Comparison of compressive strength predictions 156

6.1 Compressive strength of hybrid composites 198

7.1 Properties of glass fiber and vinylester resin 214
7.2 Properties of carbon fiber 214
7.3 Dimensional matrix 219

D.1 Physical properties of the SHPB shafts 249

LIST OF APPENDICES

A. Manufacturing of Composite Specimens for Compression Testing . . . 240

A.1 Materials and Chemicals 240
A.2 Procedure 241

B. Axial Compliance of a Misaligned Fiber 243

C. Interaction between the Axial stress and Torsional stress 245

D. Split Hopkinson Pressure Bar Setup (SHPB) 247

D.1 Experimental Setup 248
D.1.1 Material and Equipment 248
D.1.2 Details of SHPB design 249
D.2 Wave Analysis 253

CHAPTER I

INTRODUCTION

1.1 Background

The first powered flight by the Wright brothers in 1903, marked the beginning of a new chapter in structural and materials engineering. The emphasis on light weight, high stiffness and high strength in the design of aircraft structures was markedly different from the general structural design concepts prevalent at that time. Starting with the spruce and canvas plane of the Wright brothers to the modern day jet fighters manufactured from advanced materials, the unifying theme has been the emphasis on light weight with simultaneously high strength and high stiffness. Thus, advanced materials being used today in different aerospace and non-aerospace applications are a culmination of this quest for light and strong materials. Among these advanced materials, fiber reinforced polymer matrix composites (FRPC) have been one of the most promising materials in terms of variety of applications and cost effectiveness. This is apparent from the ever increasing use of fiber reinforced composites in modern day jet fighters and space crafts to sports equipment and biomedical applications.

Fiber reinforced polymer matrix composites (FRPC) can be classified based on the type of matrix system used. The matrix systems are either thermo-setting or thermo-plastic. The reinforcement commonly used in FRPC are a low stiffness fiber

(typically, kevlar fibers) to a very high stiffness fiber (carbon fibers). A detailed description of the different types of fibers and matrix systems used can be found in the text by Herakovich (1998). The advent of FRPC in aircraft structures has led to a new flexibility in design because of the tailorability of FRPC. However, the promise of these new materials has not been fully translated into reality due to two reasons; high manufacturing costs and a lack of complete understanding of their mechanical behavior, particularly the manner by which they fail, under various types of loading conditions. The main drawbacks of these materials from a structural application point of view is their low threshold for damage initiation under transverse impact and a comparatively low compressive failure strength. Both these issues have been actively researched for the past two decades.

The study of the mechanics of failure of materials that show a progression (initiation of failure through micro-cracking leading to final failure) in the sequence of failure in general, is usually referred to as *"Damage Mechanics"* . Damage mechanics deals with different aspects of damage from failure initiation through failure progression to final failure. There are various approaches to modeling failure initiation in general. Most failure modeling approaches can be broadly divided into phenomenological and mechanism based failure models. The most commonly used phenomenological models in composites (e.g. Tsai-Wu) are essentially adaptations and extensions of corresponding criteria for metals, for example, the Von-Mises criterion. The main advantage of phenomenological models is their simplicity. But these models provide very little information about the causes of failure or the effect of constituent properties on the overall failure behavior of composites. On the other hand, mechanism based failure models are based on micro-mechanics of the composite constituents. Usually mechanism based failure criteria require more information

about the composite constituent properties and are applicable to a particular failure mechanism for which the model has been developed. The mechanism based models provide more information on the causes of failure and also on the role of each individual constituent (geometric and material) of the composite. This information can be used to design composites with improved failure characteristics.

The findings reported in this thesis are concerned with understanding the compressive failure behavior of glass and carbon composites, both initiation and the mechanism of failure, under pure compression and combined compression-torsion loading. The study includes both static compressive behavior and dynamic compressive behavior of fiber reinforced composites. A mechanism based modeling approach to failure has been adopted to obtain a better understanding of the various parameters involved in the failure of fiber composites.

1.2 Motivation

It is well established that the compressive strength of fiber composites is small compared to their tensile strength (see Waas and Schultheisz (1996)). This difference has been a limiting factor in the design of composite structures. Research has focussed on understanding the reasons for this low compressive strength and also on methods to increase the compressive strength of fiber composites. Traditionally, composite materials are used in the form of laminates, where the individual laminae have fibers aligned at various angles to the direction of loading. It is complicated to model the laminate as a whole for understanding the fundamental aspects of compressive failure behavior of the laminated composite materials since both inter-laminar and intra-laminar failure modes are present. This makes the task of identifying the fundamental parameters affecting the compressive failure strength of composite materials

very difficult. Thus, researchers have focussed on understanding the compressive failure behavior of unidirectional fiber reinforced composites, which is a fundamental building block for any composite laminate. However, even the modeling and experimental work on unidirectional fiber reinforced composites presents tremendous challenges. Compressive loading experiments are the most difficult to perform due to the inherent tendency of the composite specimen to buckle in a global mode. It has been shown by Waas and Schultheisz (1996) and Haberle and Matthews (1993), that the testing method influences the value of the compressive failure stress observed in composite specimens.

Modeling the heterogenous and anisotropic fiber reinforced composites under compressive loads has been an active area of research. Camponeschi (1991) and Waas and Schultheisz (1996) provide a excellent review of the literature in this area. Recently, a review article by Naik and Kumar (1999) provides a comparison between the various failure models and experimental results. In the following section, a brief survey of the existing literature in the area of compressive behavior of fiber reinforced composites is presented. A more detailed description of the research work in composite compressive behavior can be obtained from the review articles cited above.

1.3 Literature Review

The literature in the area of compressive behavior of fiber composites can be broadly divided into two areas based on the type of loading, ie. static or dynamic. For each type of loading, we can further divide the work into those dealing with pure compressive loading and those dealing with combined compression-shear/torsion loading. Historically, the first attempts at modeling the composite compressive be-

havior was based on microbuckling of fibers in a elastic matrix. However, experimental evidence and further modeling suggested the inapplicability of the elastic microbuckling concept to predict the critical compressive stresses comparable to the experimentally observed strength values. This led to the development of new models based on experimentally observed failure mechanisms like *kinking* and *splitting* , which were physically observed during the compressive testing of specimens. Kinking is the result of localized shear deformation of the matrix accompanied by fiber failure. Kinking strength depends on the matrix shear yield properties, and possibly on the fiber strength. Splitting is a failure mechanism observed in fiber composites with brittle matrices or weak interfaces. It is controlled by the fracture toughness of the matrix and the fracture toughness of the fiber-matrix interface. A schematic of the failure mechanisms is shown in figure 1.1. A third type of failure reported in the literature is *fiber failure* . It usually occurs in composites reinforced with fibers like kevlar, which are weak in compression. For fibers like glass or carbon this failure mode is usually not observed, except after the initiation of failure by other mechanisms. In the subsequent paragraphs, a brief review of the work done by various researchers will be presented.

1.3.1 Static Loading

Pure Compression

The problem of low compressive strength in composite materials was first pointed out by Dow and Gruntfest (1960), which was later taken up by Rosen (1965). Rosen (1965) modeled the fiber composite material as a layered elastic medium with alternate layers of fiber plates and matrix plates. He found that the lowest buckling load was corresponding to the case of shear mode of buckling with long wavelengths and

gave the expression for the critical compressive stress as follows

$$\sigma_c = \frac{G_m}{(1 - V_f)} \tag{1.1}$$

where G_m is the elastic shear modulus of the matrix and V_f is the fiber volume fraction of the composite. Similar, results were also obtained by Hayashi (1965). Lager and June (1969) compared the values of compressive stress calculated from Eqn. (1.1) and found them to be higher than the experimentally observed compressive strength values of boron-epoxy composite specimens. They attributed this to the apparent anisotropy of epoxy matrix in the presence of fibers and suggested a modified form of Eqn. (1.1). Several improvements and modifications have been suggested (Sadowsky et al. (1967), Lanir and Fung (1972), Steif (1988), Waas et al. (1990) and Lagoudas et al. (1991)) to the elastic microbuckling model of Rosen (1965) but none of the models based on the elastic behavior of matrix could predict compressive stresses comparable to the experimental results, as reported, for example in Weaver and Williams (1975), Piggott and Harris (1980), Parry and Wronski (1981), Piggott and Harris (1981) and Martinez et al. (1981).

Argon (1972) came up with an important observation about the dependancy of the compressive strength of fiber reinforced composites on the misalignment of the reinforcing fibers. Fiber misalignments are present due to the manufacturing process of composites and he surmised that these local misalignments induce local shear stresses in the composite, when subjected to an external compressive load. The induced shear stress beyond the shear yield stress of the matrix causes a local degradation of the matrix shear stiffness causing the fibers to buckle. He therefore suggested that the critical compressive stress is a function of the shear yield stress, τ_y, and the fiber misalignments, ϕ, present in the composite specimens and gave the

following expression for the critical compressive stress.

$$\sigma_c = \frac{\tau_y}{\phi} \tag{1.2}$$

The analysis of Argon (1972) also indicated that the shear mode of buckling as suggested by Rosen (1965) prevailed. But the final kinking mode of failure as observed in experiment was due to the local buckling of fibers in the region of excessive shear stresses beyond the shear yield stress of the matrix. The experimental work of Weaver and Williams (1975) revealed that the kink bands consisted of broken fibers and that the kinking compressive strength of carbon composites tested increased with increasing confining pressure. Piggott and Harris (1980), Piggott and Harris (1981) and Martinez et al. (1981) in a series of compression experiments on composites reinforced with carbon, glass and kevlar fibers provided a new insight to the problem of compressive failure behavior of fiber reinforced composites. Piggott and Harris (1980), observed that the compressive strength of the fiber reinforced composites dropped with the reduction in the shear yield stress of the matrix. They also observed that the failure mode in carbon fibers was kinking whereas the glass fiber reinforced composites failed by splitting. In another set of experiments reported by Martinez et al. (1981), the effect of fiber matrix adhesion and misalignment was studied. They observed that the compressive strength is linearly varying with fiber volume fraction, V_f for values of V_f less than 0.4 and beyond this fiber volume fraction the compressive strength was seen to drop below this linear relation. They observed that the presence of kinked and misaligned fibers was to reduce the compressive strength of fiber reinforced composite. Although, kinking stress predicted from Eqn. (1.2) is lower than the prediction of Rosen's model it was still higher than

the experimentally observed values of compressive kinking stress. A new model for kinking taking into account the plasticity of the matrix was introduced by Budiansky (1983). He essentially extended Argon's work by assuming perfect plasticity in matrix and derived the expression for critical compressive stress with a zero angle kink band to be as follows

$$\sigma_c = \frac{\tau_y}{\phi + \gamma_y} \tag{1.3}$$

where γ_y is the shear yield strain of the composite and τ_y is the shear yield stress of the composite. It can be seen that for values of misalignment angle, ϕ very much greater than γ_y, Eqn. (1.3) is same as the Eqn. (1.2) obtained by Argon (1972). But as was suggested in the paper by Budiansky (1983), most experimental observations of the kink band indicate a non-zero kink band angle. Budiansky (1983), explained the phenonmenon of non-zero kink band angles by studying the elastic effects of localized imperfections. He assumed the imperfections to be of two kinds, one being a very short wave imperfection at the boundary and another a long wave imperfection. With these types of imperfections he derived bounds for the kink band angles for different ratios of E_T/G, where E_T is the transverse modulus of the composite and G is the elastic shear modulus of the composite. Budiansky and Fleck (1993), extended the above model to include the effect of strain hardening. They derived a closed form expression for critical kinking compressive stress in case of a strain hardening matrix.

$$\sigma_c = \frac{G}{1 + n(3/7)^{1/n}(\frac{\phi/\gamma_y}{n-1})^{(n-1)/n}} \tag{1.4}$$

In Eqn (1.4), G is the shear modulus of the composite and n is the exponent in a Ramberg-Osgood fit for the shear stress-strain curve of the composite. Fleck et al. (1995) presented a couple stress based theory, in which the composite is assumed to

be inextensible in fiber direction and to deform as a Ramberg-Osgood solid in shear and transverse tension, to predict the kink band width. Fleck and Shu (1995), Moran et al. (1995), Sutcliffe and Fleck (1997), and Budiansky et al. (1998) studied the microbuckle intiation and kink band propagation in fiber reinforced composites using finite element models. The imperfection was introduced in the form of an elliptical region of fiber waviness. They observed that the predicted compressive strength decreases with increasing imperfection spatial size from the elastic bifurcation value of Rosen (1965).

Using the theory of work potential developed earlier, Schapery and Sicking (1995), and Schapery (1995) studied the kink band formation in polymer matrix composites under pure compression. They postulated that a band of wavy fibers becomes a kink band when local matrix cracking occurs. The corresponding value of axial stress equals or exceeds the predicted critical stress for buckling. The kink band angle is fixed through the requirement of matrix cracking, however the compressive strength was found to be a weak function of the kink band angle. Sun and Jun (1994), also studied the effect of fiber misalignment and non-linear behavior of the matrix on fiber microbuckling and the compressive strength of a unidirectional fiber composite. Their analysis results showed reasonable correlation with available experimental data for AS4/3501-6 and AS4/PEEK graphite composites with 2 degrees to 4 degrees range of initial fiber misalignment. The problem of kinking and micro-buckling was also addressed by Kyriakides et al. (1995). A combined experimental/numerical study on compressive behavior of cylindrical samples of AS4/PEEK unidirectional fiber reinforced composites was presented. The in-situ polymer matrix properties were determined using two different test techniques and these properties were used in the 2D plane strain modeling of the unidirectional fiber reinforced composites

utilizing the finite element package ABAQUS. Initial fiber waviness coupled with the fact that the matrix exhibited strain softening in shear led to a limit load type response. Kinking was seen as the final result of the localization process initiated by the limit load instability. In a continuation of this work, Hsu et al. (1998) and Vogler and Kyriakides (1998), studied the compressive behavior under static and dynamic loading conditions.

Splitting mechanism of failure which had been observed by Piggott and Harris (1980); Bazhenov et al. (1992); Kozey (1993), and Lee (1998), was studied by Lee and Waas (1999). Lee and Waas (1999), were the first to develop a mechanism based splitting model based on linear elastic fracture mechanics, where the composite was represented via the composite cylinder model as a concentric cylinder of fiber and matrix with a interfacial crack between the fiber and the matrix. Oguni and Ravichandran (2000), independently developed a splitting model to predict the compressive strength of fiber composites. Oguni and Ravichandran (2000), also studied the effect of confining pressure on the compressive strength predictions. They also observed that under confined compression the composite failure mechanism undergoes a transition from splitting to kinking, depending on the amount of confinement.

Combined Compression-Shear

Batdorf and Ko (1986), were the first to consider the effect of remotely applied shear stress on the kinking stress. They studied a planar strip of composite under axial compression and shear. However, they omitted the remotely applied shear strain term, γ^{∞}, in their expression. Budiansky and Fleck (1993), modified the kinking stress expression for pure compression to take into account the remotely applied shear stress and gave the expression as follows,

$$\sigma_c = \frac{\tau(r) - \tau^{\infty}}{\gamma(r) - \gamma^{\infty} + \phi} \tag{1.5}$$

Jelf and Fleck (1994a), conducted combined compression-torsion tests on hollow tubes of carbon/epoxy. They observed that the compresive failure strength dropped linearly with increasing shear stress. Similar, experiments were conducted by Lee et al. (1999) and Vogler et al. (2000). Vogler et al. (2000), used rectangular coupons of AS4/PEEK to study the behavior under combined axial compression-shear loading. They developed finite element models to predict the failure envelope under combined compression-shear loading. They introduced sinusoidal imperfections into the model, and calibrated the magnitude of imperfection, such that the model predictions for compressive strength matched the experimentally observed strength values.

1.3.2 Dynamic Loading

Structures made of composite materials are exposed to dynamic loads in their regular service life. Thus, it is important that the behavior of composites under dynamic loads be studied. This is necessary to build better predictive models for both strength and stiffness of composite materials under high strain rates. There are different testing methods ranging from servo-hydraulic machines ($\leq 10s^{-1}$), to drop weight impact towers ($10s^{-1} \leq 1000s^{-1}$). For strain rates higher than $1000s^{-1}$, typically split Hopkinson pressure bar(SHPB) setup has been used.

The split Hopkinson pressure bar test setup (SHPB) or Kolsky bar, after Kolsky (1949, 1953) has been widely used for high strain rate testing of metals and there is extensive literature available on the use of SHPB for metals (Davies and Hunter (1963); Meyers (1994)). However, in the following paragraphs only literature pertaining to the use of SHPB in high strain rate testing of composite materials

will be presented. Sierakowski et al. (1971) conducted dynamic compression tests on steel/epoxy composites at strain rates of $1000s^{-1}$. They observed the failure mechanism to be different in static and dynamic compression tests on cylindrical specimens. Kumar and Garg (1988), studied the failure modes in glass fiber reinforced composites at an average strain rate of $265s^{-1}$. They studied the failure modes for composites with fibers oriented at different angles to the loading direction. They observed that in case of unidirectional fiber composites the failure was by tensile split planes parallel to the fiber direction. Hallett et al. (1999), studied two types of woven glass/epoxy material systems in compression at strain rates of $860s^{-1}$. They concluded that there is a significant increase in the initial modulus, compressive strength and ultimate strain with increasing strain rate for woven glass/epoxy composites. Yuan and Takeda (2000), used the modified SHPB to track the damage progression in GFRP composite laminates under impact loading. Wan and Takeda (1993) and Yuan et al. (1998), compared the high strain rate behavior of carbon/vinylester and glass/vinylester composites for fiber volume fraction ranging from $0.1 - 0.6$. They observed the compressive strength to increase at high strain rates for both carbon and glass fiber reinforced composites. Fan and Slaughter (1997), presented a model to predict the dynamic compressive response of polymer matrix composites. The model incorporates the effect of material non-linearity and inertia, the effect of misalignments and fiber bending stiffness. They concluded that within a range of initial fiber imperfection wavelengths, there is a preferred wave length which causes the failure to occur in the least possible time. Oguni (2000), also studied the high strain rate behavior of glass fiber reinforced composites. A modified form of splitting formula that accounts for the rate effects was developed and compared with the experimental data. It was observed that the failure mode in

case of glass composites was splitting.

1.3.3 Summary

The literature review presented above has highlighted the most relevant and important contributions to the present state of the art in the compressive strength prediction of FRPC. Considering the immense volume of literature available on the subject of compressive behavior of fiber composites, attention has been focussed only on those works which are directly relevant to the main focus of this thesis. When appropriate, additional references have been quoted in the subsequent chapters of this thesis. It is to be noted that both kinking and splitting are localized failure initiation mechanisms. That is, in compression of long slender member it is possible for splitting or kinking to occur independently of global Euler buckling. Of course, global Euler buckling may induce kinking or splitting, but, at the same time, it is possible for kinking or splitting to occur without global Euler buckling.

A brief review of the literature in the area of pure compression indicates the importance of both geometric parameters like fiber radius, r_f, misalignment angle, ϕ, fiber volume fraction, V_f, and material parameters like shear modulus of matrix, G_m, shear yield stress, τ_y and shear yield strain of the composite, γ_y on composite compressive strength. As can be seen from the literature, most of the focus has been on understanding the behavior of small diameter carbon ($d \approx 7\mu m$), fiber composites under pure compression and usually at a fixed fiber volume fraction. There is some limited work on combined compression-shear loading of carbon fiber composites but again at a fixed fiber volume fraction. Most of the past research has dealt with the issue of failure mechanism as being inherent to a particular fiber/matrix composite system. This is because most researchers, with the exception of Piggott and Harris

(1980), have studied only one material system, usually, small diameter carbon fibers in a thermosetting or thermoplastic matrix at a fixed fiber volume fraction, where the kinking failure mechanism is predominant. Lee and Waas (1999) are the first to study the dependancy of splitting compressive strength of fiber reinforced polymer composites on parameters like fiber volume fraction, V_f, and fiber type. In the current work, the compressive response of two different composites with same matrix but different reinforcements (glass and carbon), over a wide range of fiber volume fractions have been studied. This was done in order to address some of the outstanding issues on compressive failure mechanisms mentioned above. A more holistic approach to understanding the reasons for the different failure mechanisms observed during the experimental testing of glass and carbon composites has been adopted in this work. The following sections summarize the most important contributions of the present thesis.

1.4 Significant Contributions of the Current Thesis

A major goal of the present work was to understand the behavior of glass fiber and carbon fiber reinforced polymer matrix composites under pure compression, pure torsion and combined compression-torsion loading, with respect to identifying the role of constituent properties on failure mechanisms. An important associated task is the development of mechanism based mechanics models for strength prediction. The specific contributions of this thesis can be summarized as follows.

1. A closed form expression to calculate the splitting compressive strength of FRPC by using shear lag theory has been derived. The use of shear lag theory enables us to derive an expression for compliance change with respect to crack length, dc/dl, as a function of crack length. This aspect was not included in

the earlier studies on splitting mechanics carried out by Lee and Waas (1999).

2. The effect of fiber diameter on the composite compressive strength and composite compressive failure mechanism has been studied experimentally for the first time. The work reported explicitly accounts for the effect of fiber diameter. This aspect has not been investigated in prior studies on composite compressive failure.

3. A non-dimensional number to characterize the composite compressive failure mechanism has been derived. The main advantage of this number is its use to apriori predict the failure mechanism for a given fiber/matrix system. It can also provide a designer the information to tailor the failure mechanism according to the required fiber/matrix composite material system.

4. An experimental study of the combined compression-torsion behavior of glass fiber reinforced polymer matrix composites has been presented for the first time.

5. Pure compressive behavior of hybrid composites has been studied under both static and dynamic loading using the split Hopkinson pressure bar setup for first time. A new mechanics model has been developed based on the physics of the failure process.

6. 3D finite element models which are representative of the solid composite cylinders including the microstructure were developed. These were used to study the behavior of carbon composites under pure compression and combined compression-torsion loading. The results from the models with glass composites were used to understand the effect of fiber diameter on the compressive failure.

1.5 Thesis Outline

The thesis has been organised in a manner where each chapter is self contained with an introduction and conclusion. However, the references for all the chapters are presented at the end of the thesis so as to avoid repetition. Some of the theories and experimental methods which are important to understand the current work but not necessarily in line with the main focus of this thesis have been presented in the appendices. Each individual chapter deals with an aspect of the overall problem of understanding the compressive behavior of fiber reinforced composites and builds upon the information obtained from the preceding chapters.

In chapter I, a summary of the previous work done in the area of compression of fiber composites is presented. The salient features of some important analytical/numerical models are discussed and the deficiencies identified with a view to motivate the current work. Chapter II deals with the torsional behavior of glass and carbon fiber composites. A method to determine the interphase properties is presented. Understanding the torsional behavior of composites is important since the shear response of the composite/matrix plays a crucial role in the compressive response of fiber composites. The results of this chapter have been published in open literature (paper-2, listed in the next section). In chapter III, the experimental results of pure compression tests on glass and carbon composites are presented. The steady state model of splitting developed by Lee (1998) is first presented. It is then extended to the case of nonsteady crack propagation by using shear lag theory. Chapters II and III lay the ground work for understanding the combined compression-torsion loading behavior of fiber composites. The results of chapter III appeared in the open literature as paper-1 and paper-3 listed in the next section. In chapter

IV, experimental as well as analytical model results are presented for the combined compression-torsion loading of glass and carbon composites. The differences in the response of carbon and glass composites to combined compression-torsion loading are discussed. The results of this chapter have been accepted for publication and is listed as paper-4 in the next section. Chapter V contains the details of the 3D finite element micromechanics studies. The 3D model is used to better understand the mechanics of fiber failure under compression and compression-torsion loadings. In chapter VI the pure compressive failure behavior of hybrid composites is studied. Understanding the effects of hybridization of composites, with respect to failure strength and failure mechanism is important to design cost effective fiber composites. Their response under high strain rates of loading is studied using the split Hopkinson pressure bar setup. Based on the experimental and analytical/numerical results obtained in the previous chapters, a non-dimensional number is derived using the theory of dimensional analysis. This is presented in chapter VII along with a comparison of experimental data obtained from the current work and that from literature. The results in chapter VII have been submitted for publication and is listed as paper-5 in the next section.

Finally, the conclusions drawn from the present study on understanding the compression and combined compression-torsion loading behavior of fiber composites are presented in chapter VIII along with suggestions for future work.

1.6 Publications Related to this Thesis

1. Lee, S.H., Chandra S. Yerramalli and A. M. Waas, 2000, "Compressive splitting response of glass-fiber reinforced unidirectional composites," Composite Science and Technology, 60:2957-2966.

2. Yerramalli, Chandra S. and A. M. Waas, 2002, "In-situ matrix shear response using torsional test data of fiber reinforced unidirectional polymer composites," ASME Trans. Journal of Engineering Materials and Technology, 124:152-159.

3. Yerramalli, Chandra S. and A. M. Waas, 2002, "Compressive splitting failure of composites using modified shear lag theory," International Journal of Fracture, 115:27:40.

4. Yerramalli, Chandra S. and A. M. Waas, 2003, "A failure criterion for fiber reinforced polymer matrix composites under combined compression-torsion loading," to appear in International Journal of Solids and Structures.

5. Yerramalli, Chandra S. and A. M. Waas, 2002, "A non-dimensional number to classify composite compressive failure," in review.

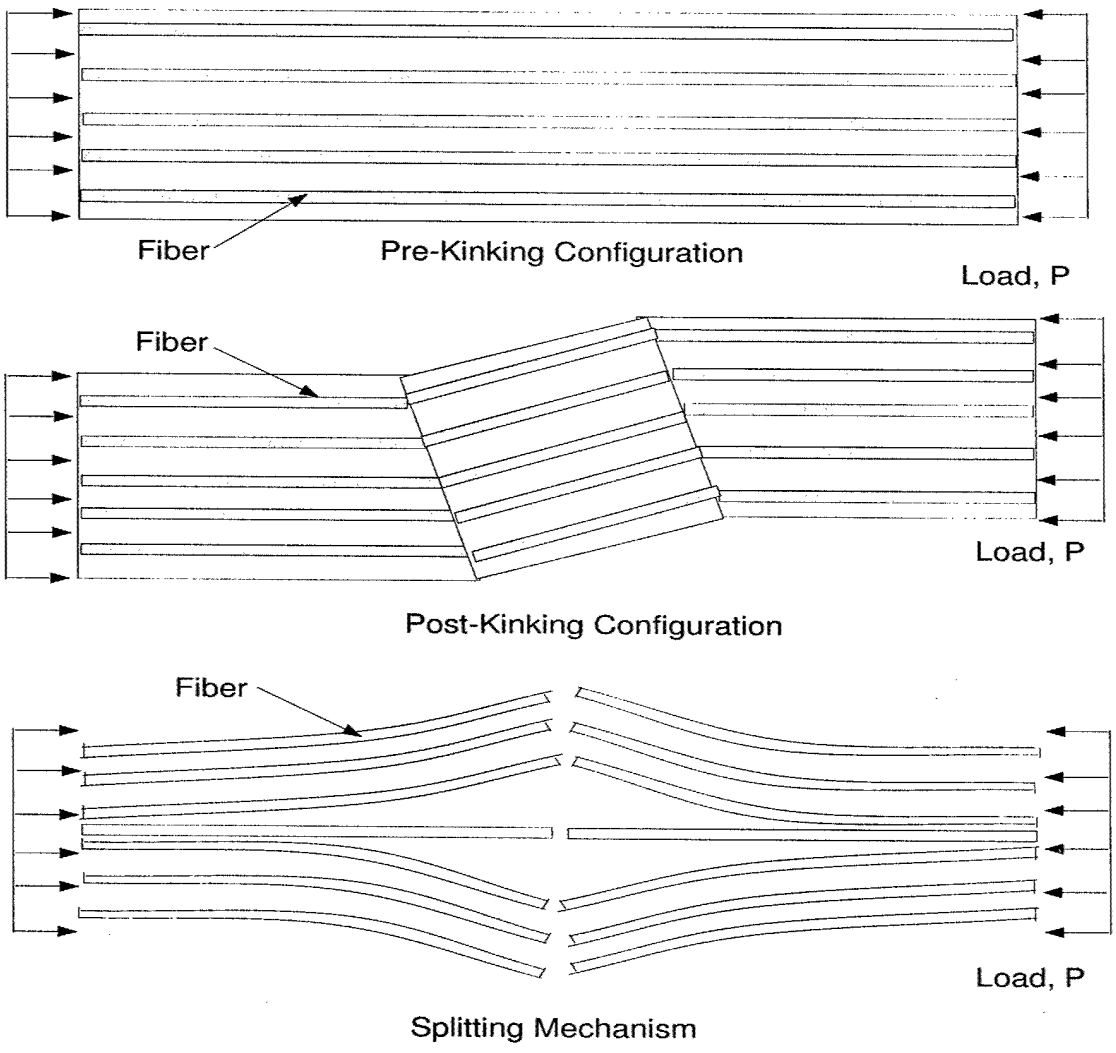

Figure 1.1: Schematic of failure mechanisms in FRPC

CHAPTER II

SHEAR RESPONSE OF POLYMER MATRIX COMPOSITES

2.1 Introduction

The response of fiber reinforced polymer composites when subjected to pure torsional loading is presented in this chapter. The response of glass and carbon FRPC under torsional loading is used to understand the behavior of in-situ matrix. In most cases, when studying the behavior of composites under various loadings, the matrix properties are taken to be equal to those of a pure matrix i.e. containing no inclusions like fibers. In the manufacturing of polymer matrix composites, it is usual to subject the composite to an elevated temperature in order to improve the curing of the polymer matrix and to accelerate the curing process. The addition of heat to the polymer system containing fibers and the subsequent cooling causes residual stresses to develop in the matrix. These residual stresses in a cured composite need to be accounted for in the analysis of a composite material. A knowledge of the effective properties of the in-situ matrix and it's subsequent use in analysis is one way to account for the physical and chemical changes that the matrix has undergone during the process of manufacturing of fiber reinforced polymer matrix composites. The measurement of the equivalent shear mechanical properties (which are referred to as

in-situ matrix shear properties) is the subject of this chapter. Unidirectional glass and carbon fibers embedded in a vinylester resin system are used as the material system for investigating the in-situ vinylester matrix properties in the present investigation. Polymer resins when mixed with a curing agent and polymerized, either at room temperature or at elevated temperature, form a solid network of cross linked polymers [see Agarwal and Broutman (1983)]. The presence of inclusions like fibers in the vinylester system causes changes in the polymerization at the vicinity of the fibers. The vinylester resin in the vicinity of the fiber which adheres to the fiber surface has different mechanical properties as compared to that of the same vinylester resin away from the fiber surface. The presence of fibers also causes a nonuniform distribution of temperature across the composite cross section during the process of curing. This, along with the differences in the coefficient of thermal expansion of the fiber and the matrix leads to the development of residual stresses. The final state of a cured vinylester depends to a large extent on the vinylester prepolymer, curing agent and also the absence or presence of inclusions. All these factors lead to a difference in the effective mechanical properties of the matrix in the presence of inclusions as compared to a pure matrix that has undergone the same thermal history. The characterization of the in-situ matrix properties is important in order to better understand the role of the matrix system in the composite as a whole. Very few studies have been done to characterize the behavior of the in-situ matrix. Yet, as has been shown by Kyriakides et al. (1995), who studied the in-situ shear behavior of a PEEK resin system for use in their compression studies, characterization of the in-situ matrix behavior is key to obtaining a better understanding of the failure mechanisms of composites, especially under compression. In their study, Kyriakides et al. (1995) assumed the fibers to be rigid in shear to determine the

matrix properties.

Of concern in the present chapter is the effect of fiber volume fraction and fiber mechanical properties on the in-situ shear properties of a vinylester thermosetting resin. The in-situ matrix values obtained have been explained by appealing to a 3 cylinder model of the composite as shown in Figure 2.1. The 3 cylinder model as can be seen from the figure consists of three concentric cylinders of fiber, interphase and matrix. The interphase properties and its characteristics are computed as shown in the present paper. Experimental studies by Piggot et al. (1986) and Pompe and Mader (2000) and various other researchers have shown that the interphase has properties different from that of the fiber as well as the matrix. It has furthermore been postulated by Waas (1992); Williams et al. (1990), that the properties of this layer are weaker than that of the matrix and the fiber in which case it has a degrading influence on the strength and stiffness of the composite. A comparison of the predictions of the 3 cylinder model and the 2 cylinder model with the experimental results for composite shear modulus are presented in this chapter.

The formation of the interphase layer is due to the non-uniform temperature distribution during the curing phase, caused by the presence of fibers in the uncured polymer. Drzal et al. (1982b, a) have suggested that the interphase formation is due to the diffusion of molecules of the hardener from matrix into fiber sizing. The temperature distribution in the polymer matrix at low fiber volume fractions is nearly uniform and the number of fibers present are comparatively few to cause any significant perturbation to the temperature field in the polymerization process of the polymer matrix that occupies most of the volume in the composite. Consequently, the matrix properties are not significantly degraded and hence the 2 cylinder model with pure matrix properties can predict the composite shear modulus with

reasonable accuracy in the low fiber volume fraction range. At higher fiber volume fractions, the fibers are relatively closely spaced and the interphase of two fibers may overlap with each other causing near elimination of the pure matrix region. Here again a two cylinder model based on a new set of matrix properties can predict the composite shear modulus quite effectively. Notice that now, the new set of matrix properties correspond to the totally interacting interphase layer. At the intermediate fiber volume fractions one needs to explicitly account for the presence of a discrete interphase. For these intermediate fiber volume fractions, a 3 phase model incorporating a stiff interphase can be used to predict the shear modulus with improved accuracy.

2.2 Experiments

2.2.1 Materials and Chemicals

For the present study two types of fibers, glass (E-glass 24μm diameter) and carbon (5μm diameter) along with vinyl-ester resin were used to manufacture composite specimens. The E-glass shear modulus, G_f=26.7GPa and carbon fiber shear modulus, G_f= 8.96GPa were obtained from Hyer and Waas (2000). Vinyl-ester (Dow-Derakane 411-C50) resin was mixed with initiator Benzoylperoxide (1% of weight of resin) and stirred till the initiator completely dissolves. The resin was then pressurized through glass tubes containing fibers. The inner diameter of the glass tubes is 6.8mm. The manufactured samples are cylindrical in shape and made of glass fibers or carbon fibers and vinylester resin in suitable proportion based on the fiber volume fraction (V_f) required. The manufacturing setup consists of a pressurizing unit and a resin reservoir. The resin from the reservoir is pressurized into the glass tubes initially filled with the fibers. Air pressure is used to force resin into

the glass tubes . The resin is cycled through the glass tubes till all the fibers are properly wetted and air bubbles are absent in the glass tubes. They are then placed in a oven and heated for 2 Hrs at 80^0 Celsius after which the tubes are allowed to cool down to room temperature. After the cooled samples have sat for 24 hours, the glass tubes containing the composites are cut into required length using a low speed Extec diamond saw. A detailed description of the sample preparation can be found in appendix A.

2.2.2 Test Procedure

Torsion tests were performed using an angular rotation control test setup. The specimens were 6.8 mm in diameter and the gage length of the specimens was approximately 35 mm. Specimens of glass/vinylester and carbon/vinylester composites of V_f ranging from 10% - 60% were tested, with approximately 3 specimens at each V_f. In addition to the composite specimens, cylindrical rod specimens made of pure vinylester material(pure matrix) were also tested to obtain the shear stress-strain curve of the pure matrix. The tests were performed using an Enduratech universal testing machine. The specimens were initially unloaded to release the tension induced in the specimen due to the tightening of the grips. The specimens were next subjected to a uniform rate of twist of 0.0635^0/min to 100^0. Some of the specimens were unloaded till the resultant torque reduced to zero as shown in Figure 2.2 and the cross-section was examined under a optical microscope. Moreover, the specimens were cross sectioned at varying radii r1, r2 and r3 as shown in Figure 2.3. The angle of inclination of fibers in the unloaded specimens were measured from the cross section pictures and then plotted as a function of distance of cross section from the center of the specimen. It can be seen that the angle γ increases approx-

imately in a linear manner with 'r' (Figure 2.4). It was observed that apart from some glass/vinylester specimens with $V_f = 10\%$, none of the specimens failed during the loading upto the final rotation angle of 100^0. The strain in the specimens were calculated using both the rotational data as well as from strain gages placed on the specimens. Three strain gages were placed on the specimen with two back to back along the axial direction and one at an angle of 45^0 to the axis of rotation. The axial strain gages were used to record the initial strain developed in the specimen due to the tightening of the grips. The reading of the strain gage placed along the 45^0 angle, in conjunction with standard strain transformation rules, is used to obtain the shear strain in the specimen. The torque vs twist data was also acquired digitally and was used to determine the shear stress in the specimen. Typical shear response curves for glass and carbon/vinylester composites as a function of fiber volume fraction are shown in Figure 2.5 and Figure 2.6. A Ramberg-Osgood fit to the experimental data was obtained and the values of Ramberg-Osgood parameters A and n are presented in Table 2.1 for glass and carbon/vinylester composites tested. In the present paper, attention is focussed only on the stress-strain behavior upto the point of maximum twist.

2.2.3 Shear Stress Analysis

The use of a solid cylinder for torsion tests precludes the possibility of using the standard torsional formula for calculation of shear stress. The shear stress in a solid cylinder varies non-linearly across the specimen cross section for large rotations. Hence, a formulation based on the work of Nadai (1950), which has been generalized by Lyon (1991) was used. If γ is the shear strain in the specimen (Figure 2.7), then

$$\gamma = \frac{r\theta}{L} \tag{2.1}$$

$$T = 2\pi \int_0^R \tau(r) r^2 dr \tag{2.2}$$

Here, T is the torque acting on the solid cylinder, $\tau(r)$ is the shear stress on any cross section at a radius 'r', θ is the angle of rotation of one end of the specimen with respect to the other and L is the specimen length. Eqn. (2.1) describes the relation for shear strain γ. Making the substitution, $\psi = \frac{\theta}{L}$ results in $r = \frac{\gamma}{\psi}$. The relation for applied torque in terms of the shear stress can be written as follows

$$T = \frac{2\pi}{\psi^3} \int_0^{\gamma(\psi)_R} \tau(\gamma) \gamma^2 d\gamma \tag{2.3}$$

In Eqn. (2.3), $\tau(\gamma)$ is a single valued function of strain. Differentiating this equation with respect to ψ and then rearranging the terms, results in Eqn. (2.4). Eqn. (2.4) was used to calculate the shear stress from experimental data.

$$\tau_R = \frac{3}{2\pi R^3} [T + \frac{1}{3} \theta \frac{dT}{d\theta}] \tag{2.4}$$

In Eqn. (2.4), R is the radius of the composite specimen and T is the applied torque. From the torsional tests of the glass/vinylester and carbon/vinylester composite specimens, the shear modulus for different V_f was obtained as shown in Table 2.2 and Table 2.3.

2.3 Test Results

A Ramberg-Osgood fit was made to the test data obtained from the torsional tests of composite specimens of V_f ranging from 10%-60%. This equation expresses shear strain in terms of shear stress in a power law fit as shown below.

$$\gamma = \gamma_e + (\frac{\tau}{A})^n \tag{2.5}$$

Differentiating Eqn. (2.5) with respect to τ provides a relation between the shear modulus and the shear stress for the composite as shown below.

$$\frac{d\gamma}{d\tau} = \frac{d\gamma_e}{d\tau} + \frac{n\tau^{(n-1)}}{A^n} \tag{2.6}$$

$$\frac{1}{G_{12}} = \frac{1}{G_e} + \frac{n\tau^{(n-1)}}{A^n} \tag{2.7}$$

In Eqn. (2.6) and Eqn. (2.7), G_{12} is the tangent shear modulus of the composite, G_e is the shear modulus in the linear range and A and n are the Ramberg-Osgood parameters to be determined from curve fitting. From Eqn. (2.6) a plot of the tangent longitudinal shear modulus of the composite G_{12} as a function of shear stress was obtained. Then, using the Halpin-Tsai equations, Eqn. (2.9), as given in the text by Daniel and Isahi (1994), the matrix shear modulus was determined.

$$G_m = G_{12}\frac{(1-\eta_2 V_f)}{(1+\zeta_2\eta_2 V_f)} \tag{2.8}$$

where $\zeta_2 = 1$ and $\eta_2 = \frac{(G_f - G_m)}{(G_f + \zeta_2 G_m)}$

for $\zeta_2 = 1$, the expression for G_{12} becomes

$$G_{12} = G_m\frac{(G_{12f} + G_m) + V_f(G_{12f} - G_m)}{(G_{12f} + G_m) - V_f(G_{12f} - G_m)} \tag{2.9}$$

where G_{12} is the composite shear modulus, G_{12f} is the fiber shear modulus, and G_m is the matrix shear modulus. The in-situ shear modulus of the matrix was calculated from Eqn. (2.9) assuming the fiber to be linearly elastic. In addition, the corresponding stress-strain curve of the in-situ matrix was also obtained. From the stress-strain curve, the value of yield stress based on the $0.7G$ intercept rule of Jelf and Fleck (1994a) was obtained as shown in Table 2.4 and Table 2.5. A comparison of the yield stress obtained from different volume fractions has been made. The

variation of the in-situ shear modulus as a function of fiber volume fraction, V_f has been explained by developing a 3 cylinder model. The development of this 3 cylinder model incorporating the concept of interphase is presented in the next section.

2.4 Interphase Model

In this section a micromechanics model including the interphase as a distinct phase between the fiber and matrix is developed. The modeling approach is similar to the one taken by Hashin (1966) and also given in Hyer and Waas (2000) using the composite cylinder model. Instead of two cylinders, we assume the composite representative volume element to be composed of three cylinders, fiber, interphase, and matrix with radii r_a, r_b, and r_c respectively. Referring to Figure 2.1, let γ_0 be the shear strain acting on the fiber, matrix and interphase in the $X_1 - X_2$ plane. Consider u, v and w as the axial, circumferential and radial displacement, respectively, of the composite as a whole. As a result of the applied shear strain, γ_0, the displacements can be written in cylindrical coordinates as follows.

$$u = 0, \quad v = -\gamma_0 x sin(\theta), \quad w = \gamma_0 x cos(\theta) \tag{2.10}$$

Furthermore, assume that the three phases are transversely isotropic and subjected to only shear strains, with the specified displacement field (Eqn. (2.10)). The displacement components for fiber can be written in a simplified manner as follows.

FIBER

$$\begin{aligned} u^f(x,\theta,r) &= (A^f r + \frac{B^f}{r})cos(\theta) \\ v^f(x,\theta,r) &= -C^f x sin(\theta) \\ w^f(x,\theta,r) &= C^f x cos(\theta) \end{aligned} \tag{2.11}$$

INTERPHASE

$$\begin{aligned} u^i(x,\theta,r) &= (A^i r + \frac{B^i}{r})cos(\theta) \\ v^i(x,\theta,r) &= -C^i x sin(\theta) \\ w^i(x,\theta,r) &= C^i x cos(\theta) \end{aligned} \tag{2.12}$$

MATRIX

$$\begin{aligned} u^m(x,\theta,r) &= (A^m r + \frac{B^m}{r})cos(\theta) \\ v^m(x,\theta,r) &= -C^m x sin(\theta) \\ w^m(x,\theta,r) &= C^m x cos(\theta) \end{aligned} \tag{2.13}$$

where A^f, B^f, C^f, A^i,B^i,C^i,A^m,B^m, C^m are the nine unknown constants which need to be determined from the boundary value problem. Using the above expressions for the displacements, the resulting non-zero stresses can be expressed as follows

$$\begin{aligned} \tau^f_{xr} &= G_{12f}(A^f + C^f - \frac{B^f}{r^2})cos(\theta) \\ \tau^f_{x\theta} &= -G_{12f}(A^f + C^f + \frac{B^f}{r^2})sin(\theta) \end{aligned} \tag{2.14}$$

$$\begin{aligned} \tau^i_{xr} &= G_{12i}(A^i + C^i - \frac{B^i}{r^2})cos(\theta) \\ \tau^i_{x\theta} &= -G_{12i}(A^i + C^i + \frac{B^i}{r^2})sin(\theta) \end{aligned} \tag{2.15}$$

$$\begin{aligned} \tau^m_{xr} &= G_m(A^m + C^m - \frac{B^m}{r^2})cos(\theta) \\ \tau^m_{x\theta} &= -G_m(A^m + C^m + \frac{B^m}{r^2})sin(\theta) \end{aligned} \tag{2.16}$$

In order to find the 9 unknown constants we use the following boundary/matching conditions to generate the equations required to solve for the unknown constants. The first condition requires the stresses and displacements to be nonsingular at $r = 0$

(in the interior of the fiber). To ensure this condition we take B^f=0. The second condition ensures the continuity of displacements across the fiber-interphase and interphase-matrix interface. Thus,

At $r = r_a$, Fiber-Interphase interface

$$u^f = u^i, \quad v^f = v^i, \quad w^f = w^i \tag{2.17}$$

At $r = r_b$, Interphase-Matrix interface

$$u^m = u^i, \quad v^m = v^i, \quad w^m = w^i \tag{2.18}$$

Similarly, ensuring the continuity of shear stress, τ_{xr}, across the interfaces will generate two more equations.

At $r = r_a$, Fiber-Interphase interface

$$\tau^f_{xr_a} = \tau^i_{xr_a} \tag{2.19}$$

At $r = r_b$, Interphase-Matrix interface

$$\tau^i_{xr_b} = \tau^m_{xr_b} \tag{2.20}$$

At the outer boundary $r = r_c$, the displacements should match the applied boundary displacements. Thus,

$$\begin{aligned} u = 0 \quad &\Rightarrow \quad (A^m r_c + \frac{B^m}{r_c^2})cos(\theta) = 0 \\ v^m(x,\theta,r_c) \quad &= \quad -Cxsin(\theta) = -\gamma_0 xsin(\theta) \\ w^m(x,\theta,r_c) \quad &= \quad Cxcos(\theta) = \gamma_0 xcos(\theta) \end{aligned} \tag{2.21}$$

Using equations (2.17) to (2.21), we obtain the expressions for all the constants in terms of the unknown γ_0. Once the constants are determined, we write the expression

for shear stress at $r = r_c$ and $\theta = 0$ as follows.

$$\tau_{xr} = \tau_{12} = G_m(A^m + C - \frac{B^m}{r_c^2}) \tag{2.22}$$

The above Eqn. (2.22) can be expressed as

$$\tau_{12} = G_{12}^c \gamma_0 \tag{2.23}$$

where the coeffecient of γ_0 on the right hand side of the expression in Eqn. (2.23) can be identified as the shear modulus of the 3 cylinder composite. The expression for G can be written as

$$G_{12}^c = -G_m \frac{\alpha V_{im}^2 + \beta V_{im} + \delta(V_f + V_f^2) + \theta(V_f - Vf^2)}{\alpha V_{im}^2 + \eta V_{im} - \theta(V_f + V_f^2) - \delta(V_f - Vf^2)} \tag{2.24}$$

The expressions for α,β,δ,θ,η are listed below

$$\begin{aligned}
\alpha &= (R_{fm}R_{im} + R_{im}^2 - R_{fm} - R_{im}) \\
\beta &= (R_{im} + 3R_{fm}R_{im}V_f + R_{im}^2 + R_{fm}R_{im} + R_{fm} + \\
&\quad R_{im}^2 V_f - 3R_{im}V_f - R_{fm}V_f) \\
\delta &= 2R_{fm}R_{im} \\
\theta &= 2R_{im} \\
\eta &= (-R_{im} + 3R_{fm}R_{im}V_f - R_{im}^2 - R_{fm}R_{im} - \\
&\quad R_{fm} + R_{im}^2 V_f - 3R_{im}V_f - R_{fm}V_f)
\end{aligned}$$

Where $R_{im} = \frac{G_{12i}}{G_m}$, $R_{fm} = \frac{G_{12f}}{G_m}$, $V_{im} = \frac{r_c^2 - r_b^2}{r_c^2}$ and $V_f = \frac{r_a^2}{r_c^2}$. The above expression for G_{12}^c reduces to the corresponding expression of the two cylinder model in the limit $G_{12i} \to G_m$. In the above expression G_m is the shear modulus of pure matrix and G_{12}^c is the experimentally determined shear modulus of composite. Also the

above expression contains interphase radius as a variable. In the present work we assume a interphase shear modulus which is slightly stiffer than the pure matrix shear modulus which leads to a value of interphase radius which is decreasing with fiber volume fraction. A detailed discussion on the in-situ matrix and its behavior as a function of fiber volume fraction, V_f, is presented in the next section.

2.5 Discussion

It was observed that the in-situ matrix shear stress-strain curve obtained was bounded by the curves of the corresponding composite and that of the pure matrix for glass/vinylester composite as shown in Figure 2.8. However, the in-situ matrix shear stress-strain curve for carbon/vinylester composite is 'softer' than the pure matrix as shown in Figure 2.9. As V_f increases, predicted values of the in-situ matrix shear modulus are 'softer' than the pure matrix. This trend is indicated in Figure 2.10 and Figure 2.11. The in-situ shear modulus of the matrix obtained from the data corresponding to the glass/vinylester matrix was found to be higher than the corresponding value obtained from the corresponding data for the carbon/vinylester matrix specimens, though the difference between the two narrows down as the fiber volume fraction increases (Figure 2.12). The in-situ shear modulus obtained from the glass/vinyl ester composite is found to be higher than the pure matrix shear modulus but decreases as the fiber volume fraction increases. In the case of carbon/vinyl ester specimens, the in-situ shear modulus is always below the pure matrix modulus as shown in Figure 2.12. These results show that as V_f increases, the in-situ matrix behavior tends to become independent of the mechanical properties of the reinforcement. Indeed, as V_f becomes large, the average spacing between adjacent fibers is reduced. Thus, the zones of inhomogeneity that develop around fibers interact with

each other resulting in an effective but uniform matrix material that is different from the pure matrix cured under the same condition but without the presence of fibers. The zones of inhomogeneity are uniform and indeed tend towards the properties of an effective matrix that has been cured in the presence of a relatively uniform temperature field but in the presence of fibers.

Figure 2.12 shows that the in-situ matrix properties depend to a large extent on the type of composite and also on the fiber volume fraction being considered. It can also be seen that the stiffness of the fiber does play a role in determining the behavior of in-situ matrix properties. In carbon/vinylester composites, the in-situ matrix shear modulus value is lower than that of the pure matrix. For both glass/vinylester and carbon/vinylester composites, the in-situ matrix shear modulus for $V_f = 60\%$ is nearly the same and lower than that of the pure matrix. This indicates that at high fiber volume fractions the in-situ matrix property is reflective of a material that has undergone changes to its mechanical properties due to the thermal history. Thus, the effective matrix material properties are different from the pure matrix properties. It can also be seen from Figure 2.12 that the V_f for which the in-situ matrix shear modulus is maximum is different for glass/vinylester and carbon/vinylester composite.

A comparison of the experimental data for shear modulus as a function of the fiber volume fraction for both glass/vinylester and carbon/vinylester composites with the 2 cylinder model is shown in Figure 2.13. The theoretical predictions of the 2 cylinder model with elastic fiber properties and pure matrix properties as input match the experimental data with reasonable accuracy in the low fiber volume fraction range ($V_f \leq 0.2$) for both types of composite specimens tested. At higher fiber volume fractions ($V_f \geq 0.5$) the predictions tend to be higher than the experimentally observed value

for shear modulus of glass and carbon/ vinylester composites. In the intermediate fiber volume fractions, the predictions of the 2 cylinder model are very much lower than the experimental results. Thus, it can be seen that the higher experimental values observed with the specimens for V_f ranging from $(0.2 - 0.4)$ are due to the presence of an effective matrix that is much stiffer than the pure matrix. In summary, the following scenario emerges. For $V_f \leq 0.2$, a 2 cylinder model with pure fiber and pure matrix properties does an adequate job of predicting the elastic shear modulus. At $V_f \geq 0.4$, a 2 cylinder model can also be used to predict composite properties, but the effective matrix shear modulus that is needed for this is less than that of the pure matrix. For $0.2 \leq V_f \leq 0.4$, a 3 cylinder model is required to properly predict the elastic shear modulus. In this V_f range, the presence of a stiffer interphase must be explicitly accounted for in order to accurately predict the composite modulus.

From the shear modulus data for glass fiber reinforced composites, a relation for the interphase radius r_b as a function of the fiber volume fraction was established. These results are shown in Figure 2.14. It was observed that the interphase radius shows a decreasing trend with fiber volume fraction in the intermediate fiber volume fraction range (0.2-0.4). In this range the interphase modulus is stiffer than that of the pure matrix. This relation was used to predict the composite shear modulus for carbon/vinylester specimens and glass/vinylester specimens and has been shown in Figure 2.13. Thus, the use of a 3 cylinder model is most appropriate for the intermediate fiber volume fraction range. At higher fiber volume fractions a degraded matrix shear modulus should be taken for predicting the composite shear modulus using the expression obtained from the 2 cylinder model.

2.6 Concluding Remarks

In this chapter, we have provided experimental results to show that the in-situ matrix properties of a polymer matrix material are influenced by the fiber volume fraction and the fiber type. It has also been observed in cement composites by Alwan and Naaman (1994), That the specific surface of reinforcement, i.e. the total contact area between fiber and matrix also influences the properties. In the current work the difference in specific surface area could be partially responsible for the difference in interphase properties of carbon and glass composites. This is because the carbon fiber diameter ($d_f = 5\mu m$) is very small compared to glass fiber diameeter, ($d_f = 24\mu m$). The longitudinal shear response of carbon fiber reinforced and glass fiber reinforced unidirectional vinylester composites having a range of fiber volume fraction have been studied. For fiber volume fraction in excess of 0.4, it has been shown that the effective matrix shear response displays an initial elastic modulus that is less than that of the pure matrix. In the following chapter, the steady state splitting model of Lee and Waas (1999) will be extended to the unsteady state case. The results obtained from the splitting model will be compared with experimental data obtained by Lee and Waas (1999) and others in literature.

	glass/vinylester		carbon/vinylester	
V_f	A_g	n_g	A_c	n_c
0.1	77.3	6.15	67	6.62
0.2	101.15	5.8	55.88	10.5
0.3	88.59	5.25	160	3
0.4	158	3	100.7	5.26
0.5	68.68	12.44	159	3.48
0.6	78.71	7.25	98.44	3.25

Table 2.1: Ramberg-Osgood parameters for glass and carbon/vinylester composites

	glass/vinylester			
V_f	S1	S2	S3	$Avg.G_{12}$ (GPa)
0	1.3	1.15	1.23	1.22
0.1	1.45	1.6	1.8	1.616
0.2	2.32	2.46	2.36	2.37
0.3	-	-	2.75	2.75
0.4	3.11	3.0	3.13	3.08
0.5	3.29	3.4	3.26	3.316
0.6	3.73	3.6	3.75	3.75

Table 2.2: Measured values of shear modulus of vinylester matrix composite

carbon/vinylester						
V_f	S1	S2	S3	S4	S5	$Avg.G_{12}$ (GPa)
0.1	1.22	1.5	1.2	1.481	1.6	1.40
0.2	1.79	1.73	1.37	1.8	-	1.673
0.3	2.52	2.72	2.2	2.4	-	2.46
0.4	2.75	2.82	2.5	3.00	-	2.768
0.5	3.15	2.89	2.8	3.15	-	2.99
0.6	3.64	3.33	-	3.75		3.575

Table 2.3: Measured values of shear modulus of vinylester matrix composite

carbon/vinylester			
V_f	G_{Insitu} (MPa)		
	G_{fe}	$0.7G_{fe}$	τ_{ylde}
0.1	1182	828	33
0.2	1108	776	35
0.3	1205	844	13
0.4	1215	851	34
0.5	1013	709	30
0.6	914	640	10

Table 2.4: The predicted values of In-situ matrix shear modulus and yield stress values

glass/vinylester			
V_f	G_{Insitu} (MPa)		
	G_{fe}	$0.7G_{fe}$	τ_{ylde}
0.1	1412	988	36
0.2	1519	1064	43
0.3	1439	1007	30
0.4	1314	920	20
0.5	1073	752	41
0.6	900	630	35

Table 2.5: The predicted In-situ matrix shear modulus and yield stress values

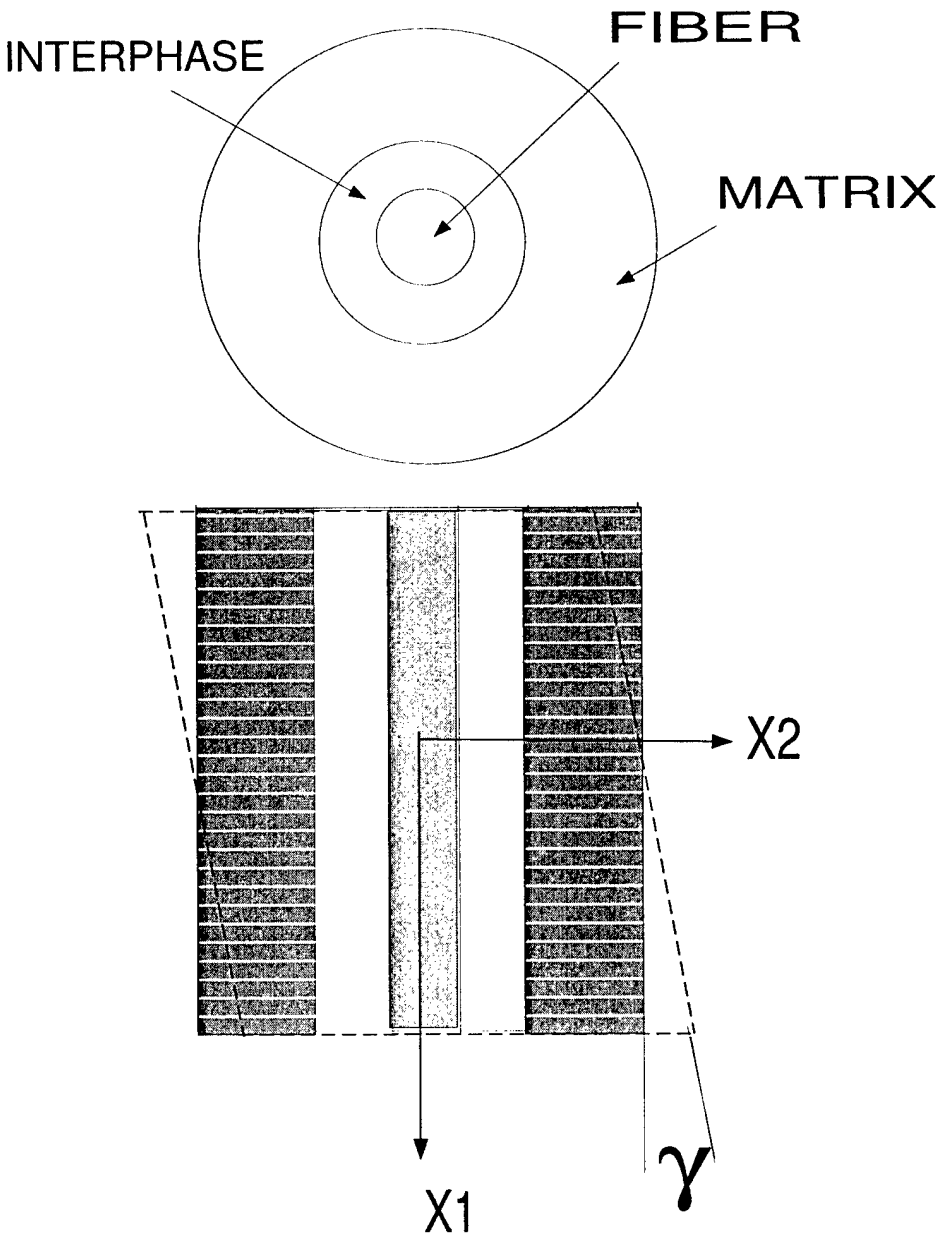

Figure 2.1: Schematic of the 3 cylinder model

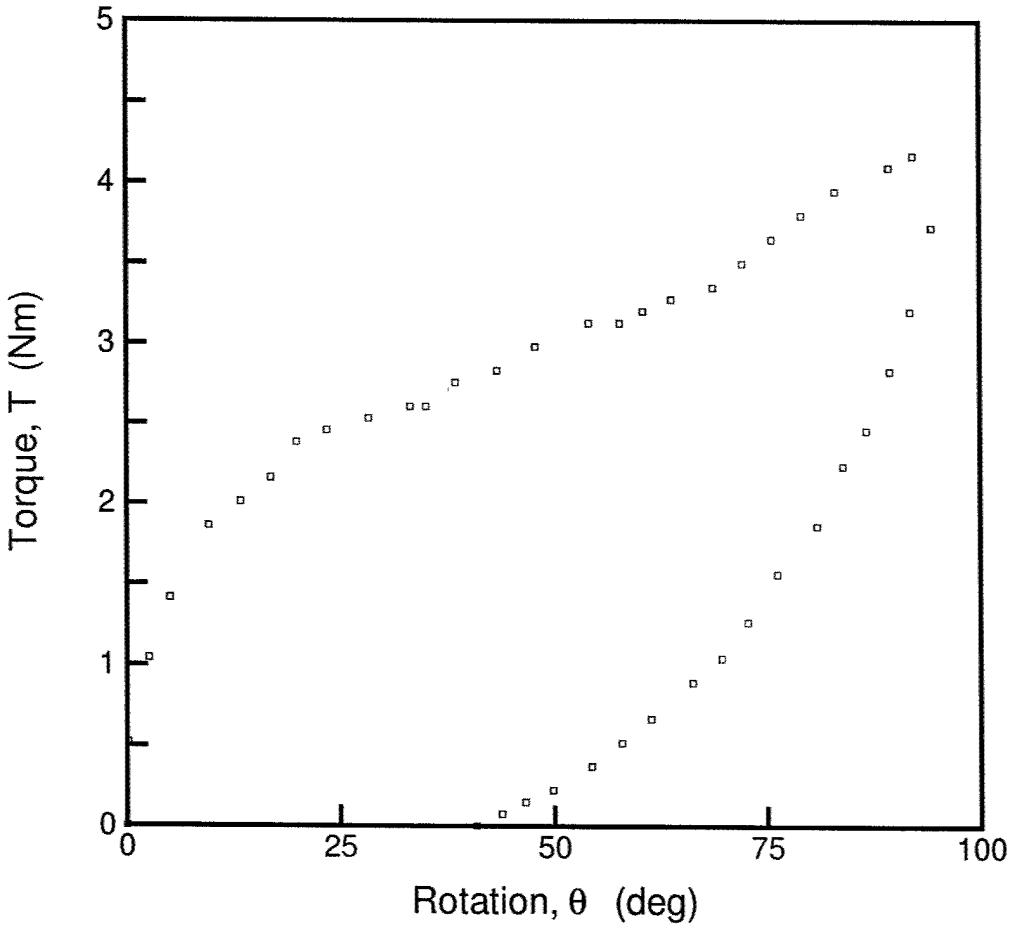

Figure 2.2: Torque (Nm) vs rotation (deg) for a carbon/vinylester composite of $V_f = 60\%$

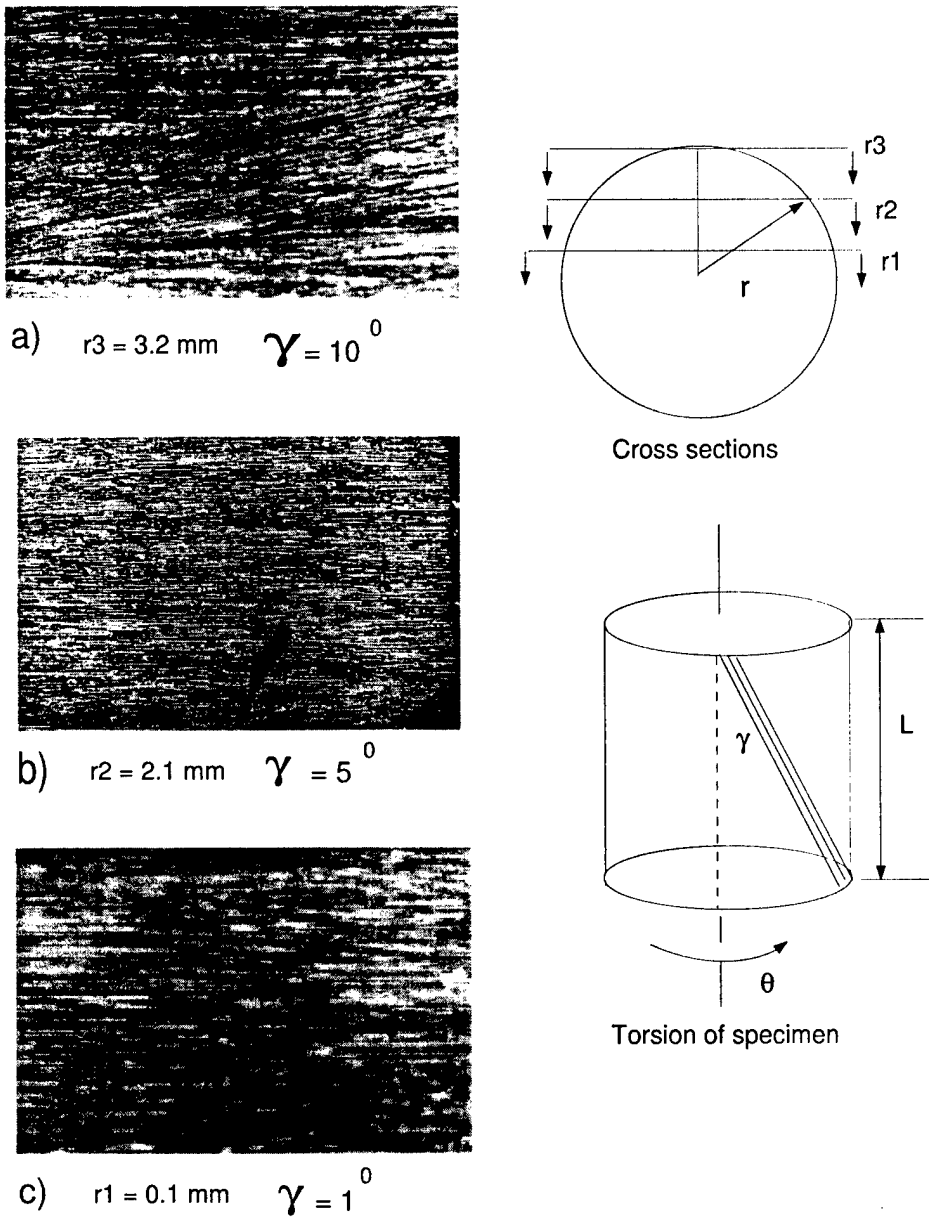

Figure 2.3: Fiber inclination at various cross sections of a torsion specimen

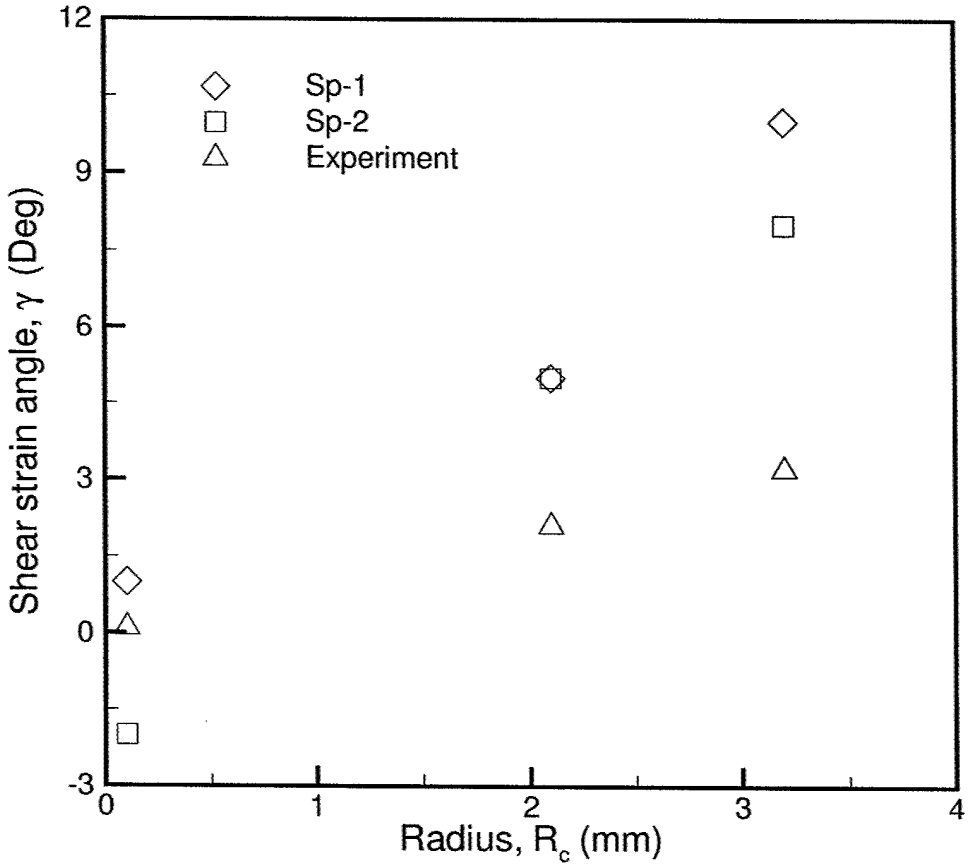

Figure 2.4: Angle of inclination γ as a function of radial distance for a carbon/vinylester composite

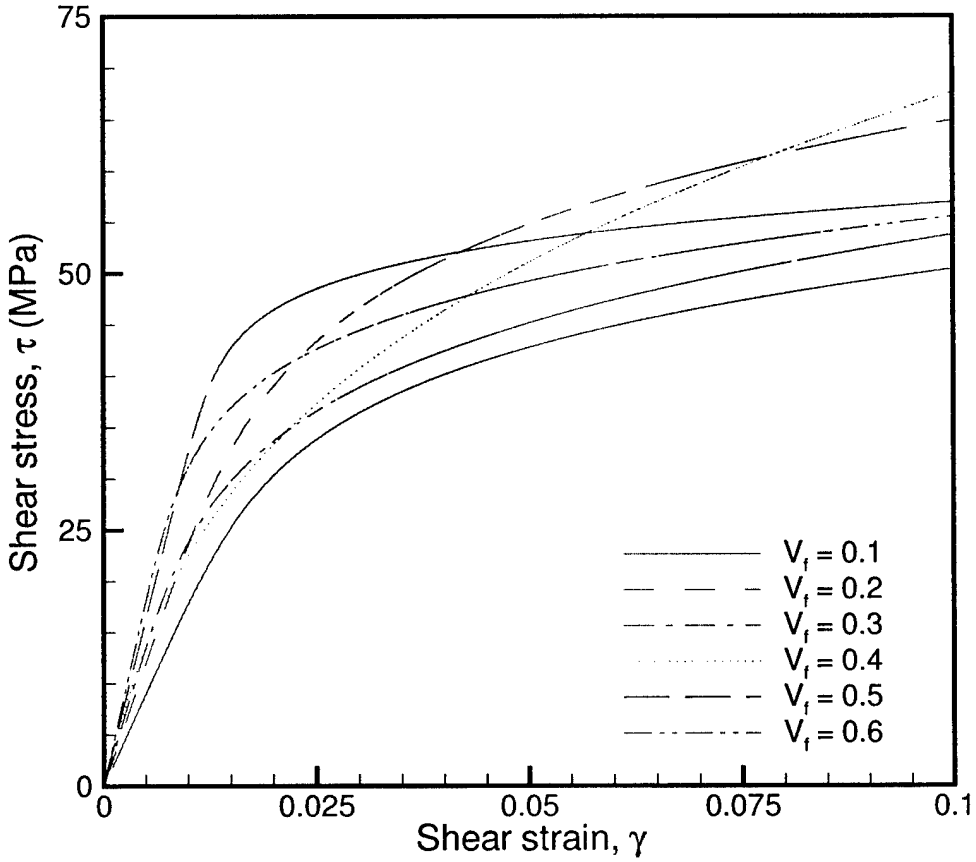

Figure 2.5: Typical shear response curves of glass/vinylester composites

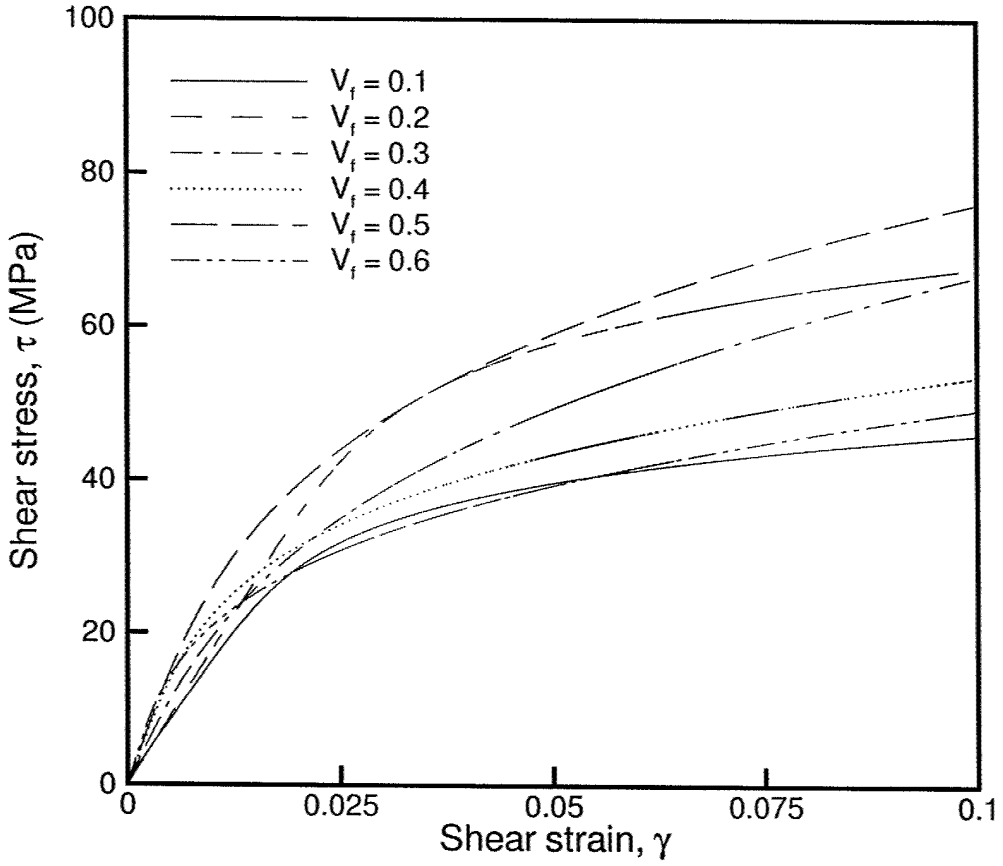

Figure 2.6: Typical shear response curves of carbon/vinylester composites

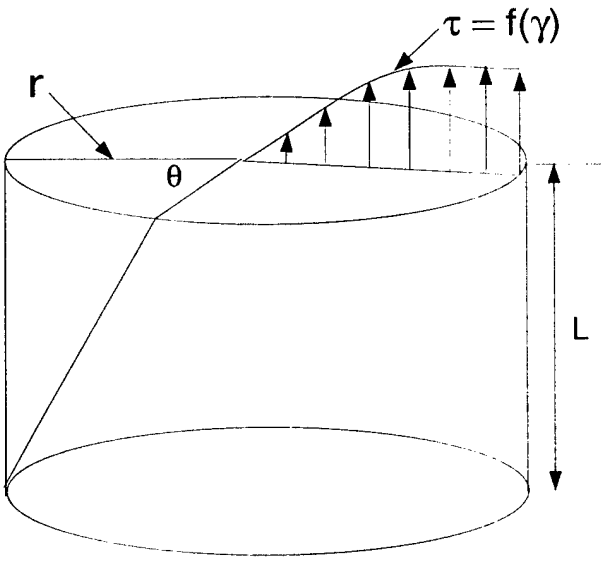

Figure 2.7: A schematic of a solid cylinder under torsion

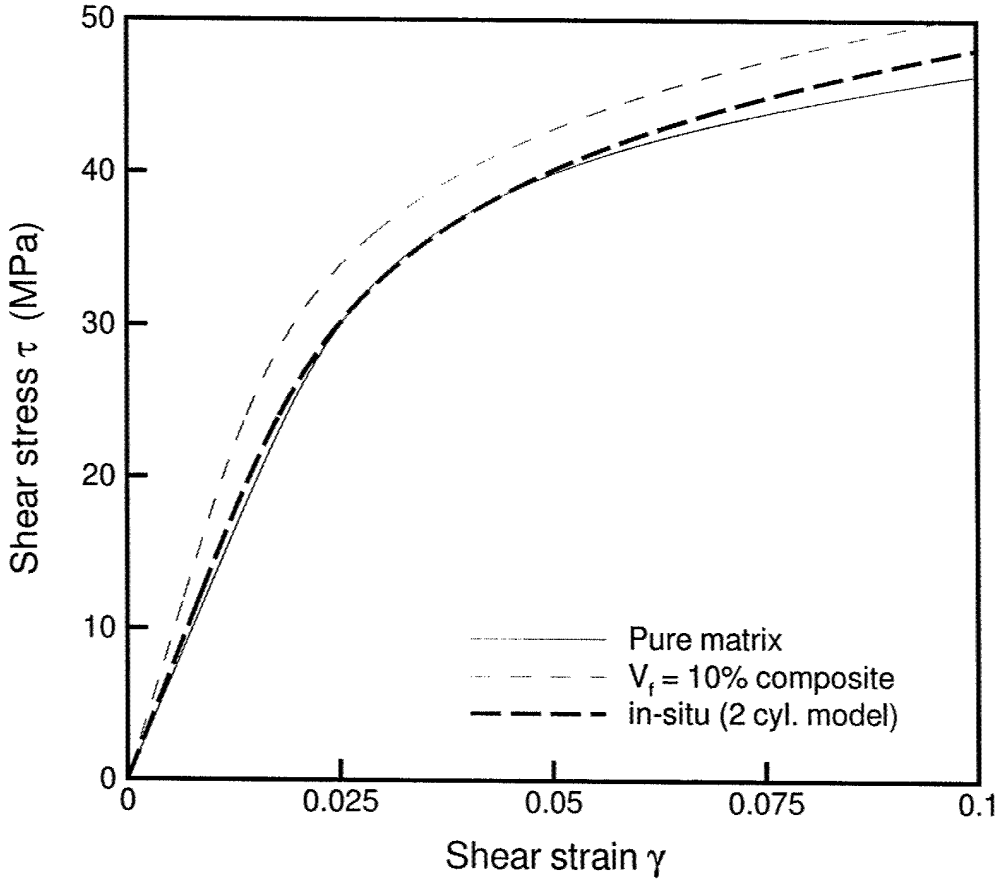

Figure 2.8: Comparison of shear stress-strain curve of glass/vinylester composite, pure matrix and in-situ matrix for $V_f = 10\%$

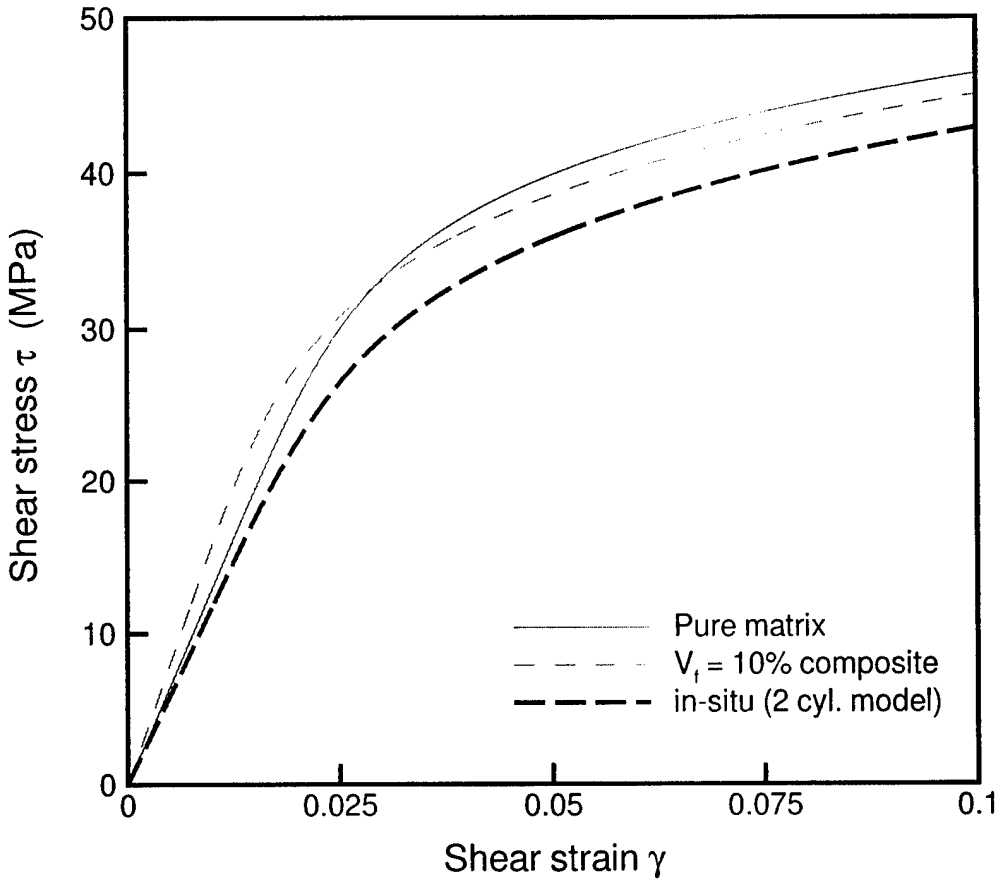

Figure 2.9: Comparison of shear stress-strain curve of carbon/vinylester composite, pure matrix and in-situ matrix for $V_f = 10\%$

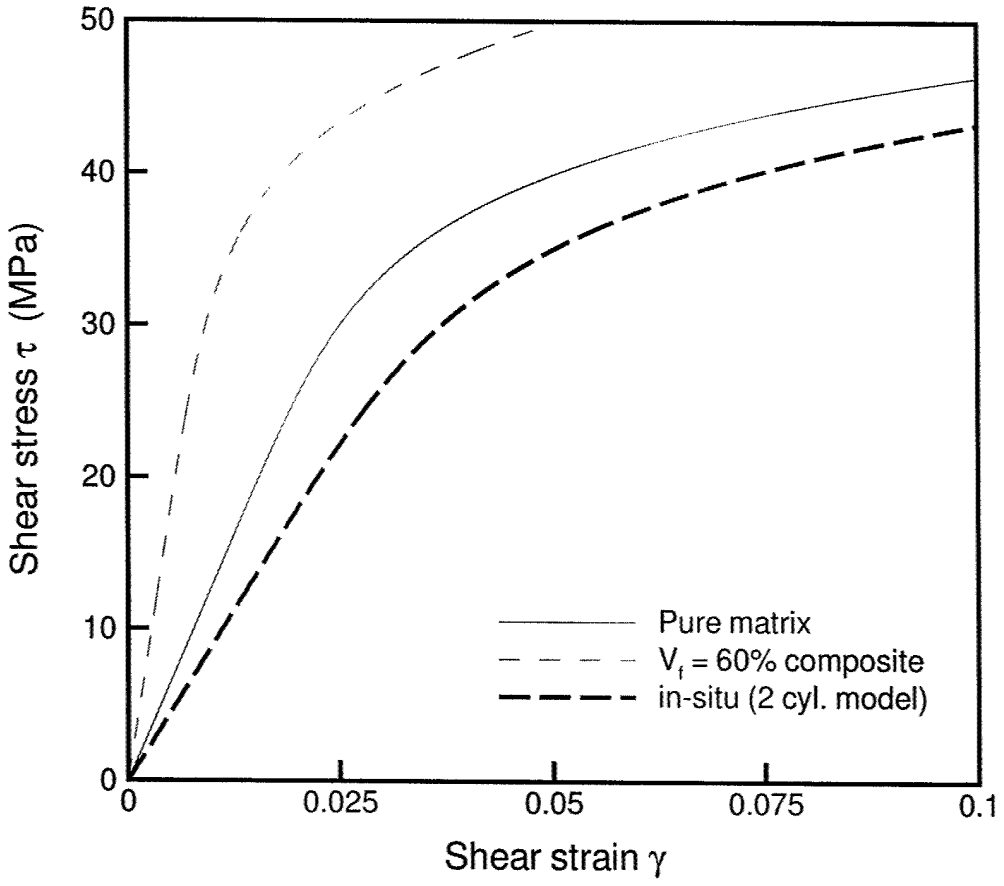

Figure 2.10: Comparison of shear stress-strain curve of glass/vinylester composite, pure matrix and in-situ matrix for $V_f = 60\%$

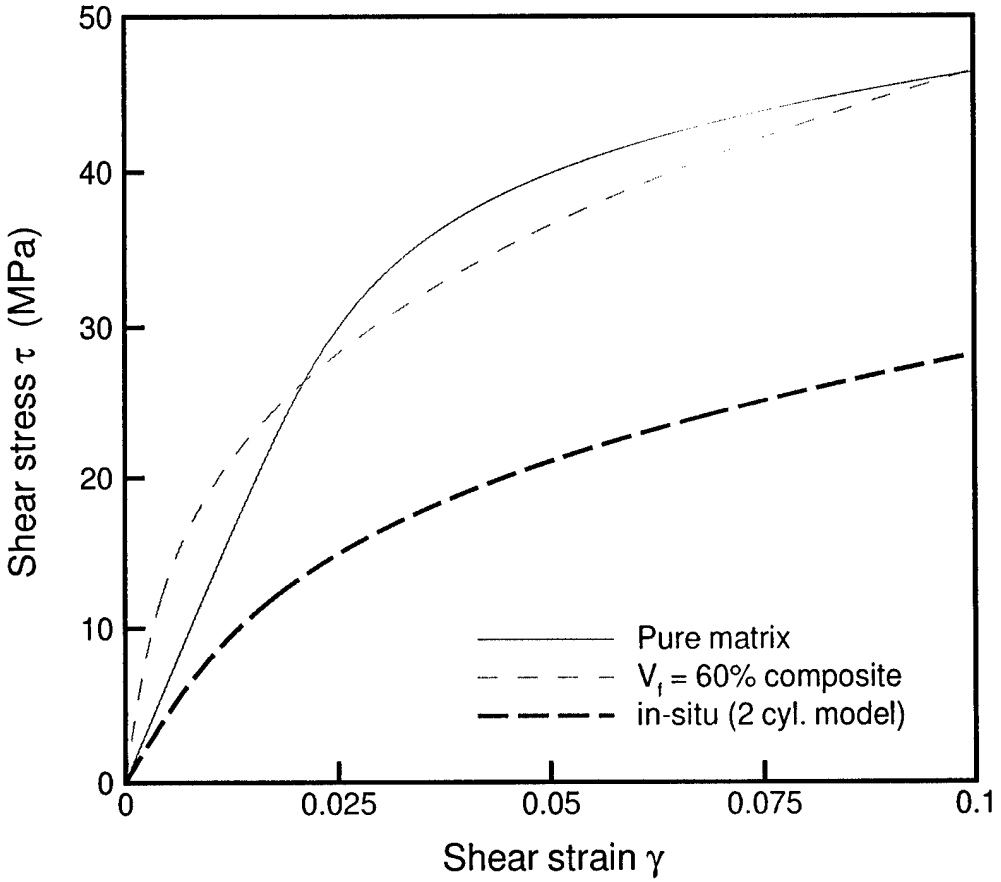

Figure 2.11: Comparison of shear stress-strain curve of carbon/vinylester composite, pure matrix and in-situ matrix for $V_f = 60\%$

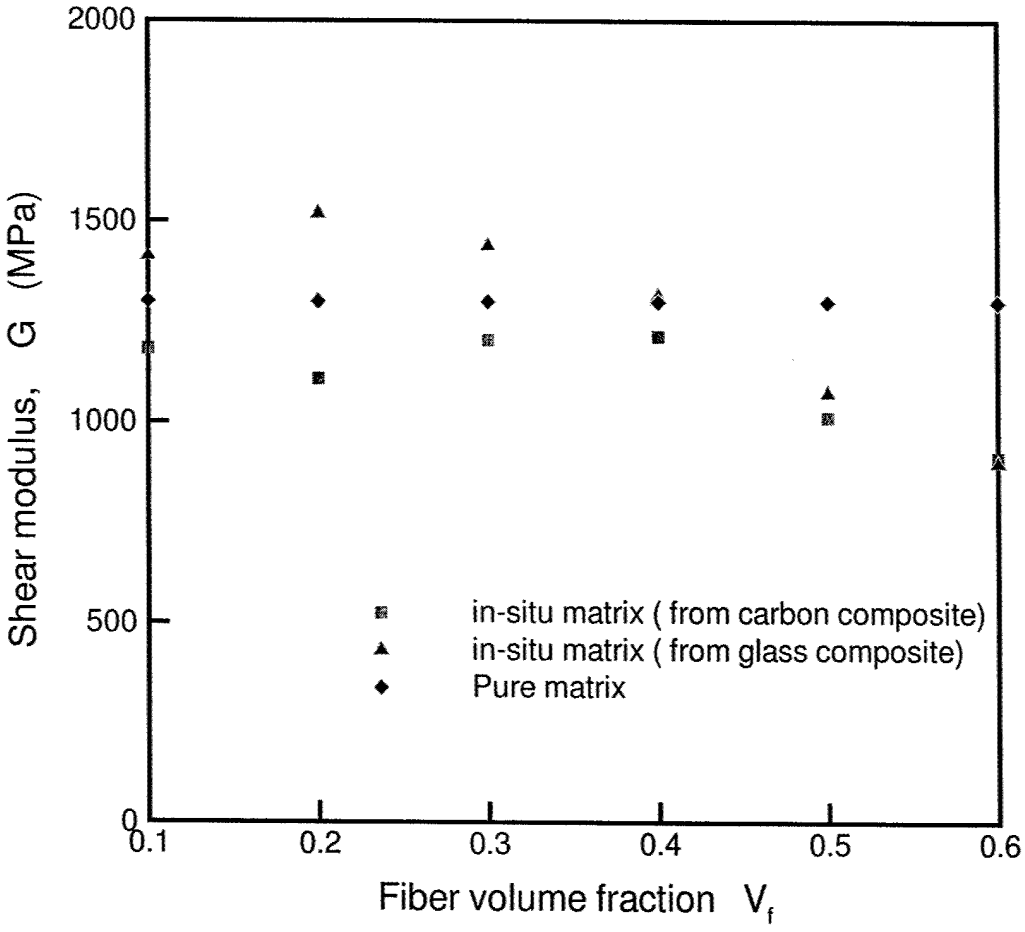

Figure 2.12: Variation of shear modulus of in-situ matrix with fiber volume fraction

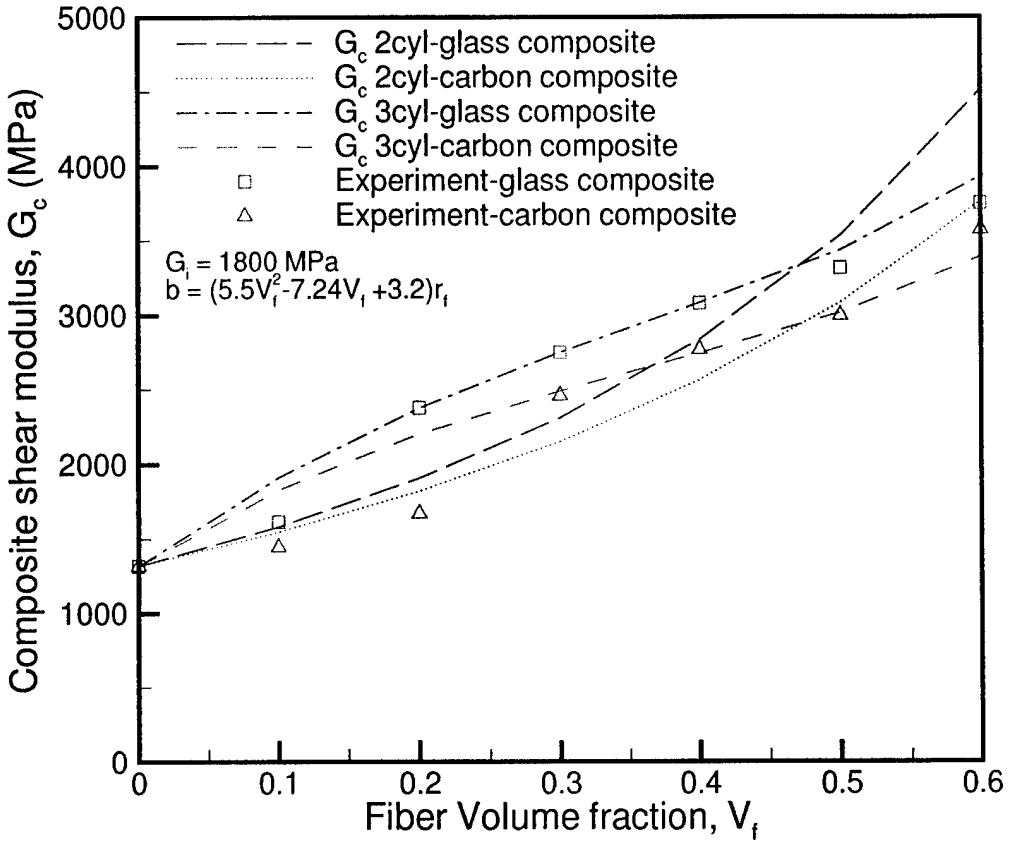

Figure 2.13: Shear modulus of glass/vinylester composite as a function of V_f

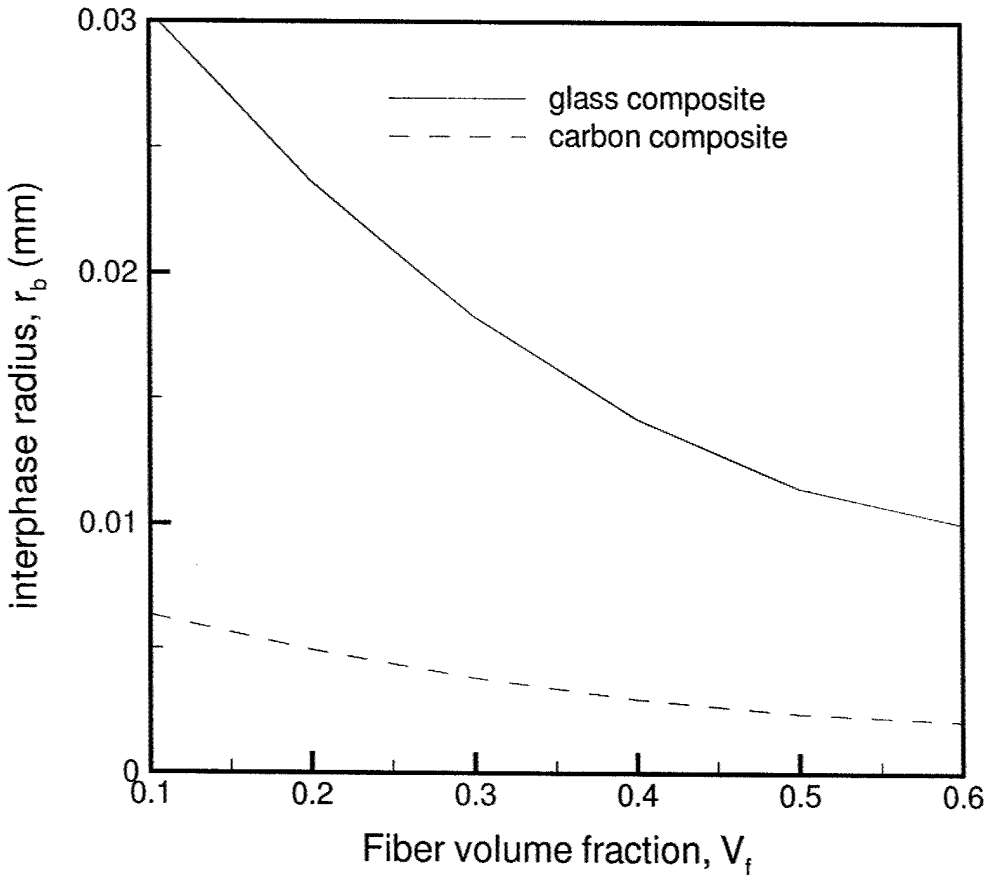

Figure 2.14: Interphase thickness as a function of V_f for G_i=1800MPa

CHAPTER III

AXIAL COMPRESSIVE RESPONSE OF FRPC; NON-STEADY STATE AXIAL SPLITTING

3.1 Introduction

It has long been recognised that the compressive strength of polymer matrix composites is the limiting factor for the use of composites in primary load bearing structures. The compression strength of polymer matrix composites is almost half of its tensile strength. Thus, understanding the behavior of polymer matrix composites under compression loading has been an active area of research as has been mentioned in the first chapter. From the available literature it is clear that the composite compressive strength is found to be dependent on various parameters like fiber radius, fiber-matrix interfacial properties, misalignment of fibers, fiber packing density, fiber volume fraction and strain gradients. Research on developing models to predict the compressive strength of composites have focussed on including the above parameters in their formulation. Various models have been developed previously to predict the compressive strength of aligned composite materials, of which the model by Budiansky and Fleck (1993) is the most widely used. Their model incorporates the effect of matrix plasticity in predicting kink banding in composites. The effect of initial fiber misalignment angle and the axial propagation of kink bands

have been studied experimentally by Kyriakides et al. (1995); Vogler et al. (2001) and Vogler and Kyriakides (2001) in a series of papers. Time dependent effects of kink evolution were studied by Schapery (1995) who also introduced the possibility of matrix cracking and its manifestation to "soften" the matrix response. Daniel et al. (1996) investigated the effect of manufacturing process induced waviness on the compressive failure of carbon fiber composites. Drapier et al. (2001) and Wisnom and Atkinson (1997), have studied the effect of strain gradients on compressive failure and found that the compressive strength increased under bending compression loading compared to pure compression loading. From the experimental investigations carried out by previous researchers, Kyriakides et al. (1995); Fleck (1997); Lee (1998); Lee and Waas (1999) and Oguni and Ravichandran (2000), it can be inferred that the initiating mechanisms for compressive failure of carbon composite materials are usually microbuckling and kinking of fibers aligned along the loading direction.

Lee (1998); Lee and Waas (1999) and Oguni and Ravichandran (2000), observed that glass fiber reinforced polymer matrix composites fail predominantly by splitting. This was observed in the optical photomicrographs which show aligned cracks between the fiber and matrix, indicating that splitting failure is akin to interfacial fiber/matrix fracture. Thus a fracture mechanics based approach was adopted by Lee (1998) and Lee and Waas (1999), to model the splitting failure of polymer matrix composites. Their model was based on linear elastic fracture mechanics and the assumption of steady state crack propagation. Independently, Oguni and Ravichandran (2000) also provided fracture mechanics based expressions for the compression splitting failure stress of composites. These authors also examined the influence of confinement on compression strength. Other important contributions related to studies on composite compressive strength are summarized in the two survey papers

by Waas and Schultheisz (1996) and Fleck (1997).

The work presented in the current chapter is concerned with the splitting mechanism of failure in compression. There are two parts to the present chapter. In the first part, a summary of the experimental results obtained by Lee and Waas (1999) are presented. In the second part, the steady state splitting model developed by Lee and Waas (1999) is extended for non-steady crack propagation in the case of short crack lengths, where the compliance change as a function of crack length is derived using modified shear lag theory. A closed form expression for the compressive splitting strength is obtained. This model is then used to to predict the compressive strength of unidirectional composites. The predicted results are compared with experimental data available in the literature and also that of Lee (1998). The model incorporates the effect of fiber diameter and the initial misalignment angle on the compressive splitting strength of aligned composites.

3.2 Summary of Experimental Results

Lee (1998) carried out a series of experiments to study the static compressive behavior of glass fiber and carbon fiber reinforced unidirectional composites. The specimens were prepared inhouse with vinyl ester resin as the matrix material. Composite specimens with six different fiber volume fractions were manufactured to study the effect of fiber volume fraction on the compressive behavior of glass/epoxy fiber composites. A detailed description of the manufacturing process and the test setup is given in appendix A. Compression tests were performed on cylindrical specimens of diameter 6.8 mm and a gage length of 12.7 mm. The length to radius ratio of the specimen was kept very small to prevent macroscopic buckling in the specimen. All the tests were conducted at room temperature in a hydraulically actuated loading

frame. The tests were performed under load control with a cross head speed of 0.0381 mm/sec. The grips were restrained from moving laterally during the compression tests. Back to back strain gages were attached at the center of the specimens to monitor the compressive strain and any bending strain.

3.2.1 Glass Fiber Composites

From the compression tests, the axial stress-strain response (referred to as the $\sigma - \epsilon$ curve) of the uni-directional glass fiber ($r_0 = 12\mu m$) reinforced vinyl ester resin composites was obtained as a function of the fiber volume fraction. Typical $\sigma - \epsilon$ curves of glass fiber composites obtained by Lee (1998) throughout the volume fraction range $10\% \sim 60\%$ are shown in Figure 3.1. The failure stress obtained by Lee (1998) for glass composites over the range of fiber volume fractions tested are presented in Table 3.1. Typical micrographs of failed glass composite specimens are shown in Figure 3.2 and Figure 3.3. It is seen that fibers are randomly located in the composite specimens. Glass fiber specimens show a splitting mode of failure (sometimes also referred to as "brooming" in the literature) as shown in Figure 3.2. The fiber/matrix interfaces split during failure and the fibers are broken in the process. Notice that fibers that are shown isolated near the region of excessive splitting do not show a smooth surface, instead substantial amounts of the resin remains attached to the fiber. This signifies that the splitting failure does not always occur 'cleanly' along the fiber/matrix interface instead the splitting crack meanders between the fiber/matrix interface and cohesively through the matrix. This also shows that splitting is not necessarily caused by poor adhesion between the fiber and matrix. Clearly, poor adhesion can lead to splitting, but as will be shown later, splitting is influenced by a number of different factors, an adhesive or cohesive fracture toughness being

one of many significant parameters.

For high fiber volume fractions($40\% \sim 60\%$), kink bands are also observed(Figure 3.3). It is postulated that these kink bands are formed on account of the synergy due to the misalignment induced during the axial splitting and the large amount of strain energy that is released at splitting. Indeed, in the glass fiber composites, isolated kink bands were never observed. When kink bands were found they were always accompanied by longitudinal fiber/matrix splitting cracks.

3.2.2 Carbon Fiber Composites

Lee (1998) also conducted compression tests on carbon fiber($r_0 = 2.5\mu m$) reinforced composites.From the compression tests, the axial stress-strain response of the uni-directional carbon fiber reinforced vinylester resin composites was obtained as a function of the fiber volume fraction. Typical $\sigma - \epsilon$ curves of carbon fiber composites obtained by Lee (1998) throughout the volume fraction range $10\% \sim 60\%$ are shown in Figure 3.4. The failure stress obtained by Lee (1998) for carbon composites over the range of fiber volume fractions tested are presented in Table 3.2. In case of carbon fibers the failure mechanism was always observed to be kinking for all the fiber volume fractions tested. Figure 3.5 and Figure 3.6 shows a typical kink band in carbon fiber composites under optical microscope and a high resolution SEM. The width of the kink band was found to be approximately $223\mu m$, however as can be seen the fibers in the kink band themselves are broken into smaller lengths. The lengths of these small fiber breaks was found to be around $32\mu m$. The kink band was inclined at an angle of 29^0 from the horizontal, which is in the range of angles reported in the literature.

In summary, the experimental results show that glass fiber($r_0 = 12\mu m$) compos-

ites fail by splitting which is the predominant mode of failure of these composites in the $10 \sim 30\%$ fiber volume fraction range. For glass fiber composites with $40 \sim 60\%$ fiber volume fraction, both splitting and kink banding is observed. However, the formation of kink bands is not progressive(signified by a clear drop in load) as in carbon fiber composites, but, leads to catastrophic failure because of the association of splitting with the kinking mode of failure. In the present case, glass fibers were untreated prior to manufacturing of the specimens and thus the nature of the interfacial fiber/matrix bond is dictated by the adhesion chemistry between glass/vinyl ester. The implications of the experimental findings that have been presented are examined next via a new analytical model for the splitting failure mode.

3.3 Axial Splitting Model - Steady State

In the following paragraphs a steady state fracture mechanics based model developed by Lee and Waas (1999) to predict the splitting compressive stress of unidirectional fiber composites is presented. Compressive splitting occurs when a preexisting flaw inside the composite specimen starts to grow when the specimen is under compression load. Splitting failure has been observed before by a number of researchers who examined the compressive strength of aligned glass fiber composites(Fleck (1997); Piggott (1981); Oguni and Ravichandran (2000)). Yet, it is noticeably absent in carbon fiber composites. Because the splitting failure is hypothesized to initiate from tiny unavoidable flaws within the composite, the compressive strength of the composite specimens are closely related to the appropriate crack toughnesses K_{IC} and/or K_{IIC}. During the process of manufacturing composite specimens, it is reasonable to expect that they might contain tiny internal interface cracks, due to fiber surface irregularities or due to non wetting. If this is the case, then it is de-

sirable to know when such interfacial flaws can become active due to the externally applied compression.

In the present study, a representative volume element (RVE) that consists of a single fiber in a matrix cylinder and containing a central interface crack is considered as a representative model of the composite with an initial interfacial flaw. An examination of the total potential energy in conjunction with principles of linear elastic fracture mechanics is used to predict the compressive load at which crack propagation occurs. Since the fibers within the composite can have an initial misalignment with respect to axial load, the influence of such fiber crookedness is also incorporated in the development of the splitting model.

3.3.1 Strain Energy Release Rate, $\mathcal{G}$

Consider a representative volume element(RVE) of the composite, consisting of a concentric cylinder of fiber and matrix, with a fiber radius, r_0 and an outer region of matrix with radius, r_1, and subjected to a external axial load, P and torque, T, as shown in Figure 3.8. Following the methodology of the composite cylinder model(CCM) as given in the text by Christensen (1991), we assume the composite to be consisting of a collection of such representative volume elements(RVE's). The outer radius of matrix in the RVE is chosen to satisfy the fiber volume fraction requirement such that $r_1^2 = V_f/r_0^2$. The outer matrix surface ($r = r_1$) is assumed to be traction free. The height of the cylinder is taken to be '2L' with a interfacial crack of '2l' embedded at the interface of fiber and matrix. The composite is assumed to have perfect bonding outside the crack region ($l \leq z \leq L$) and ($-L \leq z \leq -l$). The total potential energy is written as $\Pi = U - W$ where U is the strain energy stored in the composite cylinder and W is the work done by the external forces.

Axial Loading

The expression for strain energy release rate(SERR), $\mathcal{G}_{Axial}$ is derived below. The material is assumed to behave as a linear elastic material under the action of externally applied axial load, 'P'. The strain energy release rate, $\mathcal{G}$ (same as $\mathcal{G}_{Axial}$ for the remainder of the chapter) is defined as follows $\mathcal{G} = -\frac{d\Pi}{dA}$. The crack surface area, A is taken to be $4\pi r_0 l$. Hence, the expression for strain energy release rate can be written as $\mathcal{G} = \frac{-1}{4\pi r_0}\frac{d\Pi}{dl}$.

The total potential energy in the case of displacement control loading (The applied displacement, Δ, is held fixed during crack propagation) is,

$$\Pi = U - W, \quad U = \frac{1}{2}P\Delta, \text{ and } \quad W = 0$$
$$\mathcal{G} = -\frac{\Delta}{8\pi r_0}\frac{dP}{dl}$$

Using the definition of compliance, $c = \Delta/P$, we obtain

$$\frac{dP}{dl} = -\frac{P^2}{\Delta}\frac{dc}{dl}$$
$$\text{Hence, } \mathcal{G} = \frac{P^2}{8\pi r_0}\frac{dc}{dl} \tag{3.1}$$

For load control(The applied load, P, is held fixed in magnitude during crack propagation), we get

$$\Pi = U - W, \quad U = \frac{1}{2}P\Delta, \text{ and } \quad W = P\Delta$$
$$\mathcal{G} = \frac{P}{8\pi r_0}\frac{d\Delta}{dl}$$

Using the definition of compliance, $c = \Delta/P$, we obtain

$$\frac{d\Delta}{dl} = P\frac{dc}{dl}$$
$$\text{Hence, } \mathcal{G} = \frac{P^2}{8\pi r_0}\frac{dc}{dl} \tag{3.2}$$

Note that the expression for strain energy release rate, $\mathcal{G}$, is same under load control as well as displacement control loading due to the assumption of linear elastic material behavior.

For the cracked region in Figure 3.8 ($-l \leq z \leq l$), the stress state which corresponds to axial compression is given as follows from Hyer and Waas (2000).

Fiber;

$$\sigma_z = \frac{PE_f}{\pi r_0^2 \delta}$$

Matrix;

$$\sigma_z = \frac{PE_m}{\pi r_0^2 \delta}$$

where

$$\delta = E_f + E_m(\frac{1}{V_f} - 1)$$

All other stresses are zero.

The axial contraction of the fiber and matrix can be obtained from the axial strain corresponding to the above stresses, and is given by

$$\Delta_1 = \int_{-l}^{l} \epsilon_z dz = \frac{2Pl}{\pi r_0^2 \delta}$$

For the uncracked region in Figure 3.8 ($l \leq z \leq L, -L \leq z \leq -l$), the stress state which is three dimensional, is given as follows from Hyer and Waas (2000),

Fiber;

$$\begin{aligned}
\sigma_r &= \sigma_\theta = \frac{2P}{\pi r_0^2}\alpha\beta(\nu_f - \nu_m)(V_f^{-1} - 1) \\
\sigma_z &= \frac{\beta P}{\pi r_0^2}\left[E_f + 4\alpha\nu_f(\nu_f - \nu_m)(V_f^{-1} - 1)\right]
\end{aligned}$$

Matrix;

$$\begin{aligned}
\sigma_r &= 2\alpha\beta P\frac{\nu_f - \nu_m}{\pi r_0^2}\left(\frac{r_0^2}{r^2 V_f} - 1\right) \\
\sigma_\theta &= -2\alpha\beta P\frac{\nu_f - \nu_m}{\pi r_0^2}\left(\frac{r_0^2}{r^2 V_f} + 1\right) \\
\sigma_z &= \frac{\beta P}{\pi r_0^2}\left[E_m - 4\alpha\nu_m(\nu_f - \nu_m)\right]
\end{aligned}$$

where

$$\begin{aligned}
\alpha &= \left[\frac{2(1+\nu_f)(1-2\nu_f)}{E_f}(V_f^{-1} - 1) + \frac{2(1+\nu_m)(1-2\nu_m + V_f^{-1})}{E_m}\right]^{-1} \\
\beta &= \left[E_f + (V_f^{-1} - 1)\{E_m + 4\alpha(\nu_f - \nu_m)^2\}\right]^{-1}
\end{aligned}$$

The axial strains corresponding to these stresses are as follows.

Fiber;

$$\begin{aligned}
\epsilon_z &= -\frac{\nu_f}{E_f}\sigma_r - \frac{\nu_f}{E_f}\sigma_\theta + \frac{1}{E_f}\sigma_z \\
&= -\frac{4P\nu_f}{\pi r_0^2 E_f}\alpha\beta(\nu_f - \nu_m)(V_f^{-1} - 1) \\
&\quad + \frac{\beta P}{\pi r_0^2 E_f}\left[E_f + 4\alpha\nu_f(\nu_f - \nu_m)(V_f^{-1} - 1)\right]
\end{aligned}$$

Matrix;

$$\epsilon_z = \frac{4\alpha\beta P\nu_m(\nu_f - \nu_m)}{\pi r_0^2 E_m} + \frac{\beta P}{\pi r_0^2 E_m}\left[E_m - 4\alpha\nu_m(\nu_f - \nu_m)\right]$$

The axial contraction of the fiber and matrix are the same and is given by

$$\Delta_2 = 2\int_l^L \epsilon_z dz = \frac{2\beta P}{\pi r_0^2}(L - l)$$

Hence, the approximate total axial contraction, approximate compliance and change of compliance with respect to crack length, dc/dl of the composite are as follows.

$$\begin{aligned} \Delta &= \frac{2P}{\pi r_0^2}\left[\frac{l}{\delta} + \beta(L - l)\right] \\ c &= \frac{2}{\pi r_0^2}\left[\frac{l}{\delta} + \beta(L - l)\right] \\ \frac{dc}{dl} &= \frac{2}{\pi r_0^2}\left(\frac{1}{\delta} - \beta\right) \end{aligned} \tag{3.3}$$

In computing the above quantities, only the stress states of the cracked and uncracked regions are considered, whereas a region near the crack tip of finite size ϵ is not considered. In the present analysis, the above expression for dc/dl is used, even though we have neglected the crack tip stress field in computing dc/dl. However, as explained later, for steady state conditions, equation (3.3) is exact. In the region ϵ (Figure 3.8),the stress state is influenced by the crack tip field. However, under steady state conditions for self similar crack growth, this region translates with the crack tip resulting in an increase of l and a corresponding decrease of $(L - l)$. Thus, while the axial contraction and compliance given by Δ and c above are approximate due to the negligence of the crack tip field, the rate of compliance change due to crack advancement, given by dc/dl is exact, since the 'ϵ' region is invariant with respect to crack length. This fact enables us to calculate $\mathcal{G}$ accurately for steady state

crack propagation. When the crack is small, initially the compliance change with respect to crack length, dc/dl, is dependent on the size of ϵ, but, as the crack length increases, dc/dl, becomes independent of crack length and attains the steady state value provided in equation (3.3). The derivation of dc/dl including the dependence on ϵ is given in the following section and also in Yerramalli and Waas (2002a), for non-steady state crack growth.

From (3.3), the energy release rate per unit area is obtained as

$$\mathcal{G} = \frac{P^2}{4\pi^2 r_0^3}(\frac{1}{\delta} - \beta)$$

When $\mathcal{G}$, becomes equal to twice the critical interfacial fracture energy (γ_f) the initial crack propagates;

$$\mathcal{G} = 2\gamma_f \tag{3.4}$$

Thus,

$$\sigma_{cr} = \sqrt{\frac{8V_f^2\gamma_f}{r_0(1/\delta - \beta)}} \tag{3.5}$$

Misaligned Fibers

The expression for axial compliance for the case when the fiber is misaligned in the cracked region of the RVE can be obtained by considering a slightly imperfect fiber with an initial imperfection of $w_0(z)$. With respect to the coordinate system shown in Figure 3.8, $w_0(z)$ is chosen as

$$w_0(z) = A_0(1 - \cos\frac{\pi z}{2L})$$

where A_0 is the imperfection magnitude.

Next, using kinematics that are appropriate for geometrically nonlinear beam theory as given by Brush and Almroth (1975), the relation between the axial contraction Δ_1, and the fiber load, P_f, can be obtained as,

$$\frac{\Delta_1}{l} = \frac{-P_f}{A_f E_f}[1 + \frac{A_0^2 A_f}{2I_f}],$$

where, A_f is the fiber cross-sectional area, I_f is the area moment of inertia and A_0 is the imperfection magnitude. From this relation an effective axial stiffness for the fiber is obtained as explained in appendix B and is given below

$$(EA)_{eff} = \frac{E_f A_f}{1 + \frac{A_0^2 A_f}{2I_f}},$$

Clearly, when the imperfection vanishes, one recovers the perfect fiber axial stiffness $(EA)_f$. In the present work, the imperfection amplitude is chosen to correspond to an initial misalignment angle of 2^0.

3.3.2 Discussion

Failure stresses were predicted for both perfectly aligned fibers and misaligned fibers, but it was observed that a small amount of misalignment is always present in the fibers of a composite specimen. Hence, further discussion will be restricted only to the misaligned model of splitting failure. The angle of misalignment was taken to be 2^o for the purpose of splitting model calculations. Failure stresses for glass fiber composites predicted by the splitting model are seen to increase almost linearly with the increase of fiber volume fraction. As a result, they are lower than the test results in the low fiber volume fraction range and higher than the test results in

the high fiber volume fraction range. The slopes of these curves are dictated mainly by the value of interfacial toughness, γ_f, the fiber radius, r_f and the fiber volume fraction, V_f. Predictions from the splitting model that includes fiber misalignment are shown in Figure 3.8 for glass fiber composites. As seen in Figure 3.9 the predicted stresses using the new splitting model are in good agreement with the test data at the lower volume fractions of the glass fiber composites. The splitting model was also used to provide a comparison against the test results given by Piggott and Harris (1980). As can be seen in Figure 3.9 the predicted stress results match with the test data at the lower fiber volume fractions. At the higher volume fractions, the splitting model predicts higher stresses when using the fracture toughness of epoxy, which is more suitable for lower fiber volume fraction. This finding was also observed experimentally where the failure mode was a mix of splitting and kinking. Figure 3.10 and Figure 3.11 show the effect of change in misalignment angle on the predicted failure stresses. It can be seen that as the misalignment angle increases the predicted compressive splitting failure stress value decreases for all fiber volume fractions.

3.4 Axial Splitting Model - Shear Lag

The stress analysis in Lee and Waas (1999) and presented in the previous section included areas in the cracked and uncracked regions of the composite and excluded a small region of size ϵ around the crack tip. In this region the stress state is a function of the crack tip field. When the crack is propagating under steady state conditions, this region translates with the crack tip. Thus, the rate of change of compliance with crack length is unaffected. The expression for the rate of change of compliance $\frac{dc}{dl}$ is also independent of the crack length or the initial fiber length. For

short cracks, where the crack propagation is unsteady, Lee and Waas (1999) used the finite element method to extract the dependency of $\frac{dc}{dl}$ on crack length. A major goal of the present section is obtaining a closed form expression for the change in compliance $\frac{dc}{dl}$ as a function of crack length. This expression can then be used in determining the compressive stress of a polymer matrix composite in terms of its fracture toughness γ_f and $\frac{dc}{dl}$ in closed form. For this purpose a modified shear lag model has been used to study the stress state at the crack tip. The local shear lag based stress field has been superposed on the far field stress state of the composite obtained from the 3D elasticity equations, to obtain expressions for compliance and compliance change as a function of the crack length. In the development of this shear lag based model, only perfectly aligned fibers have been considered. The inclusion of misalignment will result in a change in the stiffness of the fiber and has already been treated in the steady state splitting model by Lee and Waas (1999) and presented in the previous section.

Consider a representative volume element (RVE) of the composite containing a single fiber of length 2L with a crack of length 2l embedded in it as shown in Figure 3.12. The single fiber is divided into four regions for the purpose of deriving an expression for compliance and the rate of change of compliance. By symmetry, only one side of the fiber ($0 < z < L$), containing the crack region ($0 < z < l$) is modeled. Assume that a region ϵ extends from the crack tip in the positive Z axis direction as well as in the negative Z axis direction. The region extending beyond ϵ is modeled as in the case of the steady state splitting model as shown in Lee and Waas (1999).

3.4.1 Shear Lag Analysis

The main assumptions in the traditional shear lag model of Cox (1952), are that the matrix carries only shear and any axial straining in the matrix is only for the purpose of load introduction. The fiber can only undergo axial contraction or extension and the fiber axial stress is zero at the fiber ends. It was observed by the authors that the classical shear lag method based on the above assumptions leads to a reasonably accurate calculation of the compliance of a cracked fiber/matrix system. But the rate of change of compliance with crack length, $\frac{dc}{dl}$ turns out to be inaccurate. This in turn leads to the inaccurate calculation of strain energy release rate. In the present work the traditional shear lag parameter $\eta_{cox}^2 = \frac{1}{r_o^2}\frac{2E_m}{E_f(1+\nu_m)ln(1/V_f)}$ as proposed by Cox (1952) has been used along with a modified set of boundary conditions since it gives an accurate value of the change in compliance with respect to crack length, $\frac{dc}{dl}$, in addition to preserving the accuracy of the compliance calculation.

For the present work, we assume that the fiber ends do carry some load and that the shear lag method is valid over the small region extending from $(l-\epsilon)$ to $(l+\epsilon)$. These modifications are introduced into the shear lag model by ensuring that the fiber axial stress at z $= (l+\epsilon)$, matches with the fiber axial stress of the uncracked region calculated using the 3D equations of elasticity. Also, at z $= (l-\epsilon)$, the fiber axial stress is equated with the steady state splitting model stress in the crack region, which is similar to what is obtained via a simple rule of mixtures based stress prediction.

Taking a small segment dz of the composite containing the single fiber as shown in Figure 3.13, we can get the radial variation of shear stress in the matrix, $\hat{\tau}$ by equating the shear forces on neighboring annuli with radii r_1 and r_2 of length dz. Then,

$$2\pi r_1 \hat{\tau}_1 dz = 2\pi r_2 \hat{\tau}_2 dz$$

From the above equation, we get the relation between $\hat{\tau}_1$ and $\hat{\tau}_2$ as $\frac{\hat{\tau}_1}{\hat{\tau}_2}=\frac{r_2}{r_1}$. Thus at any radius r, we can relate the shear stress $\hat{\tau}(r)$ to the interface shear stress $\hat{\tau}_i$.

To obtain the relation between shear strain and shear stress, consider the displacement $\hat{u}_r(z)$ of the matrix with respect to the unstressed position. Then,

$$\frac{d\hat{u}}{dr} = \gamma = \frac{\hat{\tau}_r}{G_m} = \frac{\hat{\tau}_i}{G_m}(\frac{r_0}{r}) \text{ or}$$

$$d\hat{u} = \frac{\hat{\tau}_i}{G_m}(\frac{r_0}{r})dr$$

Integrating the above equation between $r=r_0$ and $r=R$, we obtain

$$\int_{\hat{u}_r=(r_0)}^{\hat{u}_r=(R)} d\hat{u} = \frac{\hat{\tau}_i r_0}{G_m} ln(\frac{R}{r_0}) = \hat{u}_R - \hat{u}_{r_0}$$

where $\hat{u}_R$ is the matrix displacement at a distance R from the fiber and $\hat{u}_{r_0}$ is the matrix displacement at interface $r = r_0$. The value of R is based on the assumption that the matrix strain is uniform, remote from the fiber-matrix interface. Thus the appropriate value of R is dictated by the proximity of fibers which in turn depends on the fiber packing and fiber volume fraction V_f. Assuming a hexagonal packing of fibers Hashin and Rosen (1964) and also taking note of the fact that the ratio R/r_0 appears as a logarthmic term and is relatively insensitive to the details of geometry, we can write the following expression relating fiber volume fraction V_f and the ratio R/r_0.

$$V_f = \frac{\pi r_o^2}{2\sqrt{3}R^2}$$
$$(\frac{R}{r_0})^2 \approx \frac{1}{V_f}$$

From Figure 3.13, by equating the forces acting along the axial direction of the fiber we get the relation between the axial stress in the fiber and the interfacial shear stress.

$$\begin{aligned} 2\pi r_0 \hat{\tau}_i dz &= -\pi r_0^2 d\hat{\sigma}_f \\ \frac{d\hat{\sigma}_f}{dz} &= \frac{-2\hat{\tau}_i(z)}{r_0} \end{aligned}$$

Combining the above expression with the expression for interfacial shear stress $\hat{\tau}_i$ in terms of the displacements we get

$$\frac{d\hat{\sigma}_f}{dz} = \frac{-2E_m}{(1+\nu_m)} \frac{(\hat{u}_R - \hat{u}_{r_0})}{r_0^2 ln(1/V_f)} \tag{3.6}$$

differentiating Equation(3.6), we get

$$\begin{aligned} \frac{d^2\hat{\sigma}_f}{dz^2} &= \frac{-2E_m}{(1+\nu_m) r_0^2 ln(1/V_f)} \left(\frac{d\hat{u}_R}{dz} - \frac{d\hat{u}_{r_0}}{dz}\right) \\ &= \frac{\eta^2}{r_0^2}(\hat{\sigma}_f - \hat{\epsilon}_m E_f) \end{aligned} \tag{3.7}$$

In the above expression the following substitutions have been made.

$$\begin{aligned} \frac{d\hat{u}}{dz}\Big|_{r=r_0} &= \hat{\epsilon}_f = \frac{\hat{\sigma}_f}{E_f} \\ \frac{d\hat{u}}{dz}\Big|_{r=R} &= \hat{\epsilon}_m \\ \eta^2 &= \frac{2E_m}{E_f(1+\nu_m) ln(1/V_f)} \end{aligned}$$

Where $\hat{\epsilon}_m$ is the matrix strain, $\hat{\epsilon}_f$ is the fiber axial strain, $\hat{\sigma}_f$ is the fiber stress and E_f is axial fiber modulus.

Equation(3.7) is a second order ordinary differential equation, whose solution is

$$\hat{\sigma}_f(z) = E_f \hat{\epsilon}_m + B\sinh\left(\frac{\eta z}{r_0}\right) + D\cosh\left(\frac{\eta z}{r_0}\right) \tag{3.8}$$

3.4.2 Splitting Model - Shear Lag Method

In this section we present the details of the application of the shear lag model to the splitting model analysis of Lee and Waas (1999). For this purpose, the RVE can be divided into two regions - the crack region and the uncracked region.

Crack Region

In this region it is reasonable to assume that the fiber axial stress is equal to that of the axial stress obtained from the splitting model with increasing distance from the crack tip. Also in the crack region according to the shear lag model there is no shear stress hence the fiber axial stress is constant. Thus,

$$\begin{aligned} \frac{d\hat{\sigma}_{f(1)}}{dz} &= 0 \\ \Rightarrow \hat{\sigma}_{f(1)} &= A \\ \Rightarrow \hat{\epsilon}_{f(1)} &= \frac{A}{E_f} \end{aligned}$$

Integrating the expression for fiber axial strain we get $\hat{u}_{f(1)} = \frac{A}{E_f} z$ where the constant of integration has been taken to be zero since it represents a rigid body translation. The expressions for the stress and displacement field from the splitting model for the crack region are as given in Lee and Waas (1999).

$$\hat{\sigma}_{f2D} = \frac{PE_f}{\pi r_0^2 \delta}$$

from which we can obtain

$$\hat{u}_{f2D} = \frac{P}{\pi r_0^2 \delta} z$$

where $\delta = E_f + E_m(\frac{1}{V_f} - 1)$

Uncracked Region

In the uncracked region, we can take the expression of normal fiber stress as given by Equation(3.8). However in the present analysis this expression is valid in the region $l < z < l+\epsilon$. For $z > l+\epsilon$, the normal stress expression corresponding to the 3D equations of elasticity, is taken from the splitting model. Thus, at $z = l+\epsilon$, we equate the fiber normal stress $\hat{\sigma}_{f(2)}$ obtained from the shear lag analysis with that of the fiber normal stress obtained from the splitting model. Also, at the interface between the crack and uncracked region continuity of fiber normal stress and axial displacements is enforced. The expression for normal fiber strain can be obtained from Equation(3.8) and is as follows.

$$\hat{\epsilon}_{f(2)} = \hat{\epsilon}_m + \frac{B}{E_f}\sinh(\frac{\eta z}{r_0}) + \frac{D}{E_f}\cosh(\frac{\eta z}{r_o})$$

On integrating the above, we get

$$\hat{u}_{f(2)} = \hat{\epsilon}_m z + \frac{B}{E_f}\frac{r_0}{\eta}\cosh(\frac{\eta z}{r_0}) + \frac{D}{E_f}\frac{r_0}{\eta}\sinh(\frac{\eta z}{r_0}) + C2$$

Similarly an expression for the displacement field in the region beyond $z = l+\epsilon$ can be obtained from the 3D splitting model analysis and is as follows

$$u_{3d} = \frac{\beta P}{\pi r_0^2} z + C2$$

The expression for the stress σ_{3d} is as follows Lee and Waas (1999),

$$\sigma_{3d} = \frac{\beta P}{\pi r_0^2}(E_m - 4\alpha\nu_m(\nu_f - \nu_m))$$

$$\text{where } \alpha = [\frac{2(1+\nu_f)(1-2\nu_f)}{E_f}(V_f^{-1} - 1) + \frac{2(1+\nu_m)(1-2\nu_m+V_f^{-1})}{E_m}]^{-1}$$

$$\beta = [E_f + (V_f^{-1} - 1)$$

$$\{E_m + 4\alpha(\nu_f - \nu_m)^2\}]^{-1} \tag{3.9}$$

The following boundary conditions can be written for the present boundary value problem.

Crack Region

$$\text{at } z = l - \epsilon$$

$$\begin{aligned} \hat{\sigma}_{f(1)} &= \sigma_{f2D} \\ \Rightarrow A &= \frac{PE_f}{\pi r_0^2 \delta} \end{aligned}$$

and hence

$$\hat{u}_{f(1)} = \frac{P}{\pi r_0^2 \delta}(l - \epsilon)$$

Further, at $z = l$

$$\hat{u}_{f(1)} = \hat{u}_{f(2)}$$

From the condition for continuity of displacement across the crack interface the constant C2 is evaluated which is then used to get the displacement field $\hat{u}_{f(2)}$ to be,

$$\begin{aligned} \hat{u}_{f(2)} = &\frac{P}{\pi r_0^2 \delta} + \frac{B}{E_f}\frac{r_0}{\eta}[\cosh(\frac{\eta z}{r_0}) - \cosh(\frac{\eta l}{r_0})] + \\ &\frac{D}{E_f}\frac{r_0}{\eta}[\sinh(\frac{\eta z}{r_0}) - \sinh(\frac{\eta l}{r_0})] \end{aligned} \tag{3.10}$$

At $z = l$, the continuity of normal stresses provides

$$\hat{\sigma}_{f(1)} = \hat{\sigma}_{f(2)}$$

$$\frac{PE_f}{\pi r_0^2 \delta} = E_f \hat{\epsilon}_m + B\sinh(\frac{\eta l}{r_0}) + Dcosh(\frac{\eta l}{r_0}) \tag{3.11}$$

Uncracked Region

at $z = l + \epsilon$

$\hat{\sigma}_{f(2)} = \sigma_{f3D}$, which translates to

$$E_f\hat{\epsilon}_m + B\sinh(\frac{\eta(l+\epsilon)}{r_0}) + D\cosh(\frac{\eta(l+\epsilon)}{r_0}) = \frac{\beta P}{\pi r_0^2}[E_m - 4\alpha\nu_m(\nu_f - \nu_m)] \quad (3.12)$$

To ensure compatibility, we equate the displacements $u_{f(2)}$ and u_{f3D}. This provides,

$$\hat{\epsilon}_m(l+\epsilon) + \frac{B}{E_f}\frac{r_0}{\eta}\cosh(\frac{\eta(l+\epsilon)}{r_0}) + \frac{D}{E_f}\frac{r_0}{\eta}\sinh(\frac{\eta(l+\epsilon)}{r_0}) = \frac{\beta P(l+\epsilon)}{\pi r_0^2} + C3 \quad (3.13)$$

Equation(3.13) enables to obtain the constant C3 in terms of the remaining constants B and D. The constants B and D can be evaluated from the two Equations(3.11) and (3.12). Knowing B and D, C3 and C2 can be determined. Expressions for the constants B and D are given below.

$$D = \frac{\Theta}{\left[\frac{\cosh(\frac{\eta l}{r_o})\sinh(\frac{\eta(l+\epsilon)}{r_o})}{\sinh(\frac{\eta l}{r_o})} - \cosh(\frac{\eta(l+\epsilon)}{r_o})\right]}$$

$$B = \frac{-\cosh(\frac{\eta l}{r_o})\Theta}{\sinh(\frac{\eta l}{r_o})\left[\frac{\cosh(\frac{\eta l}{r_o})\sinh(\frac{\eta(l+\epsilon)}{r_o})}{\sinh(\frac{\eta l}{r_o})} - \cosh(\frac{\eta(l+\epsilon)}{r_o})\right]}$$

where $\Theta = \frac{P}{\pi r_o^2}\left[\frac{E_f}{\delta} - \beta \left[E_f + 4\alpha\nu_f(\nu_f - \nu_m)(\frac{1}{V_f} - 1)\right]\right]$

The total axial displacement can be written in terms of the integrals of the fiber

axial strains as follows.

$$\Delta = \underbrace{2\int_0^l \hat{\epsilon}_{f(1)}dz}_{CrackRegion(1)} + \overbrace{2\int_l^{(l+\epsilon)} \hat{\epsilon}_{f(2)}dz + 2\int_{(l+\epsilon)}^{L} \epsilon_{f3D}dz}^{UncrackedRegion(2)}$$

On substituting the expressions for the axial strains in the above integrals results in,

$$\Delta = 2\int_0^l \frac{P}{\pi r_0^2 \delta}dz + 2\int_l^{(l+\epsilon)} [\hat{\epsilon}_m + \frac{B}{E_f}\sinh(\frac{\eta z}{r_0}) + \frac{D}{E_f}\cosh(\frac{\eta z}{r_0})]dz + 2\int_{l+\epsilon}^{L} \frac{\beta P}{\pi r_0^2}dz \quad (3.14)$$

We can observe from the above equations for total displacement Δ that as $\epsilon \to 0$ (meaning the region ϵ around the crack tip vanishes), the second integral vanishes and also the third reduces to the same expression as given in Equation 3.5 giving us the displacement expression obtained with steady state crack propagation assumption.

3.4.3 Strain Energy Release Rate, $\mathcal{G}$

The total potential energy Π of the RVE under consideration, when subjected to a compressive load, P is $U - W$, where U is the strain energy stored in the RVE and W is the work done. The expression for strain energy release rate is

$$\mathcal{G} = \frac{d\Pi}{dA}$$

where $A = 4\pi r_0 l$ is the crack surface area and r_0 is the fiber radius. The overall compliance of the RVE, c is defined as;

$$c = \frac{\Delta}{P} \quad (3.15)$$

where Δ is the axial compressive displacement of the composite and P is the external compressive load. The expression for Δ is substituted from Equation(3.14). For either case of load control or displacement control, the strain energy release rate can

be written as

$$\mathcal{G} = \frac{P^2}{8\pi r_0}\frac{dc}{dl}$$

The fracture toughness γ_f is half of the value of G at the time of initiation of crack propagation.

$$\mathcal{G} = 2\gamma_f$$

The compressive stress σ_c can be related to the fracture toughness of the material γ_f by the following the expression

$$\sigma_c = \sqrt{\frac{16\gamma_f V_f^2}{\pi r_o^3(\frac{dc}{dl})}} \tag{3.16}$$

3.4.4 Solution

The expression for Δ in the form of the integral given in Equation(3.14) is evaluated to get the displacement.

$$\begin{aligned}\Delta &= 2\Big\{\frac{Pl}{\pi r_o^2\delta} + \frac{P\epsilon}{\pi r_o^2\delta} \\ &+ \Big\{\frac{B}{E_f}[\cosh(\frac{(l+\epsilon)\eta}{r_o}) - \cosh(\frac{l\eta}{r_o})] \\ &+ \frac{D}{E_f}[\sinh(\frac{(l+\epsilon)\eta}{r_o}) - \sinh(\frac{l\eta}{r_o})]\Big\}\frac{r_o}{\eta} \\ &+ \frac{P\beta(L-l-\epsilon)}{\pi r_o^2}\Big\}\end{aligned} \tag{3.17}$$

We get the relation for compliance c by dividing Equation(3.17) by the load term P. Thus,

$$\begin{aligned}c &= 2\Big\{\frac{l}{\pi r_o^2\delta} + \frac{\epsilon}{\pi r_o^2\delta} \\ &+ \Big\{\frac{B}{E_f}[\cosh(\frac{(l+\epsilon)\eta}{r_o}) - \cosh(\frac{l\eta}{r_o})] \\ &+ \frac{D}{E_f}[\sinh(\frac{(l+\epsilon)\eta}{r_o}) - \sinh(\frac{l\eta}{r_o})]\Big\}\frac{r_o}{\eta} \\ &+ \frac{\beta(L-l-\epsilon)}{\pi r_o^2}\Big\}\end{aligned} \tag{3.18}$$

Equation(3.18), is an expression for compliance of the system in terms of the crack length, l, and crack tip influence zone ϵ. The rate of change of compliance, $\frac{dc}{dl}$ is obtained by differentiating Equation(3.18) with respect to the crack length, l. This expression for dc/dl can be substituted into Equation (3.16) to obtain the compressive splitting strength, which for a steady state crack propagation case reduces to Equation (3.5).

$$\begin{aligned}\frac{dc}{dl} &= \frac{2}{\pi r_o^2}\Big[\frac{1}{\delta} - \beta\Big] \\ &+ \Big[\frac{r_o}{\eta E_f}\Big\{(\frac{dB}{dl} + D)(\cosh(\frac{(l+\epsilon)\eta}{r_o}) - \cosh(\frac{l\eta}{r_o})) \\ &+ (\frac{dD}{dl} + B)(\sinh(\frac{(l+\epsilon)\eta}{r_o}) - \sinh(\frac{l\eta}{r_o}))\Big\}\Big] \qquad (3.19)\end{aligned}$$

It can be seen in the above equation that the first term corresponds to the steady state behavior(independent of crack length, l) and the second term, which contains the crack length l and the crack tip influence zone size ϵ, is due to non steady effects. The constants B and D in the above expression are functions of crack length l. For determining the rate of change of compliance with crack length, the previously described expressions were coded in MAPLE (symbolic math package) and evaluated for a glass/epoxy composite system of fiber volume fraction ($V_f = 10\%$). For the ease of calculation the half length of fiber L, half crack length l and the crack tip influence zone ϵ were all expressed as a factor of the fiber radius r_o. The fiber half length L was taken to be 20 times the fiber radius for the present calculations. The normalized crack length $n1 = \frac{l}{r_o}$, and the normalized crack tip zone, $n = \frac{\epsilon}{r_o}$, are used as parameters. Plots of normal stress variation along the length of fiber, compliance and rate of change of compliance as a function of $n1$ and n are shown in Figures 3.14-3.17. The following material properties of the glass fiber and vinyl-ester matrix were used in the analysis.

Glass Fiber

$$r_o = 0.012mm$$

$$E_f = 72000MPa$$

$$\nu_f = 0.22$$

Vinyl-ester Resin

$$E_m = 3585MPa$$

$$\nu_m = 0.36$$

3.4.5 Discussion

As the equation for the rate of change of compliance with crack length, $\frac{dc}{dl}$, indicates, compliance change is no longer independent of the crack length l or the crack tip influence zone parameter ϵ. However, the value of ϵ is initially unknown since the crack tip zone advances with the crack and also the region of influence does not remain constant. Thus the first step in evaluating $\frac{dc}{dl}$ would be to determine the value of ϵ. However, before determining the value of ϵ, a study of the normal stress variation along the fiber length is necessary. A plot (Figure 3.14) of the normalised stress(σ_f/σ_{3D} with a normalised length factor(z/r_0) indicates that there is a discontinuity between the 2D stress state in the cracked region and the 3D stress state in the uncracked region, which is bridged by the modified shear lag model. The value of ϵ controls the gradient of the stress in this bridging region, with increasing values of ϵ decreasing the stress gradients. Hence, for a given crack length it is necessary to take ϵ as large as possible. But, it has to be kept in mind that the value of ϵ cannot exceed the half crack length l and at the same time ϵ should be smaller than L-l. As shown in Figure 3.15, the compliance of the fiber/matrix system is

plotted as a function of the crack length paramater for different values of ϵ. For a particular ϵ we can see that the compliance vs crack length plots are straight lines, implying that the slope ($\frac{dc}{dl}$) is a constant. If we mark the lower tip of the straight lines with black dots as shown in Figure 3.15, we can observe that the slope of the locus of these points is initially varying and then approaches a constant after some crack length paramater $n1$, indicating the steady state. The variation of compliance obtained from the present shear lag model, the FEM results of Lee and Waas (1999), and the steady state expression are plotted as a function of crack length factor,$n1$ and is shown in Figure 3.16. The slopes of all the three curves in the linear region are nearly equal. Similarly, for the compliance change $\frac{dc}{dl}$, the curve of $\frac{dc}{dl}$ vs ϵ as a function of n becomes nearly flat beyond $\epsilon \geq 1.5r_o$ as seen in Figure 3.17. It can be seen from Figure 3.17 that when the crack length is small, as expected $\frac{dc}{dl}$ is a function of crack length and the crack tip zone, even if we take the crack tip zone, ϵ equal to the crack length, l.

The value of rate of change of compliance obtained with the present integrated approach using the modified shear lag model is found to be 3.59715 X $10^{-}5$ $(N/mm)^{-}1$ which is approximately equal to the value obtained from the steady state analysis, 3.597186 X $10^{-}5$ $(N/mm)^{-}1$ and the FEM value of 3.1881 X $10^{-}5$ $(N/mm)^{-}1$ given in Lee and Waas (1999). This value of $\frac{dc}{dl}$ was obtained for a ϵ of 0.024mm and crack length, l of 0.096mm. The total length of fiber considered was about $40r_o$. As seen in Figure 3.17, for this crack length and ϵ, the $\frac{dc}{dl}$ value has reached its asymptotic value. Thus the present analysis incorporating the shear lag model to account for the crack tip stress state provides an analytical approach to study both unsteady crack growth of short cracks and steady state crack behavior as crack length increases. It replaces the need to resort to finite element based computation for short crack

length (unsteady crack growth). In Table 3.3 and Table 3.4, we have compared the compressive strength predictions of the splitting model using Equation (3.16) with the FEM data provided in Lee and Waas (1999) for fiber volume fractions of 10% and 60%. The value of fracture energy for a perfectly aligned composites was taken from Lee and Waas (1999). It is seen that the predicted values of compressive splitting strength are very high for $V_f = 60\%$. As shown in the previous section the compressive strength predictions better approximate the experimental results when a small degree of imperfection is introduced into the fibers in the cracked zone.

3.5 Conclusions

Compressive response and failure characteristics of glass fiber reinforced unidirectional composites have been examined experimentally and an analytical model has been introduced to predict compressive splitting. The model predictions have been compared against experimental data obtained by the authors and also others. Glass fiber composites demonstrated a splitting failure mode for low fiber volume fraction ($V_f = 10\% \sim 30\%$) and a combined splitting/kink banding failure mode for high fiber volume fraction ($V_f = 40\% \sim 60\%$). The present analytical model has examined how the various parameters in a composite influences its compressive strength for low V_f. For the high V_f range, the kinking mode of failure has been thoroughly examined in Lee (1998). Also, at high V_f the values of fracture energy, γ_f could be different due to the difference in properties of the interphase as mentioned in chapter II.

The analysis results for the splitting failure mode showed that the splitting failure mode is favorable for glass fiber composites at low fiber volume fraction. The model also shows that the ratio of axial moduli between fiber and matrix, the fiber diameter

and the fiber volume fraction are just as important as the fiber/matrix interfacial fracture toughness towards dictating the mechanism of compressive failure. Thus, the present model can be utilized for design purposes, where compressive strength is a critical design parameter. Its validity for the low V_f range has been justified.The splitting model also provides a means to assess the fiber volume fraction(for given constituents of a composite) at which the failure mechanism transitions between kink banding and splitting.

V_f	Stress$[MPa]$				
[%]	No.1	No.2	No.3	No.4	Average
0.0	92.8	82.5	83.4		86.2
10.0	275.2	339.8	329.9		315.0
20.0	366.5	355.7	464.8		395.7
30.0	499.0	567.7	486.0		517.6
40.0	374.0	654.0	451.9	458.2	484.5
50.0	376.2	627.2	684.7	516.6	551.2
60.0	658.8	863.1	545.3	599.2	666.6

Table 3.1: Maximum stress values of glass-fiber composites, Lee (1998)

V_f	Stress $[MPa]$					
[%]	10.0	20.0	30.0	40.0	50.0	60.0
No.1	163.8	373.0	425.8	478.7	358.4	493.0
No.2	235.2	321.3	407.5	400.4	389.3	527.5
No.3	180.9	342.6	388.5	418.5	349.8	454.1
No.4					384.9	393.1
No.5					512.8	
No.6					440.5	
Average	193.3	345.6	407.3	432.5	406.0	466.9

Table 3.2: Maximum stress values of carbon-fiber composites, Lee (1998)

	Glass/vinylester	
V_f	Splitting model $\frac{dc}{dl}$	FE model $\frac{dc}{dl}$
10	$3.59715X10^{-5}$	$3.1881X10^{-5}$
60	$2.801X10^{-5}$	$2.4042X10^{-5}$

Table 3.3: $\frac{dc}{dl}$ values obtained from splitting and FE models

	Glass/vinylester	
V_f	Splitting model $\sigma_c(MPa)$	FE model $\sigma_c(MPa)$
10	298	312.25
60	1998.45	2157.36

Table 3.4: Compressive stress values obtained from splitting and FE models with $\gamma_f = 1.0546X10^{-}4KJ/m^2$

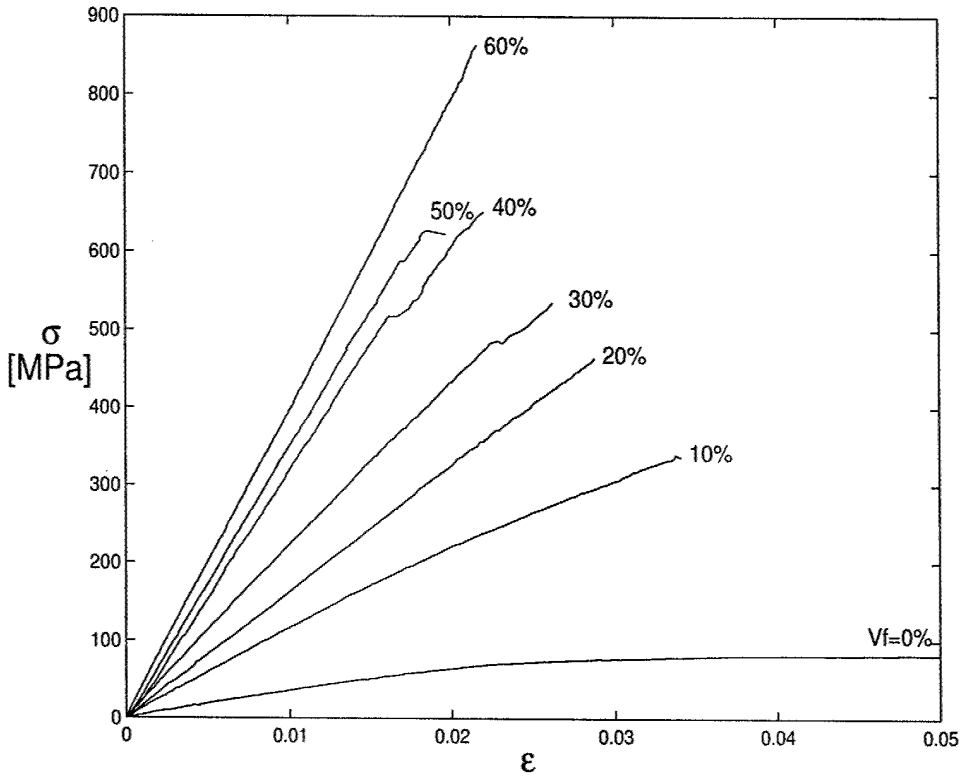

Figure 3.1: Typical compressive stress-strain curve of glass-fiber specimen

a) A high magnification view of a broken glass fiber

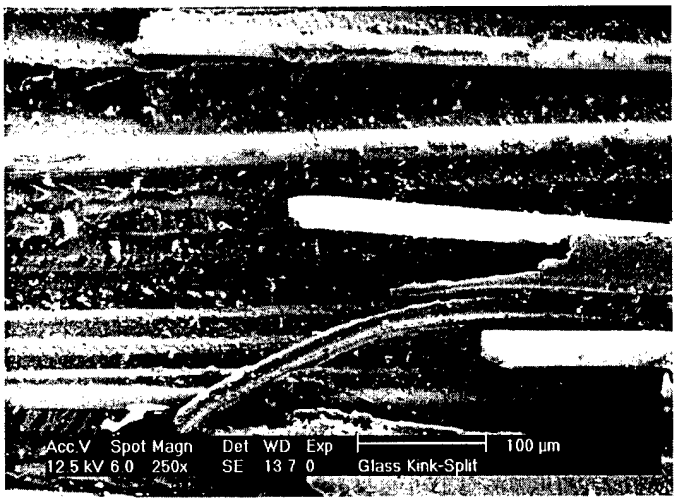

b) A high magnification view of splitting surface in a glass/epoxy composite

Figure 3.2: Typical splitting failure mode of glass fiber composite specimen (V_f = 30%)

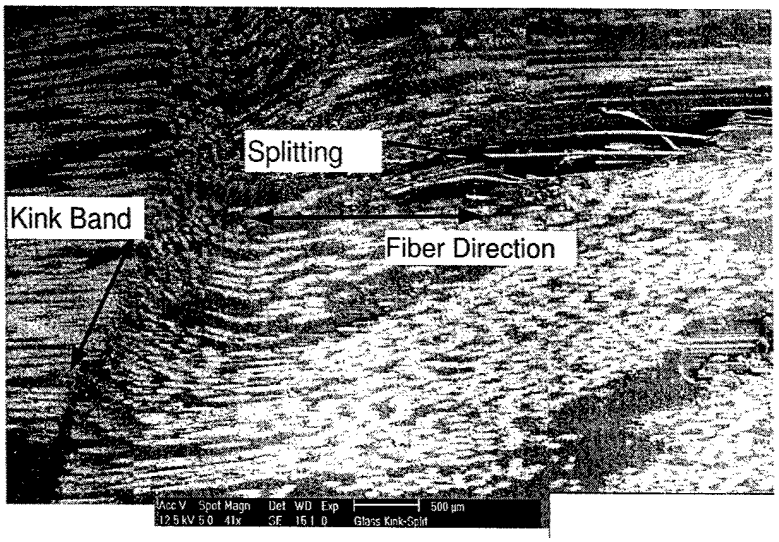

Glass / Epoxy composite Vf = 50% showing kinking and splitting failure

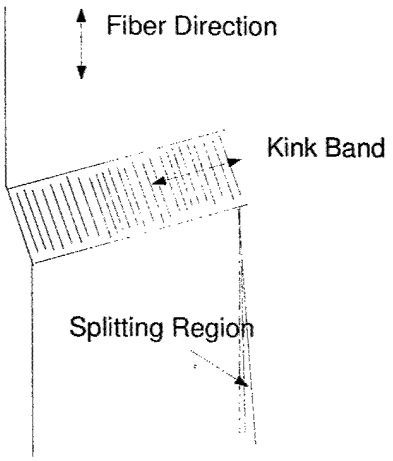

A schematic of Kink band-Splitting failure seen in Glass/Epoxy Composites

Figure 3.3: Kinking/splitting failure mode of glass fiber composite specimen (V_f = 50%)

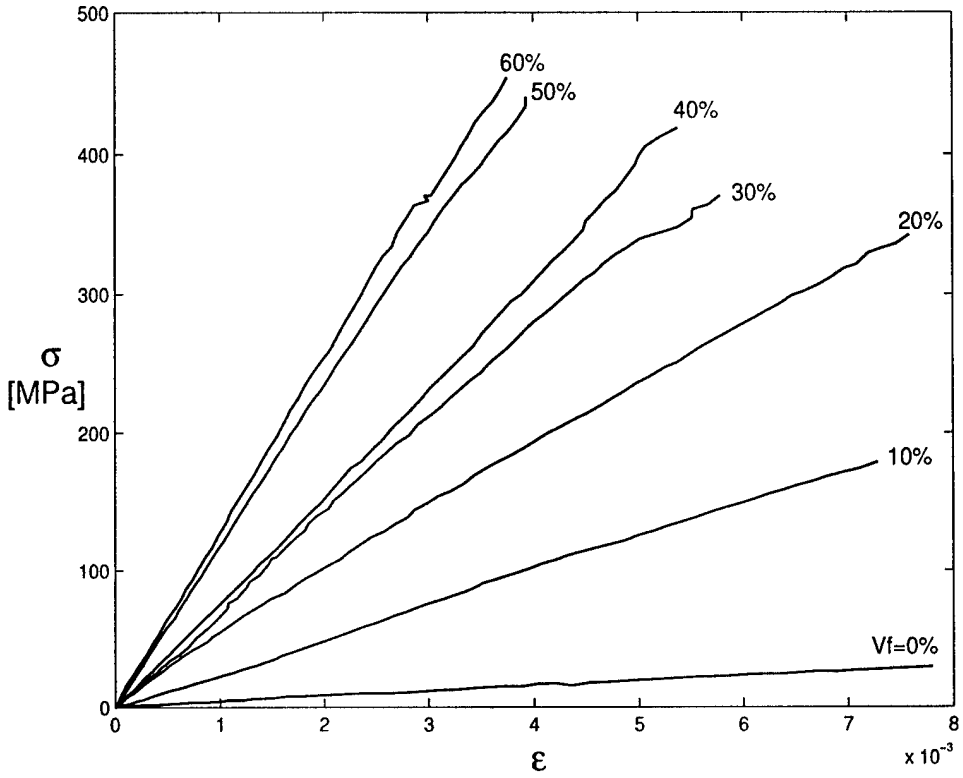

Figure 3.4: Typical compressive stress-strain curve of carbon-fiber specimen

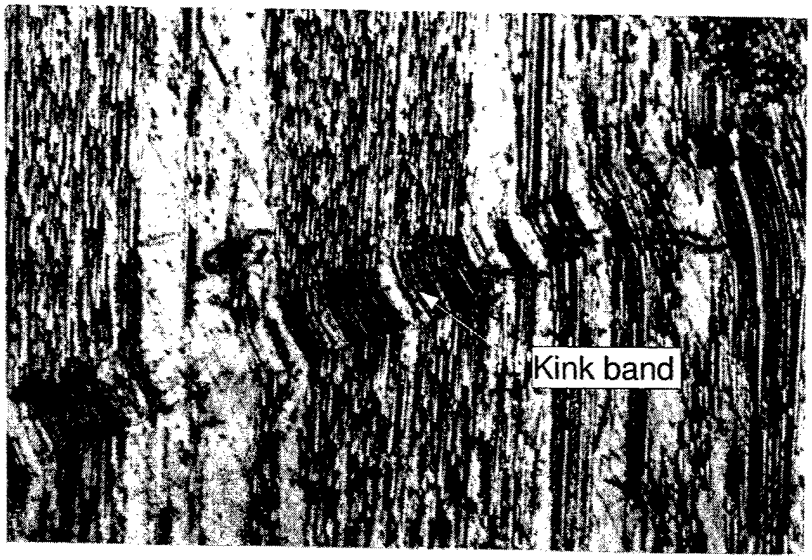

Figure 3.5: An optical microscope picture of a kink band in carbon composite

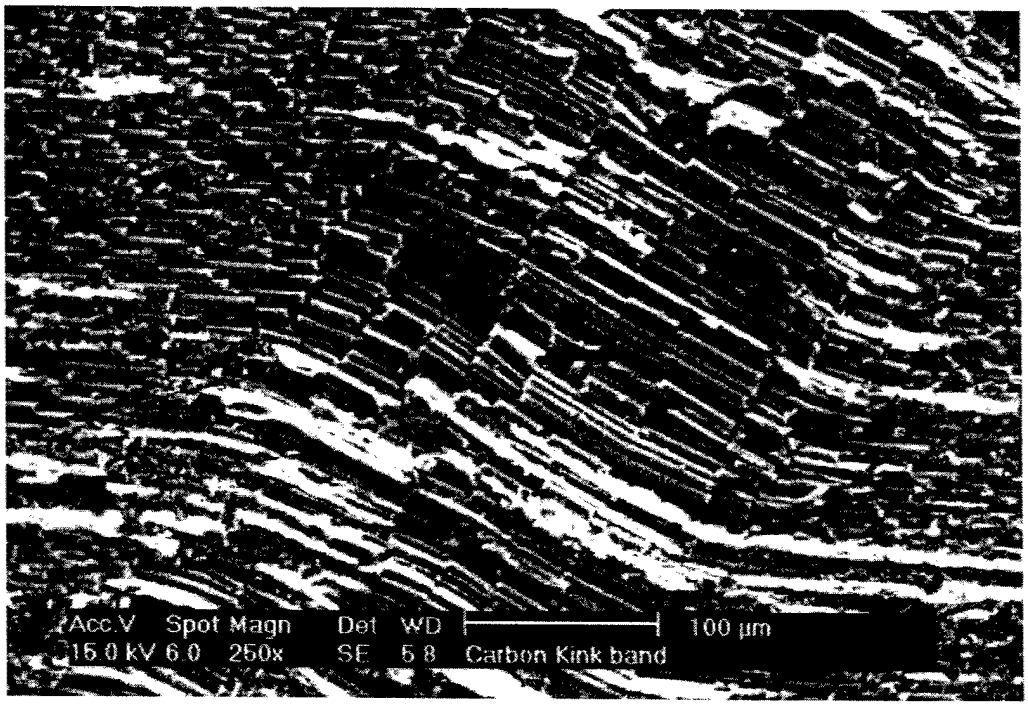

Figure 3.6: A high resolution picture of the kink band under SEM

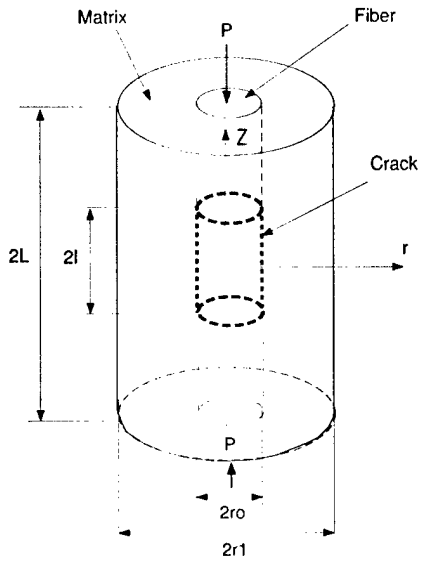

Composite with initial crack

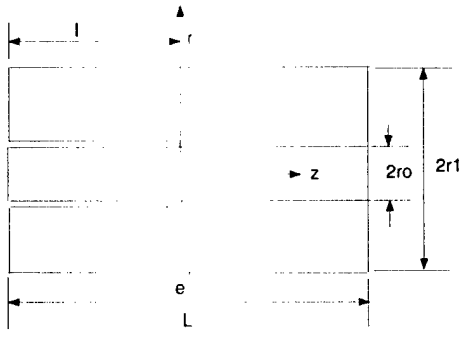

Detail of the crack tip region

Figure 3.7: Composite model with initial crack

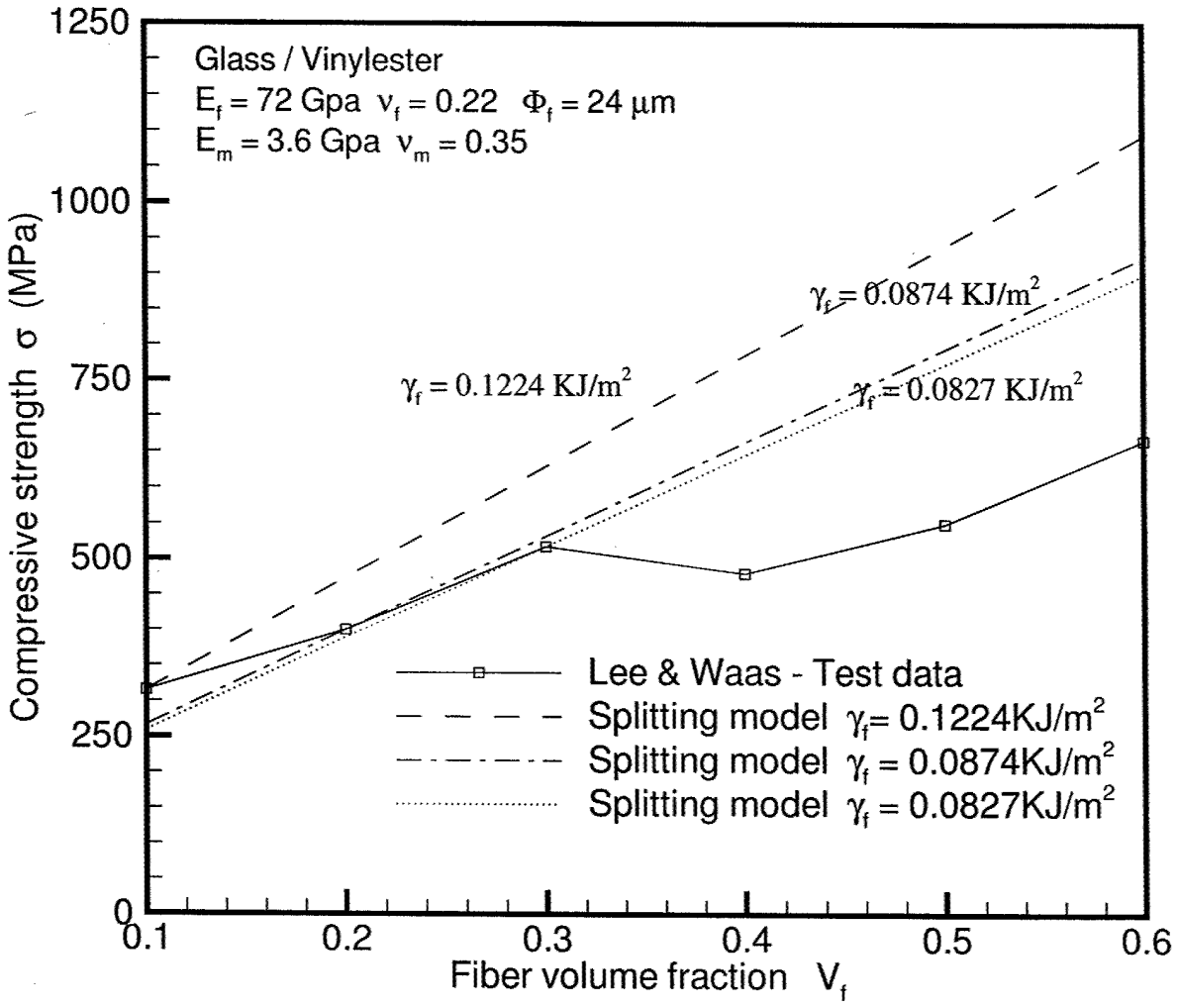

Figure 3.8: Variation of compressive strength σ with fiber volume fraction V_f for a glass epoxy composite material with different values of fracture energy γ_f and misalignment angle $\phi = 2^0$

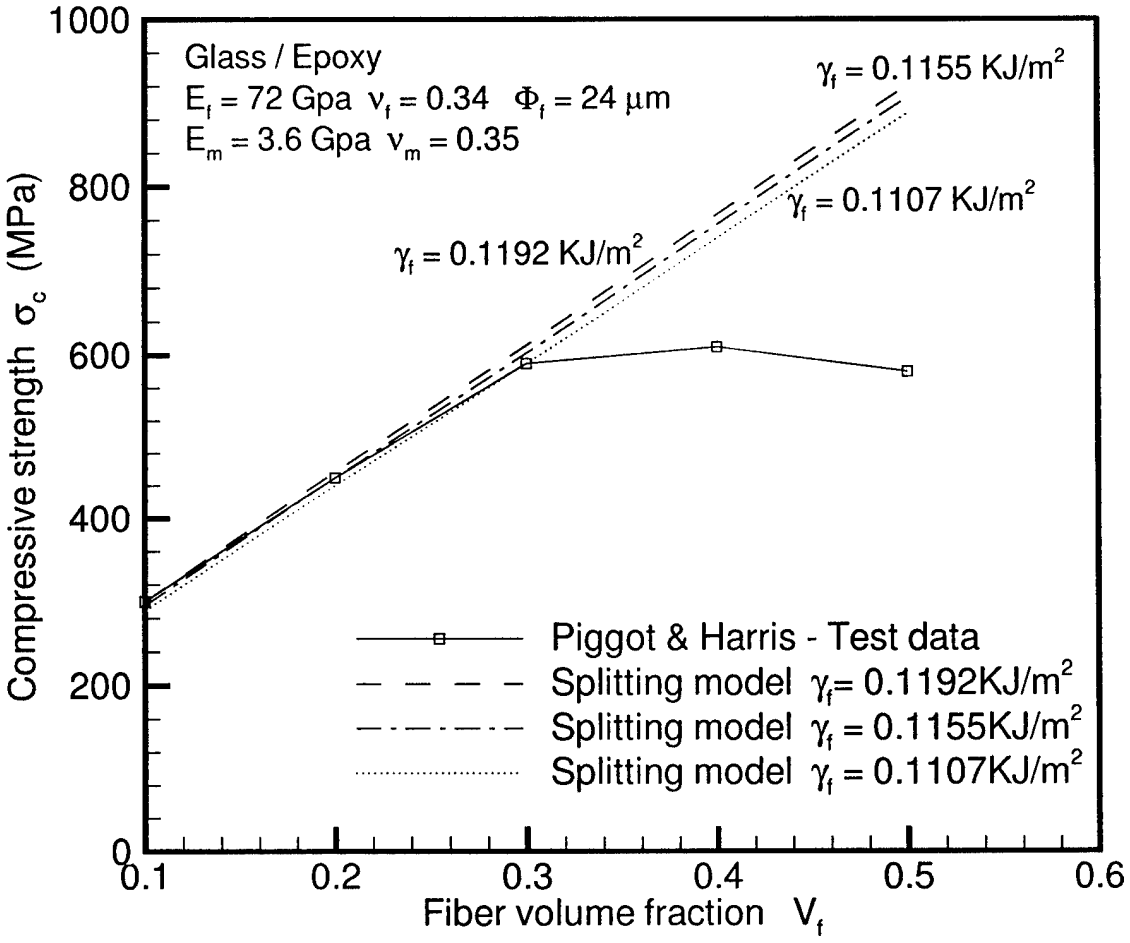

Figure 3.9: Variation of compressive strength σ with fiber volume fraction V_f for a glass epoxy composite material with different values of fracture energy γ_f and misalignment angle $\phi = 2^0$

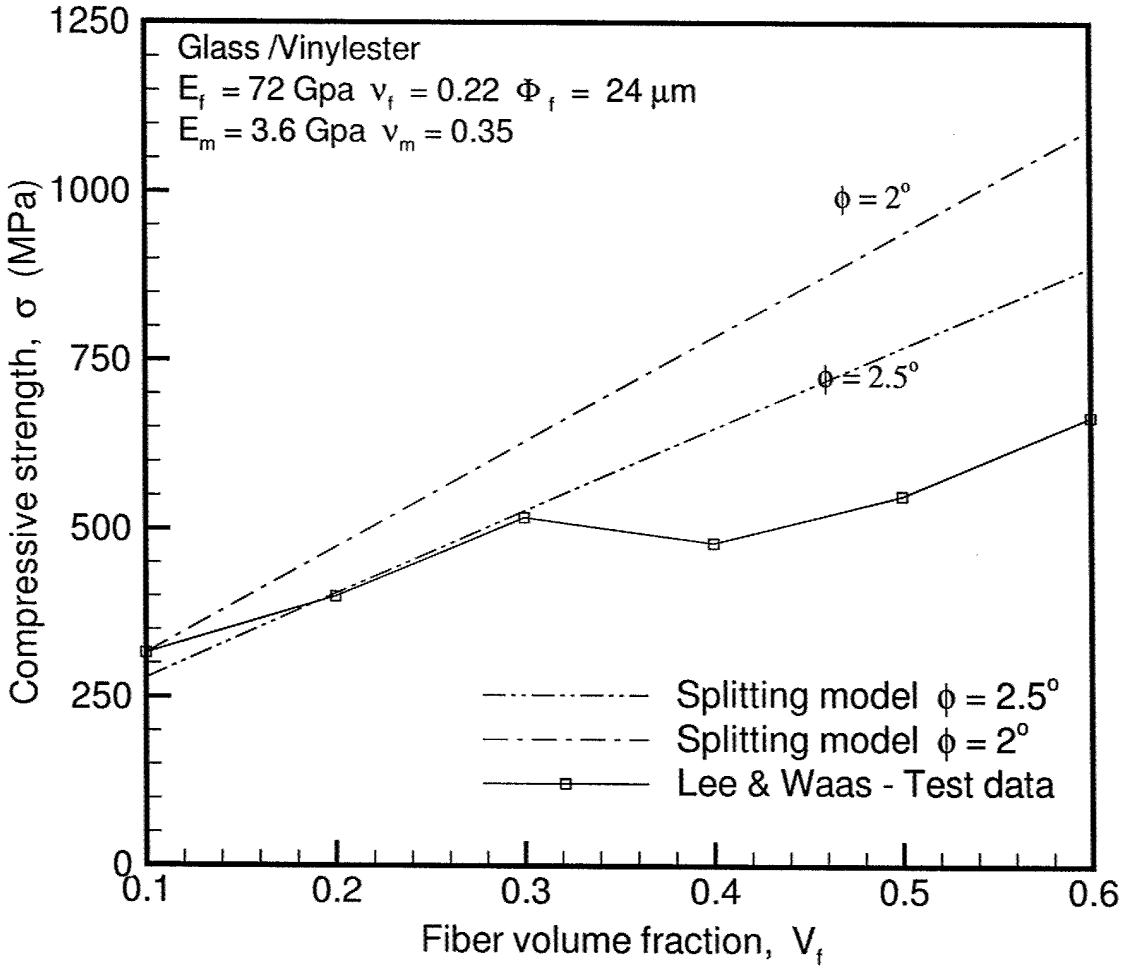

Figure 3.10: Variation of compressive strength σ with fiber volume fraction V_f for a glass epoxy composite material with different values of misalignment angle $\phi = 2^0$ and $\gamma_f = 0.1224\ KJ/m^2$

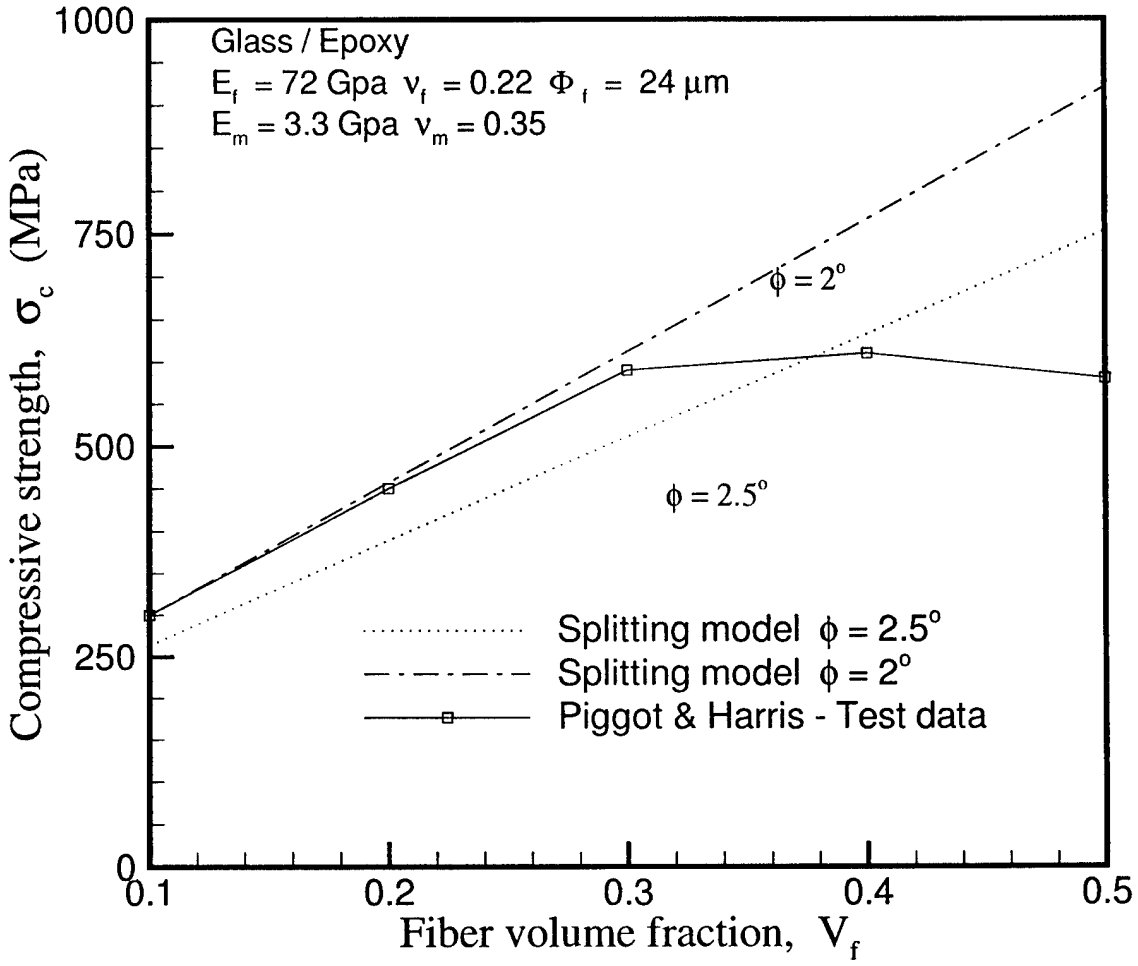

Figure 3.11: Variation of compressive strength σ with fiber volume fraction V_f for a glass epoxy composite material with different values of misalignment angle $\phi = 2^0$ and $\gamma_f = 0.119\ KJ/m^2$

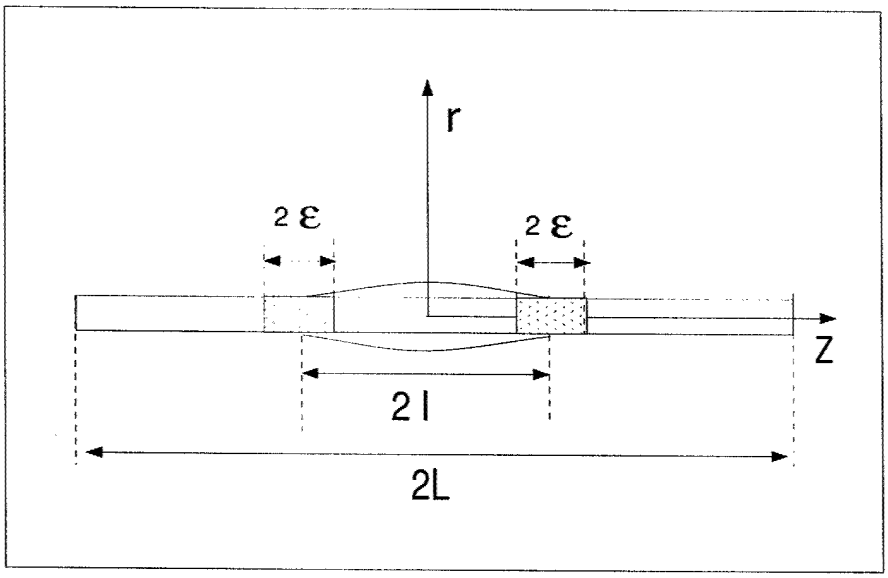

a) A single fiber with a crack embedded in matrix

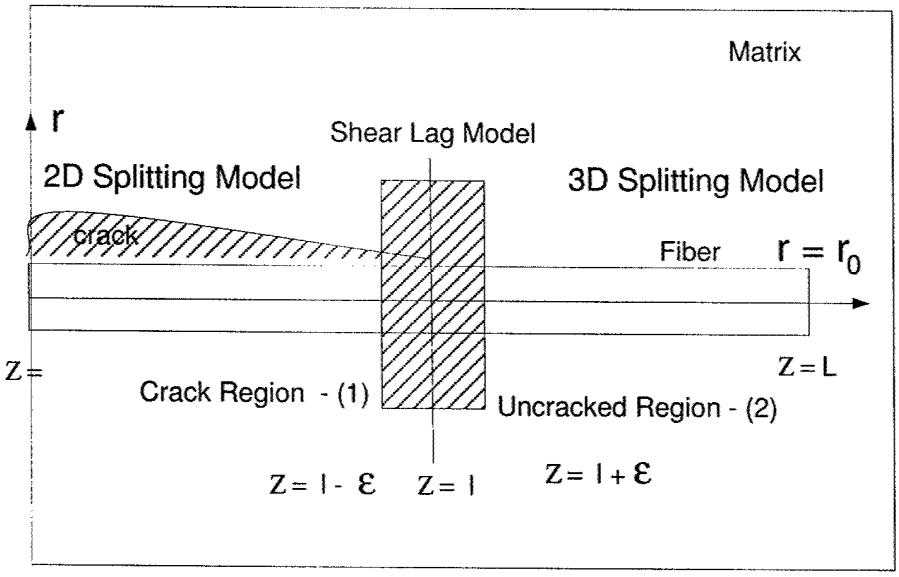

b) Crack and Uncracked regions

Figure 3.12: RVE showing the various regions of analysis

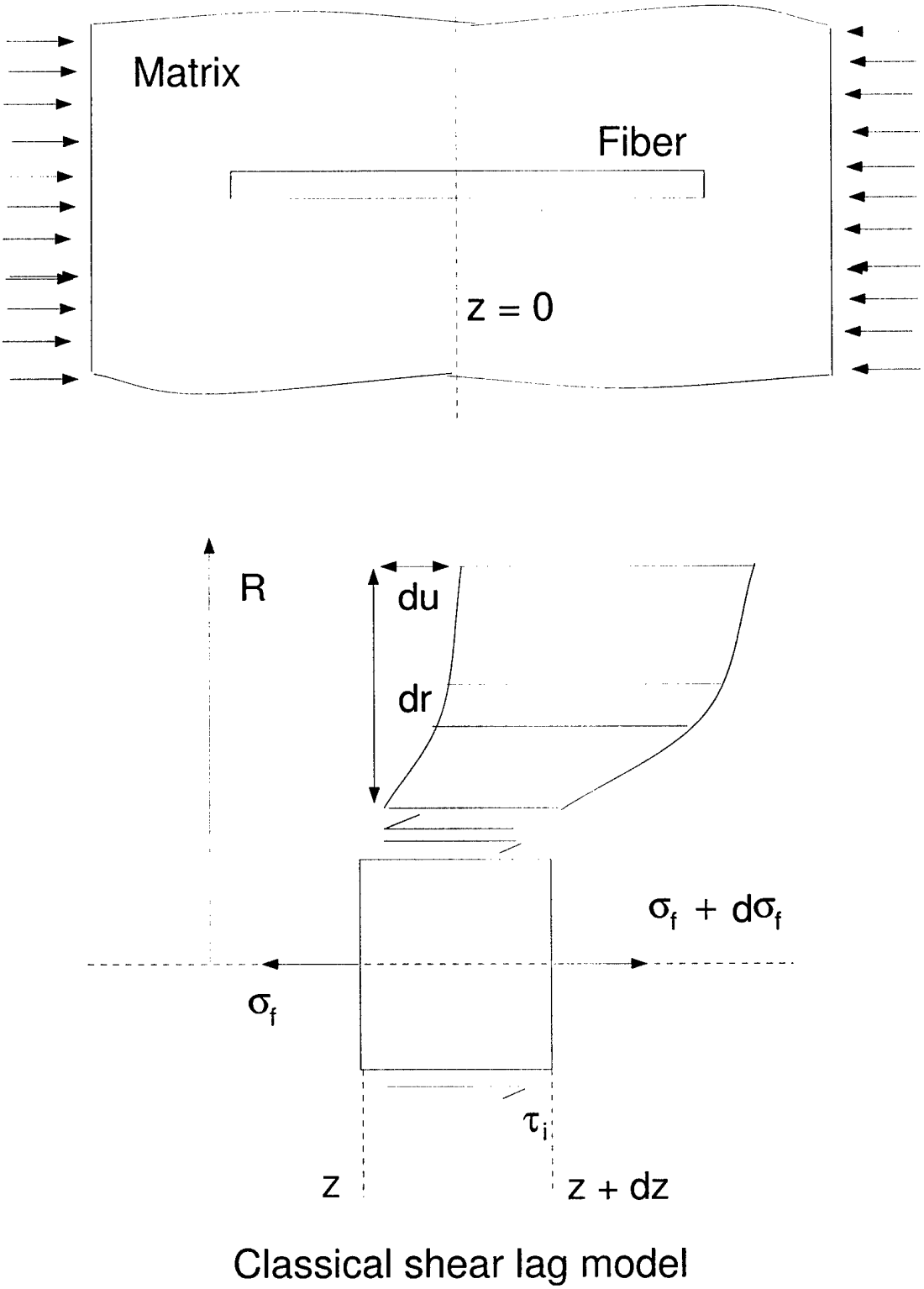

Figure 3.13: Free body diagram of a small segment of fiber and attached matrix

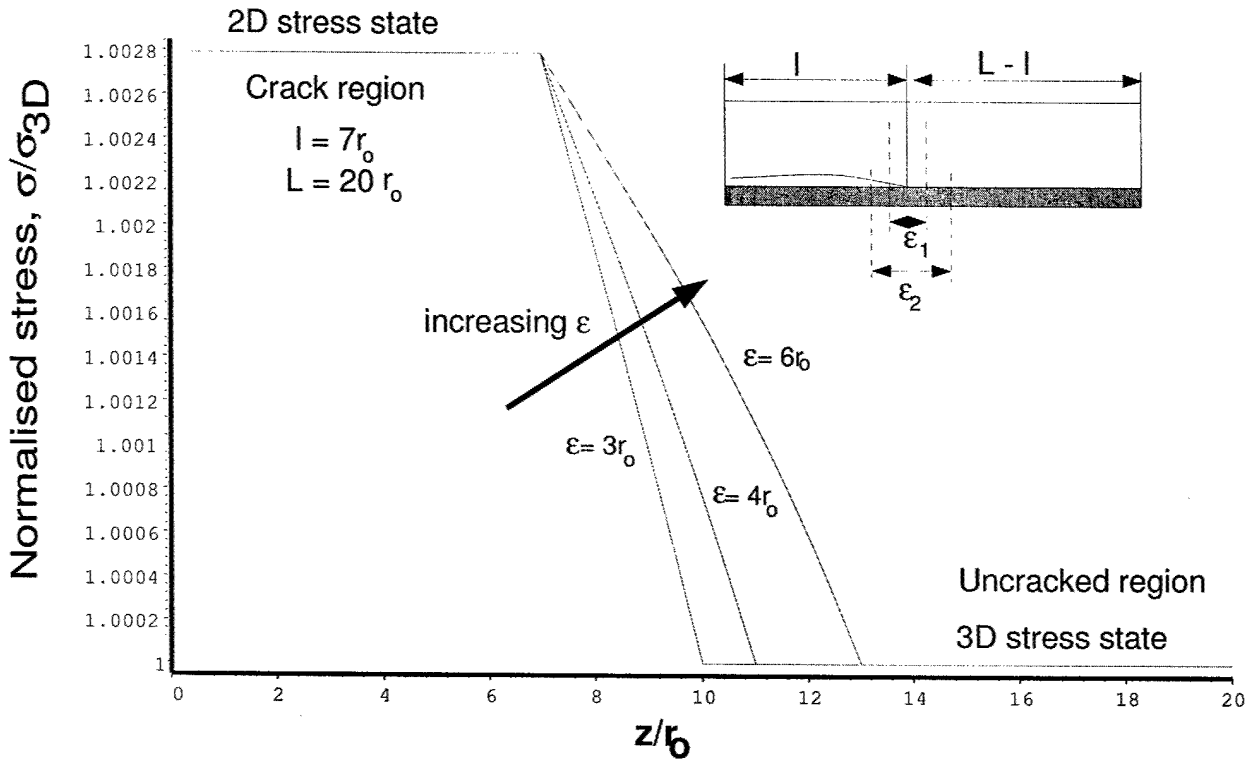

Figure 3.14: Variation of normalised stress along the length of fiber as a function of increasing ϵ with crack length factor n1 = 7

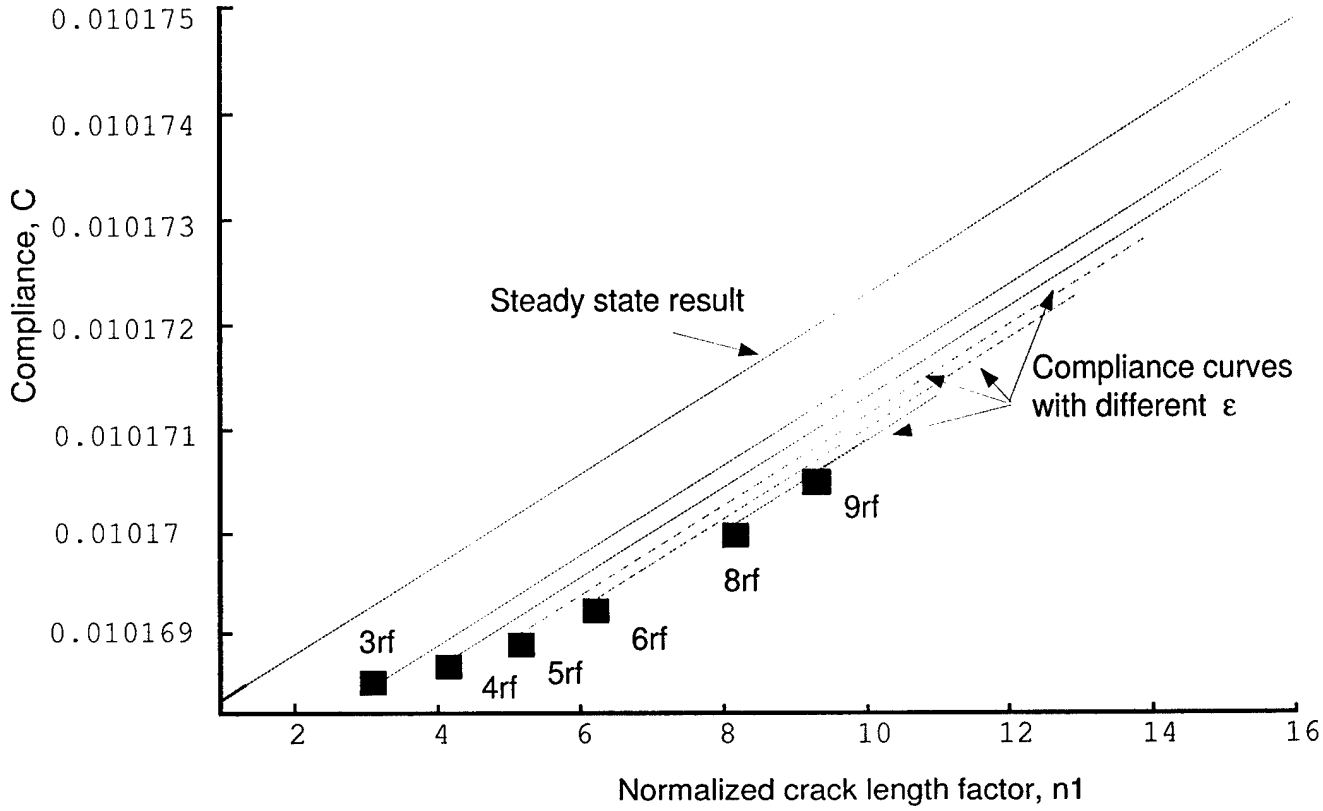

Figure 3.15: Curves of compliance as a function of normalized crack length for different values of ϵ and $L = 20r_o$

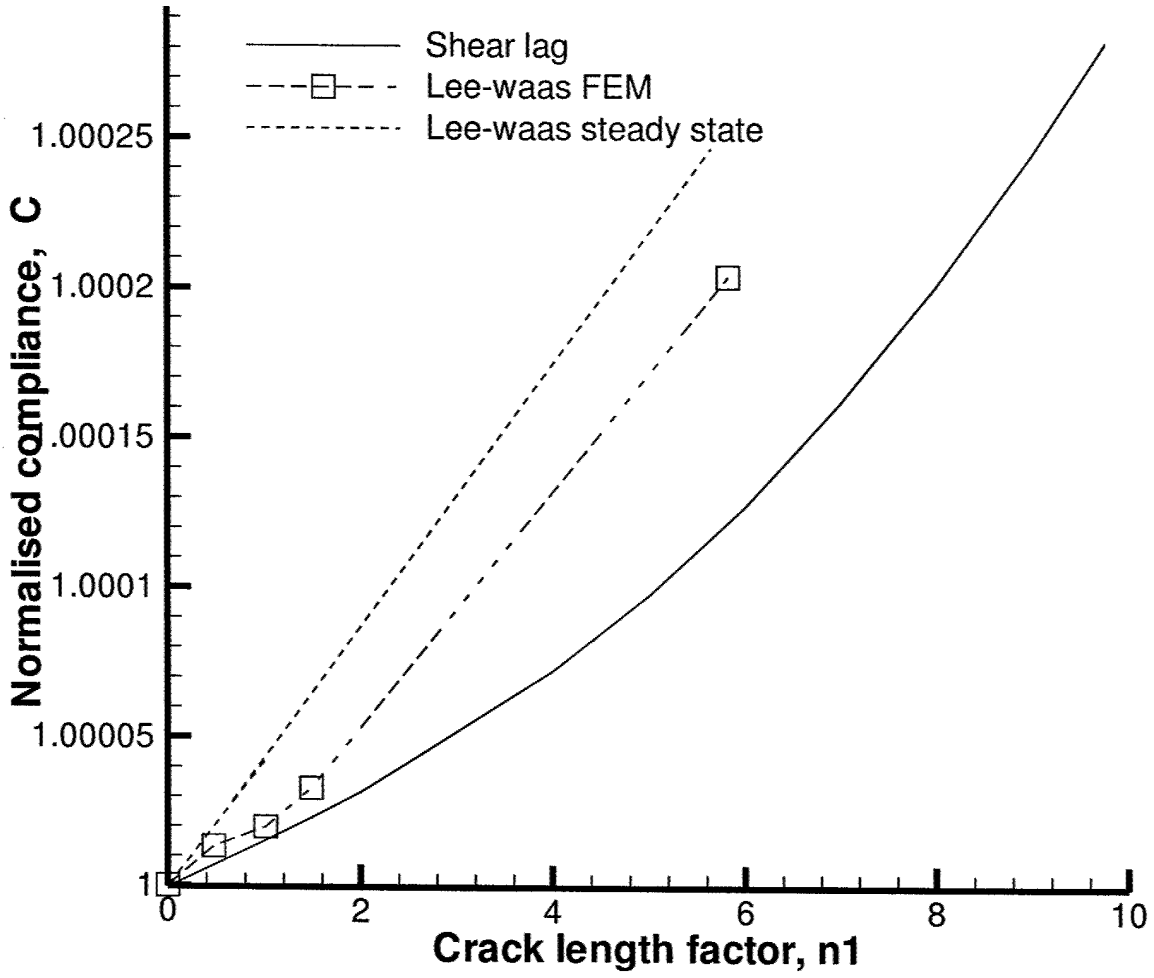

Figure 3.16: Normalized compliance with normalized crack length factor, n1

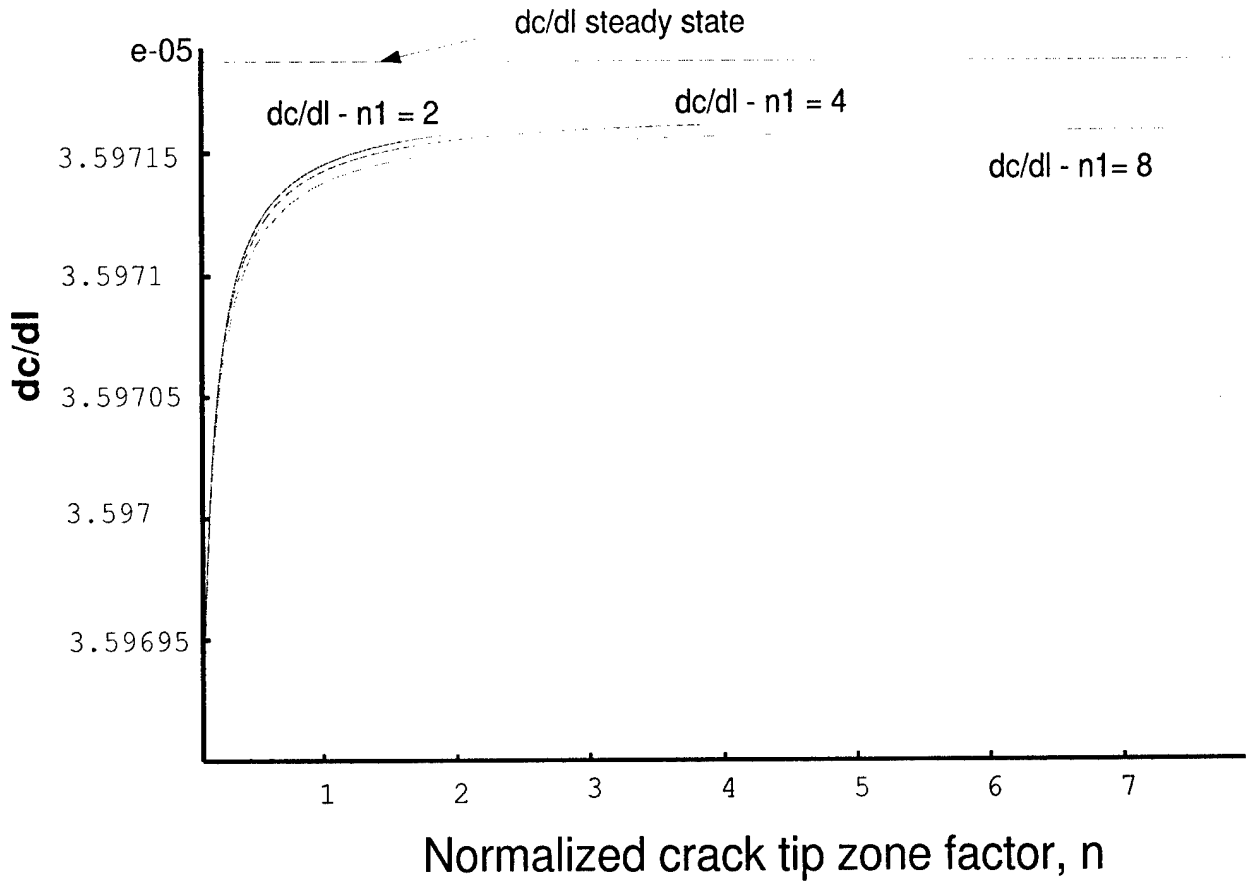

Figure 3.17: Curves of rate of change of compliance with crack length $\frac{dc}{dl}$ as a function of crack length with varying ϵ and $L = 20r_o$

CHAPTER IV

COMBINED COMPRESSION TORSION RESPONSE OF FRPC

4.1 Introduction

The role of shear stresses in dictating the compressive strength of unidirectional fiber composites has been highlighted by the kinking models of Budiansky and Fleck (1993). Information obtained from the combined compression-shear loading experiments on fiber composites can be used to understand the effect of shear stresses on the compressive strength. In previous studies, researchers have focussed on combined compression-shear of small diameter carbon fiber composites. However, a study of the combined compression-torsional response of fiber reinforced composites with a view to examining the effect of fiber diameter and fiber mechanical properties is absent in the literature. In this chapter, results will be presented from a combined compression-torsion experimental study of both glass and carbon fiber reinforced composites. Ideally, combined compression-torsion experiments are done on thin walled cylindrical tubular specimens, Mendelson (1983). However, with FRPC, the process of manufacturing thin-walled tubular specimens introduces unwanted machining and thermall effects that render the material to be different than that of the bulk composite.Consequently, solid cylindrical test specimens are used for the experi-

ments. An appropriate analysis of the solid cylindrical test specimens, to extract the important shear stress-strain data, when subjected to combined compression and torsion, is carried out based on the work of Lyon (1991) who extended an earlier analysis by Nadai (1950). The effect of remotely applied shear stress on the overall compressive strength of composites is modeled by using a fracture mechanics based failure criteria. Furthermore, the Budiansky-Fleck kinking analysis is modified to account for the non-linear shear stress distribution across the solid cross-section of the specimen.

The existing literature in the area of compressive behavior of FRPC can be broadly divided into two areas based on the failure mechanism being investigated. The first is the microbuckling of fibers in an inelastic matrix leading to kinking of fibers under the action of pure compression loading and another is the splitting failure of composites. The splitting failure mode in glass composites has been reported by Piggott (1981); Piggott and Harris (1980), Lee and Waas (1999) and Oguni and Ravichandran (2000). Splitting is a distinctly different failure mechanism from kinking. This mechanism, like kinking, is found to be a compressive strength limiting feature in glass composites. Lee and Waas (1999), and independently, Oguni and Ravichandran (2000) developed fracture mechanics based failure models for predicting the compressive splitting strength of FRP composites. Compressive splitting has also been observed in other brittle materials like rock and certain classes of ceramics(Nemat-Nasser and Horii (1982); Nemat-Nasser and Deng (1994)). Splitting failure in these materials have been modeled by appealing to ideas of fracture mechanics, for example, the wing-crack model(Horii and Nemat-Nasser (1985, 1986)).

In FRPC, compared to splitting, the kinking failure mode has been studied exhaustively through experiment and analytical/numerical modeling [Argon (1972),Bu-

diansky (1983); Fleck et al. (1995); Fleck (1997); Kyriakides et al. (1995); Vogler and Kyriakides (1999); Hsu et al. (1999),Vogler and Kyriakides (2001)]. Argon (1972) and later Budiansky (1983) were the first to develop models for kinking failure in composites. They observed that the fibers in a unidirectional fiber reinforced composite are not perfectly straight. Owing to this, they reasoned that fiber mislignments cause the development of local shear stresses in the composite under the action of remote pure compressive loads. When these shear stresses exceed the value of the shear yield stress of the matrix the fibers undergo shear buckling leading to failure in compression. Later Budiansky and Fleck (1993) extended the above ideas to include the effect of matrix strain hardening on the compressive strength of fiber composites. Similarly, the effect of strain gradients on compressive strength of carbon fiber composites has been investigated and reported in Wisnom and Atkinson (1997) and Drapier et al. (2001). Recently, the possibility of kinking initiating due to internal fiber breaks has been given consideration by Narayanan and Schadler (1999). A survey of the literature on compressive failure can be referred to in the review paper by Waas and Schultheisz (1996) and a more recent one on the various compressive strength models by Naik and Kumar (1999). Based on previous research it can be inferred that the compression strength of polymer composites depends on the fiber mechanical properties, matrix shear properties, fiber/matrix interface fracture energy, fiber volume fraction, V_f, and initial misalignment of fibers. Understanding the effect of each of these parameters on the observed compressive strength and the mode of failure is very important if a proper understanding of the compressive behavior of composites is to be attained. Of the above parameters, induced local shearing stresses governed by the response of the matrix in shear and the interfacial fracture energy of the composite play an important role in determining the failure mechanism

and the failure strength of the composite.

The presence of shearing stresses, during the application of compressive loads on the specimen, induces misalignments in the fibers which would degrade the performance of the composite under compressive loads. Thus, combined axial/torsional loading of solid cylindrical specimens will help in understanding the effect of shear on the composite compressive strength in a systematic manner. Relatively few experimental results are available for the combined compression-shear loading of polymer matrix composites. Jelf and Fleck (1994a) conducted tests on hollow composite tubes made of carbon/epoxy with a fiber volume fraction, V_f of 65%. A constant value of shearing stress was applied to the tubes, after which the compression load was increased until failure. They found that the composite compressive strength decreased linearly with increasing values of remotely applied shear stress. Even though a cylindrical tube is an ideal geometry to study the response of composite materials under combined compression/shear loading, the manufacturing of the walled tubular specimens of FRPC results in specimen behavior that may not be representative of FRPC bulk behavior. Studies on the effect of shear on composite compressive strength were also reported in Vogler et al. (2000); Vogler and Kyriakides (2001). Tests were conducted on flat coupons of AS4/PEEK composites with a specially prepared test bed to apply shearing stresses and compression stresses simultaneously. These studies reported that the compression strength of AS4/PEEK specimens dropped in a linear manner with increasing values of remotely applied shear stresses. Vogler et al. (2000) performed finite element analysis of AS4/PEEK under combined compression and shear loading to compare with the experimental work. These previous investigations on the effect of combined loading on compressive strength have been restricted to carbon composites at fixed fiber volume fraction, V_f, and under non-proportional

remote loading. The focus of these studies was the effect of shear on altering the details of kinking. The present study, on the other hand is focussed on understanding how various parameters influence the mode of failure under combined loading. To do this, we have chosen to examine the behavior of solid cylindrical specimens of glass fiber/vinylester and carbon fiber/vinylester unidirectional composites at a fixed fiber volume fraction of $V_f = 50\%$ when subjected to proportional compressive/shear loading.

The chapter is organised as follows: Experimental details and results pertaining to the combined compression-torsion experiments are presented first followed by an extension of the Budiansky-Fleck model to a solid circular cylindrical configuration. This analysis is followed by the introduction of a new splitting model appropriate for combined loading. This new model is an extension of the earlier work by Lee and Waas (1999). This is followed by a discussion and comparison of the experimental results with model predictions. Finally, concluding remarks are offered.

4.2 Experimental Details

Solid cylindrical specimens of $V_f = 50\%$ were manufactured using an in-house composite manufacturing facility. Composites were made using both E-glass (Vetrotex-certainteed) fibers of 24.1 μm diameter and IM-7-12K carbon fibers(Hexcel corporation) of 5 μm diameter with vinylester resin (Dow Derakane 411-C50). The specimens were cut with a fine diamond tip saw using a low speed cutting machine into lengths of 63.5 mm. The gage length of the specimen was about 12.7mm and the average diameter of the specimen was 6.8 mm. The specimens were subjected to pure compression, pure torsion and combined compression-torsion under displacement control loading, rotation control loading and combined displacement-rotational control load-

ing respectively. The tests were performed on a Axial-Torsional MTS machine which had the capacity to simultaneously apply axial and torsional loads. The strains in the specimens were measured by attaching three strain gages on the specimen surface, two along the axial direction on opposite surfaces and the third one at an angle of 45^o to the vertical. The third strain gage was used to calculate the shearing strain and the two strain gages along the generators of the cylindrical specimen were used to measure the axial strain in the specimen. Apart from the strain gage data, data was collected on the cross head displacement, cross head rotation, axial force and the torque acting on the specimen. As has been reported in the literature (Martinez et al. (1981); Vogler and Kyriakides (1999)), the type of gripping influences the failure strength of the fiber reinforced polymer composite under compression. As can be seen in Figure 4.1 the rectangular block grips provide uniform continuous contact with the sides of the specimen. In contrast, the collet grips have some grooves to improve gripping in torsion, which leads to non-uniform discontinuous contact. Pure compression tests were done using the block grips along with the setup shown in Figure 4.2 which resulted in a slightly lower compressive strength. We observed that the initiation of kink bands in the carbon fiber composites occurred inside the grips. The use of collet grips resulted in a higher compressive strength. For the combined compression-torsion tests it is required that the specimen be gripped in such a manner that there is no slip between the specimen surface and the interior of the grip, while rotating the specimen and simultaneously applying an axial load. The grooves in the collet grips provide the above functionality. Hence, collet grips were used along with an adapter to mount onto the MTS cross head.

4.2.1 Testing Plan

Initially pure compression and pure torsion tests were performed on the composite specimens, which correspond to the vertical and horizontal axis of the loading diagram as shown in Figure 4.3. The pure compression tests were performed under displacement control at a uniform cross head displacement of 0.0381 mm/s and the pure torsion tests were performed at a uniform cross head rotation of 0.0635 deg/min. As can be seen in Figure 4.3 different loading paths were adopted and the failure mechanism and failure strength in each case was noted. The loading ratio was defined in terms of the axial displacement and the arc displacement as $\frac{\Delta}{R\theta}$, where Δ is the axial cross head displacement, θ is the applied cross head rotation and 'R' is the radius of specimen. This was repeated for both glass and carbon composites.

4.2.2 Experimental Results

In this section, important features of the experimental results will be presented. The combined compression-torsion loading of solid cylindrical specimens of glass and carbon fiber composites was done under displacement and rotational control. Figure 4.4 shows the proportional loading for a glass/vinylester composite specimen with $\Delta/r\theta = 5.23$ as sensed by the strain gages in the gage section of the specimen. For this type of loading ratio, Figure 4.5 shows the plot of axial stress as a function of shear stress. It can be seen that the curve is non-linear except at the initial stages of loading. The linear variation of axial stress with shear strain for the same specimen is shown in Figure 4.6. Hence, it can be inferred that the non-linear nature of the axial stress-shear stress curve is because of the non-linearity induced by the shear response of the composite. This can be seen in Figure 4.7 where the shear stress is plotted as a function of the axial strain. A plot showing the failure envelope of glass/vinylester

and carbon/vinylester composites are shown in Figure 4.8 and Figure 4.9.

An important obervation that can be made from the experimental data of the combined loading tests of glass/vinylester and carbon/vinylester composite specimens is the distinct difference in both the response to remote shear stress, and in the failure mechanisms. It was found that the glass composites failed by a combination of splitting and kinking at high values of $\Delta/r\theta$. The splitting failure of glass composites is usually characterized by extensive brooming of fibers in the split region as indicated in Figure 4.11. Figure 4.12 is a high resolution SEM micrograph of a longitudinal section in the splitting region of the glass composite. It can be seen from the SEM pictures that there is extensive fiber/matrix debonding and fiber breakage. Whereas, at lower values of $\Delta/r\theta = (0.4 - 0.6)$ the failure was by kinking and is shown in Figure 4.13. These observations are similar to those made by Piggott and Harris (1980) in which they found the failure mode changing from kinking/splitting to kinking as the matrix became softer. In their work they used a matrix material with different curing times to obtain a range of matrix stiffness and yield stress values for the matrix. The present work indicates that the effect of remote shear stress beyond the shear yield stress is similar to that of a partially cured matrix. Thus, matrix stiffness and matrix yield stress are important parameters in determining the failure mechanism. The failed glass composite specimens were cross sectioned and observed under SEM to study the failure mode. Figure 4.11 and Figure 4.13 show that there is a change in failure mode as the shear stress at failure exceeds the shear yield stress of the composite i.e. as the $\Delta/r\theta$ value becomes low.

Carbon composites, however, failed by kinking as seen in Figure 4.14, throughout the range of loading ratios for which the tests were conducted. These experimental findings indicate the importance of constructing a failure model that can capture

different and distinct failure mechanisms. Clearly, kinking is not the only strength limiting mechanism of failure. Our intent in the next section is to establish analytical models for kinking and splitting with a view to understanding which parameters influence the different mechanisms of failure.

Some other observations that were made from the experiments are as follows. For high values of $\Delta/r\theta$, the compressive strength of some specimens were found to increase. This could be due to the fact that for small rotations of cross sections, the applied shear strain acts in a manner to reduce the misalignements thus leading to an increase in compressive failure strength. Further, for high values of $\Delta/r\theta$ (which implies high compression and low rotation) torque reversal was observed. This can be seen in Figure 4.10, where the torque undergoes a change in sign. This can be attributed to the result of the interaction between the induced shear strain caused by the applied axial compression and the sense of the shear strain due to the applied end rotation. In cases of high $\Delta/r\theta$, the induced shear strain must be higher than the applied shear(due to rotation) causing the relaxation in torque sensed by the torsional load cell. In a load control experiment this could lead to an instability in torsion, which was the primary reason for conducting the present experiments under displacement and rotation control.

4.3 Analysis

The modified Budiansky-Fleck model(MBF) for kinking failure in solid composite cylinders under combined compression-torsion loading is presented, followed by a novel energy based splitting failure model in pure compression, pure torsion and combined compression-torsional loading.

4.3.1 Kinking Analysis

The Budiansky-Fleck model is based on the assumption that the shear stress variation is a known function of the radius of the specimen. However, in case of solid cylindrical specimens the shear stress distribution is not a known function of the radius. Hence, the current formulation of Budiansky-Fleck model was modified to apply it to the case of solid cylindrical specimens. For solid cylindrical specimens, under pure torsion, Lyon (1991) who extended the work of Nadai (1950), has shown that the expression for the shear stress τ_R at radius, $r = R$ in terms of the applied torque, T and the rotation θ is as given below in equation(4.1).

$$\tau_R = \frac{3}{2\pi R^3}[T + \frac{\theta}{3}\frac{dT}{d\theta}] \tag{4.1}$$

The expression for critical compressive stress in the presence of remotely applied shear stress, τ^∞ is derived for a zero angle kink band as follows. As shown in Figure 4.15, the free body diagram of a small segment at a distance 'r' from the center of the cylindrical specimen is considered in the deformed configuration with a uniform axial stress σ_Z acting along the Z direction. Then, taking a balance of moments on this segment, one obtains the following expression for axial stress in terms of the remote shear stress, τ^∞, the shearing response of the composite material, $\tau(r)$, within an element of kinked fibers, the initial misalignment angle of the fibers, ϕ, and the applied shear strain, $\gamma(r)$.

$$\sigma_z = \frac{\tau(r) - \tau^\infty}{\phi + \gamma(r)} \tag{4.2}$$

In the case of solid specimens, the shear stress $\tau(r)$ is not a linear function of 'r', hence its variation with 'r' is unknown and cannot be evaluated. However, the variation of shear stress, $\tau(r)$ is known as a function of shear strain, γ, which is a

linear function of 'r' given by $r\theta/l$, where θ is the rotation and l is the specimen gage length. Therefore the first step in developing the MBF is to express the shear stress as a function of shear strain, γ. This is achieved by expressing the specimen radius 'r' as $\frac{\gamma l}{\theta}$. Using the above substitution for 'r' and multiplying both sides of equation(4.2) by $r^2 dr d\theta$ and integrating, we can write equation(4.2) as

$$\int_0^{2\pi}\int_0^{\gamma_R} \sigma_z(\phi+\gamma)\frac{\gamma^2}{\nu^3}d\gamma d\theta \;=\; \int_0^{2\pi}\int_0^{\gamma_R} \tau(\gamma)\frac{\gamma^2}{\nu^3}d\gamma d\theta - \int_0^{2\pi}\int_0^{\gamma_R} \tau^{\infty} r^2 dr d\theta \quad (4.3)$$

where ν is twist per unit length, θ/l. Simplifying the above equation we obtain the following expression for average critical compressive stress, σ_z, where, we substitute T the applied torque for $\int_0^{2\pi}\int_0^{R}\tau^{\infty} r^2 dr d\theta$ and γ_R for shear strain at $r = R$. Then,

$$\sigma_z \;=\; \frac{\frac{1}{\gamma_R^3}\int_0^{\gamma_R}\tau(\gamma)\gamma^2 d\gamma - \frac{T}{2\pi R^3}}{\frac{\phi}{3}+\frac{\gamma_R}{4}} \quad (4.4)$$

The integral term in (4.4) represents the shear response of the composite material and can be obtained from a pure torsion test of the composite with similar fiber volume fraction. In equation(4.4), if we substitute $\alpha\sigma_z$ for $\frac{T}{2\pi R^3}$, where α is the loading ratio, then we obtain an expression for σ_z in terms of the shear response of the composite, loading ratio, α, the misalignment angle, ϕ, and the induced shear strain, γ_R at $r = R$, as given below in equation(4.5). On solving equation(4.5) we get a limit load for σ_z at some value of γ. This represents the critical kinking compressive stress for the composite.

$$\sigma_z \;=\; \frac{\frac{1}{\gamma_R^3}\int_0^{\gamma_R}\tau(\gamma)\gamma^2 d\gamma}{\alpha+\frac{\phi}{3}+\frac{\gamma_R}{4}} \quad (4.5)$$

4.3.2 Splitting Analysis

Splitting failure mode has been observed in glass composites by Piggott (1981), Lee and Waas (1999) and Oguni and Ravichandran (2000). The micrographs of the

failed specimens as seen in Figure 4.11 and Figure 4.12 reveal that the fiber/matrix interfaces split during failure and the fibers are broken. Some of the fibers in the region of splitting actually show the matrix attached to the fiber surface. This indicates that the splitting failure does not always happen along the interface but sometimes meanders into the matrix region away from the fiber/matrix interface. In high fiber volume fractions (0.4-0.6), kink bands are also observed along with the fiber/matrix splitting failure cracks in glass composites. However, for the glass composites tested isolated kink bands were never formed as observed in carbon composites. Based on these observations Lee and Waas (1999) developed a energy based splitting failure model. In following sections, we have extended the splitting model of Lee and Waas (1999) and presented in chapter III, for pure compression to the case of pure torsion and combined compression-torsion. To avoid repetition, only the derivation for torsional and combined compression-torsional loading is presented in the following sections.

Strain Energy Release Rate, $\mathcal{G}$

Consider a representative volume element(RVE) of the composite, consisting of a concentric cylinder of fiber and matrix, with a fiber radius, r_0 and an outer region of matrix with radius, r_1, and subjected to a external axial load, P and torque, T, as shown in Figure 4.16. Following the methodology of the composite cylinder model(CCM) as given in the text by Christensen (1991), we assume the composite to be consisting of a collection of such representative volume elements(RVE's). The outer radius of matrix in the RVE is chosen to satisfy the fiber volume fraction requirement such that $r_1^2 = V_f/r_0^2$. The outer matrix surface ($r = r_1$) is assumed to be traction free. The height of the cylinder is taken to be '2L' with a interfacial crack

of '2l' embedded at the interface of fiber and matrix. The composite is assumed to have perfect bonding outside the crack region ($l \leq z \leq L$) and ($-L \leq z \leq -l$). The total potential energy is written as $\Pi = U - W$ where U is the strain energy stored in the composite cylinder and W is the work done by the external forces.

Torsional Loading

Strain energy release rate expressions for a cylindrical specimen of linear elastic and non-linear elastic material under the action of pure torsion, 'T' are developed below. Closed form expressions of the strain energy release rate for a linear elastic material are obtained in terms of the compliance of the material.

The strain energy release rate expression for a cylinder of radius r_0, under rotational (displacement control) and torsional(load control) loading is derived as follows. For rotational control(The applied rotation, θ, is held fixed during crack propagation), we have,

$$\Pi = U - W, \quad U = \frac{1}{2}T\theta, \text{ and } W = 0$$
$$\mathcal{G} = \frac{\theta}{8\pi r_0}\frac{dT}{dl}$$

Using the definition of compliance, $c = r_0\theta/T$, we get

$$\mathcal{G} = \frac{T^2}{8\pi r_0^2}\frac{dc}{dl} \tag{4.6}$$

For torque control(The applied torque, T, is held fixed during crack propagation),

the expressions are,

$$\Pi = U - W, \quad U = \frac{1}{2}T\theta, \text{ and } W = T\theta$$
$$\mathcal{G} = \frac{T}{8\pi r_0}\frac{d\theta}{dl}$$

Using the definition of compliance, $c = r_0\theta/T$, we get

$$\mathcal{G} = \frac{T^2}{8\pi r_0^2}\frac{dc}{dl} \tag{4.7}$$

The expression for dc/dl for a solid circular cylinder of length '$2l$' and made of linear elastic material is $2/(GJ)$ where G is the shear modulus of the material and J, is the polar moment of inertia given by $\pi r_0^4/2$. Hence, we can write the expression for strain energy release rate as follows

$$\mathcal{G} = \frac{T^2}{4\pi r_0^2 GJ}$$

When the strain energy release rate becomes equal to $2\gamma_f$ the crack will propagate leading to failure. The critical failure stress in torsion can then be written in terms of γ_f as follows.

$$\tau_{cr} = 4\sqrt{\gamma_f G/r_0} \tag{4.8}$$

For a non-linear elastic material, the expression for strain energy release rate, $\mathcal{G}$ (we continue with the notation $\mathcal{G}$ even though J is standard notation for non-linear materials), can be obtained as follows. For displacement control(The applied rotation, θ, is held fixed during crack propagation),

$$\begin{aligned} \Pi &= U - W \\ U &= \int_V \int_0^\gamma \tau(\zeta) d\zeta dV = 4\pi l \int_0^{r_1} \int_0^\gamma \tau(\zeta) d\zeta r dr \\ W &= 0 \end{aligned} \tag{4.9}$$

$$\mathcal{G} = -\frac{d\Pi}{dA} = -\frac{1}{4\pi r_0}\frac{dU}{dl} \tag{4.10}$$

In equation (4.9), the inner integral is a known function of ζ, where ζ is a dummy variable for the purpose of integration. But, the outer integral in 'r' has to be first converted in terms of shearing strain γ since for a solid cylinder we do not know the distribution of τ with respect to the radius of cylinder, r. Using the relations $\gamma = r\nu$, and $dr = d\gamma/\nu$, in the integral of equation (4.9) we get the following integral. Here, 'ν' is the twist per unit length given by the ratio θ/l

$$U(\gamma) = 4\pi l \int_0^{\gamma_{r_1}} [\int_0^\gamma \tau(\zeta) d\zeta\ ]\ \ \gamma/\nu^2 d\gamma \tag{4.11}$$

Differentiating equation (4.11) with respect to 'l' we get

$$\frac{dU}{dl} = 4\pi \int_0^{\gamma_{r_1}} [\int_0^\gamma \tau(\zeta) d\zeta]\ \ \gamma/\nu^2 d\gamma \tag{4.12}$$

where ζ is a dummy variable and γ_{r_1} is shear strain at radius, r_1.

Combined Compression-Torsion loading

Consider a concentric cylinder of fiber and matrix with a debond of length '$2l$' as shown in Figure 4.16. We can divide this representative volume element(RVE) into a cracked region of linear elastic fiber and a non-linear elastic matrix and an uncracked region of non-linear elastic composite. Now let this RVE be subjected to a combined set of axial and torsional loads as shown in Figure 4.16. 'P' is the axial compressive load and 'T' is the torsional load. The total strain energy release rate under combined compression-torsion loading can be written as the sum of axial and torsional strain energy release rate contributions. It should be noted that we are implicitly assuming that the non-linear torsional response is unaffected by the presence of axial stress. In appendix C , we have described an analysis where the matrix and thus, the composite is treated as a deformation theory of plasticity solid. It turns out that the interaction effects (between axial stress and shear stress) are negligible and the problem can be addressed by appealing to superposition where the total energy release rate contribution is computed as the sum of $\mathcal{G}_{Axial}$ and $\mathcal{G}_{Torsion}$, with each of their contributions computed with an assumption of non-interaction between axial stress and shear stress. Thus,

$$\mathcal{G}_{Total} = \mathcal{G}_{Axial} + \mathcal{G}_{Torsion} \tag{4.13}$$

In the present case, it was observed during the experiments that the axial stress - strain curve remains linear up to the point of failure even under combined compression-

torsion loading. Hence, strain energy release rate, $\mathcal{G}_{Axial}$ is obtained based on linear elastic material behavior. In torsion, the strain energy release rate, $\mathcal{G}_{Torsion}$, is obtained by adding the strain energy release rate contributions from a linear elastic fiber and non-linearly elastic matrix in the cracked region and a non-linearly elastic composite in the uncracked region under torsional load.

$$\begin{aligned} \mathcal{G}_{Torsion} &= -\frac{1}{4\pi r_0}\frac{dU}{dl} \\ &= -\frac{1}{4\pi r_0}[\underbrace{\frac{dU}{dl}_{fiber} + \frac{dU}{dl}_{matrix}}_{crackedregion} + \underbrace{\frac{dU}{dl}_{composite}}_{uncrackedregion}] \end{aligned} \tag{4.14}$$

Now, explicit relations for the terms entering in equation (4.14) are given below for both the cracked region and the uncracked region. In the cracked region the fiber is assumed to be linear elastic hence the term dU/dl_{fiber} can be written as

$$\frac{dU}{dl}_{fiber} = \frac{\tau^2\pi^2 r_0^2}{2G_{fiber}} \tag{4.15}$$

Also, in the cracked region, the matrix is debonded from the fiber and is modeled as a non-linear elastic material for the calculation of dU/dl_{matrix}.

Matrix

$$\frac{dU}{dl}_{matrix} = 4\pi\int_{\gamma_{r_0}}^{\gamma_{r_1}}(\int_0^{\gamma}\tau_m(\zeta)d\zeta)\gamma/\nu^2 d\gamma \tag{4.16}$$

Uncracked region

In the uncracked region away from the crack tip we model the composite as a homogenous non-linear elastic material. Thus, the expression for $dU/dl_{composite}$ can be written as follows

Composite

$$\frac{dU}{dl}_{composite} = 4\pi \int_0^{\gamma_{r_1}} (\int_0^{\gamma} \tau_c(\zeta)d\zeta)\gamma/\nu^2 d\gamma \tag{4.17}$$

From equations (3.5,4.15-4.17) we can write an expression for the total strain energy release rate(SERR) of the composite as

$$\begin{aligned} \mathcal{G}_{Total} = {} & \frac{\sigma_c^2 r_0}{4V_f^2}(\frac{1}{\delta} - \beta) + \frac{\tau^2\pi^2 r_0^2}{2G_{fiber}} + \frac{1}{r_0}\int_{\gamma_{r_0}}^{\gamma_{r_1}} (\int_0^{\gamma} \tau_m(\zeta)d\zeta\ )\ \gamma/\nu^2 d\gamma + \\ & \frac{1}{r_0}\int_0^{\gamma_{r_1}} (\int_0^{\gamma} \tau_c(\zeta)d\zeta\ )\ \gamma/\nu^2 d\gamma \end{aligned} \tag{4.18}$$

When the total strain energy release rate, $\mathcal{G}_{Total}$ becomes equal to $2\gamma_f$, then splitting failure occurs. Therefore, we can write the above equation for compression strength, σ_c, under combined loading as,

$$\begin{aligned} \gamma_f = {} & \frac{\sigma_c^2 r_0}{8V_f^2}(\frac{1}{\delta} - \beta) + \frac{\tau^2\pi^2 r_0^2}{4G_{fiber}} + \frac{1}{2r_0}\int_{\gamma_{r_0}}^{\gamma_{r_1}} (\int_0^{\gamma} \tau_m(\zeta)d\zeta\ )\ \gamma/\nu^2 d\gamma + \\ & \frac{1}{2r_0}\int_0^{\gamma_{r_1}} (\int_0^{\gamma} \tau_c(\zeta)d\zeta\ )\ \gamma/\nu^2 d\gamma \end{aligned} \tag{4.19}$$

4.4 Solution Procedure

Equation (4.19) relating γ_f to the axial stress and shear stress acting on the composite is solved numerically to obtain the critical value of compressive stress and the corresponding value of shear stress. The input parameters required to solve equation (4.19) are the elastic and geometric properties of fiber, the complete nonlinear shear response of the pure matrix and the complete nonlinear shear response of the composite and the fiber volume fraction of the composite. Table 4.1 shows the properties used in the present failure model. The shear responses were incorporated in the analytical solution by using the Ramberg-Osgood fit parameters obtained from Yerramalli and Waas (2002c) and are given in Table 4.2. With the above input parameters, the equation is solved for the critical value of shear stress or compressive stress for different values of loading ratios, 'κ' , where κ is defined as σ/τ. The critical value of shear stress or compressive stress is attained when for a particular value of κ, the right hand side of equation (4.18) exceeds the left hand side value of critical fracture energy, γ_f. A range of γ_f values of $0.1224 KJ/m^2$ to $0.0408 KJ/m^2$ has been used to study the effect of fracture energy on the predicted failure envelope.

4.5 Discussion

As has been discussed in the experimental results section, the combined axial compression-torsion loading of solid circular cylindrical specimens of glass/vinylester and carbon/vinylester composites indicated that the remotely applied shear stress caused a degradation in the composite compressive behavior leading to a decrease in the failure strength. However, there was a difference in the response of carbon composites to remote shear stress as compared to that of glass composites. The carbon composites show a nearly linear reduction in compressive strength as the remote

shear stress is increased, which matches with the prediction of the MBF model, equation(4.5). This can be observed in Figure 4.18, where the axial compressive strength is plotted against a normalized torque defined as $\frac{T}{2\pi R^3}$. Using misalignment angles in the range of $2^0 - 4^0$ the predictions from the modified Budiansky-Fleck MODEL appear to bound the experimental data. On the other hand, the glass/vinylester composites were found to be initially unaffected by the remotely applied shear stress. When the remote shear stress has exceeded a critical value, a drop in compressive strength was observed as can be seen in Figure 4.19.

The results in Figure 4.19 indicate that the MBF kinking model predictions($\phi = 4^0$) are inaccurate for the glass composites which were tested under combined compression-torsion loading. It is to be noted that for $\phi = 2^0$, the MBF prediction for compressive strength becomes higher but the trend is still inconsistent with the experimental data. This is because the glass composites tested fail by splitting as observed in experiments, instead of failing in a kinking mode. This observation indicates the need for a model that explicitly accounts for the effect of fiber properties and the fiber/matrix interfacial fracture energy on the composite compressive strength. The current fracture mechanics based model is used to compare the predicted and the observed experimental values for the failure envelope under a combined state of compression-torsion loading. The value of fracture energy as a function of fiber volume fraction of the composite is not available but a initial value of $\gamma_f = 0.1224 KJ/m^2$ has been chosen to predict the failure envelope. The failure envelope predictions based on this value of γ_f are very high since this value of γ_f corresponds to the fracture energy of pure epoxy and is more suitable for lower volume fractions. Also, the failure of glass composites at high volume fractions was seen to be a combination of splitting and kinking. Hence, the failure model was used to predict the failure envelope for a range

of fracture energy ($\gamma_f = 0.1224KJ/m^2, \gamma_f = 0.0612KJ/m^2, \gamma_f = 0.0408KJ/m^2$). The correlation between the predicted stresses and the experimentally obtained data is good as indicated in Figure 4.20. The better correlation between the predicted value of compressive strength and experimentally observed strength for a lower value of γ_f could indicate that the interfacial fracture energy reduces at higher fiber volume fraction. The new model captures the trend of the failure data and the correlation is much better in the range where the loading ratio, κ is high. At lower values of κ the model predicts higher values of compressive strength than the observed experimental values. However, it should be noted that the failure mode in case of higher values of shear stress(i.e. lower κ) was not pure splitting but a combination of matrix crushing and splitting, which is not taken into account by the current splitting fracture model. When the loading is pure torsion the value of shear yield stress based on a 0.7G intercept criteria has been used. This is because polymer composites do not show a definite yield point and thus this data point is arbitrarily chosen based on the 0.7G criteria. To better understand the initial insensitivity of the glass composites to remote shear stress, a plot of axial strain energy release rate(SERR) and torsional SERR as a precentage of the total SERR with respect to the applied shear stress, τ, is shown in Figure 4.21. It can be seen from Figure 4.21 that upto a significant value of remote shear stress, τ, the axial SERR contribution to the total SERR is nearly 100% indicating that remotely applied shear stress does not play a role in inducing failure as seen in experiments. When the shear stress τ reaches a critical value, which is about $40 - 50$MPa for the glass composites there is a sudden rise in the contribution from the torsional SERR and it reaches a peak value of 100% for pure torsion loading.

4.6 Conclusions

Motivated by the experimental results obtained, we have presented a new fracture mechanics based model to predict splitting failure in unidirectional composites subjected to remote combined axial compression and torsional loading. Experimentally it was found that the response mechanism of glass fiber composites to remote shear stress is different from that of the carbon fiber composites. The results indicate that the conventional Budiansky-Fleck model is applicable to carbon fiber composites, where the failure is due to buckling of fibers in an inelastic matrix. In glass composites there seems to be a critical value of remote shear stress beyond which the compressive strength of the composite degrades very rapidly. This difference in sensitivity to the remote shear stress led us to develop a new fracture mechanics based failure model which captures the initial insensitivity of compressive strength to shear stress and the subsequent steep drop in compressive strength when the remotely applied shear stress is very high. Apart from the difference in sensitivity to remote shear stress exhibited by carbon and glass composites, the failure mechanism is also found to be different. In glass composites the failure mechanism changed from splitting to kinking. A combination of matrix crushing and splitting was observed as the remote shear stress was increased. A single model which can effectively tackle the mode transition from splitting to kinking failure and vice-versa would be ideal. Conceivably, such a model would have to be implemented numerically, perhaps using the finite element method.

	E_f(MPa)	μ_f(MPa)	r_0(mm)
Glass fiber	72000	29508	0.012
Vinylester	3585	1318	

Table 4.1: Properties of glass fiber and vinylester resin

	V_f	μ_c(MPa)	A	n
Glass composite	0.5	3260	68.68	12.44
Vinylester	0	1318	65.44	7.9603

Table 4.2: Ramberg-Osgood fit for shear stress-strain curve of glass/vinylester and pure vinylester specimens

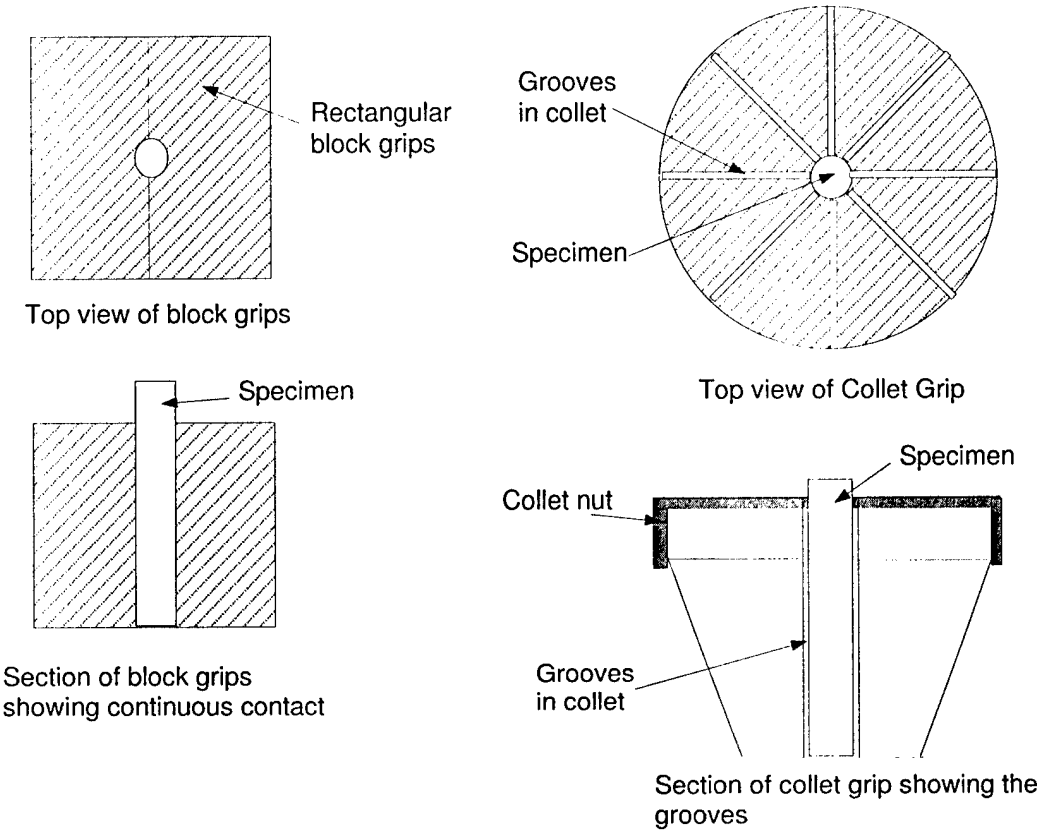

Figure 4.1: Grip cross sections

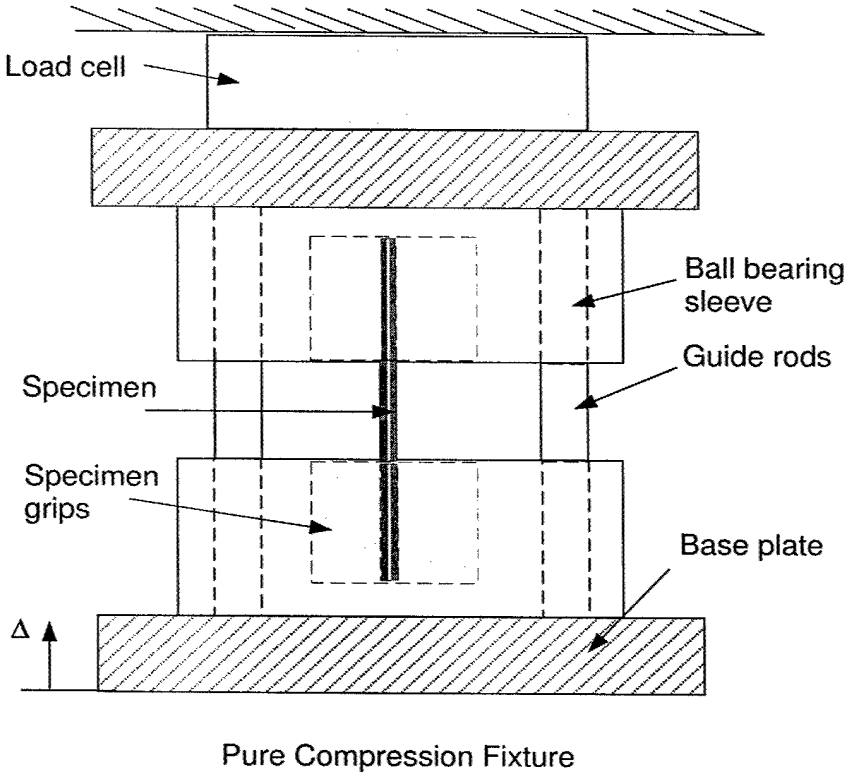

Figure 4.2: Pure compression test setup

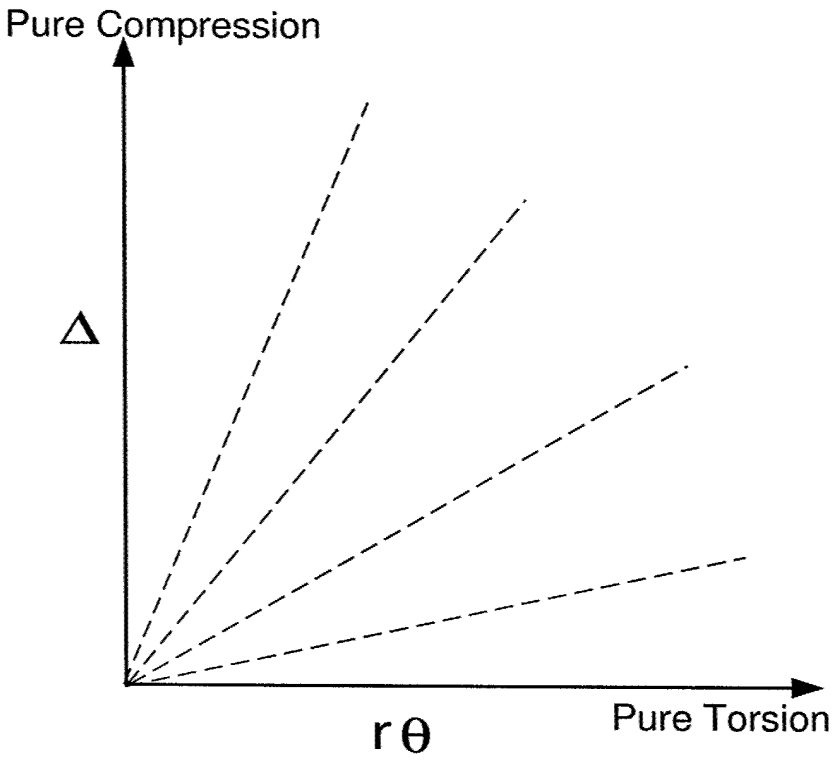

Figure 4.3: Different loading paths in a displacement/rotation control test

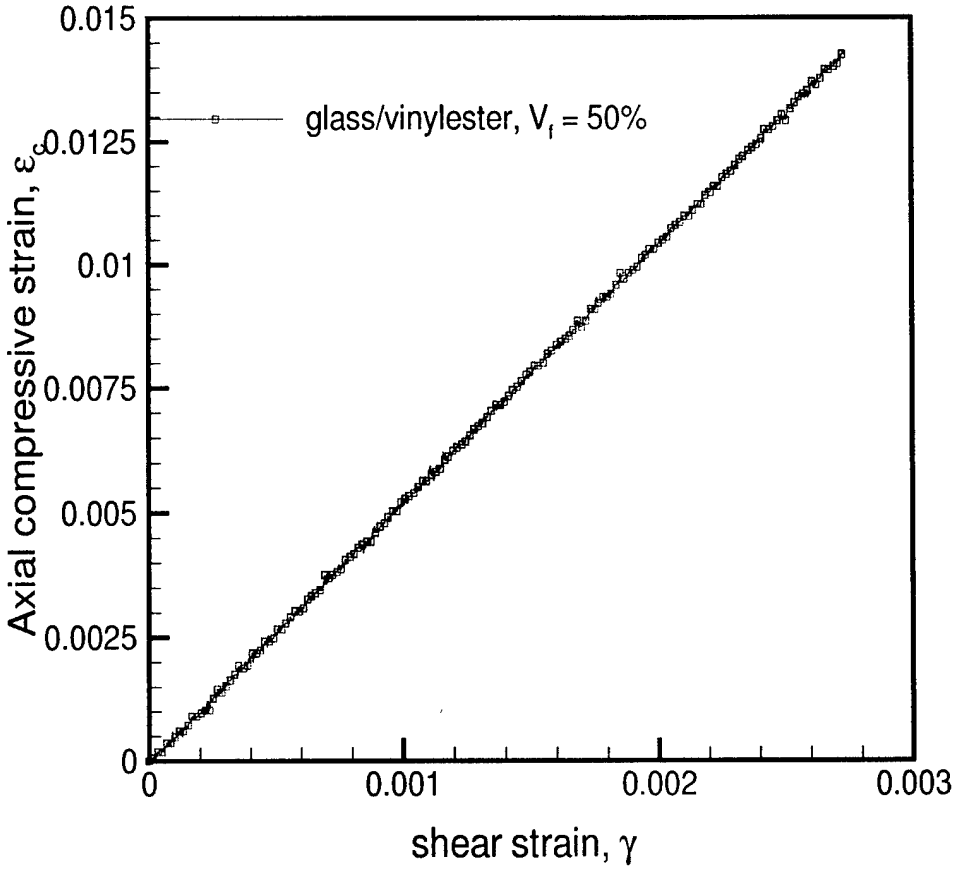

Figure 4.4: Axial strain as a function of shear strain for $\Delta/r\theta = 5.23$ and glass/vinlyester composite

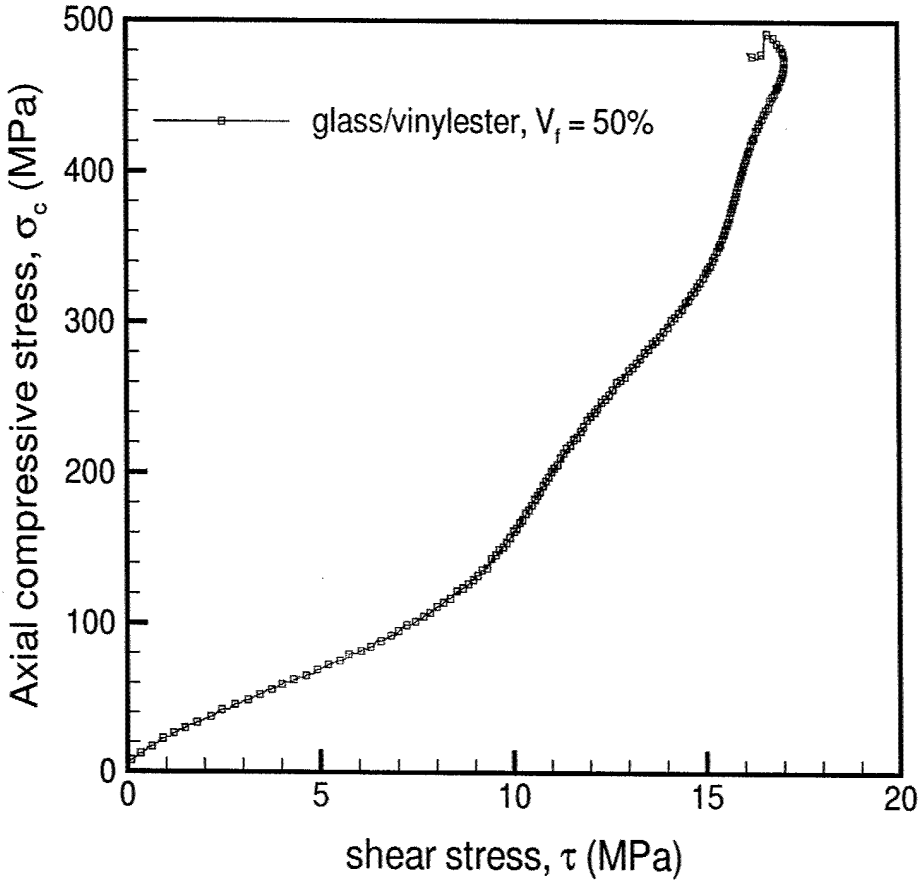

Figure 4.5: Axial stress vs shear stress for $\Delta/r\theta = 5.23$ and glass/vinylester composite.

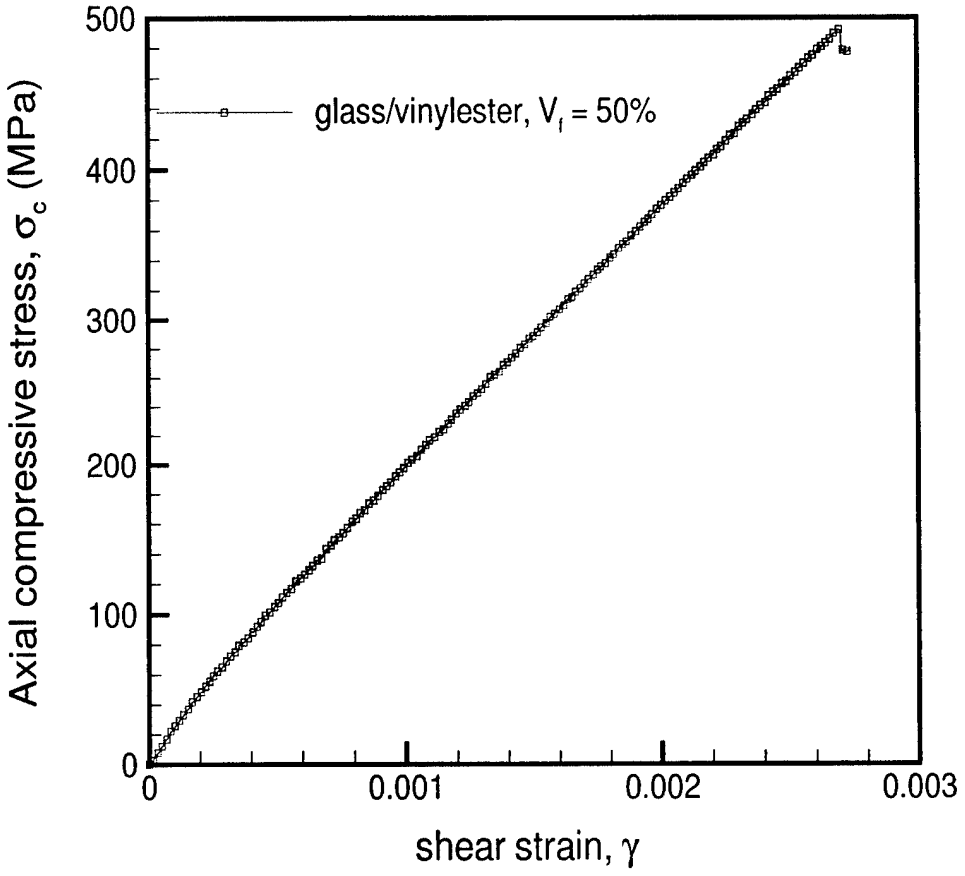

Figure 4.6: Axial stress variation with applied shear strain for $\Delta/r\theta = 5.23$ and glass/vinylester composite

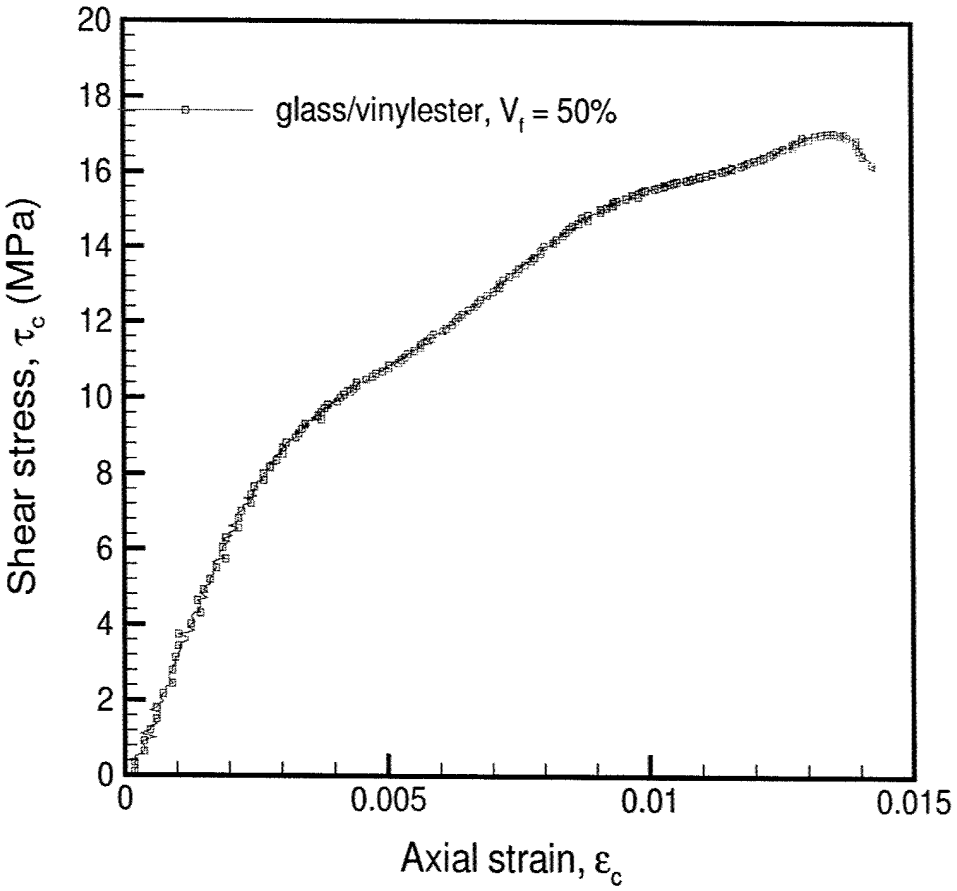

Figure 4.7: Shear stress variation with applied axial strain for $\Delta/r\theta = 5.23$ and glass/vinylester composite

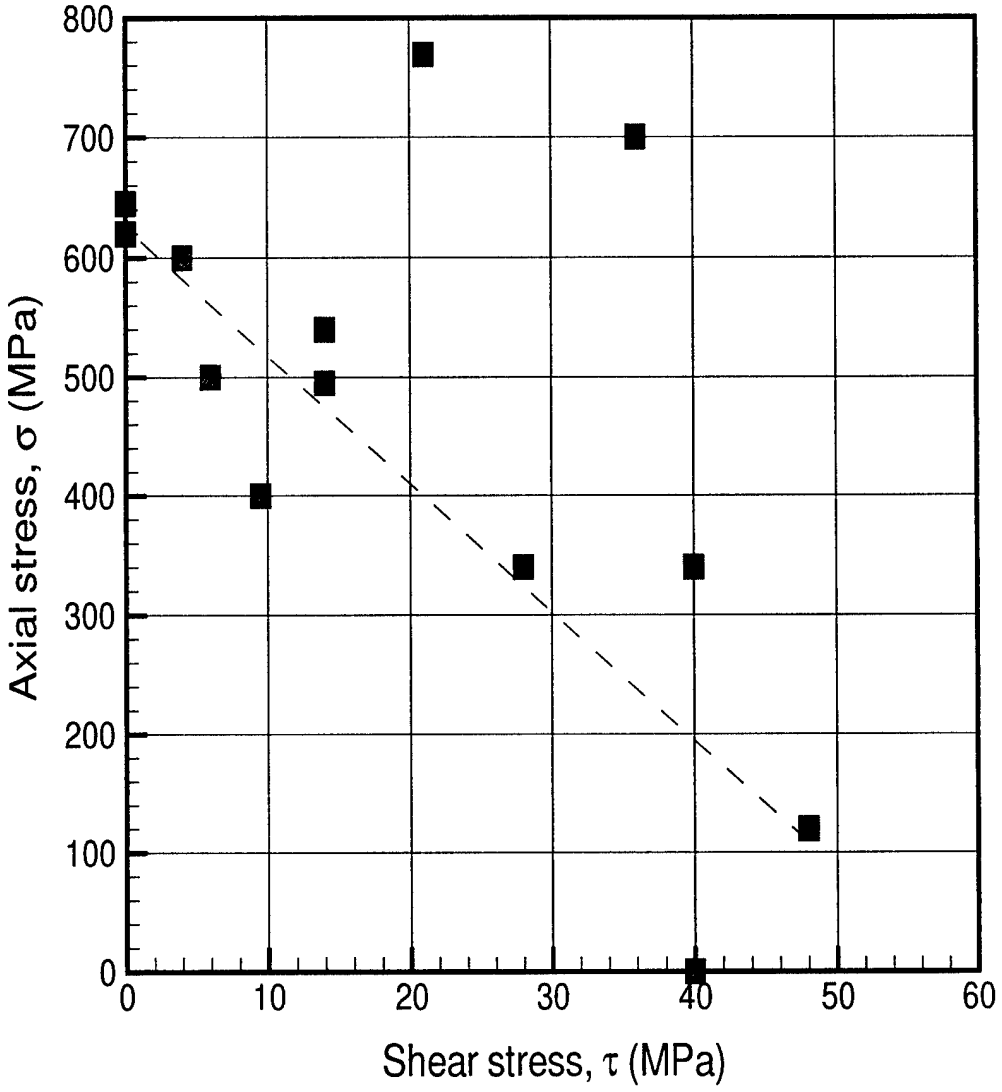

Figure 4.8: Failure envelope for a carbon/vinylester composite of $V_f = 50\%$

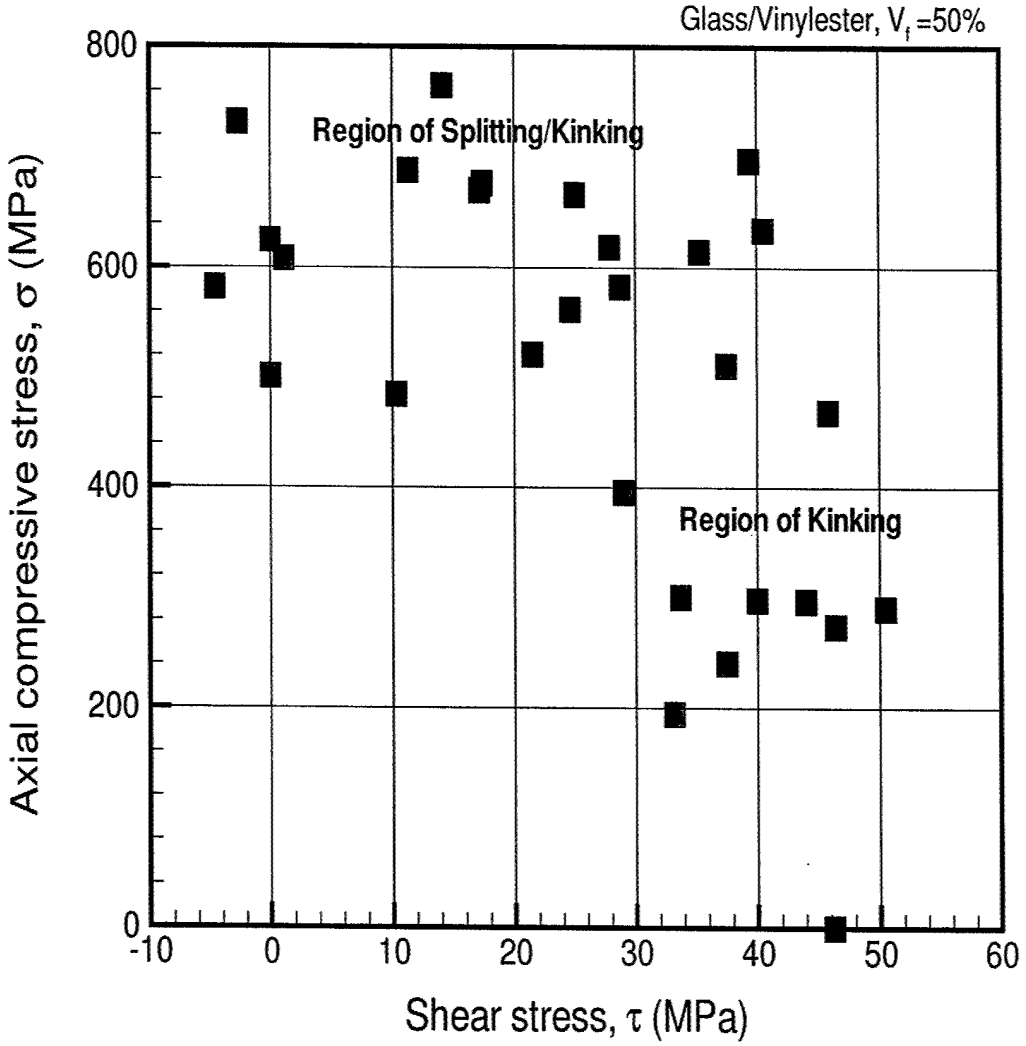

Figure 4.9: Failure envelope for a glass/vinylester composite of $V_f = 50\%$

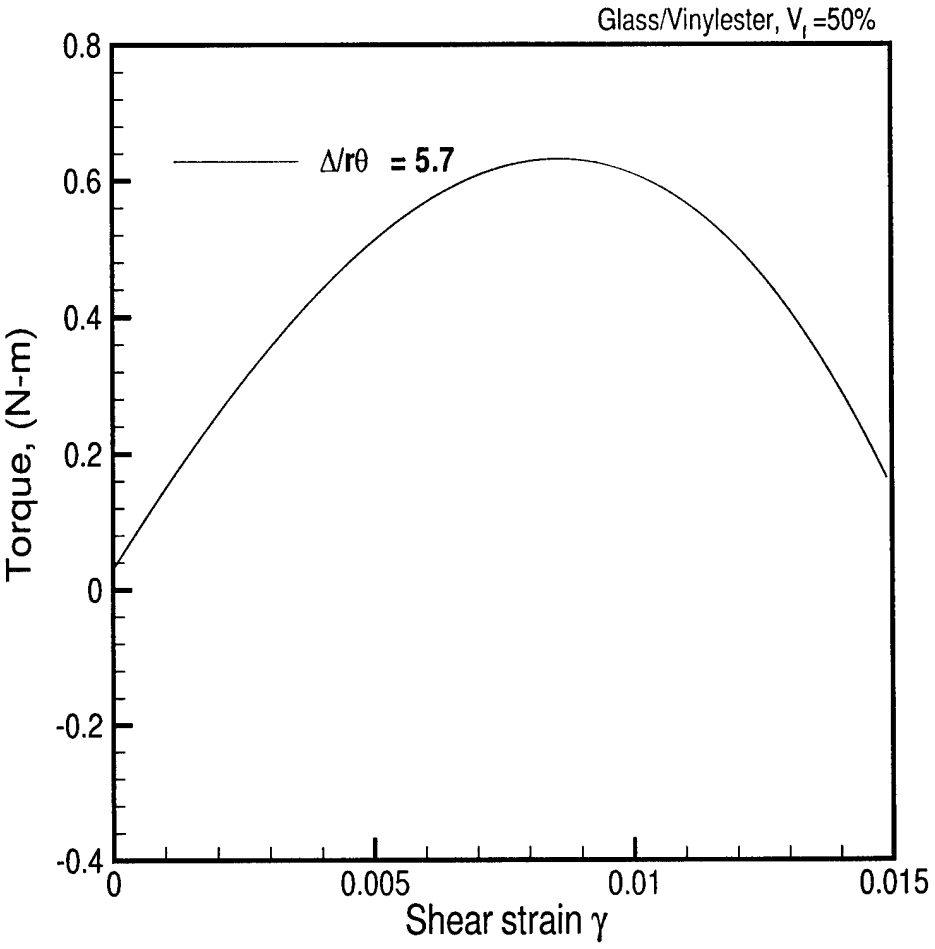

Figure 4.10: Plot showing the stress reversal in glass composite for high values of $\Delta/r\theta$

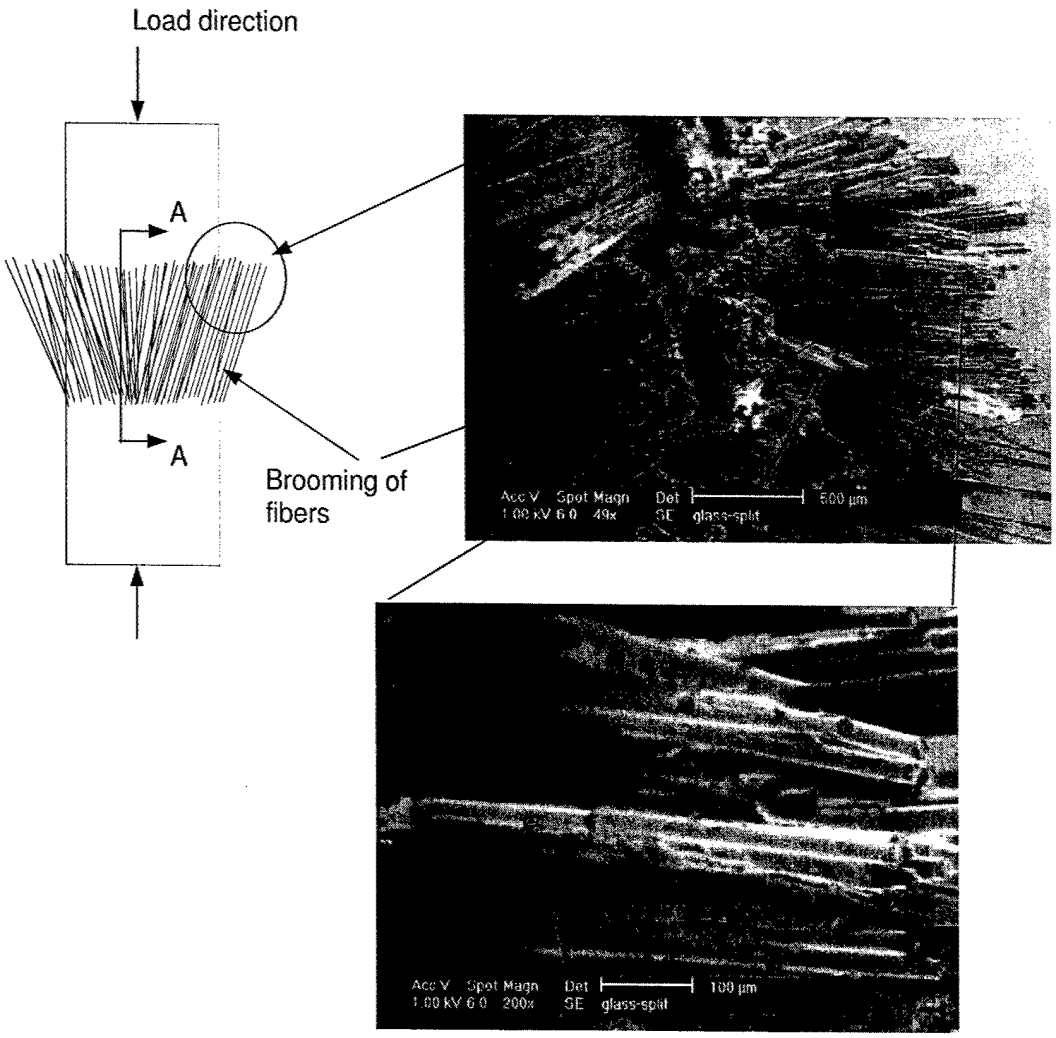

Figure 4.11: Typical image of a split region in glass composites with extensive brooming of fibers

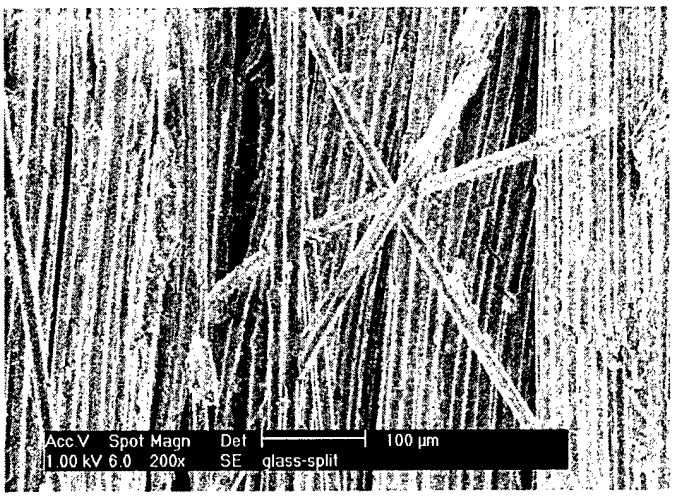

Figure 4.12: Image at the cross section A-A of the splitting zone in a glass composite, $V_f = 50\%$

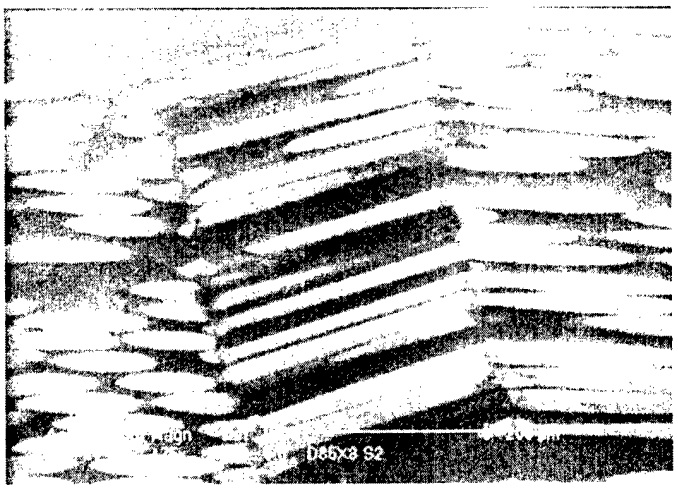

Figure 4.13: Kinking failure in glass composites at $\Delta/r\theta = 0.59$

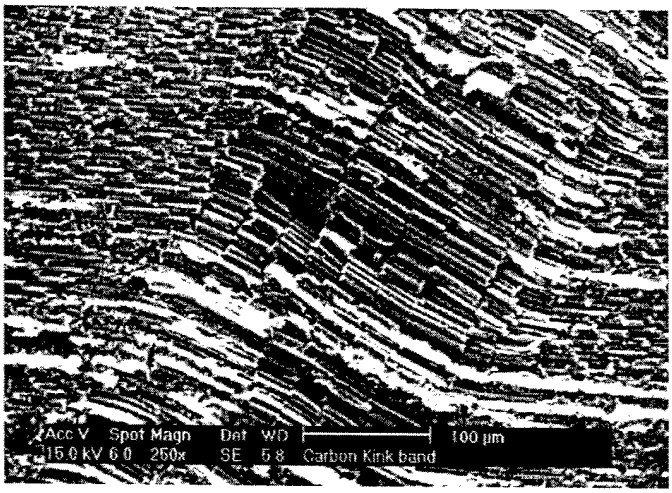

Figure 4.14: Kinking failure in carbon composites

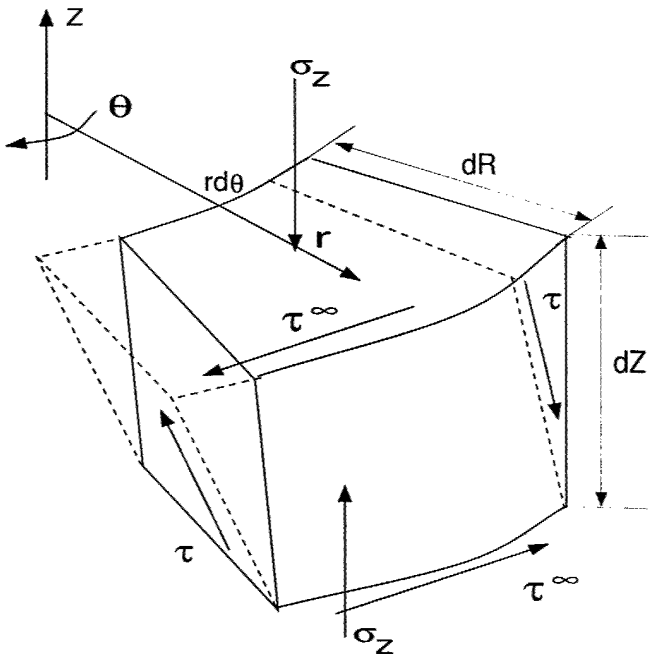

Figure 4.15: Free body diagram of a kinked segment of a cylinder under combined compression and torsion

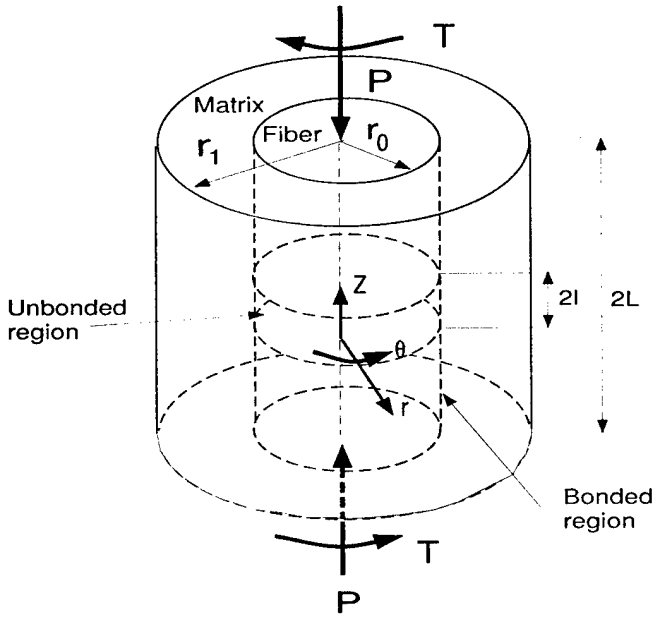

Figure 4.16: Composite cylinder under compression-torsion loading

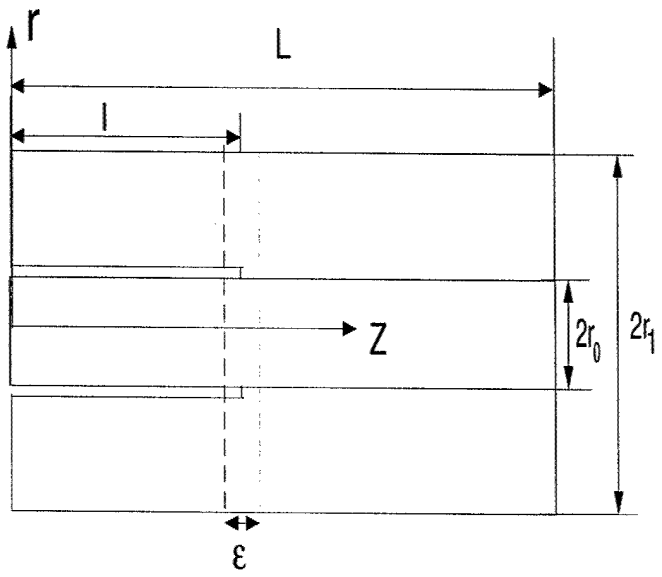

Figure 4.17: Schematic cross section of fiber-matrix cylinder showing the crack tip details

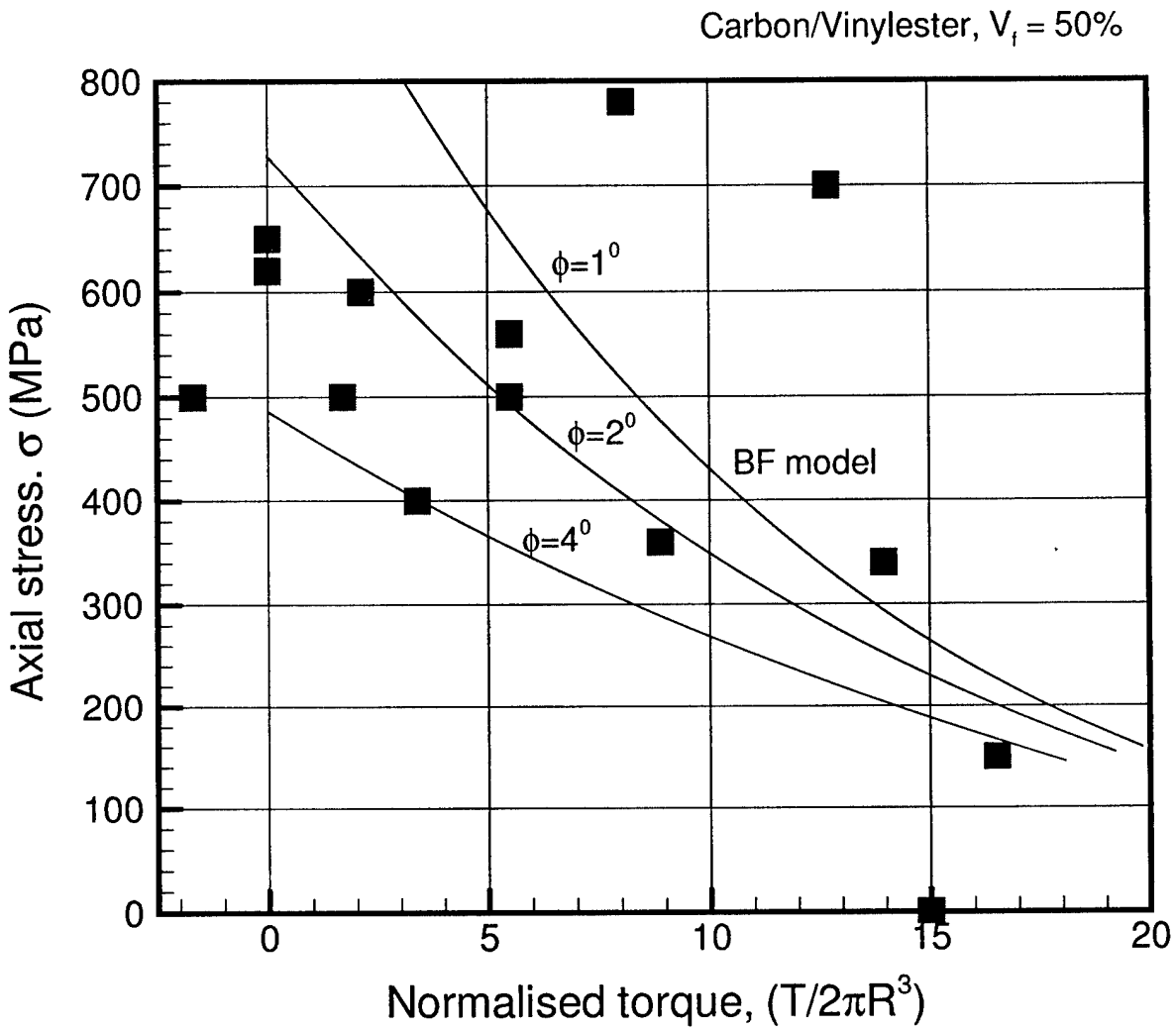

Figure 4.18: Combined compression-torsion failure plot for carbon/vinylester composite of $V_f = 50\%$

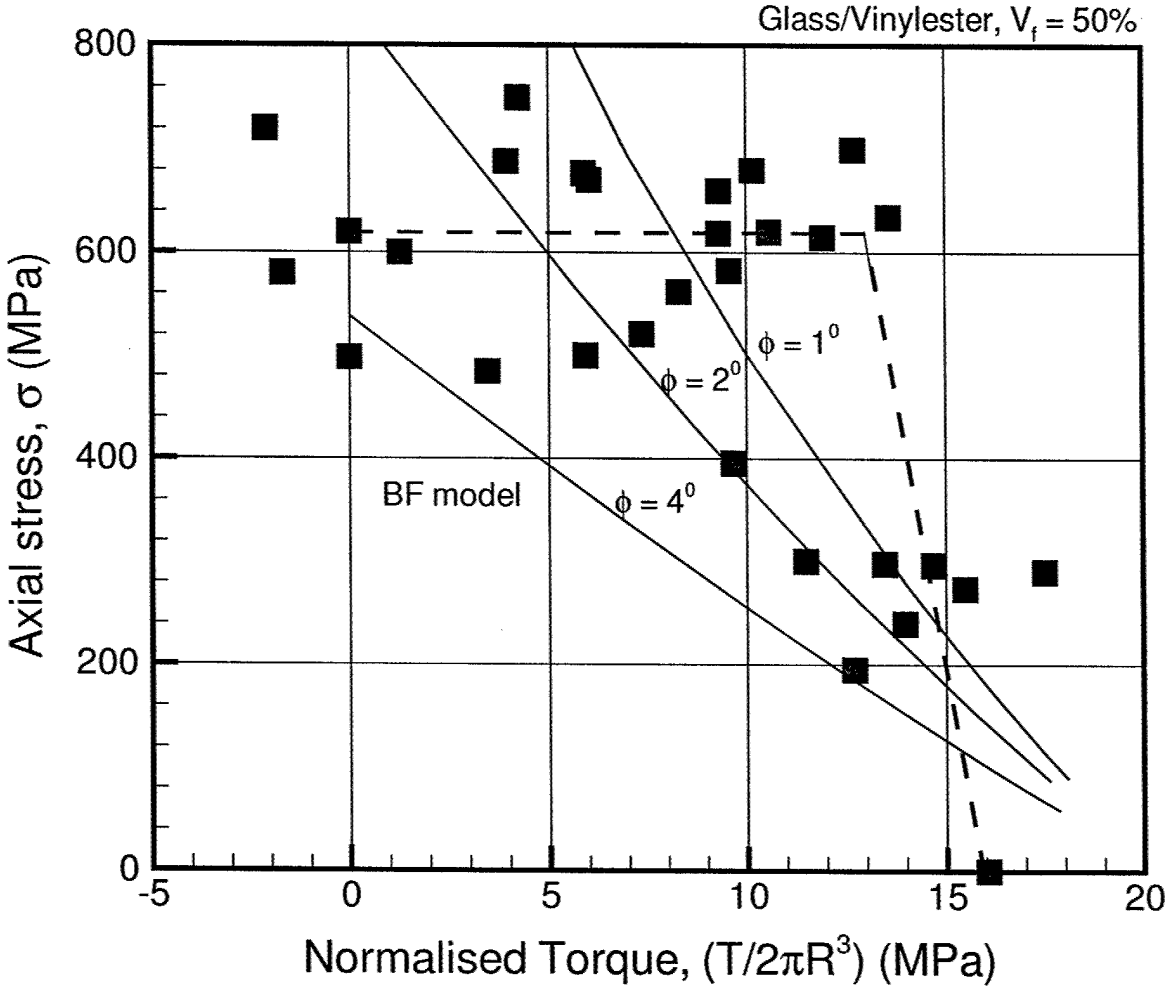

Figure 4.19: Combined compression-torsion failure plot for glass/vinylester composite of $V_f = 50\%$

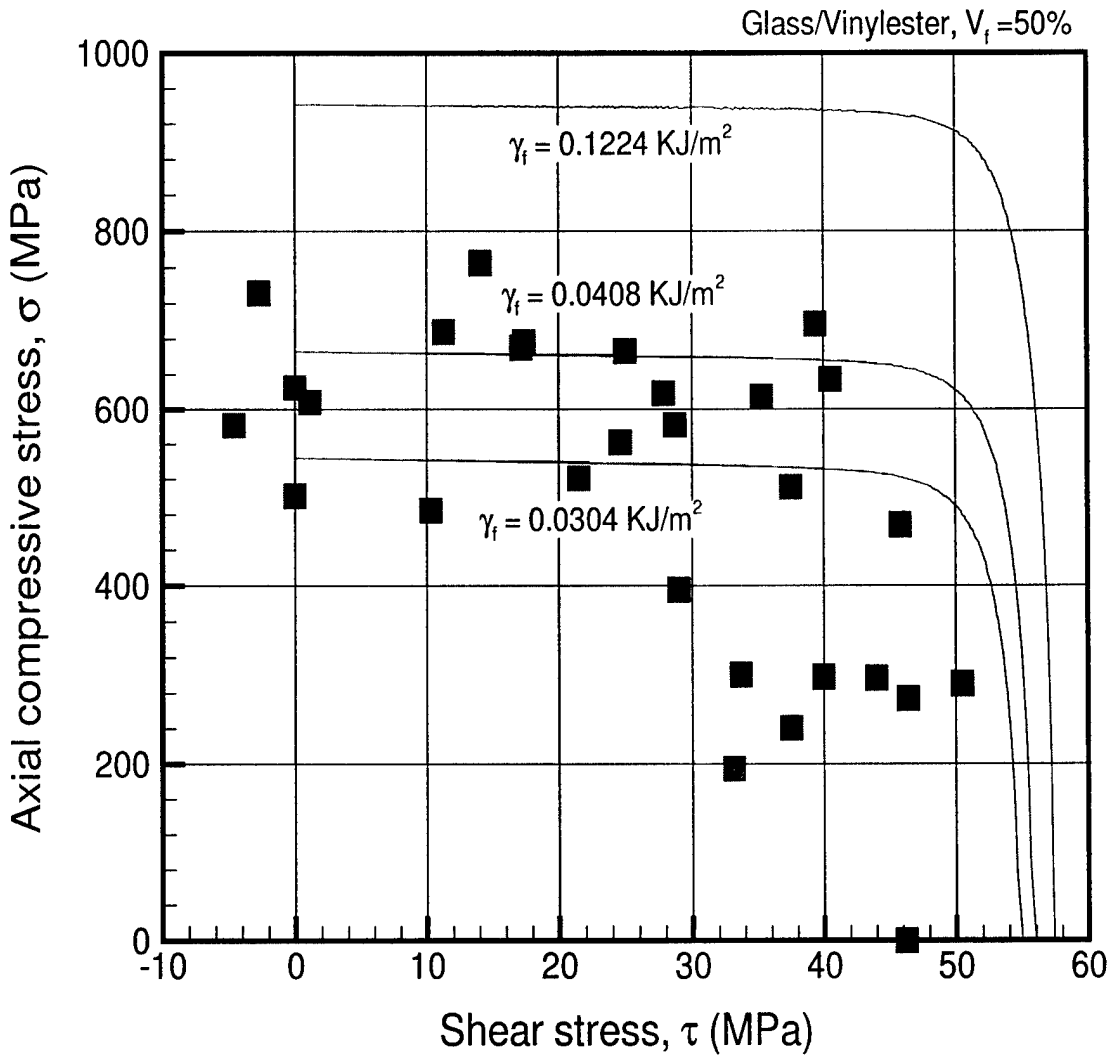

Figure 4.20: Comparison of the new fracture critieria with experimental data for a glass/vinylester composite of $V_f = 50\%$

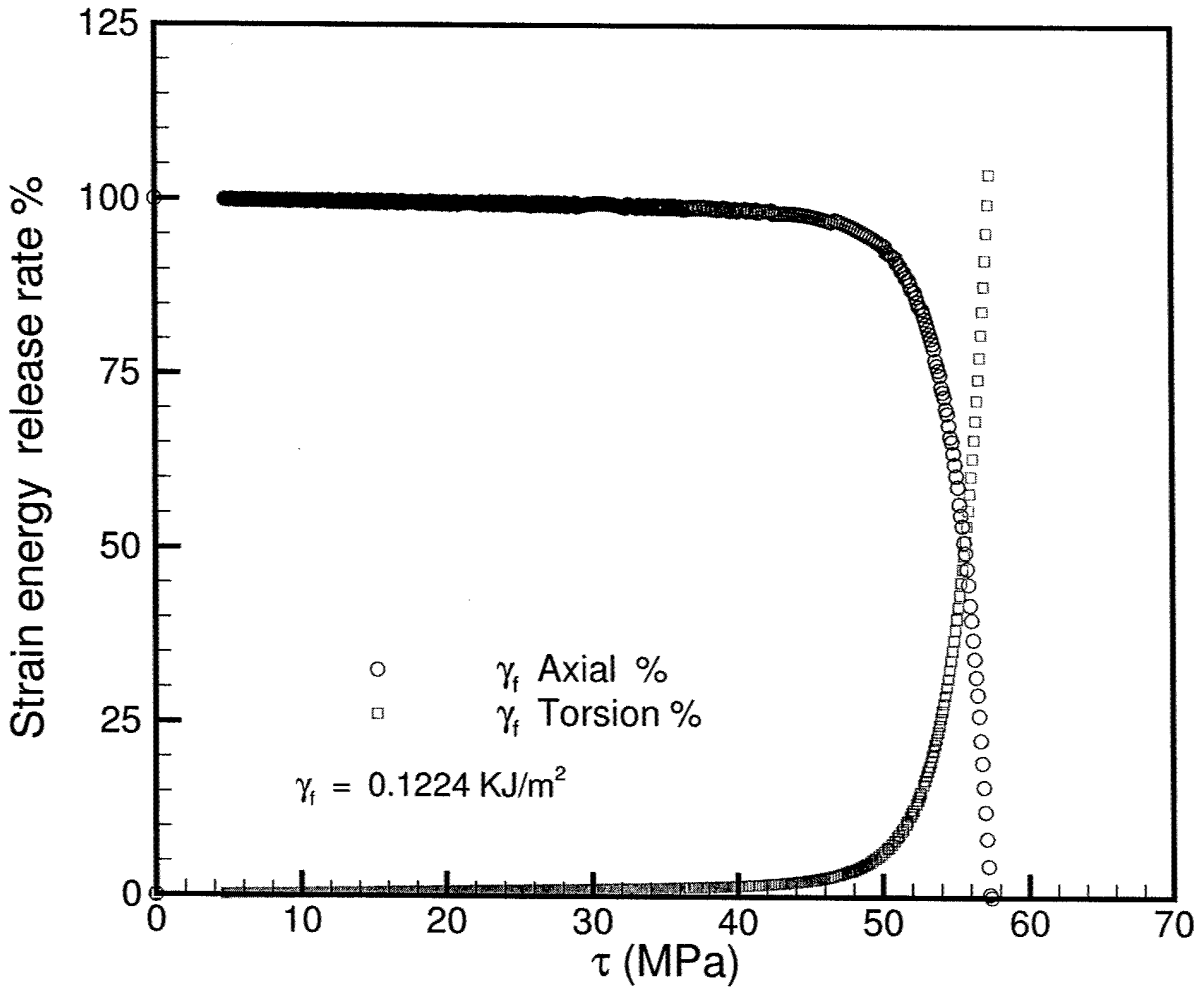

Figure 4.21: Variation of axial and torsional SERR with shear stress, τ for glass/vinylester composite of $V_f = 50\%$

CHAPTER V

RESPONSE OF FRPC TO COMPRESSION, TORSION AND COMBINED COMPRESSION-TORSION LOADING - A FINITE ELEMENT BASED STUDY

5.1 Introduction

Results obtained from experiments and analytical models presented in the previous chapters indicate the complexity and the difficulty in modeling the undirectional fiber composite failure behavior accurately. In this chapter, a 3D finite element micro-mechanics model of the fiber composite is presented. One of the important reasons for implementing a 3D model is to understand the 3D effects in the kinking process observed in the composites during experimentation. Since the specimens are cylindrical in shape, numerical simulation of combined compression-torsion loading requires that the solid cylindrical shape be modeled accurately in order to let shear stresses develop as a function of the cylinder radius.

All previous analytical and numerical attempts to analyze the kinking failure mechanism, are two dimensional, based on a model of the composite that assumes it to be a two constituent alternatingly layered medium under plane strain conditions. A comprehensive summary of the literature on modeling upto 1999 is contained in

the papers by Waas and Schultheisz (1996), Fleck (1997), and Naik and Kumar (1999). Beyond this time work has been done by Lee and Waas (1999), Vogler et al. (2000, 2001) and Vogler and Kyriakides (1999, 2001).

In one of these papers, Vogler et al. (2000), the composite is modeled as a 3D plate but the fibers are assumed to be periodic in the third dimension and hence only a 2D slice of the composite is considered. In a real composite cylindrical specimen the fibers are arranged in a random fashion and the three dimensionality of the random arrangement of fibers in a cylinder cannot be modeled in a 2D manner. It can be argued that a 2D model of FRPC captures the appropriate mechanics at large fiber volume fractions, however, a 3D model is most appropriate to study compressive behavior, particularly to capture the influence of the complex shear state that develops in the sandwiched matrix between the fibers in the region where kink bands (deformation localization) develop and to properly account for the effect of finite fiber bending stiffness in the kink band. Some of the issues that are of particular interest in the current finite element study are as follows; (a) Comparison of the predicted compressive strength between a true 3D finite element model and a corresponding 2D model under pure compression, (b) the effect of orthotropic fiber properties on the predicted peak stress at a given angle of misalignment, and (c) the dependancy of the peak load on the fiber diameter. The resolution of the above issues would establish, among other things the dependancy of critical kinking stress on the fiber radius. It is to be noted that previous analytical models of post-kinking assume that the kink band is already developed, Budiansky and Fleck (1993). Consequently, the effect of fiber bending stiffness on the predicted kink strength is not accounted for. The effect of fiber radius, which essentially accounts for finite fiber bending stiffness is directly captured via a 3D micro-mechanics based finite element model.

5.2 Modeling

The unidirectional fiber reinforced composite cylinder was modeled using a 8 noded reduced order brick element, C3D8R in the commercial finite element software, ABAQUS. Hourglass stiffness control was adopted to prevent the hourglassing of the brick elements. The composite cylinder geometry consisting of cylindrical fibers and matrix was meshed using the commercial meshing software HYPERMESH. Total of 37 fibers were included within a cylinder for both glass and carbon composite finite element models. An isometric view of the 3D finite element model is shown in figure 5.1. The carbon composite and glass composites were modeled for a fiber volume fraction of 0.5. In case of glass composite finite element model, the fiber diameter was changed to study the effect of fiber diameter on the peak stress. For this purpose the number of fibers were kept the same for both fiber diameters. This results in two glass composite models with different composite outer radius, r_c. The length of both models were kept the same. A 2D FE model of carbon composite was also generated. Details of each of these models are given in Table 5.1. In case of carbon fiber, the effect of orthotropy of the carbon fiber on the predicted stress response was studied. The orthotropic properties of carbon fiber are obtained from Lee and Waas (1999) and are as follows, $E_{11} = 276000(MPa)$, $E_{22} = E_{33} = 8760(MPa)$, $G_{12} = G_{13} = 12000(MPa)$, $G_{23} = 3244(MPa)$, $\nu_{12} = 0.35$. The assumed isotropic properties of carbon fibers are given in Table 5.2. 2D finite element models of carbon were also used to predict the compressive strength of carbon composite with, $V_f = 0.5$, so that the 2D and 3D model predictions could be compared against each other and also against the analytical prediction of Budiansky and Fleck (1993).

5.2.1 Initial Geometric Imperfection

An important feature in studies related to compressive response of structures is the effect of initial geometric imperfection on the load-end shortening, $(P-\Delta)$ curve. In cases where the $P-\Delta$ curve shows a load maximum (limit load), it is of interest to determine the effect of imperfection

magnitude on the load maximum. By doing so, one can generate a plot of maximum load against imperfection magnitude. From this plot, one can obtain the maximum load in the limit of vanishing imperfection magnitude (see figure 5.27 for carbon fiber composite 3D FE model).

For the purpose of generating an appropriate initial geometric imperfection shape, a linear buckling analysis of the models was performed and the buckling mode shapes (eigenmodes) were used to introduce the imperfection into the finite element models. As can be seen from figure 5.3 and figure 5.4, eigenmode-1 is a deformed cantilever mode and is a long wavelength imperfection mode. Whereas, eigenmode-3 is a mode that generates a localised imperfection. Thus, a combination of these two modes was used with varying amounts of magnitude to introduce a series of initial geometric imperfections in the composite. These imperfections lead to initial fiber misalignment that can be categorized through an initial fiber misalignment angle, (ϕ) . The imperfection angle can be calculated based on the mode shapes chosen to perturb the original geometry. From the eigenmodes, the normalized displacement $(U1, U2, U3)$ for each mode can be obtained. Then, using the displacements in the $2-3$ plane, $(U2, U3)$, we can calculate the radius vector, r_d, by which the nodes are displaced in the $2-3$ plane. Also, knowing the location of these nodes along the 1 direction (the fiber direction), the imperfection angle can be calculated. The maximum values of the radius vector, r_d, for different mode shapes and the location of these maximum

values are given in Table 5.3. In case of using more than one mode shape to generate the initial imperfection (as has been done here with mode-1 and mode-3), mesh, the imperfection angle is calculated as follows. If δ_1 is the mode-1 radius vector and $s1$ is the scaling factor, then the actual perturbation of the mesh, Δ_1, would be $s1 \times \delta_1$. Similarly, for mode-3, with $s3$ as the scaling factor and δ_3 as the radius vector, then the actual perturbation of the mesh, Δ_3, would be $s3 \times \delta_3$. Thus, the total perturbation of the mesh, Δ_{tot}, would be a linear combination of these two perturbations given by $\Delta_1 + \Delta_3$. The imperfection angle, ϕ can be obtained from $tan^{-1}(\Delta_{tot}/H1)$. The maximum value is taken as the imperfection angle of the mesh. However, it should be noted that the imperfection angle calculated is predicated on the basis that the mesh is being deformed in a homogeneous manner. As can be seen in figure 5.3 and figure 5.4, the displaced shape is non-homogeneous and thus the misalignment angle is a function of the axial position at which it is measured. The average initial fiber misalignment will be smaller than that based on the estimate $tan^{-1}(\Delta_{tot}/H1)$. Once the eigenmode results are obtained from the finite element model, the compressive response studies on the perturbed mesh is carried out in a truly non-linear setting. For this, the fibers are assumed to be linearly elastic, the matrix is modeled as a $J2$ incremental theory of plasticity solid (Mendelson (1983) and an arc-length tracing nonlinear solution process (RIKS method) is used to obtain the $P - \Delta$ curve. An arc-length procedure is needed to accomodate any 'snap-back' that can develop in the $P - \Delta$ response. The complete non-linear uni-axial stress-strain curve of the matrix that is used in these studies are shown in figure 5.5. The non-linear curve is also the curve between equivalent stress and equivalent strain for a J2 plastic solid (Mendelson (1983)).

5.2.2 Model Implementation

The straight fiber finite element models were perturbed using the procedure described in the preceding section to generate 3D finite element models of the composite with known initial geometric imperfections and then subjected to pure torsional loading, (rotational control), Axial loading, (displacement control), and combined compression-torsional loading in a geometrically non-linear setting. A multi-point constraint (MPC) option available in the ABAQUS software was used to constrain the motion of all the nodes on the top surface to move along the axial direction at the prescribed rate of displacement. The use of a MPC card is useful in the torsion and combined compression-torsion loading cases since the rotation on the MPC node is translated into displacements along the tangential and radial directions for the face nodes. A schematic of the FE model along with the MPC node and the axis locations are shown in figure 5.6. The boundary conditions used for pure compression, pure torsion and combined compression-torsion loading cases are shown in Table 5.4-5.6. For all the loading conditions the model was allowed to 'breathe', i.e. the displacements along the 2 and 3 directions were allowed on both the faces. It should be noted that the solid elements lack a rotational degree of freedom but the MPC node has 6 degrees of freedom (DOF). Thus, the MPC BEAM connection constrains only the common degrees of freedom between the MPC node and the face nodes.

The procedure used for studying the compressive response of carbon fiber composites is as follows; first the 3D finite element model was used to generate the torsional response. The matrix non-linear properties were 'calibrated' to obtain the composite shear stress-shear strain ($\tau - \gamma$) response of the 3D FE model to be similar to the experimentally measured shear stress-shear strain curve. The model response was compared against the experimental shear stress-strain curve as shown in figure 5.7.

The following is to be noted. The linear part of the $\tau - \gamma$ curve was found to match the linear part of the experimentally obtained $\tau - \gamma$ curve exactly. In order for the FE models $\tau - \gamma$ curve to match the experimental $\tau - \gamma$ curve in the non-linear regime, the non-linear (plastic) part of the $\sigma - \epsilon$ curve shown in figure 5.5 had to be changed. This is because, the present 3D FE model is a representative microsection (containing 37 fibers) of the much larger laboratory specimen that contains approximately '125,000' fibers within a radius of '$3.35mm$'. For the purpose of studying compressive response and combined compression-torsion response, a numerical FE model of a representative micro-section is deemed equivalent to the actual laboratory specimen when both the FE model and the laboratory specimen contain the same fiber volume fraction and the same overall composite $\tau - \gamma$ response curve. After this 'equivalence' was established, the 3D models were used to generate compressive response curves and the response curves for combined compression-torsional loading. We will first discuss the pure compressive response. The pure compressive response curves for a range of initial imperfection magnitudes are shown in figure 5.8. In the plot, σ_c is the macroscopic axial stress (axial load divided by the initial microsection cylinder crossectional area) and ϵ_c is the macroscopic strain based on end-shortening (i.e. the axial end shortening divided by the initial microsection cylinder length). A note about the initial imperfection is in order. Recall, that two curves were given in figure 5.27. In the first curve, the initial imperfection (misalignment angle) is based on the magnitude of the mode-1 imperfection (even though, both mode-1 and mode-3 imperfections are included in the 3D FE model). This is because, as explained earlier, the misalignment angle is a function of axial position. Thus, for comparison purposes, it is clearer to define the imperfection based the mode-1 shape. The second curve is based on defining the misalignment angle to include both mode-1 and

mode-3 imperfection. The misalignment angle indicated is based on the definition that includes only mode-1 imperfection.

The carbon fiber composite response curves were first generated with isotropic properties of carbon fiber. For the case corresponding to the maximum value of misalignment, the properties of carbon fiber were changed to reflect material orthotropy and the compressive response was obtained. As can be seen the maximum load is unaffected by fiber orthotropy but the post peak response is much softer in case of orthotropic fiber properties. The initial stiffness predicted by the 3D finite element model is nearly same for all the models with different imperfections, thus, establishing the "smallness" of the range of imperfection magnitudes selected for study.

An explanation of a typical $\sigma - \epsilon$ curve as shown in figure 5.8 is in order. At first, the model behaves linearly. With continued loading (consider the $\phi_1 = 0.25^0$ case, for example), the matrix material in the region of initially misaligned fibers is subjected to increasing amounts of shear strain. This results in a progressively decreasing shear stiffness of the matrix (inferred from the shear stress-shear strain curve of the composite, figure 5.7), which in turn, provides decreasing support to the fibers. A point is reached (peak load or limit load), when the competition between the elastic restoring force of the fiber is overcome by the action of the external compressive load that deflects the fiber into a progressively deteriorating (in shear) matrix. Beyond this limit load, there can be 'snap-back' (both the macroscopic stress, σ, and the macroscopic axial strain, ϵ can decrease), resulting in an unstable equilibrium path. In the context of a laboratory experiment, the snap-back can be interpreted as a drop in stress instantaneously (at fixed ϵ) to the curving back path of the $\sigma - \epsilon$ curve (see dashed line in figure 5.8). In figure 5.9, the compressive response for the FE model with a misalignment angle of $\phi_1 = 1^0$ is shown. The response can be divided

into three regions; the first is the pre-peak region where the response is linear, next, a post-peak region where the decrease in stress is very rapid, and, finally, a stage referred to as the plateau region where the stress is approaching a near constant value. Corresponding to these three regions, the displaced shape of the FE mesh has been plotted in figure 5.10 and figure 5.11. In figure 5.10, the displaced shapes shown for step-1 are in the pre-peak region. It can be seen that the shape distortion is minimal. The meshes corresponding to step-4 lie near the peak and in the post-peak region of the curve. It can be seen that the deformation in the mesh gradually increases as the stress starts to decrease beyond the peak stress value. As explained previously, the matrix starts to yield in shear in the locations of maximum fiber misalignment thus causing a narrow band of fibers to rotate and propagate seemingly with no resistance, causing the macroscopic stress to drop. In the post-peak region, the mesh starts to show the formation of a distinct kink band and this distinctiion becomes clear as can be seen in the deformed mesh corresponding to step-6. The deformed mesh for step-6, increment 10 is shown in the stress response curve and it can be seen that the point lies in the plateau region. Another, important observation that can be made from this 3D finite element simulation of kinking is the formation of circumferential ripples indicative of matrix regions which undergo shearing strains of different sense (positive and negative shear). Unlike 2D simulation of kink bands where the matrix material within the kink band shows shearing of one sense (positive or negative), the outer surface of the composite in the 3D case shows 'ripples' which is reflected in the zig-zag nature of the deformed mesh in the kinked region. In fact as will be seen in figure 5.12, figure 5.13, and figure 5.14, the circular shape of the composite no longer remains circular. In these figures, a slice of the composite without the embedded fibers is shown. Figure 5.13 and figure 5.14 correspond to the post-peak region of

the compressive stress reponse curve. The side view of the deformed cross-section shows the ripples. On the deformed mesh contours of inplane shear strain, γ_{yz} are superposed. The value of γ_{yz} increases as the post-peak region is reached. This also corresponds to the fact that the shape of the circular section no longer remains circular causing inplane shear strains to develop. Contours of the uni-axial strain, ϵ_{xx} in the composite are presented in figure 5.15, figure 5.16, and figure 5.17. The strain contours are superposed on a deformed mesh. It can be seen that, in the pre-peak region (step-1) the total strains are still low, even though, one can notice the formation of a band of high strain region starting from one end of the composite and spreading diagonally across the surface. In the post-peak region (step-4) the strains start to increase and the strain localization initiates along the previously mentioned band. As we go into the post-peak region, the band of high strain region starts to grow and spread. The value of the peak strain in the band also increases. The region with elevated strain corresponds to the region of localized deformation of the mesh as seen in figure 5.11. A longitudinal section of the FE model for the carbon composite (with only the fibers) is presented in figure 5.18 and figure 5.19. The axial shear strain contours, γ_{xz}, are superposed over the deformed mesh. This is of interest in case of orthotropic fibers (like carbon), where the fiber itself has a microstructure. High values of inplane shear strain can cause the fiber to fail by shearing between outer layers and the fiber core (eg. in a onion skin core type of structure, Herakovich (1998)). A similar procedure was used to generate the perturbed mesh and obtain the compressive response of carbon fiber composite for 2D finite element model. The comparison between the predicted stress values for a 2D model and a 3D model are given in Table 5.7. As it can be seen the 3D model predictions are significantly lower at the same angle of misalignment as compared to the 2D model predictions and the

Budiansky-Fleck model predictions from equation (1.3).

The finite element model was next used to simulate the combined compression-torsion loading on a composite cylinder. 3D FE simulations were performed only for carbon fiber composites. The boundary conditions were applied as explained in the previous paragraph. Proportional displacement and rotational controlled boundary loading was applied to the finite element model. Typical response curves are shown in figure 5.20 and figure 5.23. It can be seen that as load, P, increases the torque first increases and then starts to decrease. This was also observed in the combined loading reported in chapter IV (see figure 4.10) experiments where reversal in torque was observed for some specimens. This reduction in torque leads to catastrophic instabilities, when experiments are done in torque and force control instead of rotational and displacement control. The failure point is taken as the point on the P - Δ curve where the load starts to decrease. Simulations were done with different ratios of $\Delta/r\theta$ and the failure envelope obtained in the FE simulation is plotted along with the experimental data in figure 5.24.

5.2.3 Size Effects - Effect of fiber diameter

The 3D finite element micromechanical model of the glass fiber composite was used to study the effect of fiber diameter on the peak stress under axial compression loading. For this purpose, two types of models were developed; one is called as a micro-mechanically scaled model and the other is a structurally scaled model. In micro-mechanically scaled model, the FE models for both fiber diameters contained the same number of fibers and had similar fiber volume fraction. Thus, the outer radius of the FE model was different. In case of structurally scaled model, the outer radius of both FE models and the fiber volume fraction was kept the same. This

requires that the number of fibers in both models be different. In case of FE model with small fiber diameter, the number of fibers were taken to be 37 and in case of the FE model with large fiber diameter, the number of fibers were taken to be 19. Both the micromechanically scaled FE model and the structurally scaled FE model was developed using the pre-processing software HYPERMESH, as explained in the modeling section.

Micro-mechanically Scaled Model

The shear stress-shear strain response from both the models were found to be nearly same (Figure 5.25). Thus, an equivalence was established between the two FE models. Recall, that the two glass composite models contain 37 fibers packed in a cylinder such that the overall fiber volume fraction, $V_f = 0.5$. The dimensions of the models are given in Table 5.1. The 3D models were next used to generate the compressive stress-compressive strain response for both the cases. For the larger diameter fibers, the initial misalignment values were varied. However, for comparing with the small fiber diameter model, two FE models with same value of initial misalignment were studied. From the response curves in figure 5.26, it can be seen that the peak stress in case of large fiber diameter model is high compared to the FE model with small fiber diameter (at the same initial angle of misalignment). The analytical kinking stress prediction of Budiansky and Fleck (1993) (see equation (1.3) would predict the peak stress to be same for both cases since the composite shear stress-shear strain response is same for both models. However, as can be seen from the present FE model results, the peak stress is different with different reinforcing fiber diameters. This indicates that fiber bending stiffness plays an important role in the determination of the peak stress associated with kink banding. This novel result has not been identified in previous 2D FE studies of kink banding (see Vogler

et al. (2001), Lee and Waas (1999)). It should be noted that the analytical model for kinking by Budiansky and Fleck (1993) does not take into account the bending stiffness of the fibers and extensibility of the fibers.

Structurally Scaled Model

In case of structurally scaled models, the FE models were first subjected to pure torsion and the properties of the matrix material was calibrated to obtain a similar global shear stress-shear strain response for both models with different diameter fibers as shown in figure 5.27. The compressive response of the FE models were next studied to understand the effect of fiber diameter on the peak compressive load. For, comparison purposes the fiber misalignment was kept the same for both FE models with different fiber diameters. It can be seen from figure 5.28, that the peak compressive stress is different for both models and the model with a larger fiber diameter has a higher peak compressive stress for the same angle of misalignment. Thus, it is clear from both the structurally and micro-mechanically scaled models that the fiber diameter does influence the peak compressive stress. The tendency is for the peak stress to increase with fiber diameter. The increase in composite compressive strength with increase in fiber diameter, as has been shown here, has been observed experimentally by Schutz (1994).

In case of micro-mechanically scaled FE model results as shown in figure 5.29 and figure 5.30, the maximum strains in the fiber are also noted on the plot. It can be seen that for the same macroscopic axial strain, the local fiber strain was higher in the small fiber diameter finite element model. This indicates the possibility of fiber breaking as the mechanism for initiation of kinking in case of small fiber diameter glass composite (this has been pointed out in the paper by Narayanan and Schadler (1999) and Garland et al. (2001)). In case of large diameter glass fibers,

there are two possibilities. The fiber breaking strain is reached before or after the localized kink banding instability corresponding to a peak load. In the current study, assuming a fiber breaking strain of 0.02 for glass, it can be seen that, in the large fiber diameter model, the maximum fiber strain exceeds the peak fiber strain almost at the maximum load point in the stress response curve. However, for the small fiber diameter model the fiber strain exceeds the peak fiber strain much below the attainment of the maximum stress. Thus, initiation of kink banding, much like what has been observed by Narayanan and Schadler (1999) and Garland et al. (2001), can occur due to damage zones formed on account of fiber breaks prior to the attainment of a maximum load associated with a kink banding instability predicated on models that do not account for finite fiber bending stiffness. This shows that the onset of kink banding and the associated kink band angle is highly dependent on the fiber radius and the fiber breaking strain. The fiber breaking is not a quantity that can be obtained from a simple tension tests in general. For example, in case of carbon fibers that have a microstructure, the breaking strain under bending (with through thickness gradient loading) is different than the breaking strain in tension (where ther is no through the thickness gradient in loading). These aspects have been pointed out by Wisnom et al. (1997) and Quek (2002).

5.3 Conclusions

The results from a 3D finite element based micromechanics study into the kinking failure of unidirectional fiber composites was presented. It can be seen that the fiber diameter plays an important role in the determination of the compressive strength of FRPC. The results clearly indicate that the possibility of kinking initiating due to a fiber break cannot be ignored in the case of small fiber diameter fiber com-

posite. This finding is consistent with microscopic experimental observation (based on Raman spectroscopy to track fiber breaks, as has been done by Narayanan and Schadler (1999); Garland et al. (2001)) on the initiation of kink bands. The combined compression-torsion FE simulations show that the failure strength drops in a non-linear fashion as compared to the predictions of the Budiansky-Fleck kinking model. The 3D finite element simulations show the importance of finite fiber bending stiffness on the maximum stress and the presence of a complex three dimensional stress state in the matrix region.

Model Name	Total Elements	Total Nodes	Length L (μm)	Radius $r_c(\mu m)$	Fiber radius $r_f(\mu m)$	V_f
Carbon-1	64704	68673	64	21.5	2.5	0.5
Carbon-2D	10000	30349	710	250	2.5	0.5
Glass-1	64704	68673	306.43	58	6.75	0.5
Glass-2	64704	68673	306.43	103	12	0.5

Table 5.1: 3D finite element model details

	E_f(MPa)	ν
Glass fiber	72000	0.22
Carbon fiber	276000	0.35
Vinylester	3585	0.36

Table 5.2: Material properties of fiber and matrix

H_1	Mode-1	Mode-3
64	1.0334	0
32	0.5050	1.0179

Table 5.3: Normalised displacements from buckling analysis of FE model(carbon-1)

Node/face	U1	U2	U3	θ_1	θ_2	θ_3
MPC node	Δ	Free	Free	Free	Fixed	Fixed
Bottom	Fixed	Free	Free	-	-	-

Table 5.4: Boundary conditions for pure compression

Node/face	U1	U2	U3	θ_1	θ_2	θ_3
MPC node	Fixed	Fixed	Fixed	θ	Fixed	Fixed
Bottom	Free	Fixed	Fixed	-	-	-

Table 5.5: Boundary conditions for pure torsion

Node/face	U1	U2	U3	θ_1	θ_2	θ_3
MPC node	Δ	free	free	θ	Fixed	Fixed
MPC node1	Fixed	Fixed	Fixed	Fixed	Fixed	Fixed

Table 5.6: Boundary conditions for combined compression-torsion

	σ_c(MPa)	ϕ
Carbon-3D	495	2.3^0
Carbon-2D	581	2.0^0
BF-model	720	2.0^0

Table 5.7: Comparison of compressive strength predictions

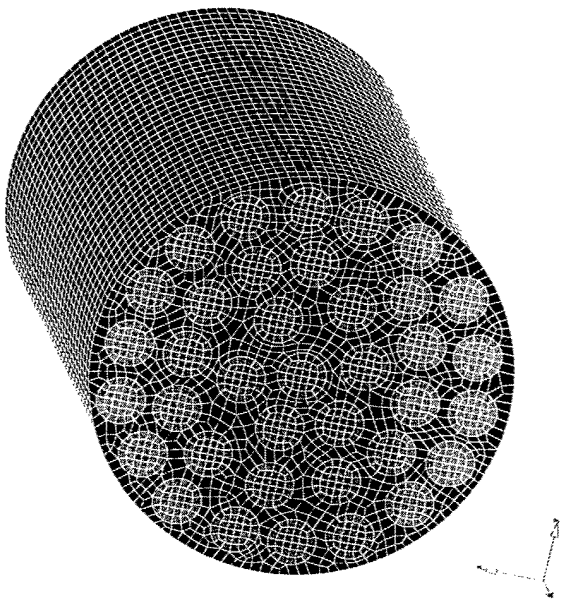

Figure 5.1: A 3D finite element micro-mechanical model of a composite cylinder

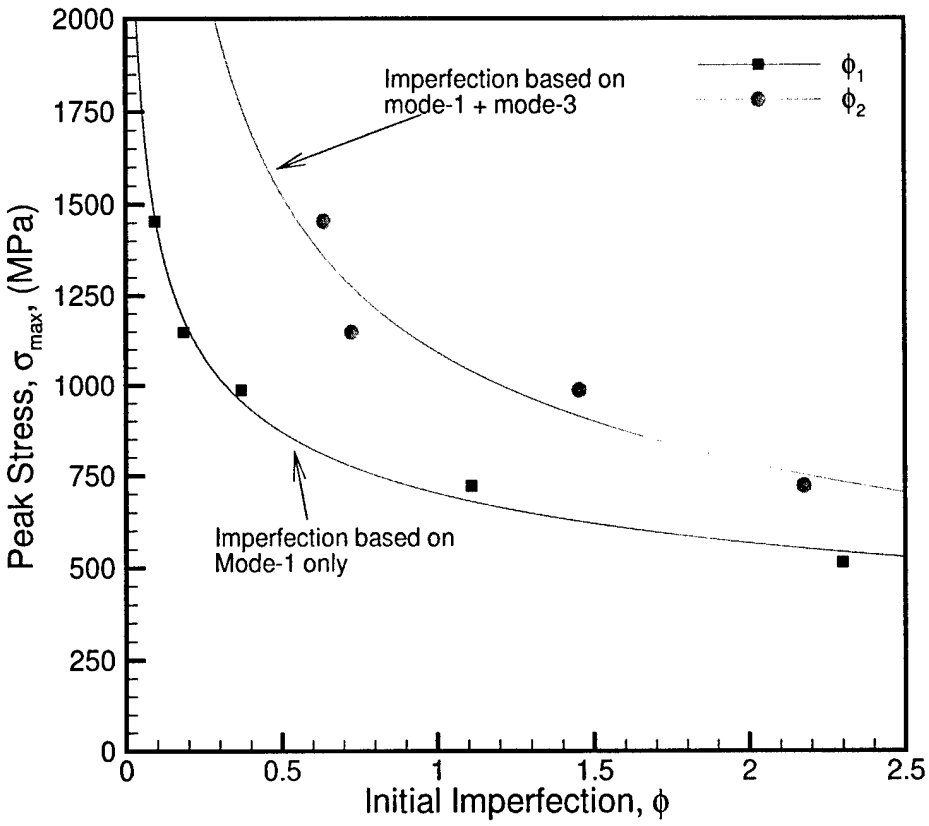

Figure 5.2: Peak stress, σ_{max} as a function of initial imperfection, ϕ

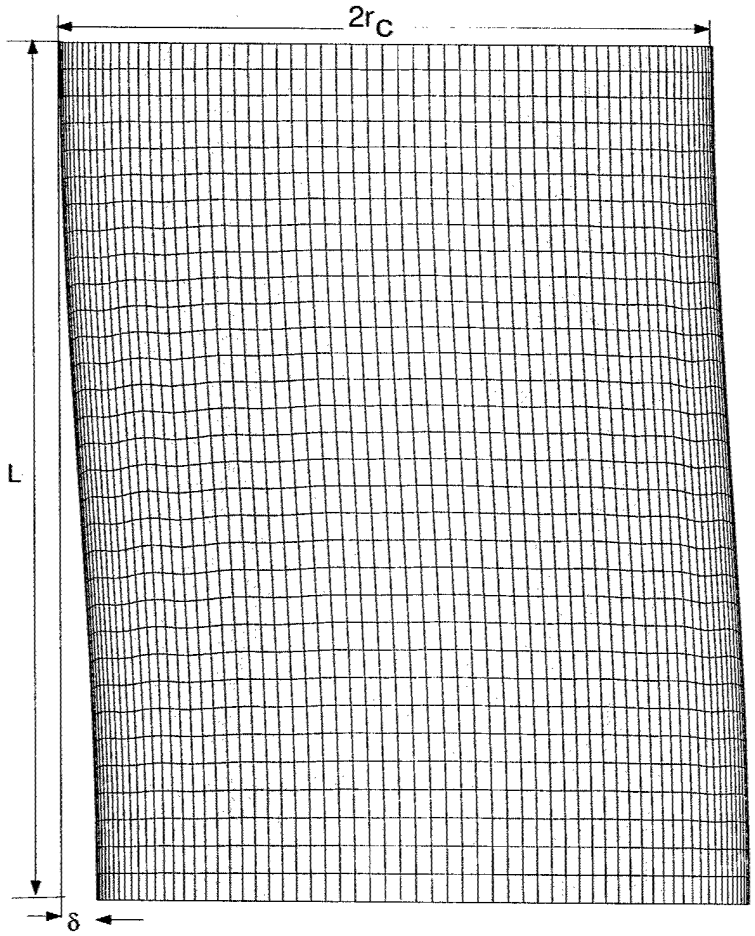

Figure 5.3: Mode-1 displacement of 3D FE model

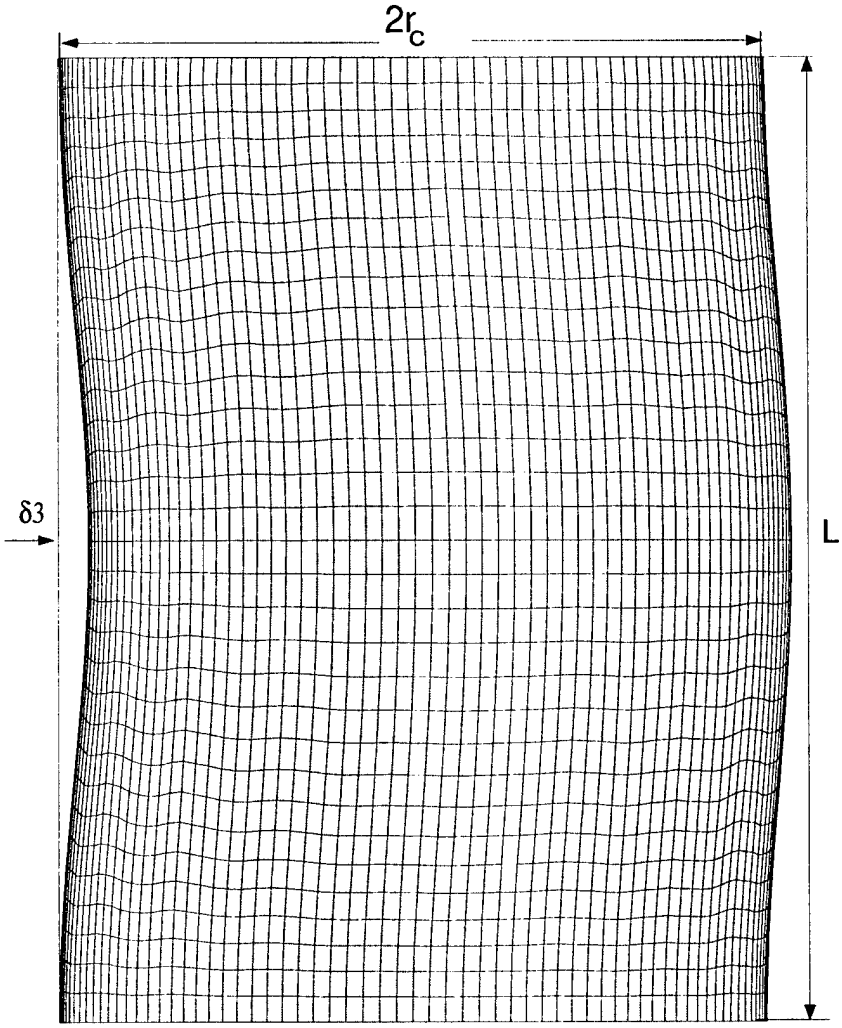

DISPLACEMENT MAGNIFICATION FACTOR = 8.63
EIGENMODE 3 EIGENVALUE = 2.43

Figure 5.4: Mode-3 displacement of 3D FE model

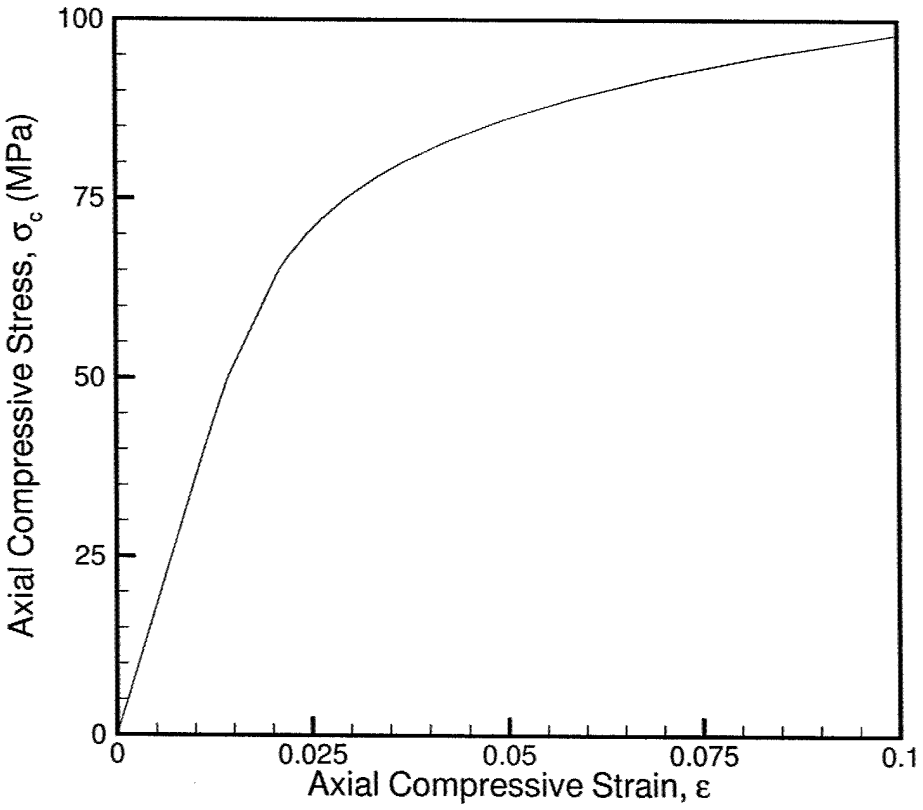

Figure 5.5: Pure compression response of vinylester matrix used as input for FE modeling

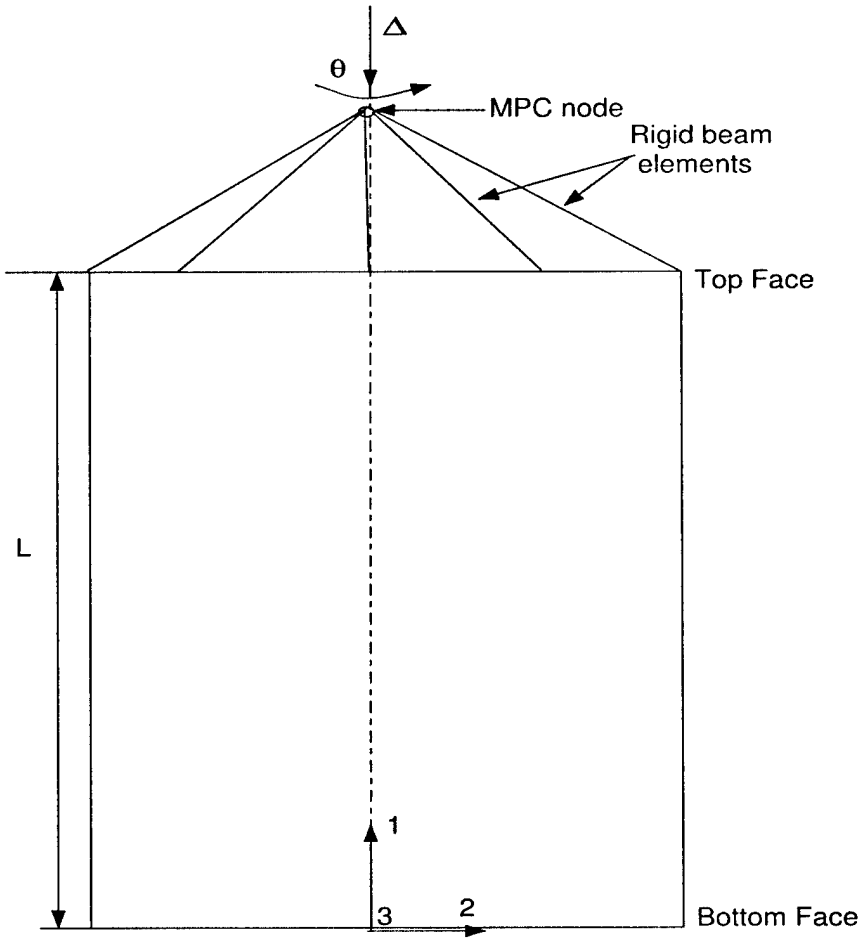

Figure 5.6: A schematic of the FE model for pure compression and pure torsion

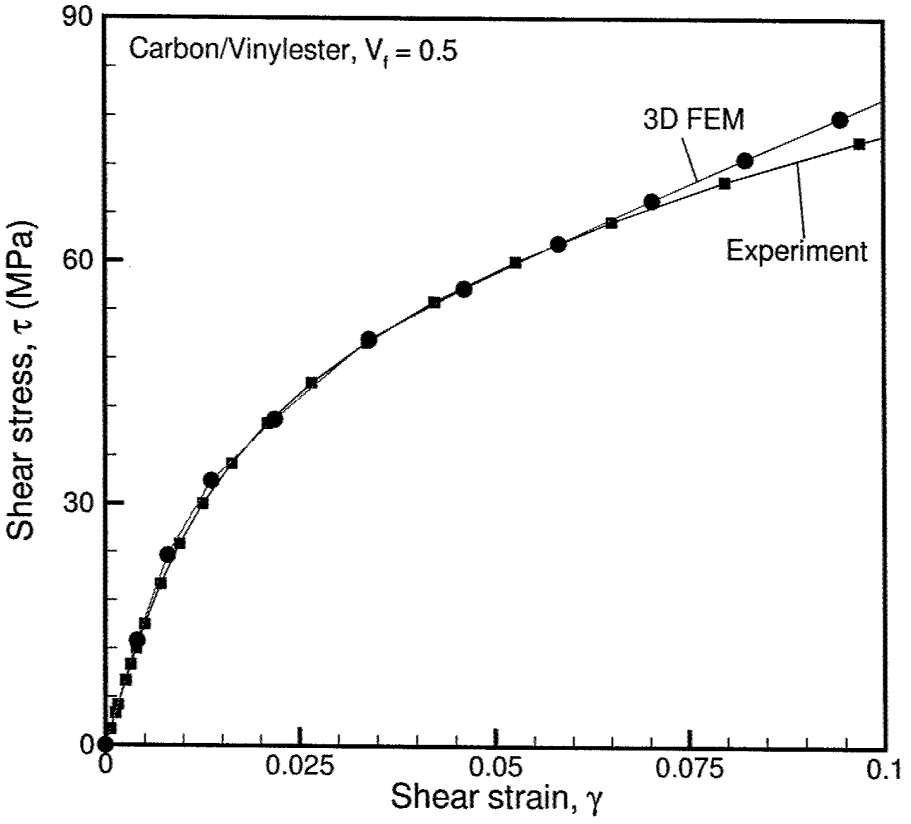

Figure 5.7: Comparison of the experimental and 3D FE shear stress-strain curve for a carbon/vinylester composite of $V_f = 0.5$

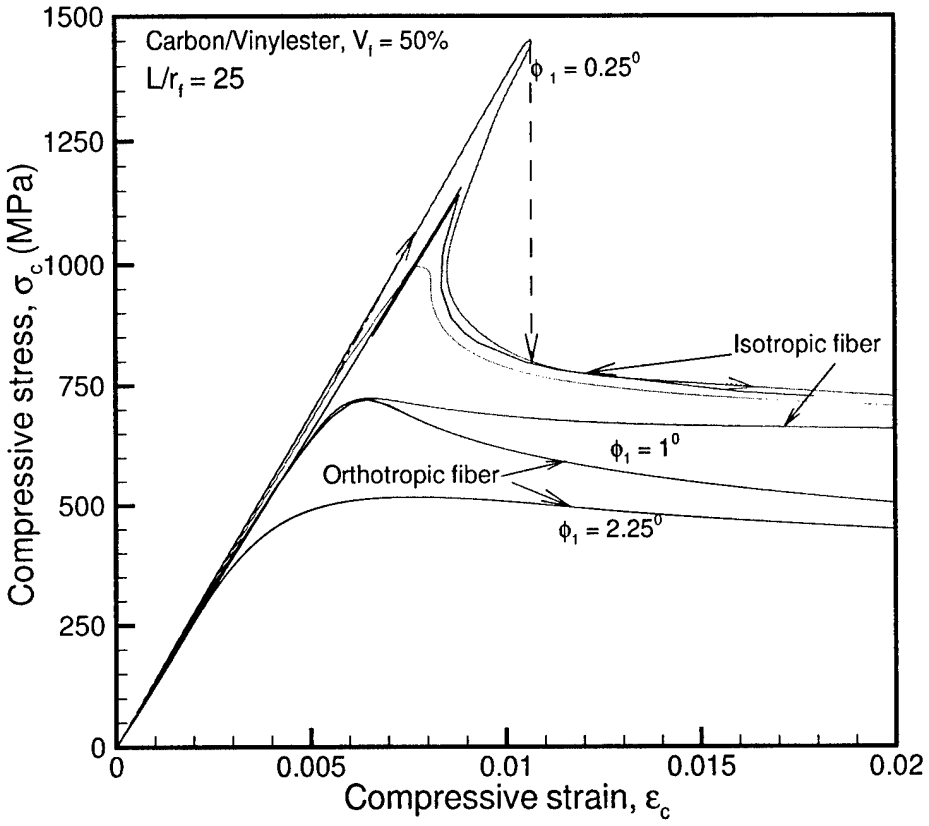

Figure 5.8: Compressive response curves of carbon/vinylester composite of $V_f = 0.5$ for different values of imperfections

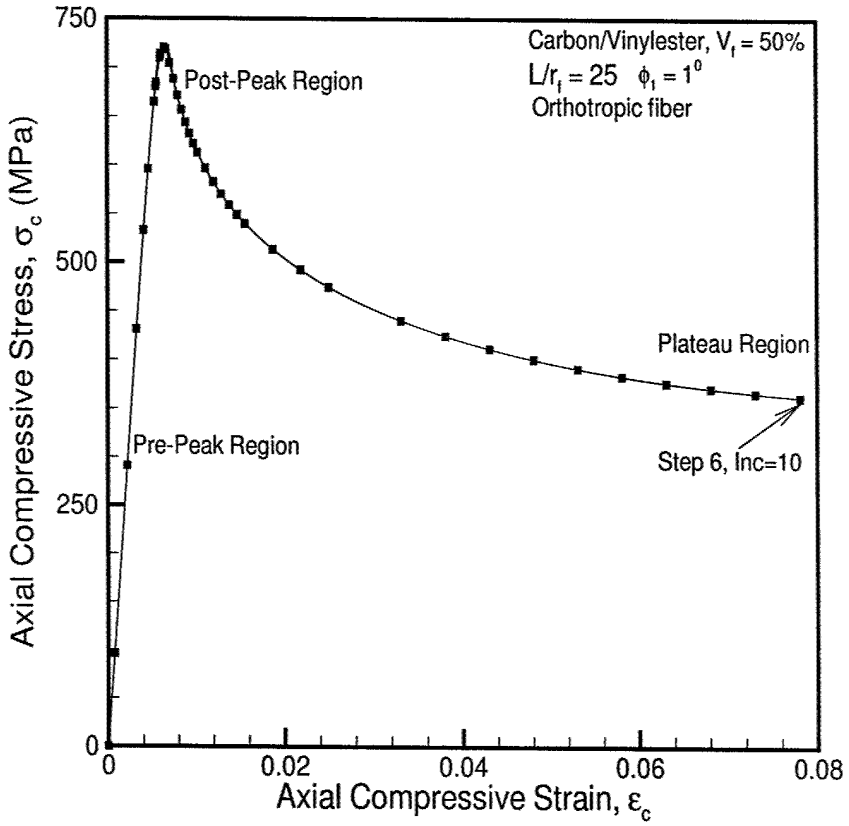

Figure 5.9: Compressive response curve of carbon/vinylester composite of $V_f = 0.5$ and $\phi_1 = 1^0$ with orthotropic fiber properties

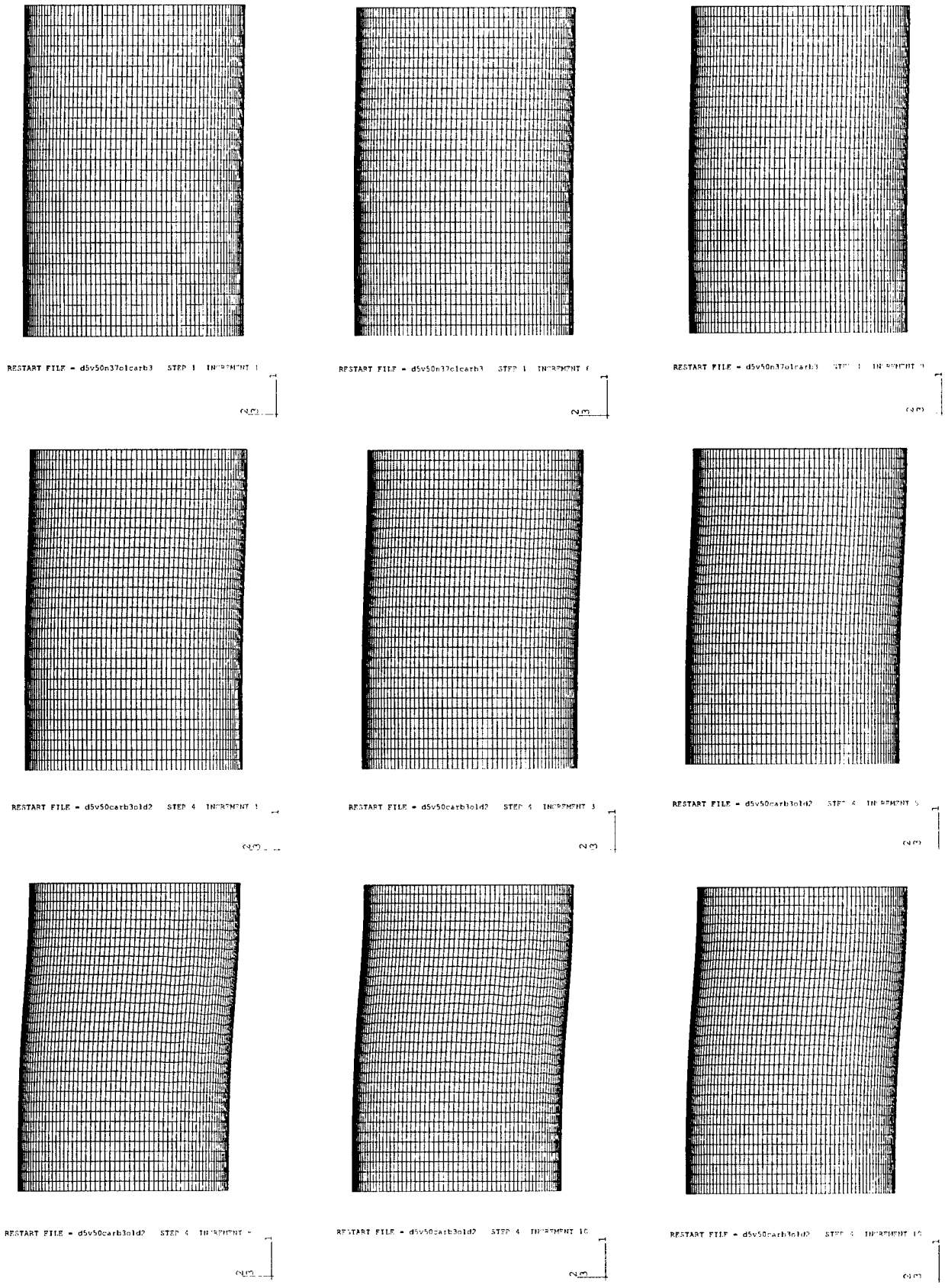

Figure 5.10: Deformed mesh of carbon/vinylester composite of $V_f = 0.5$ and $\phi_1 = 1^0$ with orthotropic fiber properties

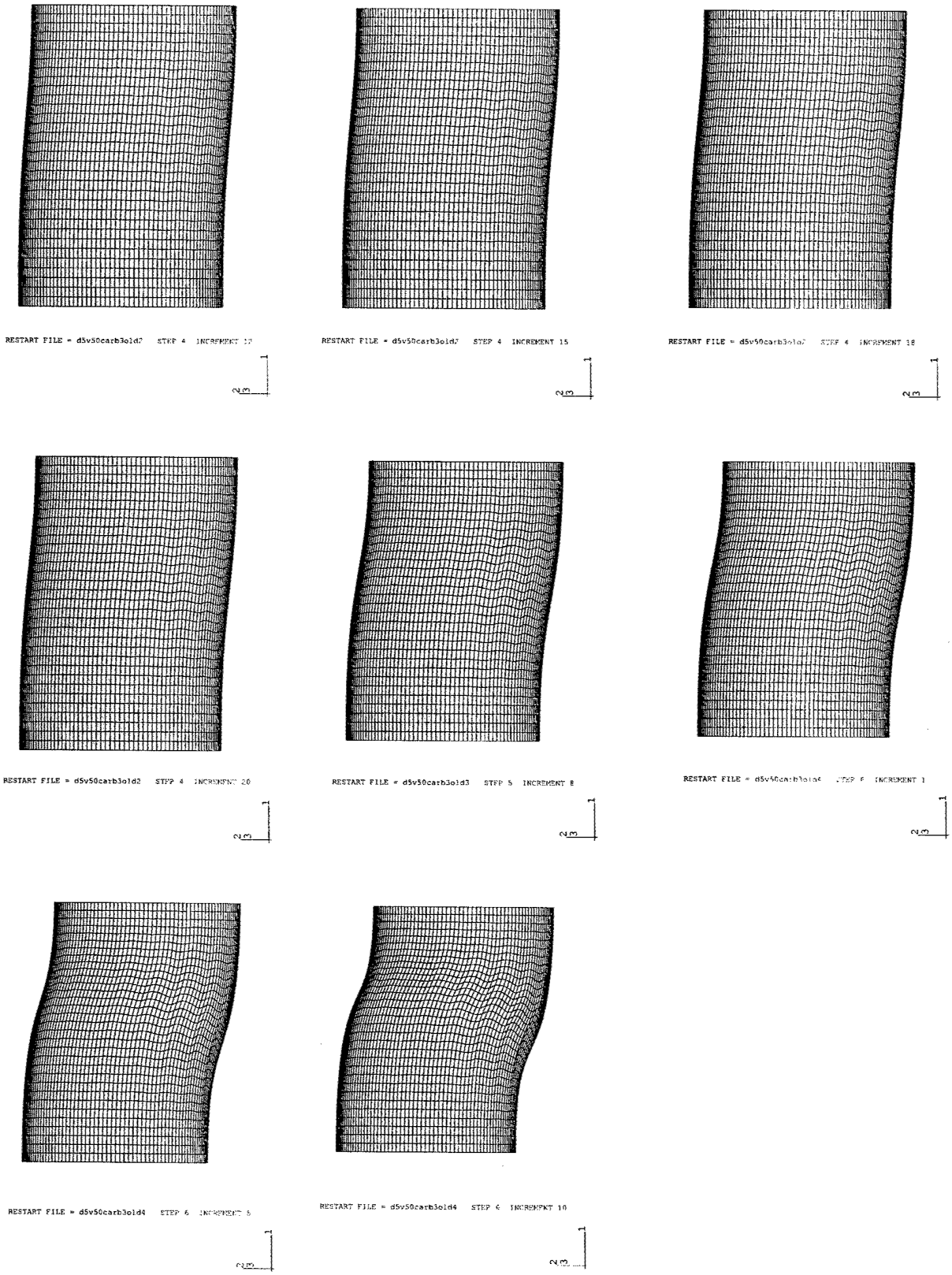

Figure 5.11: Deformed mesh of carbon/vinylester composite of $V_f = 0.5$ and $\phi_1 = 1^0$ with orthotropic fiber properties

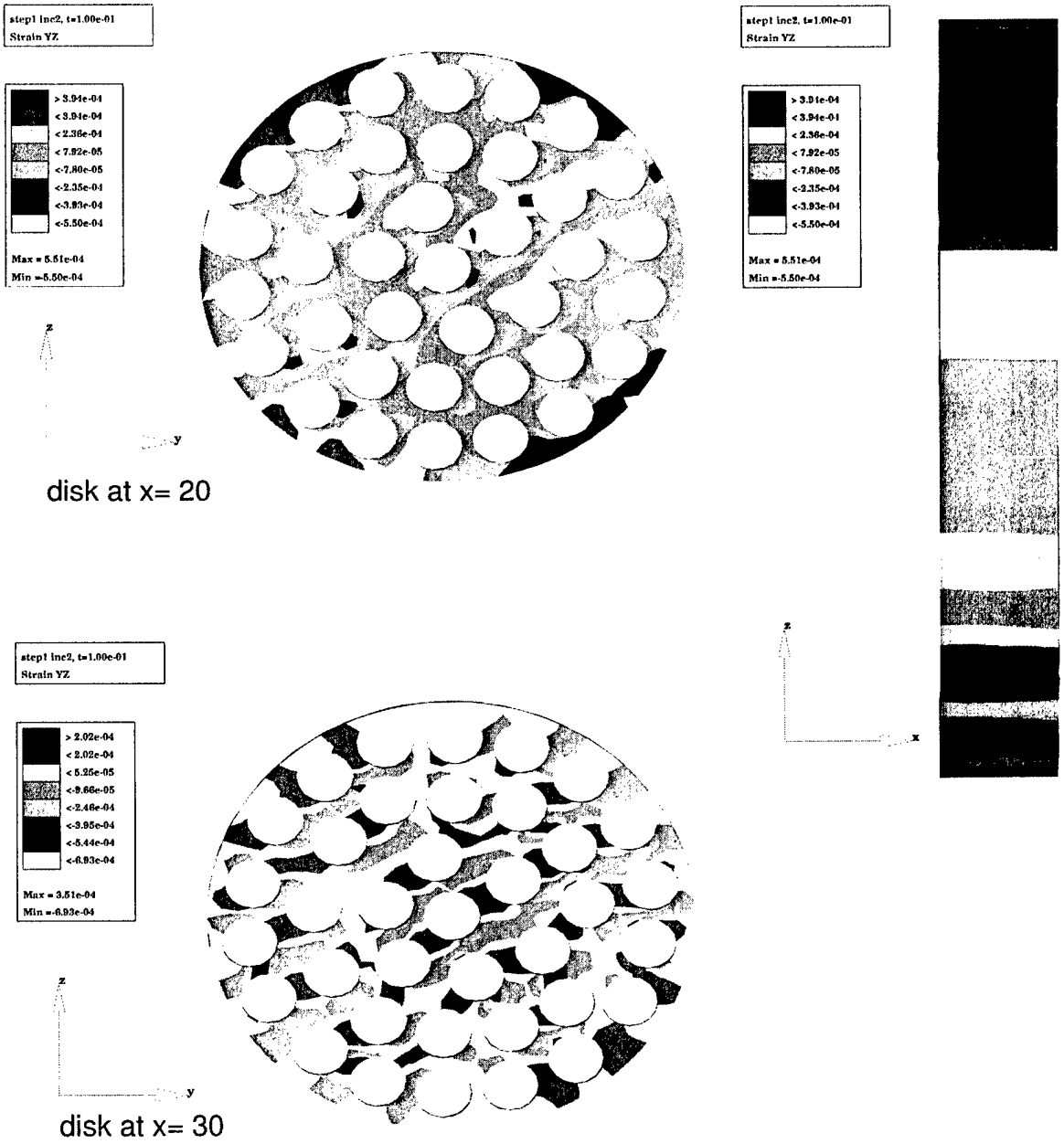

Figure 5.12: Deformed mesh of a slice of the carbon/vinylester composite of $V_f = 0.5$ and $\phi_1 = 1^0$ with orthotropic fiber properties

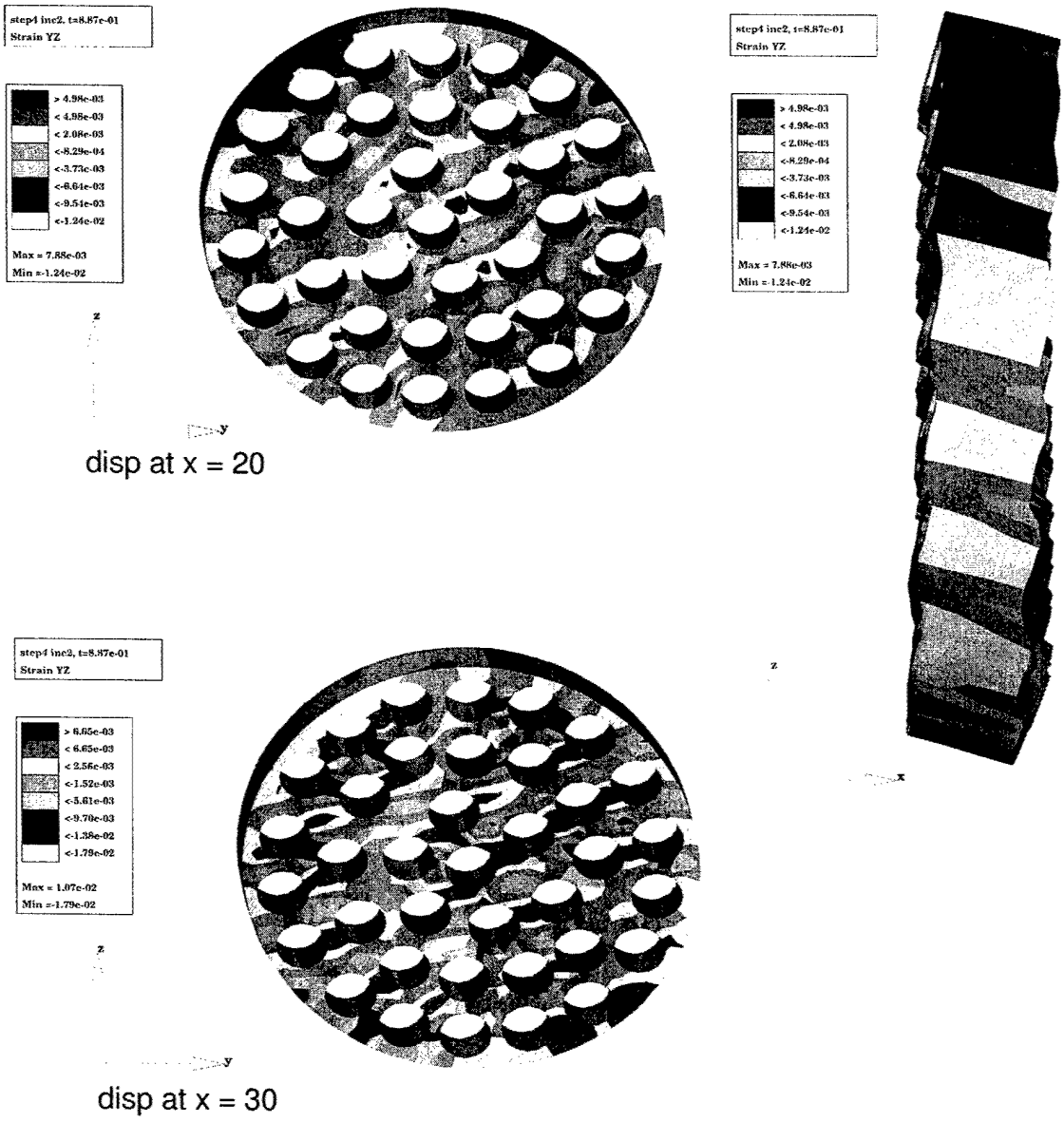

Figure 5.13: Deformed mesh of a slice of the carbon/vinylester composite of $V_f = 0.5$ and $\phi_1 = 1^0$ with orthotropic fiber properties

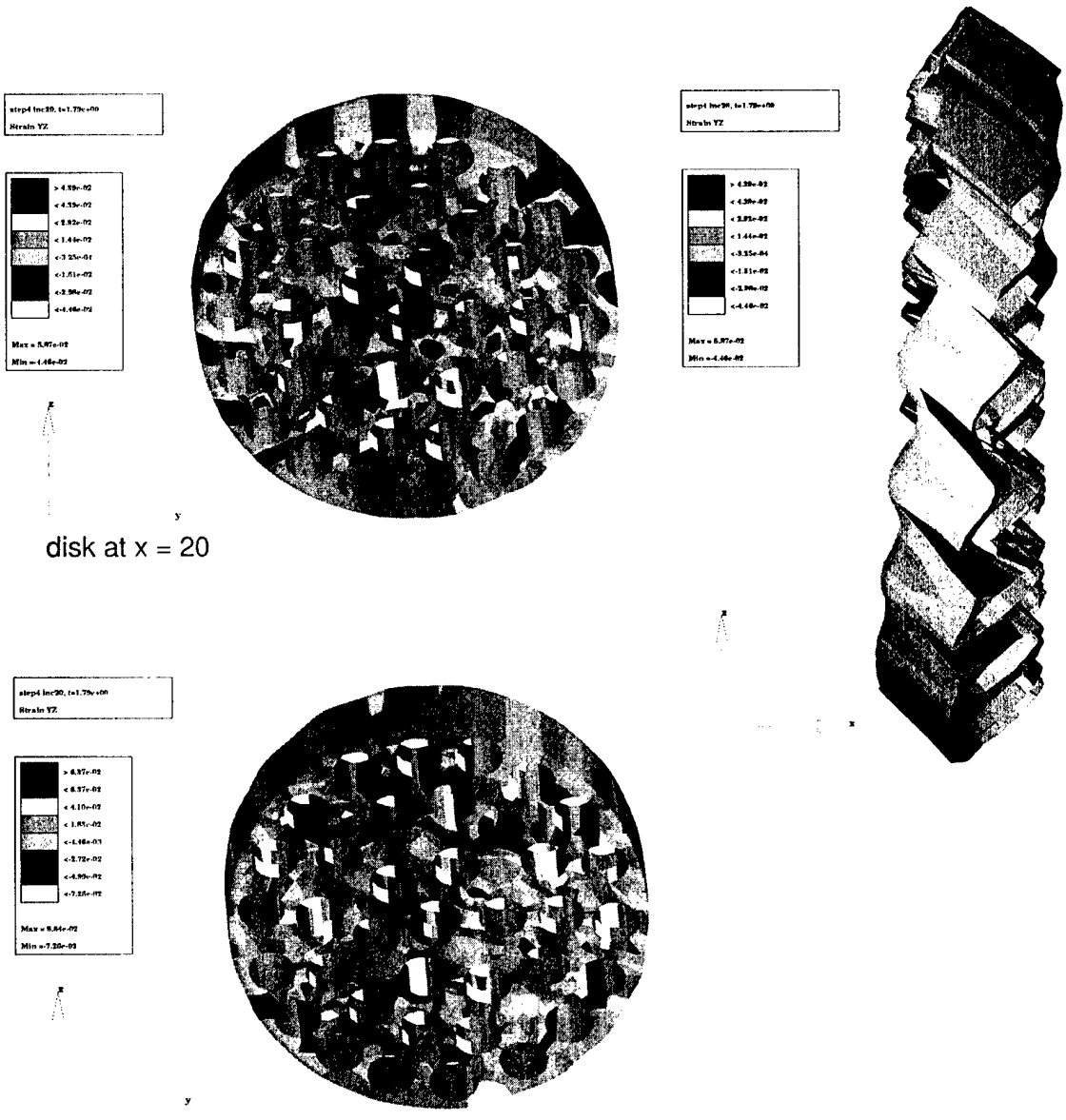

Figure 5.14: Deformed mesh of a slice of the carbon/vinylester composite of $V_f = 0.5$ and $\phi_1 = 1^0$ with orthotropic fiber properties

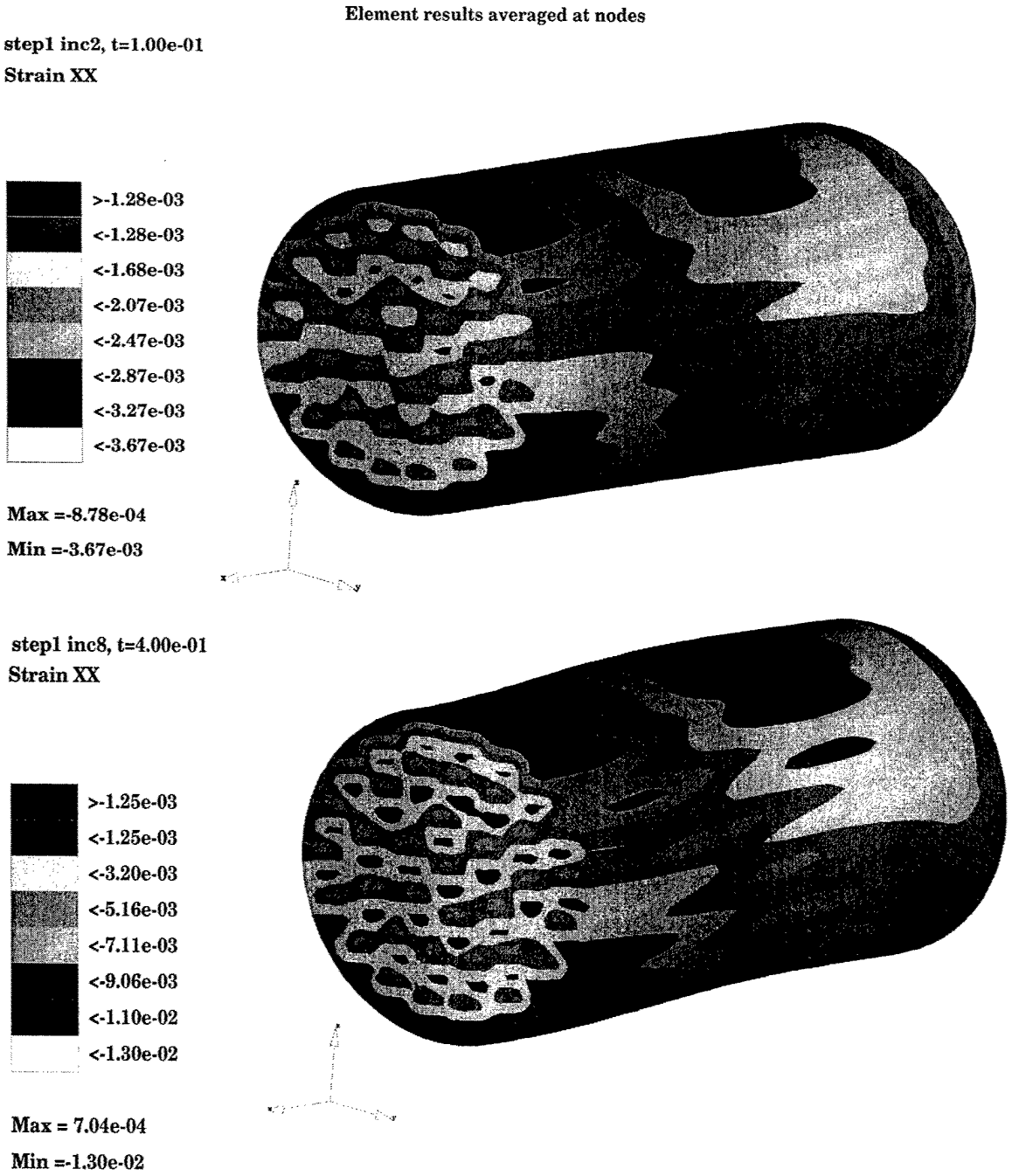

Figure 5.15: Contours of ϵ_{xx} for the carbon/vinylester composite of $V_f = 0.5$ and $\phi_1 = 1^0$ with orthotropic fiber properties

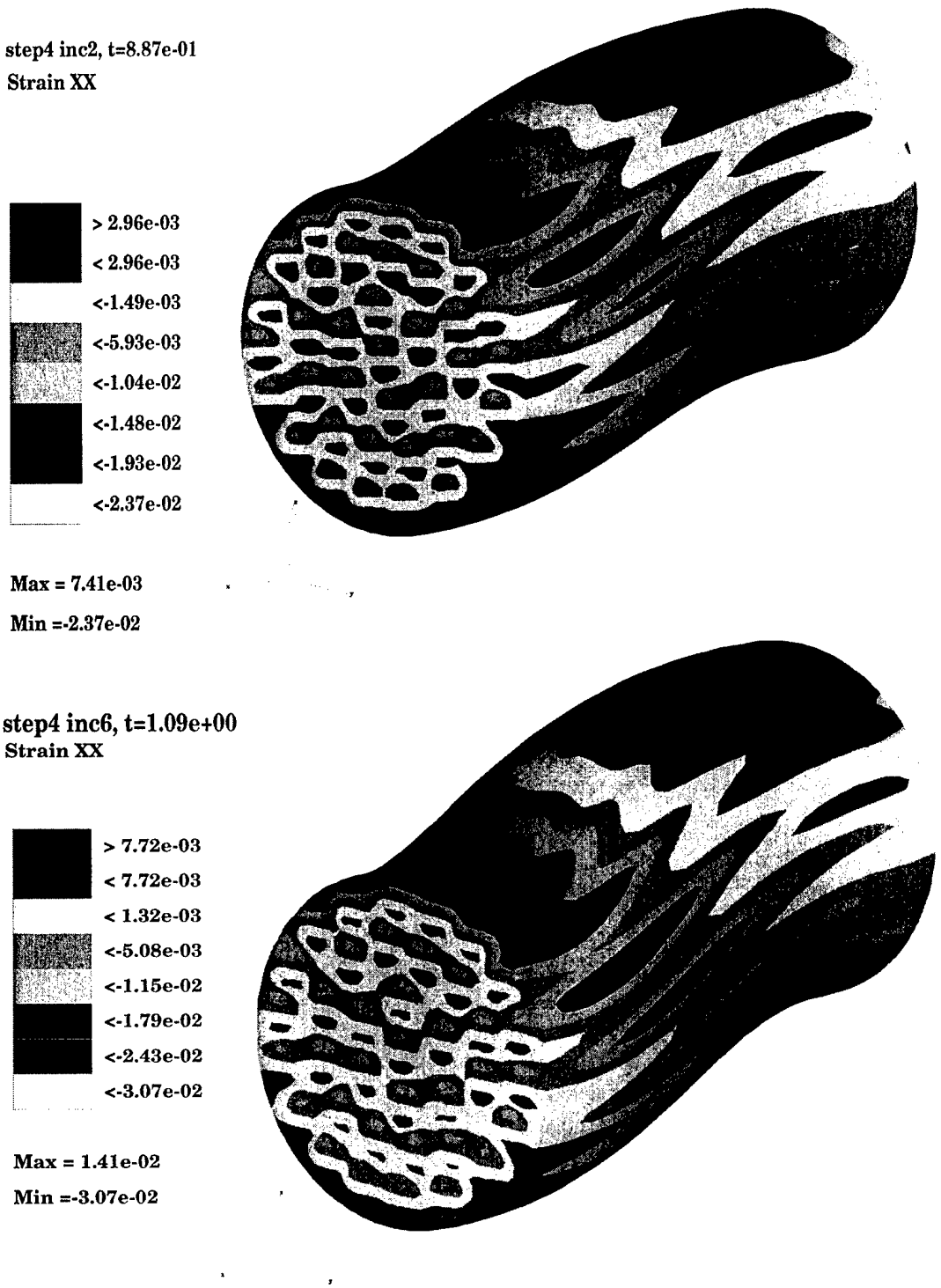

Figure 5.16: Contours of ϵ_{xx} for the carbon/vinylester composite of $V_f = 0.5$ and $\phi_1 = 1^0$ with orthotropic fiber properties

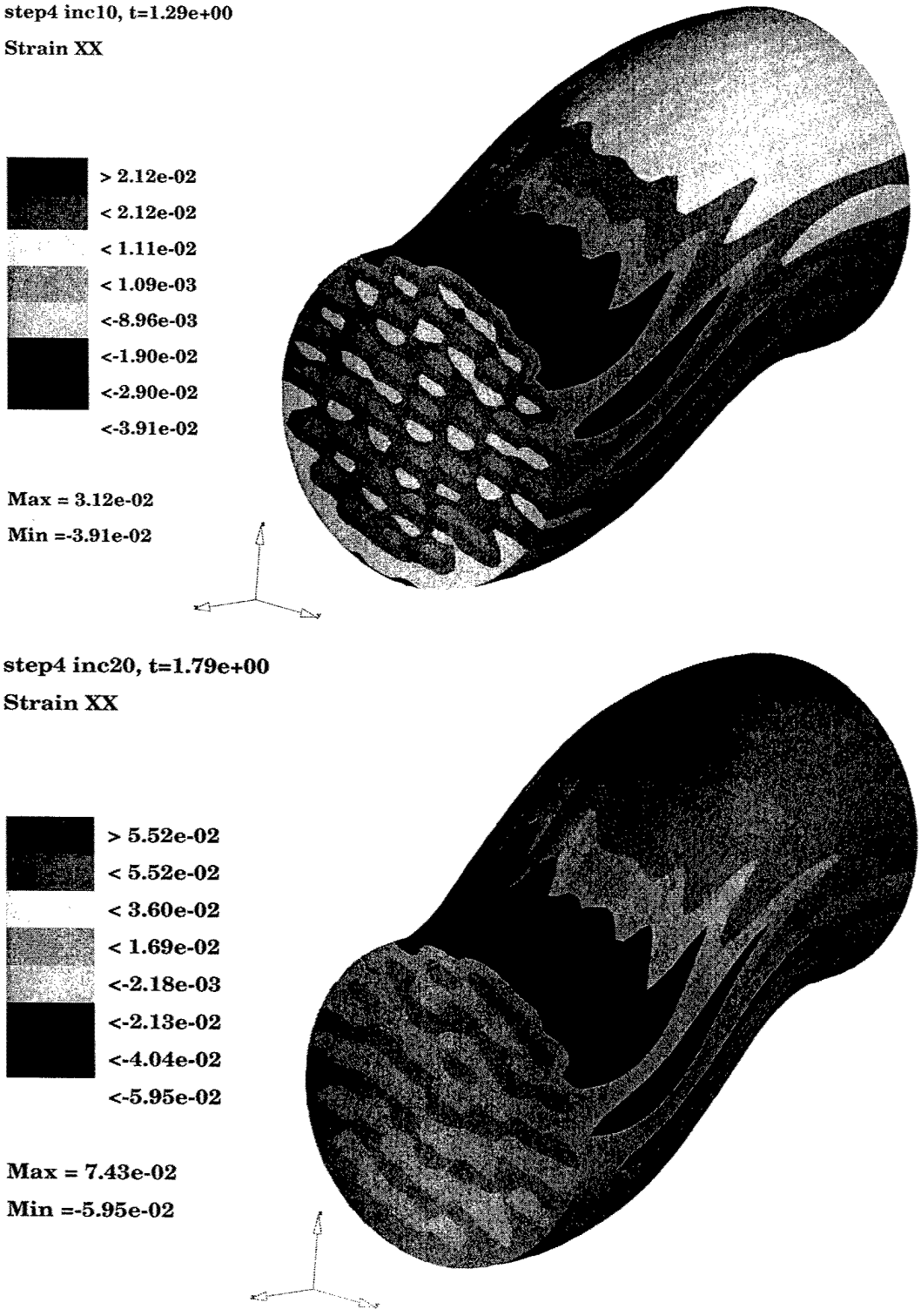

Figure 5.17: Contours of ϵ_{xx} for the carbon/vinylester composite of $V_f = 0.5$ and $\phi_1 = 1^0$ with orthotropic fiber properties

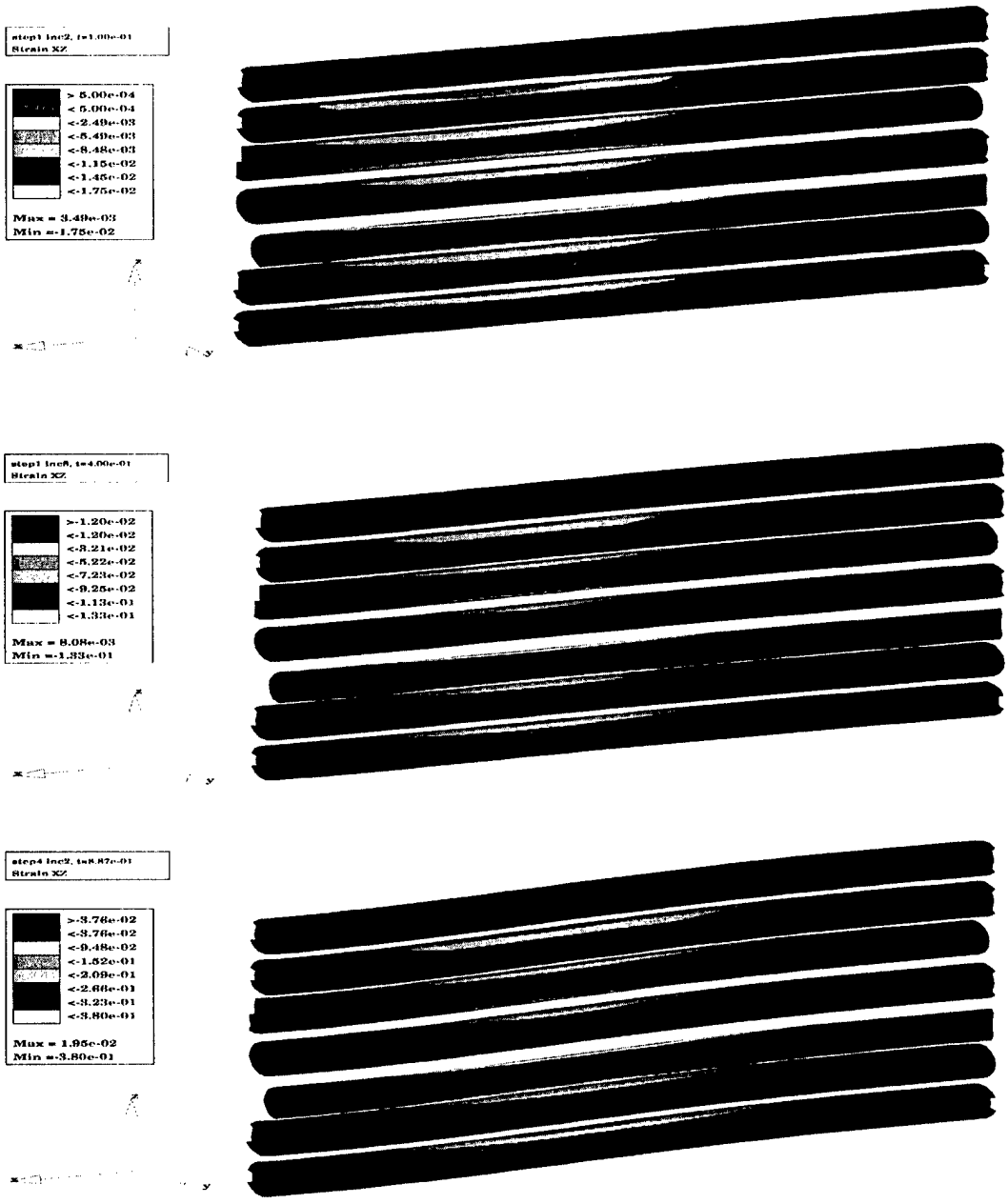

Figure 5.18: Contours of γ_{xz} for the carbon/vinylester composite of $V_f = 0.5$ and $\phi_1 = 1^0$ with orthotropic fiber properties

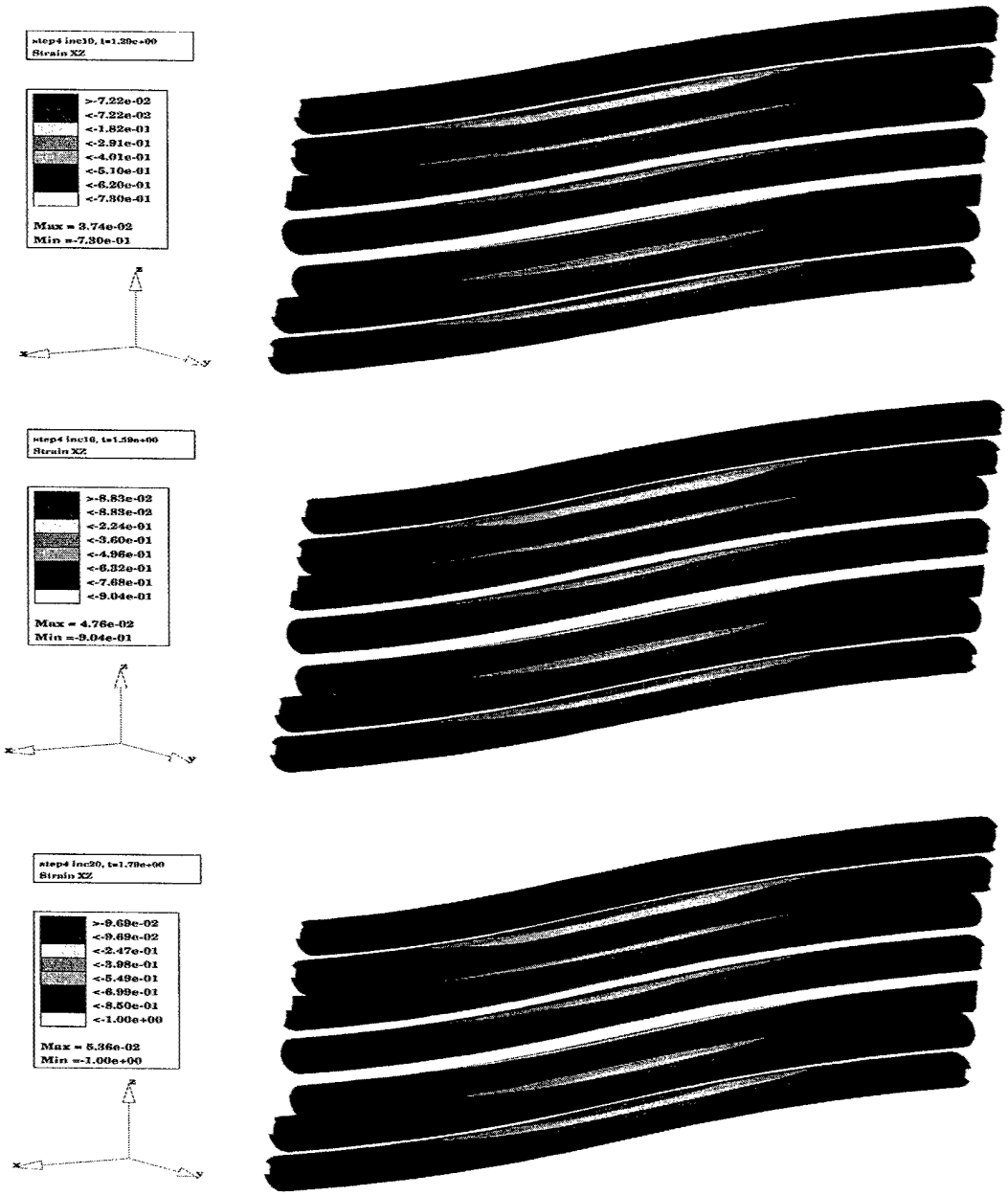

Figure 5.19: Contours of γ_{xz} for the carbon/vinylester composite of $V_f = 0.5$ and $\phi_1 = 1^0$ with orthotropic fiber properties

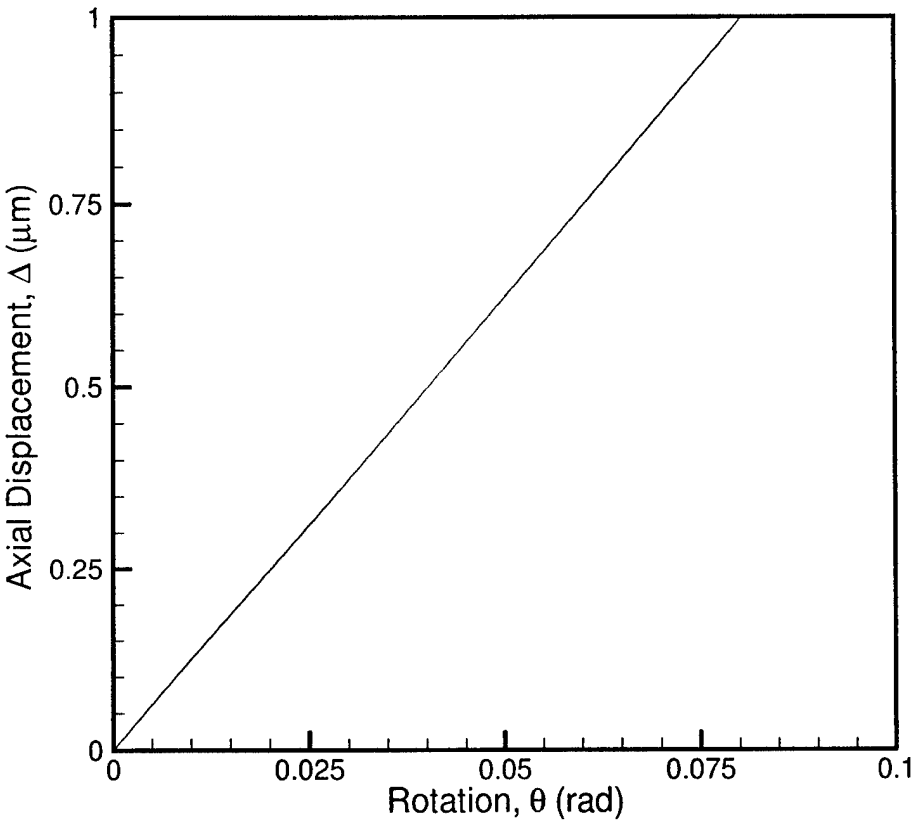

Figure 5.20: Displacement and rotational control loading of 3D FE model

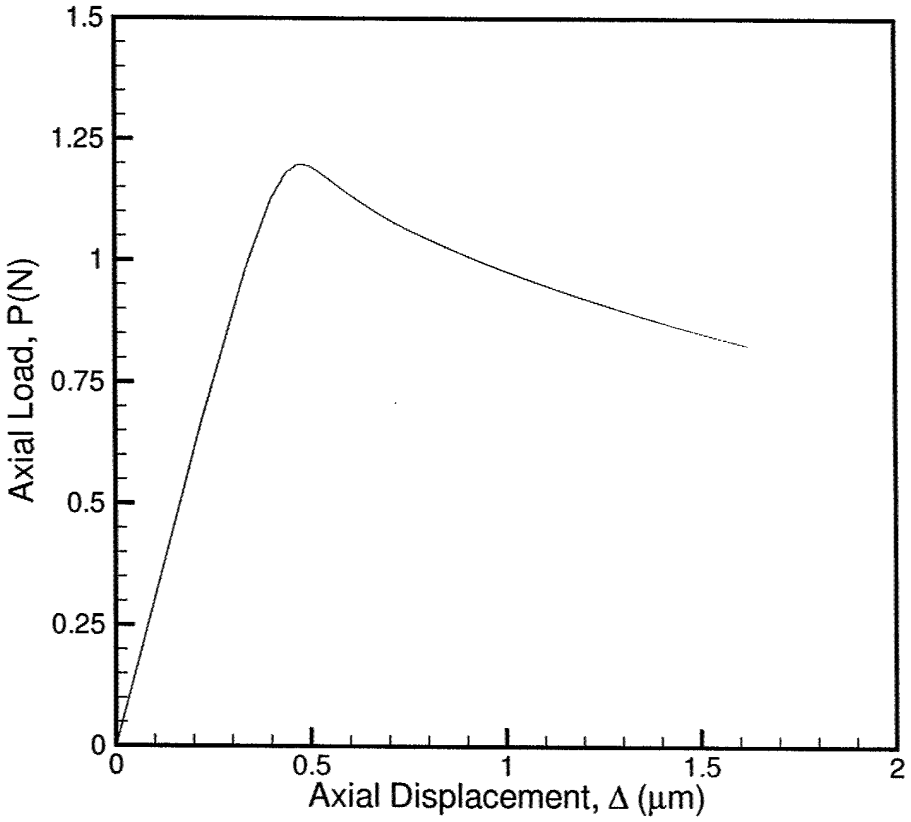

Figure 5.21: Load vs displacement reponse of 3D FE model under combined compression-torsion

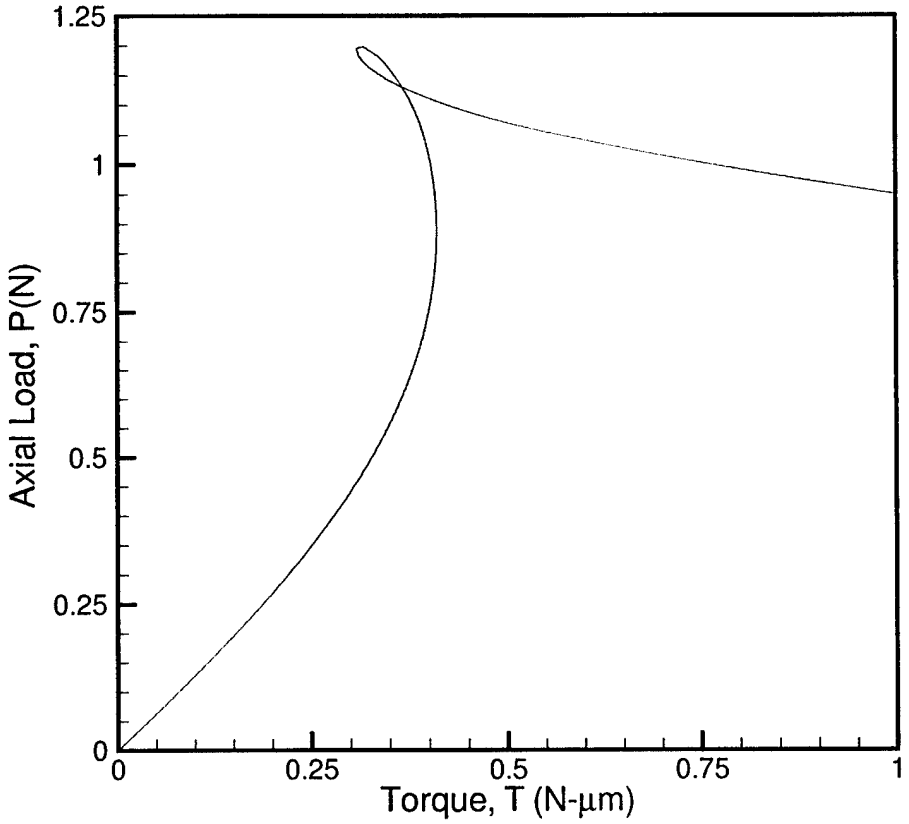

Figure 5.22: Load vs torque reponse of 3D FE model under combined compression-torsion

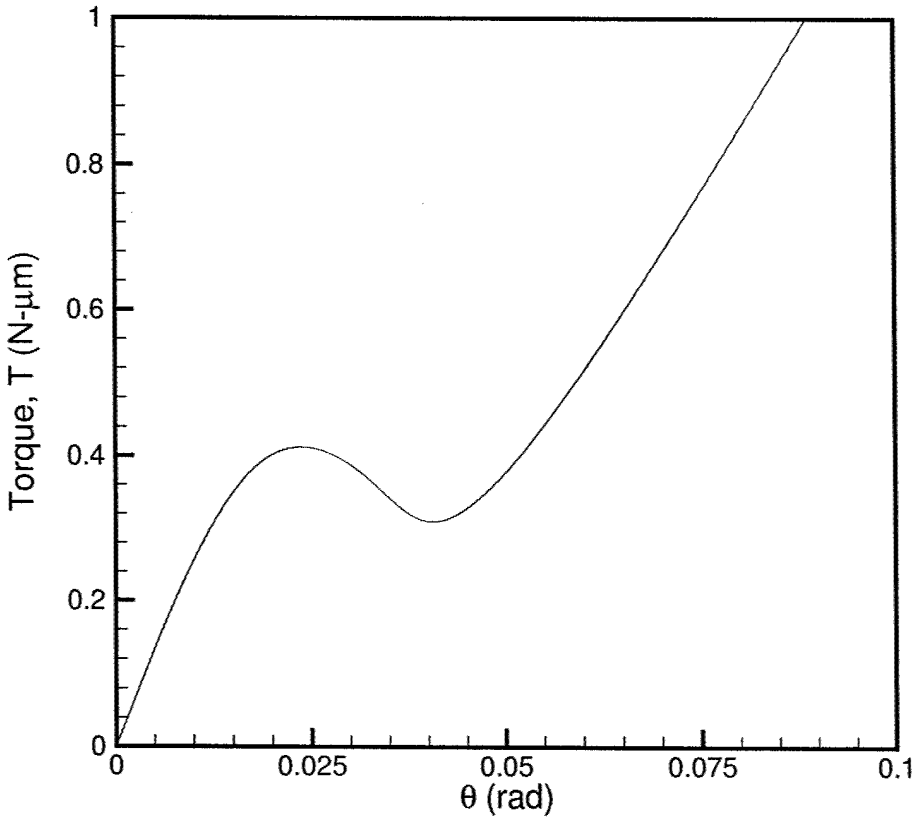

Figure 5.23: Torque vs theta reponse of 3D FE model under combined compression-torsion

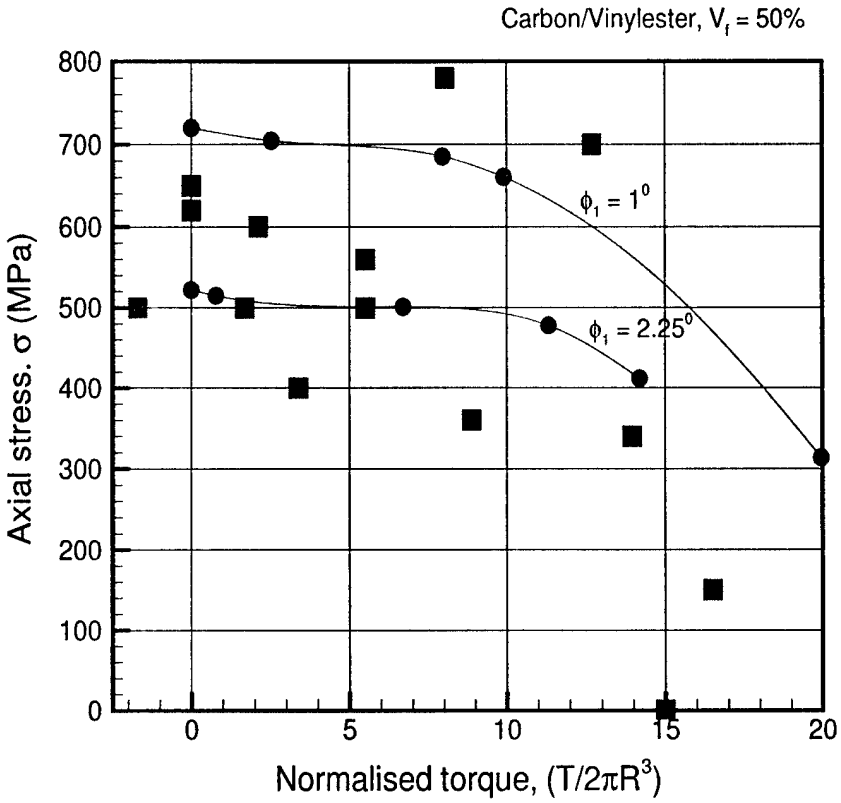

Figure 5.24: Comparison of combined compression-torsion failure envelope of 3D FE with experimental data

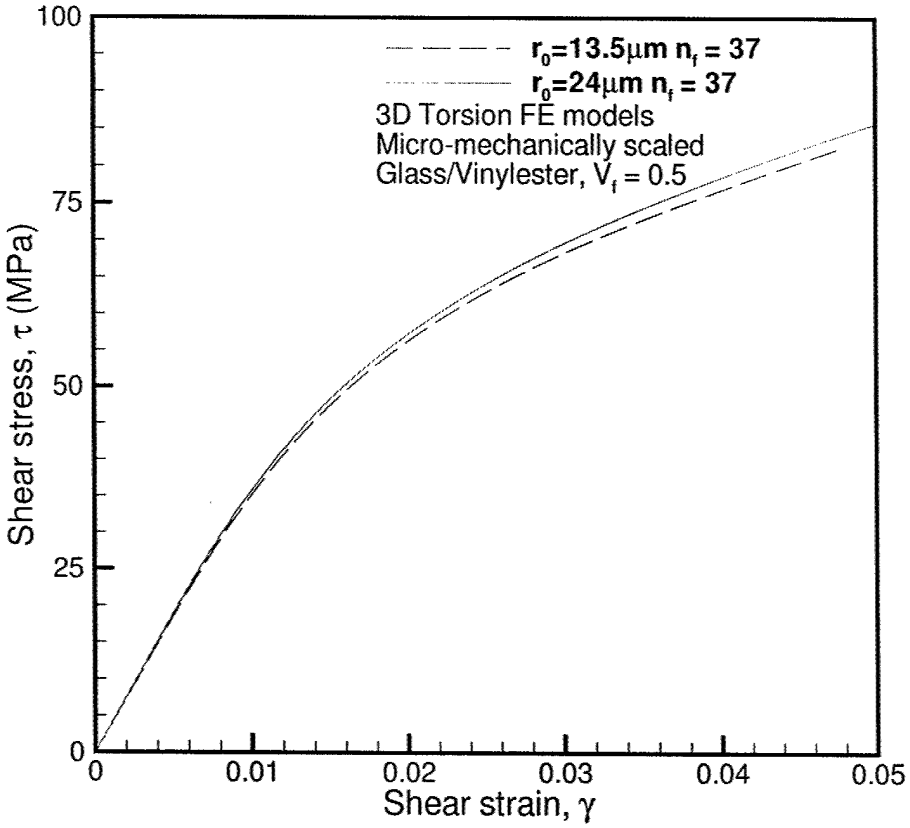

Figure 5.25: Torsional response of a 3D FE model of a glass composite of $V_f = 0.5$ for micro-mechanically scaled models

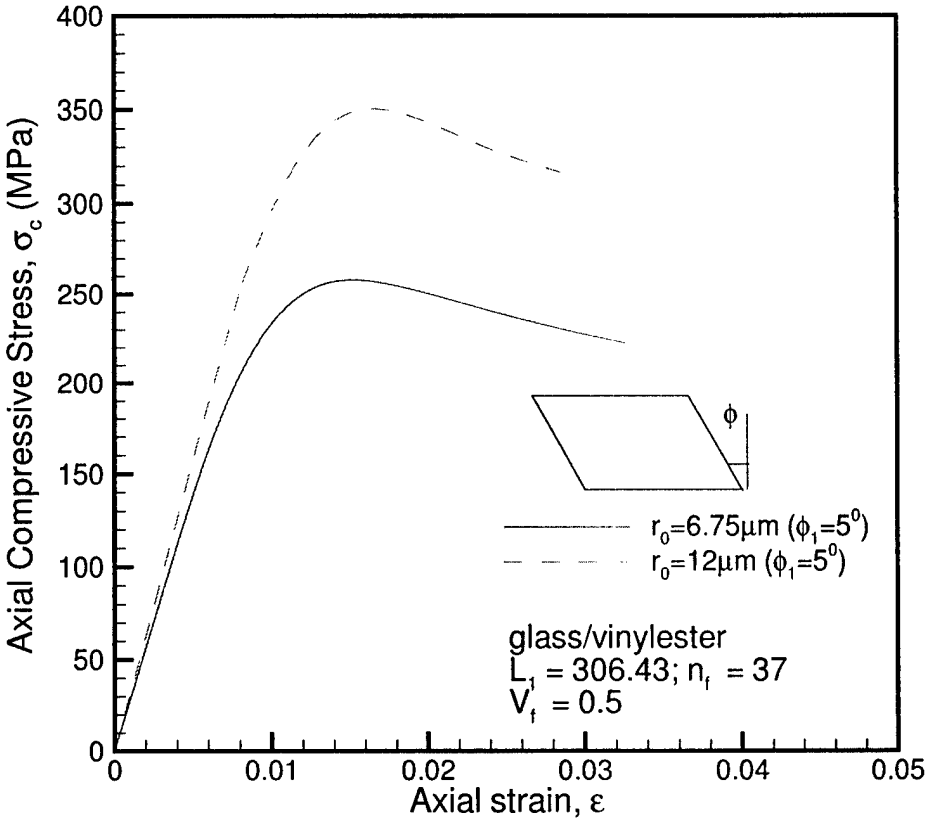

Figure 5.26: Compressive stress response of a 3D FE model of a glass composite of $V_f = 0.5$ for micro-mechanically scaled models

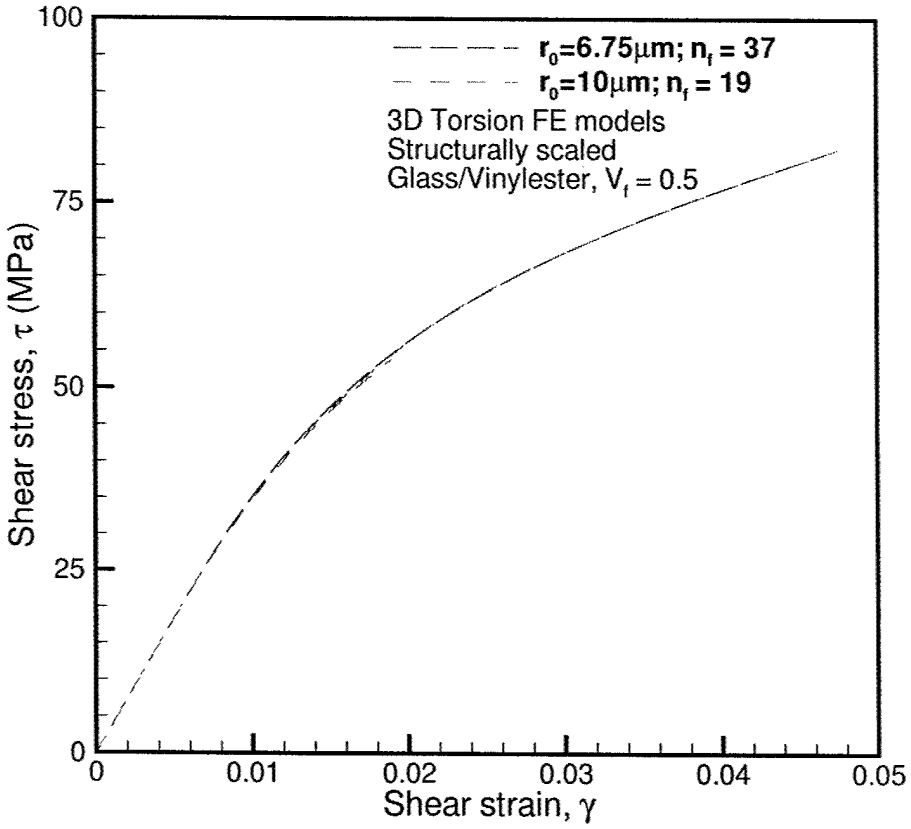

Figure 5.27: Torsional response of a 3D FE model of a glass composite of $V_f = 0.5$ for structurally scaled models

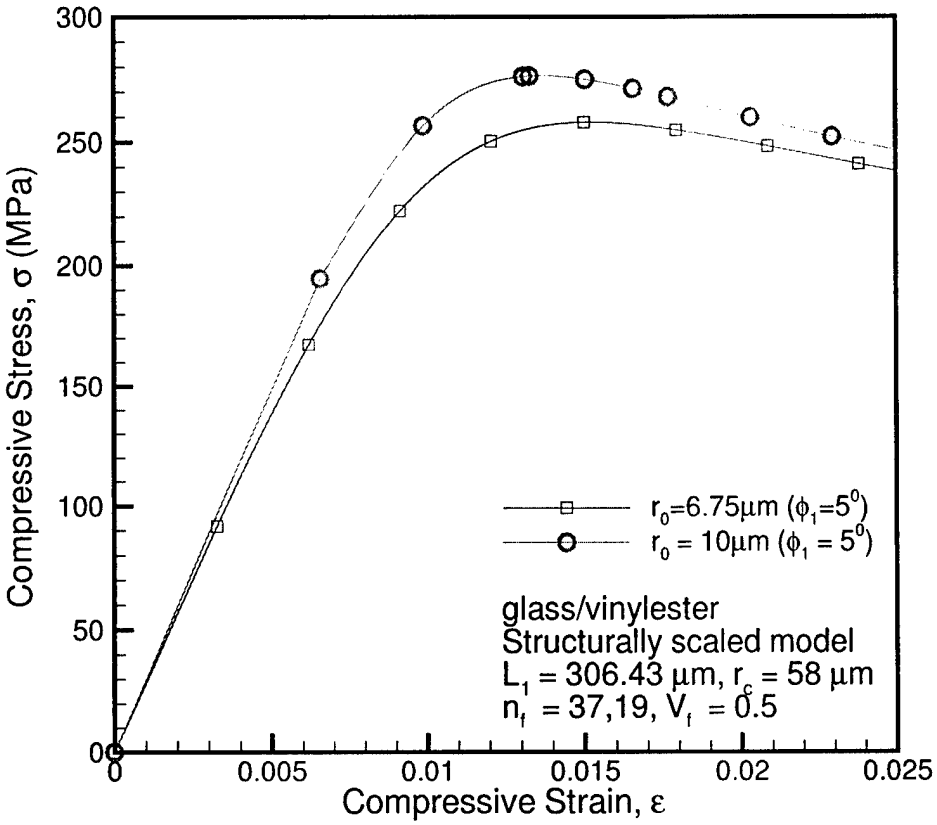

Figure 5.28: Compressive stress response of a 3D FE model of a glass composite of $V_f = 0.5$ for structurally scaled models

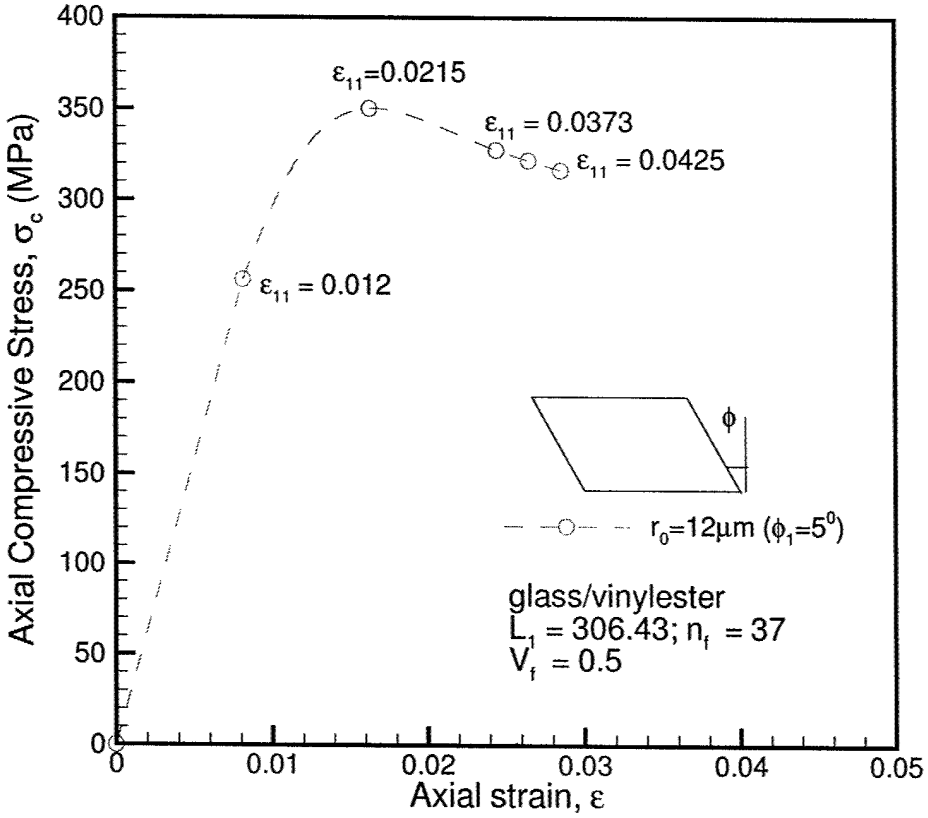

Figure 5.29: Compressive stress response of a 3D FE model of a glass composite of $V_f = 0.5$ and $r_f = 12\mu m$

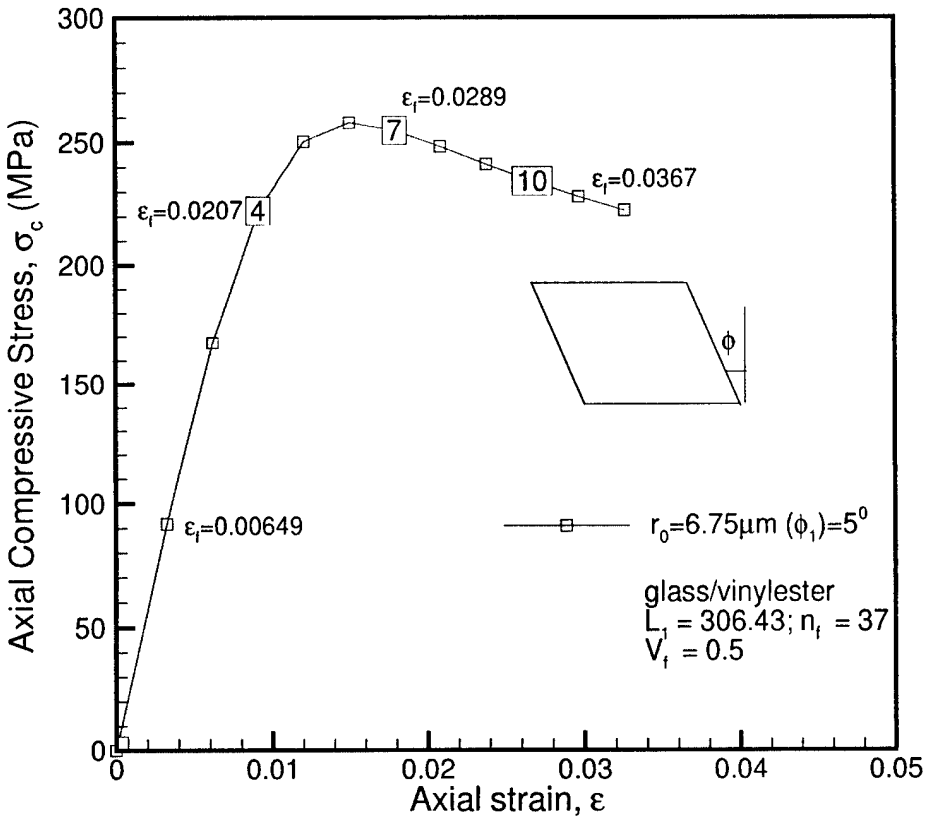

Figure 5.30: Compressive stress response of a 3D FE model of a glass composite of $V_f = 0.5$and $r_f = 6.75\mu m$

CHAPTER VI

STATIC AND DYNAMIC COMPRESSIVE RESPONSE OF HYBRID (GLASS/CARBON) COMPOSITES

6.1 Introduction

Fiber composites being man-made materials provide us the means to tailor the properties according to the requirements by choosing the constituents (fiber and matrix) in a optimum manner. Hybridization of fiber composites enhances this property of fiber reinforced composite materials. Hybridization can be done in both geomtry (e.g. plain weave woven fabrics with stitching in the transverse direction) or materials (by using two or more types of reinforcing fibers). Hybridization in composites can lead to benefits in cost and enhancement of mechanical properties. Previous studies on the mechanical behavior of hybrid composites have focussed mainly on tensile and impact behavior of hybrid fiber composites, Aveston and Sillwood (1976); Dorey et al. (1978). An exception to this is the work of Piggott and Harris (1981), who studied the static compressive response of hybrid glass/carbon composites. Investigations on the Dynamic compressive stress response and the strain rate effects on compressive strength of hybrid (glass/carbon) composites has not been investigated in the open literature. Lee (1998), Yuan and Takeda (2000) studied the compressive

behavior of unidirectional glass and carbon composites under high strain rates. Yuan and Takeda (2000) conducted high strain rate tests on glass fiber composites at strain rates of $\dot{\epsilon} = 1000s^{-1}$. They observed the failure stress to increase with increasing strain rate. Tests were also conducted by varying the specimen temperature. It was observed that the failure strength of the specimen was a decreasing function of increasing temperature. This was due to the degradation in the matrix mechanical properties. The failure mechanism was observed to be splitting in case of glass fiber composites and kinking in the case of carbon fiber composites.

Results presented in the previous chapters have shown that the failure strength and failure mechanism of glass fiber reinforced composites are different from carbon fiber reinforced composites. Thus, it was felt that hybridization of composites by mixing carbon and glass fibers may lead to results that reinforce and delineate the earlier conclusions regarding the failure mechanism, failure strength prediction and the dependancy of failure mechanism on parameters such as fiber type and interface. Based on the results presented in the previous chapters and on the work by, Fleck (1997); Lee and Waas (1999); Vogler and Kyriakides (1999), and Vogler et al. (2000), it is known that the compression strength of polymer composites depends on the fiber type, matrix shear properties, fiber/matrix interface toughness and misalignments of the fibers. In case of pure carbon composites, kinking is the dominant failure mechanism whereas for glass composites, splitting was found to be the predominant failure mechanism. By hybridizing the composite, one would ideally like to acheive a higher strength or change in failure mode. In their paper, Piggott and Harris (1981) studied the effect of hybridization of glass/carbon composites experimentally. They also conducted experiments on hybrid(carbon/kevlar) composites under pure compression. They observed that the effect of hybridization(glass/carbon) was to reduce

the compressive strength of the composite. However, in the case of carbon/kevlar hybridization, they observed an increase in strength with hybridization. In this chapter, results obtained from studying glass/carbon fiber hybrid polymer matrix composites under static and dynamic compressive loading are presented. For this purpose, an overall fiber volume fraction, $V_f = 0.3$ was chosen. The fiber content of individual constituents were varied from pure glass to pure carbon, while keeping the overall fiber volume fraction fixed at 0.3. Results presented in the previous chapters showed that the failure mode underwent a transition from pure splitting to splitting/kinking around $V_f \approx 0.3$. Thus, it was felt that an overall $V_f = 0.3$ was ideal for studying the influence of different constituents on the failue mechanisms.

6.2 Experiments

Pure compression tests were performed on cylindrical composite specimens. The specimen diameter was approximately $6.8mm$ and the gage length of the specimen was $12.7mm$. Two back to back strain gages were attached to record the strain in the gage section and also to check the loading alignment. The specimens were manufactured with a range of hybrid ratios of glass/carbon. The specimens were compressed in a MTS hydraulically actuated machine for static loading and in a split Hopkinson pressure bar (SHPB) setup for dynamic loading. Details of the specimen manufacturing process and the SHPB setup are included in the appendix D. The total volume fraction of fibers, V_f was kept constant at 0.3. The ratio of glass to carbon fibers was varied from the case of pure glass, $V_{gc} = 1$ to pure carbon, $V_{cc} = 1$, with the following constraint; $V_{gc} + V_{cc} = 1$. The individual fiber volume fraction at any ratio is obtained by the following relations for glass, $V_{fg} = r_{0g}^2/r_c^2$ and for carbon, $V_{fc} = r_{0c}^2/r_c^2$. In the experiments for both static and dynamic the values

of V_{gc} chosen were as follows, $\{1, 0.9, 0.7, 0.5, 0.3, 0.1, 0\}$ and the value for V_{cc} can be obtained from the constraint relation. These new terms for the individual fiber volume fractions are defined below in terms of the fiber radius.

$$\begin{aligned} V_g &= \frac{r_{0g}^2}{r_{mg}^2} \\ V_c &= \frac{r_{0c}^2}{r_{mc}^2} \\ V_{gc} &= \frac{r_{mg}^2}{r_c^2} \\ V_{cc} &= \frac{r_{mc}^2}{r_c^2} \\ V_{fg} &= V_{gc} \times Vg \\ V_{fc} &= V_{cc} \times Vc \end{aligned} \tag{6.1}$$

6.2.1 Static Compression

The hybrid composites were tested to failure in a quasi-static manner. Typical stress vs strain responses obtained from the experiments during the testing of hybrid composites is plotted in figure 6.1. It can be observed that as the carbon fiber volume fraction, V_{fc}, increases the failure strain decreases. The minimum strain to failure does not correspond to that of pure carbon but to a hybrid ratio with a very low percentage of glass fibers. The static tests on hybrid composites show that the effect of mixing carbon to glass fibers is to reduce the compressive strength as shown in figure 6.2. The failure mechanism changed from splitting in pure glass composites ($V_{gc} = 1$) to kinking failure in carbon composites ($V_{cc} = 1$) as the percentage of carbon fibers increased in the hybrid composite. The change in the failure mechanism was found to occur around a hybrid ratio of 0.5. The measured elastic modulus of the hybrid composites was plotted as a function of the hybrid ratio and, analytically,the composite rule of mixtures was found to adequately approximate the experimental

data as can be seen in figure 6.3. Similarly, it was observed that as the percentage of carbon fibers increase in the composite, the strain to failure decreases decreases. Thus, the use of hybrid glass/carbon composites did not lead to an increase in static compressive strength.

6.2.2 Dynamic Compression

The hybrid composite specimens were also tested under high strain rate loading using a split Hopkinson pressure bar (SHPB) test setup. Details of the UM Aerospace department SHPB and the technique of establishing stress-strain data and strength data under dynamic loading are given in Appendix D.

The SHPB setup consists of a impactor bar, incident bar and the transmission bar. Usually a fourth bar called the throw-off bar acts like a momentum trap. In the present SHPB setup the four bars were made of 440C case hardened stainless steel. The specimen is sandwiched between the incident bar and the transmission bar. The specimen/bar interfaces are greased so as to reduce friction. The specimen length and diameter are kept very small compared to the length of the SHPB bars. This ensures that the one dimensional wave propagation assumptions are met and also that the specimen attains a uniform state of strain in a short time as compared to the duration of the loading pulse. The SHPB setup was first used to test aluminum6060 alloy specimens to validate the experimental setup and the computer programs that are subsequently used to extract the specimen stress and strain data from the strain gage signals. This particular alloy of aluminum is strain rate independent and can be useful in validating the SHPB test setup. As shown in figure 6.4 and figure 6.5 the compressive stress response of both specimens under varying strain rates is approximately same. Once the setup and the computer programs were validated, the

hybrid composite specimens were tested under high strain rate loading conditions. Figure 6.6 shows the variation of stress with strain rate. It can be seen that initially the strain rate is varying and only in a short period before failure that the strain rate achieves a nearly constant value. In case of high strain rate tests on hybrid composites, the failure strength was observed to increase at each hybrid ratio (glass/carbon) as shown in figure 6.7. There is wide scatter in the data due to which definite conclusions on the dependancy of failure strength on strain rate cannot be drawn. However, in general it can be seen that the failure strength increases with increasing strain rate for all hybrid ratios. Typical stress response curves obtained for a composite with hybrid ratio of $V_{gc} = 0.5$ is shown in figure 6.8. A typical oscilloscope trace of the strain gage signals obtained from the strain gages on the incident bar and the transmission bar are shown in figure 6.9. The specimens used in the high strain rate tests were completely destroyed. The hybrid composites with greater percentage of glass fibers exhibited brooming type of failure surfaces. In case of hybrid composites with higher percentage of carbon fibers, the failure surfaces did not show brooming. For all hybrid ratios, glass fiber composites show characteristics of splitting failure like brooming and disintegration of matrix. The exact failure mechanism could not be established in these tests since the specimen undergoes repeated loading under a series of compressive stress pulses. This leads to complete disintegration of the specimens.

6.3 Analysis

For analysing the static compressive response of hybrid composites, a model similar in concept to the concentric cylinder model of chapter III is utilized. The hybrid composite is assumed to consist of an assemblage of space filling concentric cylinders

of carbon/matrix and glass/matrix distributed uniformly and mixed according to their respective constituent volume fractions and with an overall fiber volume fraction, $V_f = 0.3$, as shown in figure 6.7. Thus, for example, for a hybrid ratio of 0.3, ie. $V_{gc} = 0.3$, the glass cylinder radius will be $r_{mg} = (V_{gc}/V_{fg}) \times r_{og}^2$ and similarly, the carbon cylinder radius will be $r_{mc} = (V_{cc}/V_{fc}) \times r_{oc}^2$. In the experiments, a failure mode transition was observed as the percentage of glass fibers reduced from 100% to 0% by the replacement of glass fibers by carbon fibers. Hence, both kinking and splitting failure mechanisms are modeled at the individual concentric cylinder level and next assembled to obtain the composite behavior under suitable assumption.

Splitting

In case of splitting analysis, all the expressions for stresses, strains and the expression for compliance remain the same as those of the splitting model presented in chapter III. The only difference being that these expressions are now calculated for the individual components of the hybrid composites. Thus, in case of a glass/carbon hybrid composite, we will have the expressions for critical compressive stress (from chapter III, equation (3.5)) written as follows.

$$\sigma_g^{sp} = \sqrt{\frac{8V_f^2\gamma_{fg}}{r_{0g}(1/\delta_g - \beta_g^{sp})}} \tag{6.2}$$

$$\sigma_c^{sp} = \sqrt{\frac{8V_f^2\gamma_{fc}}{r_{0c}(1/\delta_c - \beta_c)}} \tag{6.3}$$

Similarly, for kinking, we can write the critical kinking stresses for both glass and carbon composite cylinder. From chapter IV equation (4.5), we obtain the expression for kinking stress as follows by substituting $\alpha = 0$.

$$\sigma_g^k = \frac{\frac{1}{\gamma_{rmg}^3}\int_0^{\gamma_{rmg}} \tau(\gamma)\gamma^2 d\gamma}{\frac{\phi_g}{3} + \frac{\gamma_{rmg}}{4}} \tag{6.4}$$

$$\sigma_c^k = \frac{\frac{1}{\gamma_{rmc}^3}\int_0^{\gamma_{rmc}} \tau(\gamma)\gamma^2 d\gamma}{\frac{\phi_c}{3} + \frac{\gamma_{rmc}}{4}} \tag{6.5}$$

Here, the subscripts g and c stand for glass and carbon respectively and the superscripts sp and k are for splitting and kinking failure mechanisms. We first adopt an iso-strain assumption to assemble the individual concentric cylinder level results and extract composite level properties. To ensure compatibility between glass concentric cylinder and the carbon concentric cylinder, we equate the axial strains in both composite cylinders. From, the 3D stress analysis results in chapter III, we can obtain the expressions for strains.

$$\begin{aligned} \epsilon_{fg}^{3D} &= \epsilon_{fc}^{3D} \\ \frac{2\beta^g P_g}{\pi r_{og}^2} &= \frac{2\beta^c P_c}{\pi r_{oc}^2} \\ P_c = P_g \frac{\beta^g}{\beta^c} \frac{r_{oc}^2}{r_{og}^2} & \end{aligned} \tag{6.6}$$

Using the expressions for fiber volume fractions given in equation (6.1), we can write equation (6.6) as

$$P_c = P_g \frac{\beta^g}{\beta^c} \frac{V_{cc}}{V_{gc}} \tag{6.7}$$

Equation (6.7), gives a relation between the load carried by a carbon composite cylinder, P_c, in terms of the load carried by a glass composite cylinder, P_g, at a given hybrid ratio as determined by V_{cc} and V_{gc}. To obtain an expression for the total load carried by the complete composite, we need to rely on stress equilibrium along the axial direction to obtain a relation between the loads carried by individual constituents and the total load, P_{total}. Thus,

$$\begin{aligned} P_{total} &= P_c + P_g \\ &= P_g[1 + (\beta^g/\beta^c)(V_{cc}/V_{gc})] \end{aligned} \tag{6.8}$$

Equation (6.8), provides an expression to calculate the total load carried by the hybrid composite when a critical condition is reached for any of the individual con-

stituent composite cylinders (either splitting or kinking). Defining, $(\beta^g/\beta^c)(V_{cc}/V_{gc}) = \psi$, we can write

$$P_g = \frac{P_{total}}{(1+\psi)} \tag{6.9}$$

$$P_c = \frac{P_{total}\psi}{(1+\psi)} \tag{6.10}$$

The stress in a glass concentric cylinder can be obtained by referring to figure 6.10 and noting that r_{mg} is the radius of the glass composite cylinder and using equations (6.9), we obtain

$$\begin{aligned} \sigma_g &= \frac{P_g}{\pi r_{mg}^2} \\ &\quad \text{but } \pi r_{mg}^2 = V_{gc}\pi r_c^2 \\ &= \frac{P_{total}}{(1+\psi)\pi r_c^2 V_{gc}} \\ &= \frac{\sigma_{total}}{(1+\psi)V_{gc}} \end{aligned} \tag{6.11}$$

Therefore, we can write the total stress expression as

$$\sigma_{total} = \sigma_g(1+\psi)V_{gc} \tag{6.12}$$

Similarly, we can obtain the total stress, σ_{total}, in terms of the stress in carbon concentric cylinder, σ_c, by following the above procedure. This results in,

$$\sigma_{total} = \sigma_c(1+1/\psi)V_{cc} \tag{6.13}$$

In equation (6.12) and equation (6.13), σ_g and σ_c are the values calculated by equations (6.2-6.4). This completes the iso-strain failure model in the hybrid composite.

Next, we adopt an iso-stress assumption to model failure in hybrid composites. Previous work on compressive failure by Yao and Chou (1989) and Martinez et al. (1981), showed that unidirectional hybrid composite displays a wide disparity in

strain between the glass and carbon fibers. That is, when a hybrid composite containing a mixture of a flexible fiber and relatively stiff fiber are loaded in compression, the stiffer fiber reaches a critical stress state earlier than the compliant fiber. Thus, a iso-strain assumption will lead to a prediction of increase in strength for the case of addition of stiffer fibers (carbon) to a less stiff fiber(glass) reinforced composite. However, in an iso-stress approach, it is assumed that the composite carries a stress, σ which is transmitted to both glass concentric cylinder and a carbon concentric cylinder as schematically shown in figure 6.10. Thus, the critical composite stress is calculated when either of the constituent cylinders first reaches a critical stress state. For instance, if the glass concentric cylinder reaches the condition of splitting, then the critical failure stress is calculated in glass composite using equation (6.2). As the volume fraction of glass decreases the compressive strength will now decrease. Results as predicted by the iso-strain model and the iso-stress model are shown in figure 6.11, where, experimental results are also presented. It can be seen that, for small values of V_{gc}, the iso-strain kinking model captures the experimental data very well. Beyond $V_{gc} = 0.15$, the iso-strain kinking model underestimates the compressive strength. This is because, as V_{gc} increases, the expressions for kinking (equation (6.4) based on the assumptions of pure kinking ceases to be valid. In a hybrid composite, the surrounding glass fibers offer more constraint to kinking (confinement) and thus, the kinking expression of equation (6.4) will underestimate the compressive strength. On the other hand, in this region, $0.5 < V_{gc} < 1$, the iso-stress model adequately capture the experimental data for compressive strength. Thus, when the compliant fiber dominates the hybrid composite, the iso-stress model predictions capture the experimental data, while for hybrid composites dominated by the stiffer fiber, the iso-strain model appears to capture the experimental strength data. It is to

be noted that both models must be used with the appropriate failure mechanism as observed in the experiment. A mechanism based failure modeling approach as presented here appear to adequately explain the static compressive strength data for hybrid composites.

6.4 Conclusions

As the results from the hybrid test data indicate, mixing of glass and carbon fibers in a single composite actually leads to a deterioration in the measured strength of the composite. The splitting and kinking models for pure composites were modified to account for the presence of another type of fiber in the composite. Using equation (6.12) and equation (6.13), we can obtain the total stress on the composite when either of the individual composite cylinder reaches the critical stress in splitting or kinking. The total stress values obtained by using glass and carbon composite cylinder stresses is plotted in figure 6.11. Here, the total stress predicted by the splitting of glass is consistently increasing with the addition of carbon fibers. This is due to the fact that the addition of carbon fibers increases the value of ψ, which leads to a increase in the total stress, σ_{total} from equation (6.12). Also, the total stress predicted by the splitting of carbon composite cylinders consistently decreases with increasing glass fiber volume fraction or decreasing carbon fiber volume fraction. The total stress predicted by carbon kinking stress for $\phi = 3^0$ is seen to match with the experimental data upto $V_{fg} = 0.15$. Beyond this glass volume fraction this prediction provides a lower bound for the predicted values. However, it should be noted that the failure mechanism was not pure kinking beyond glass volume fraction of 0.15. Thus, explaining the decrease in failure stress on the addition of carbon fibers to a glass composite is not possible based on the models where the strain in both carbon

and glass composite cylinders is assumed to be same. However, the decrease can be explained by using a iso-stress model as shown in figure 6.11.

In case of high strain rate test data of the hybrid composites it can be seen that the failure strength does show a definite increase at each hybrid ratio but the scatter in data makes it difficult to find a specific relation between the strain rate and the strength. However, as can be seen from figure 6.12, the failure strength shows a increase across all hybrid ratios as compared to the static test data.

V_{fg}	Strength (MPa)			$Ave.Strength(MPa)$
0	425	-	-	425
3	320	250	340	303.3
9	385	345	320	350
15	300	265	235	296.7
21	345	340	320	335
27	430	405	385	406.7
30	484	520	480	494.7

Table 6.1: Compressive strength of hybrid composites

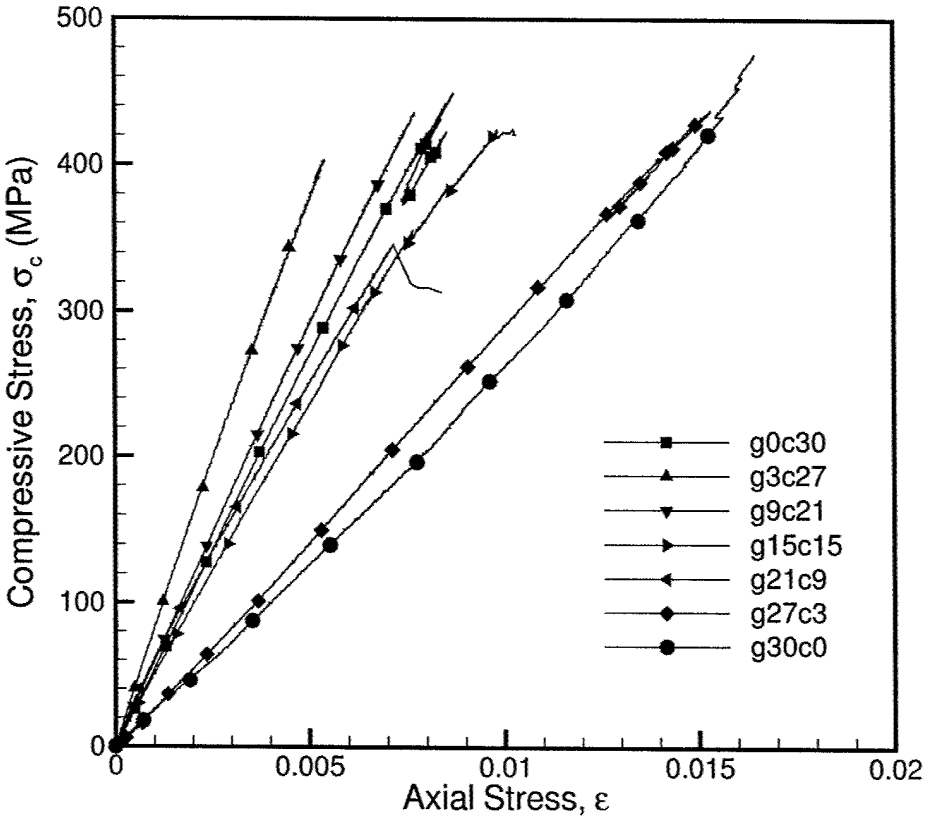

Figure 6.1: Typical compressive response of hybrid composites as a function of the hybrid ratio for a global fiber volume fraction of 30%

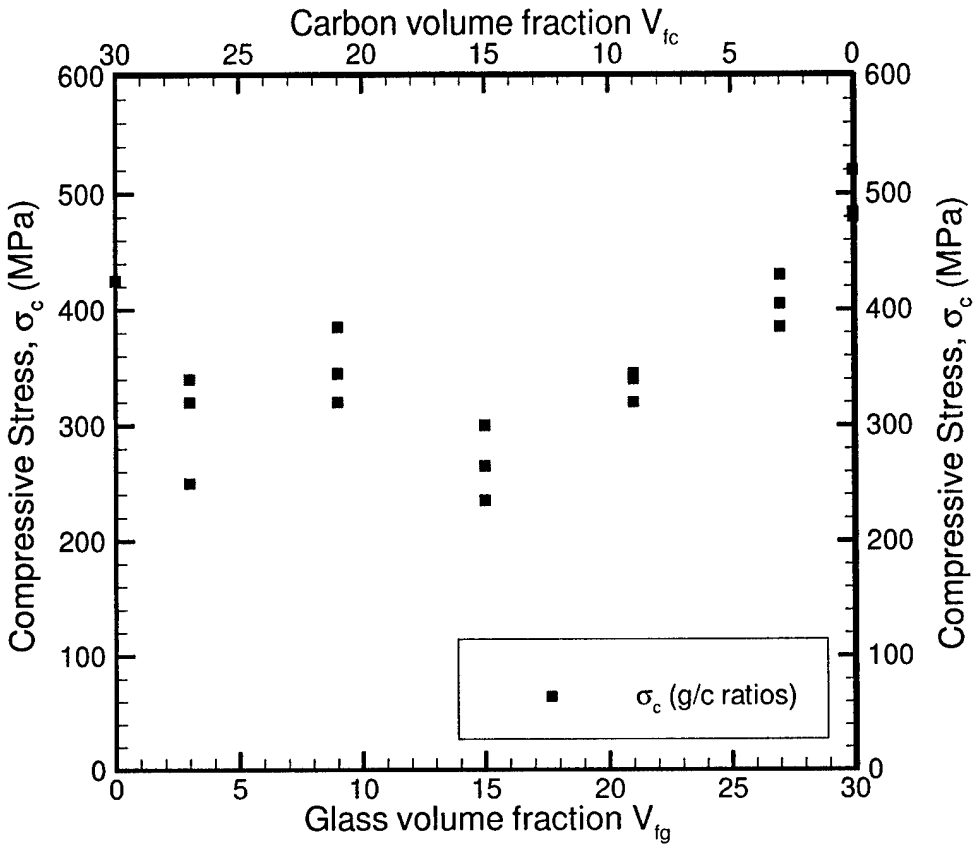

Figure 6.2: Variation of failure strength as a function of the hybrid ratio for a global fiber volume fraction of 30%

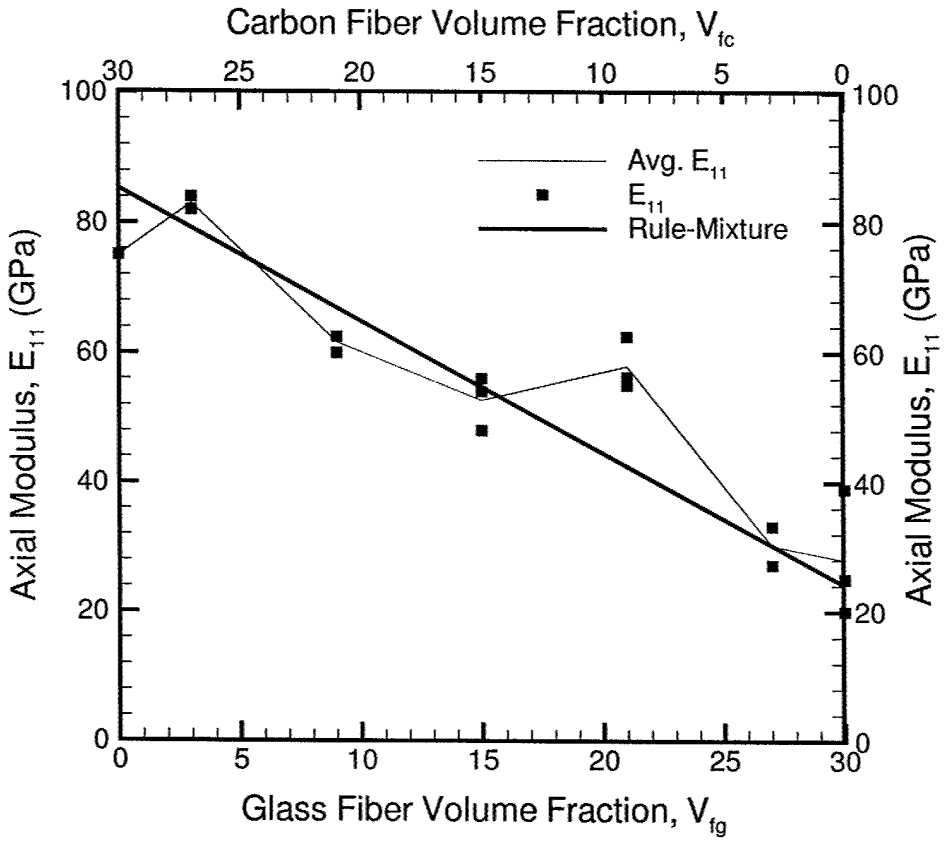

Figure 6.3: Variation of elastic modulus as a function of the hybrid ratio for a global fiber volume fraction of 30%

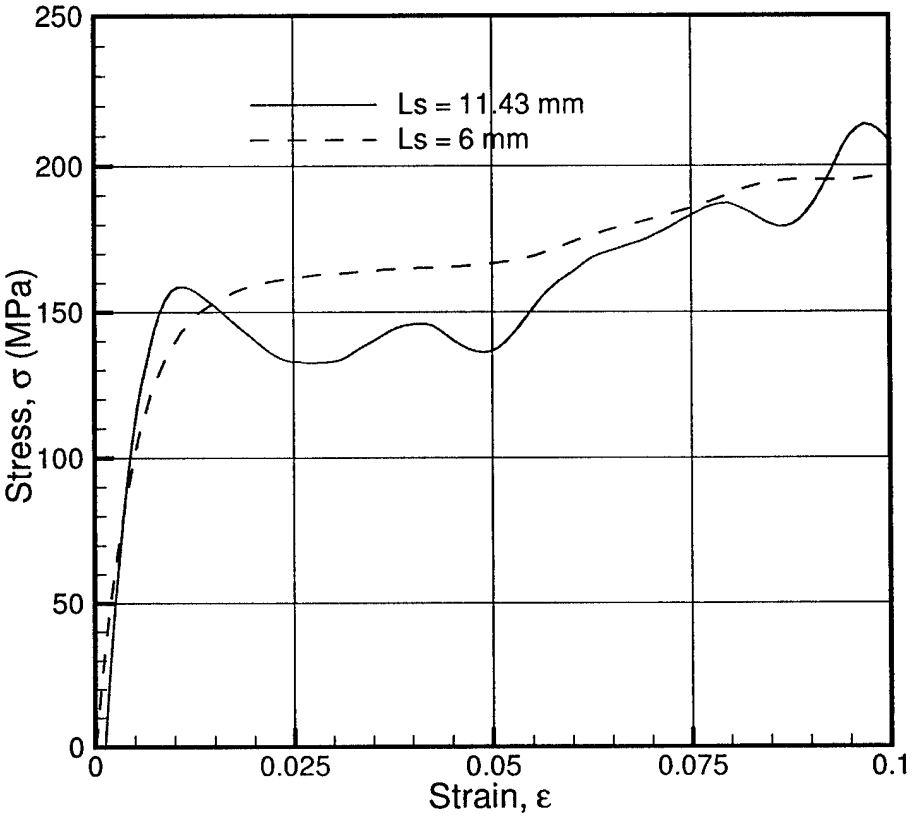

Figure 6.4: The compressive stress response of a Aluminum6060 alloy under high strain rate tests.

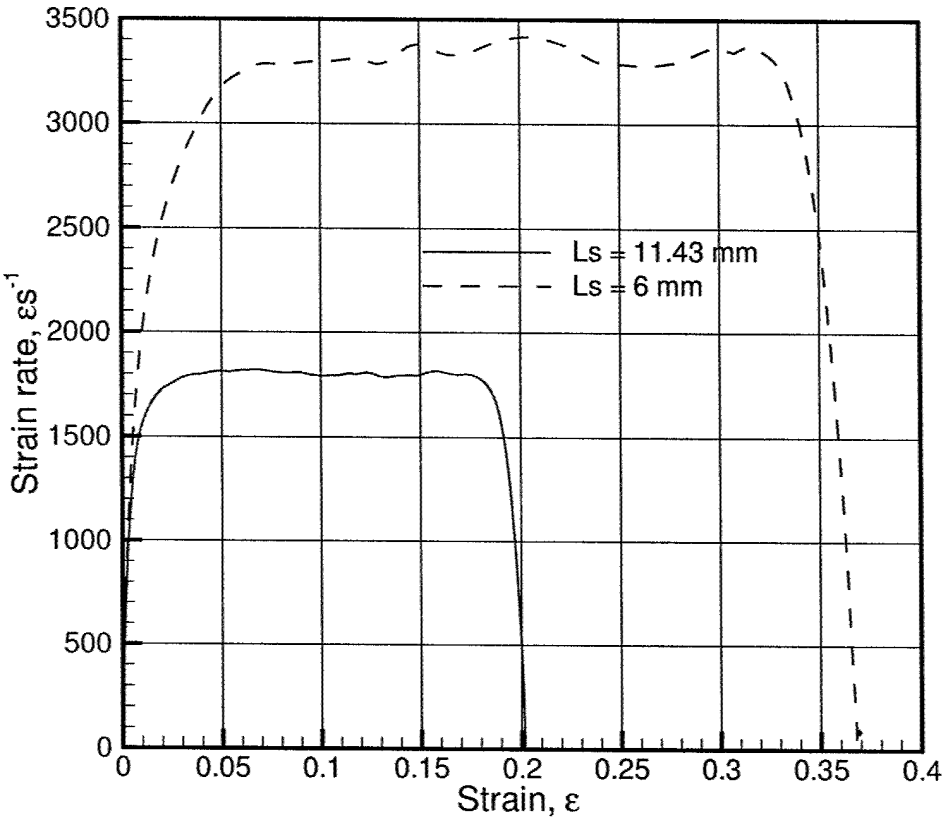

Figure 6.5: Variation of strain rate with the applied strain for aluminum6060 alloy specimens

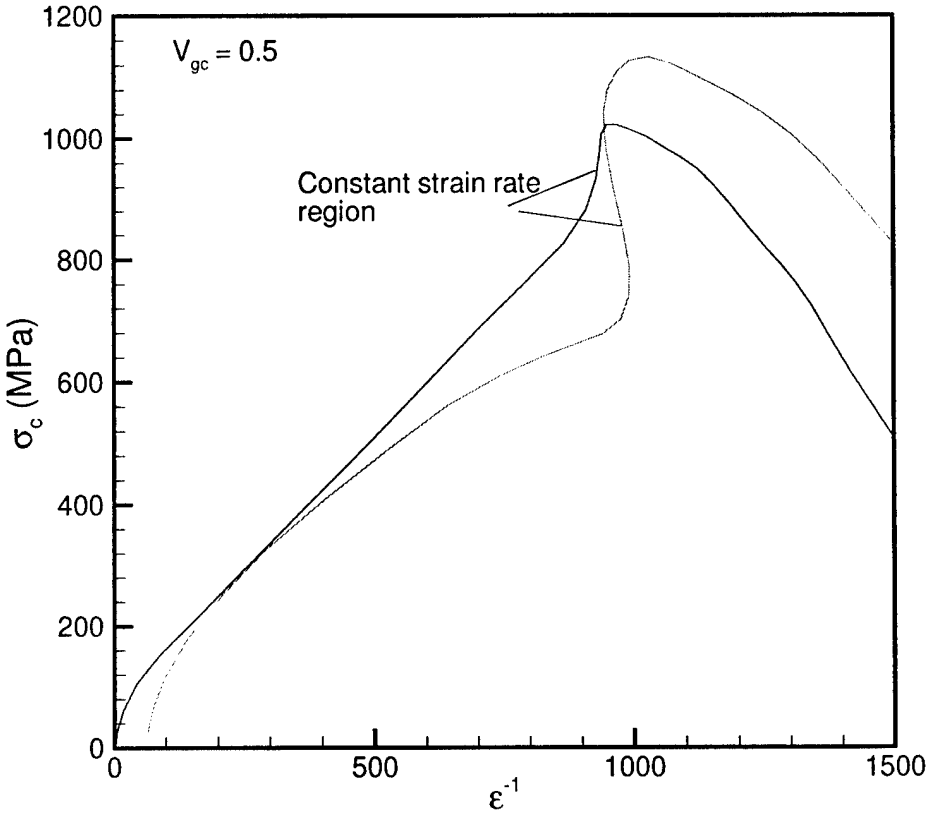

Figure 6.6: Variation of stress with strain rate for $V_{gc} = 0.5$

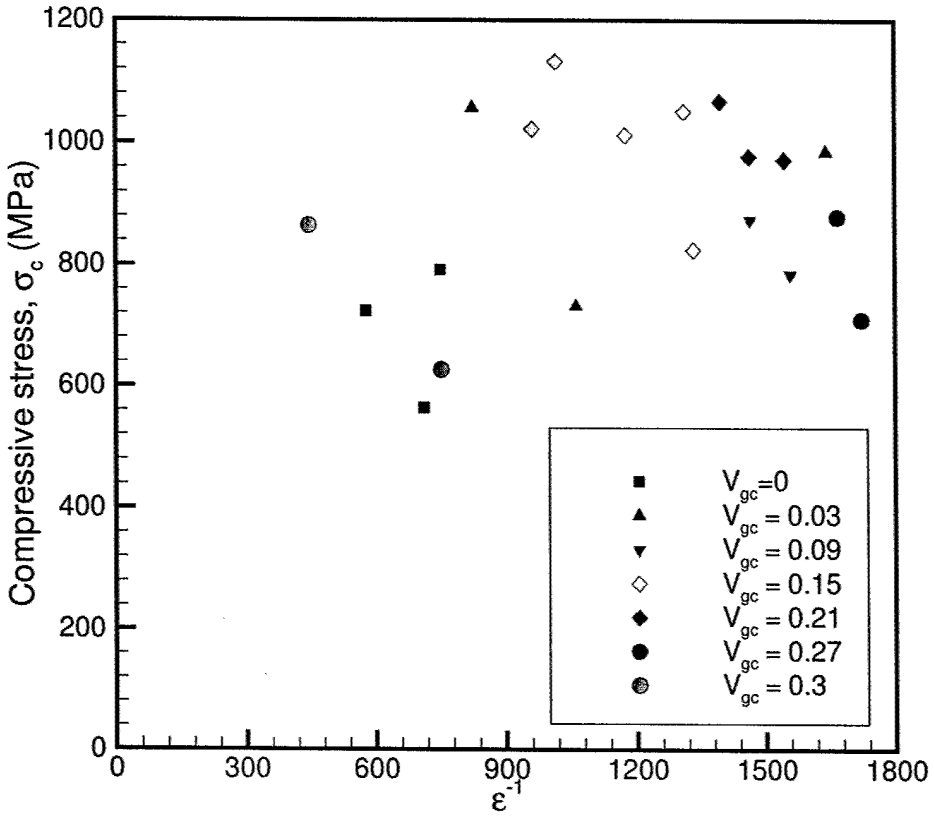

Figure 6.7: Variation of failure strength with strain rate, for different hybrid ratios

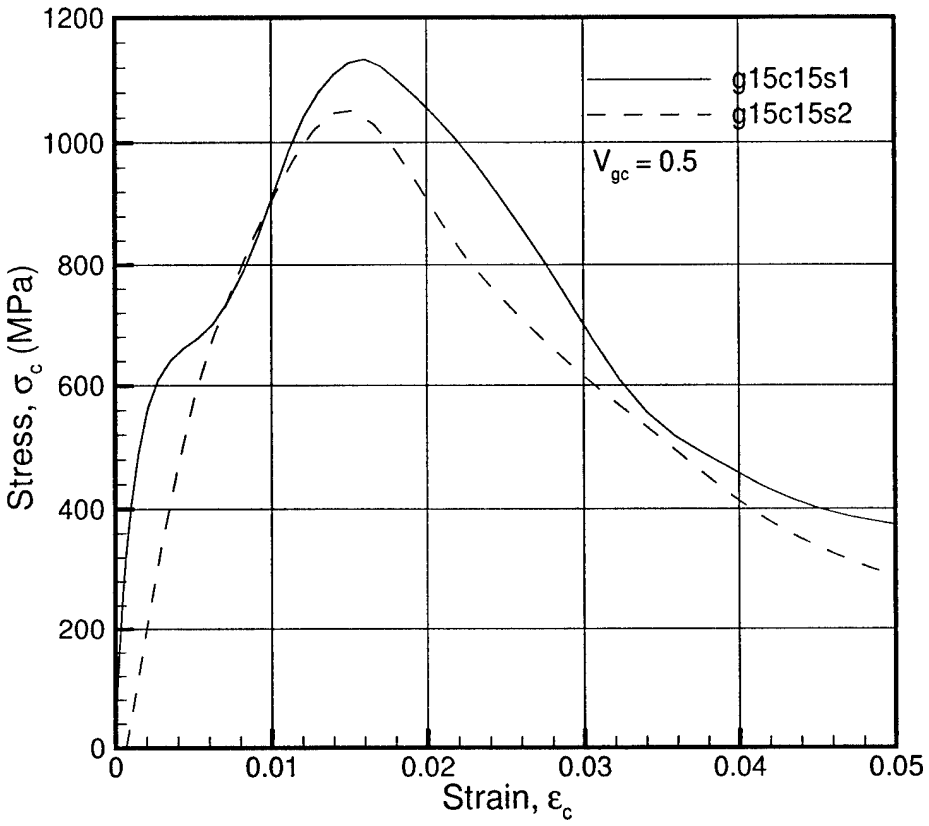

Figure 6.8: Typical stress strain curves for a composite of hybrid ratio, $V_{gc} = 0.5$

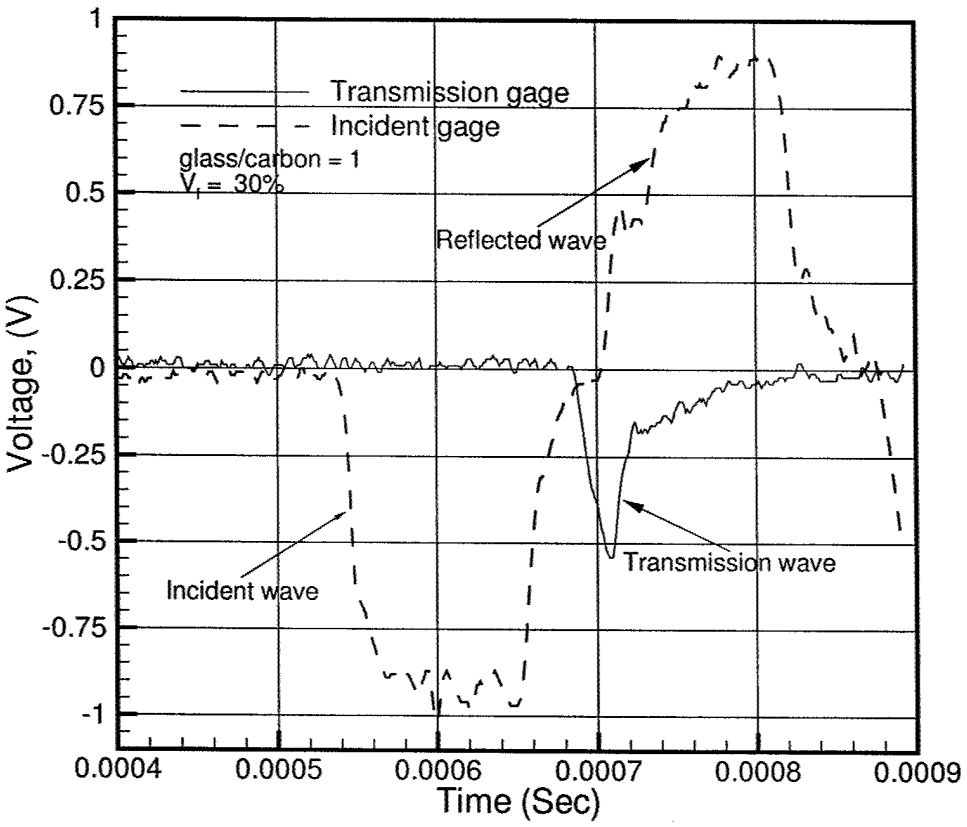

Figure 6.9: A typical strain gage signal obtained from the SHPB test on a hybrid composite of g/c ratio 1

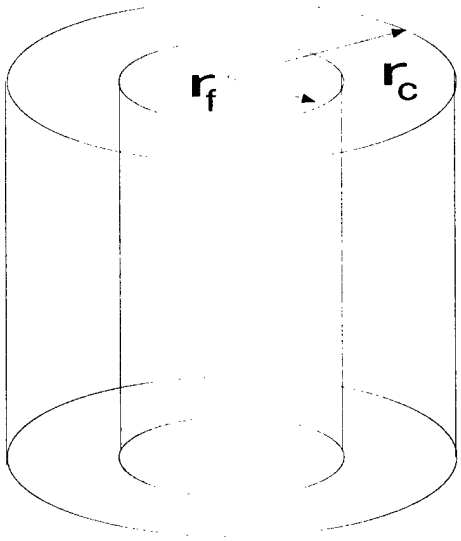

a) Conventional two cylinder concentric model RVE (inner fiber/outer radius)

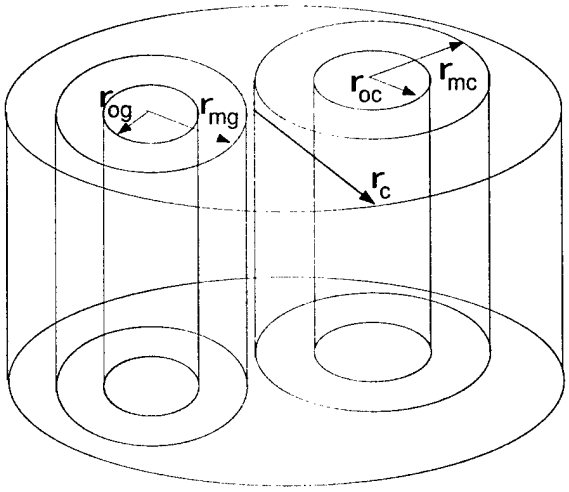

b) Modified to a Hybrid composite case with outer cylinder assumed to consist of individual concentric cylinders of fiber/matrix

Figure 6.10: Concentric cylinder models

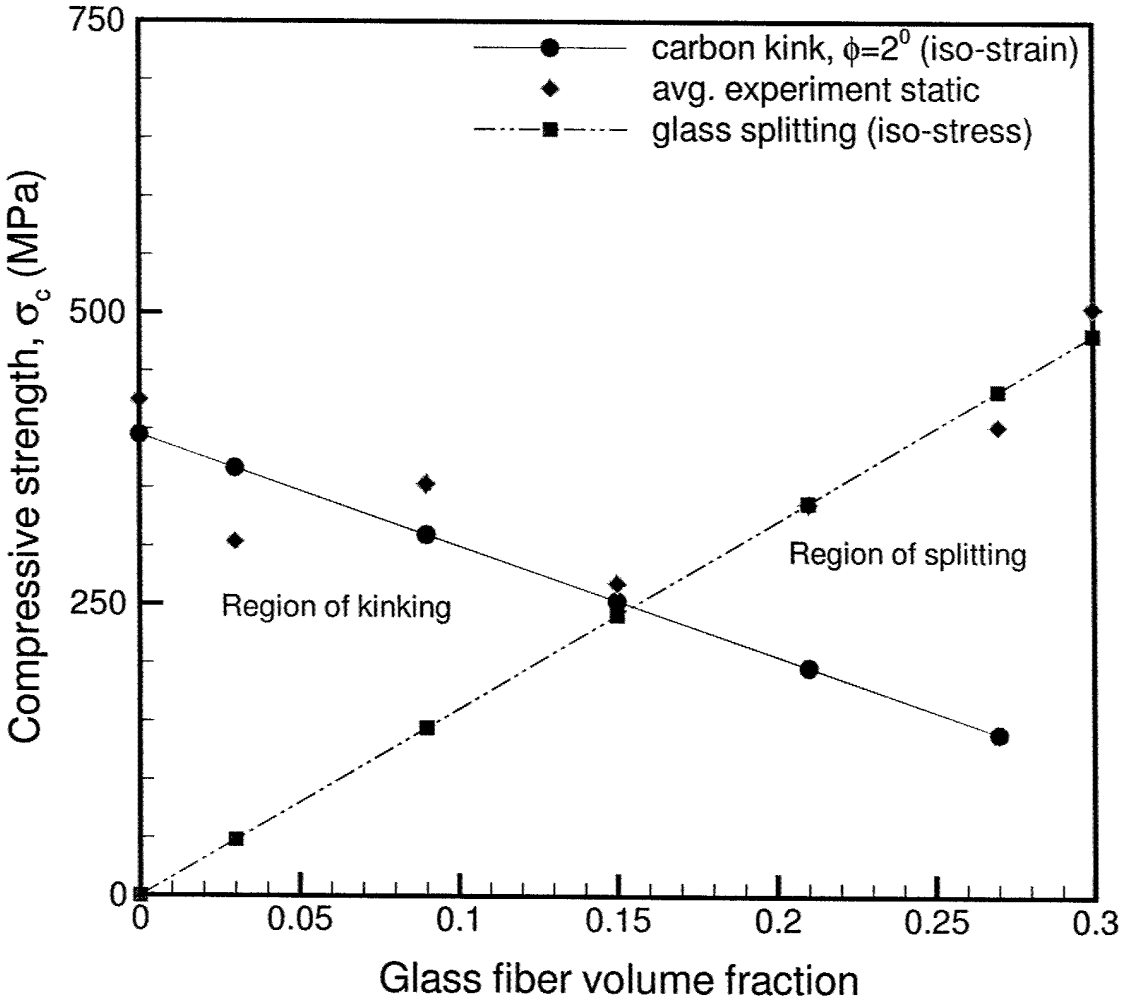

Figure 6.11: Failure model predictions for hybrid composites (static loading)

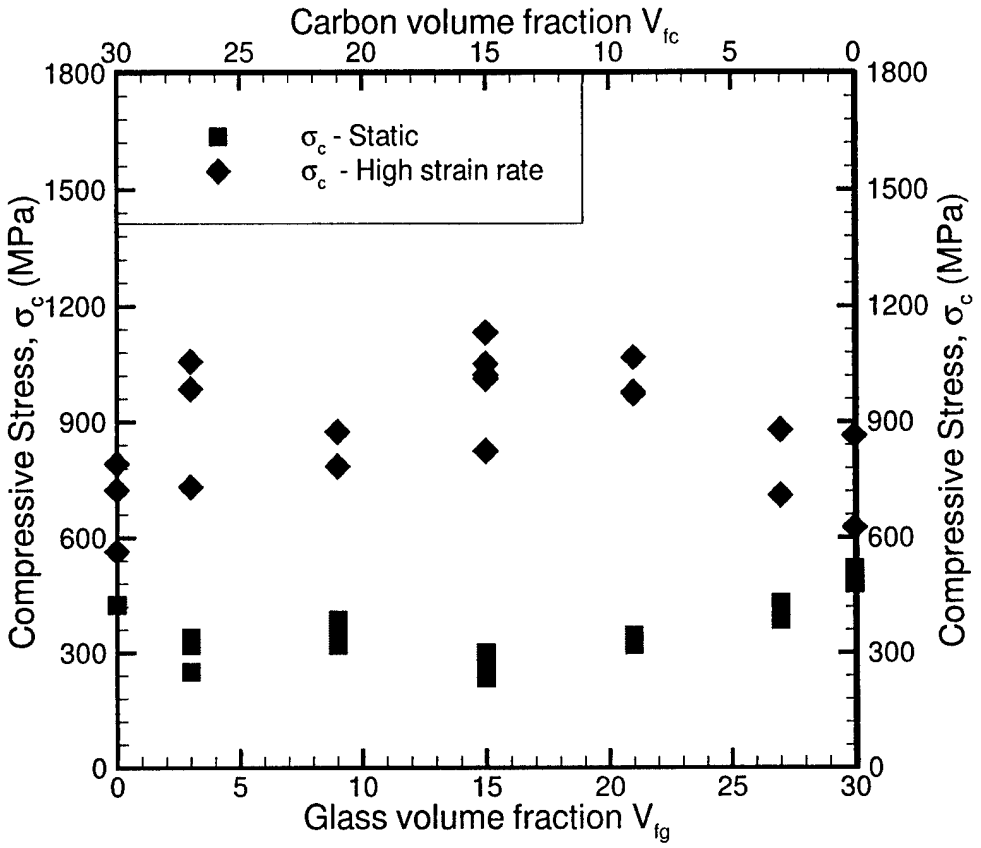

Figure 6.12: Variation of failure strength with strain rate, for different hybrid ratios

CHAPTER VII

A NON-DIMENSIONAL NUMBER TO CLASSIFY COMPOSITE COMPRESSIVE FAILURE

7.1 Introduction

Mechanism based compressive failure strength prediction models presented in the previous chapters, provide a better understanding into the failure behavior of composites. However, these models require that we know before hand the failure mechanism of the composite under the given loading and constituent material properties. Thus, a method to predict the failure mechanism is very useful not only from the view point of predicting the failure mechanism apriori but also in understanding the various factors effecting the failure mechanism of composites under compression. Initial work into understanding compressive strength behavior of fiber reinforced polymer matrix composites(FRPC) was based on an elastic micro-buckling analysis by Rosen (1965). Later, Argon (1972), and Budiansky (1983), and Budiansky and Fleck (1993), realized that misalignments in fiber reinforcement cause the development of local shear stresses which coupled with matrix inelasticity lead to buckling of fibers locally. The failure mode resulting from this mechanism is called kinking. Compared to kinking failure, composites with brittle matrices or fibers of large di-

ameters tend to fail by fracture along the fiber matrix interface. This mechanism, which is governed by transverse stresses and the fiber-matrix interface fracture energy is referred to as splitting. Lee (1998), and Lee and Waas (1999); Lee et al. (2000), developed splitting failure models for fiber reinforced polymer matrix composites under pure compression loading using the strain energy release rate concept. Independently, Oguni and Ravichandran (2000), obtained expressions for splitting compressive strength of fiber reinforced polymer matrix composites in the presence of lateral confining pressure.

Details of the kink band failure mode under pure compression and combined compression and shear have been extensively studied by Kyriakides et al. (1995); Vogler and Kyriakides (1999) and Hsu et al. (1999), who have used the AS4/PEEK material system at a fixed volume fraction in their experiments. The effect of fiber mechanical properties and fiber volume fraction has been studied by Yerramalli and Waas (2002b). Other practical considerations of kinking, such as the effect of adjacent plies(Drapier et al. (1999)) and the effect of stress gradients (Jelf and Fleck (1994b); Berbinau et al. (1999); Khamseh and Waas (1992); Ahn and Waas (1999)), have also received attention. Compared to the focus on kinking failure, relatively little has been done in studying splitting failure. Experiments conducted by Piggott (1981); Piggott and Harris (1980), Lee and Waas (1999), and Oguni and Ravichandran (2000), on glass and carbon fiber reinforced polymer matrix composites under pure compression provided insight into parameters affecting the splitting compressive strength of polymer matrix composites. Recent work by Yerramalli and Waas (2002b), have highlighted the effect of combined loading on failure mechanisms while work by Oguni et al. (2000), showed the effect of multiaxial compression on failure mode transition in E-glass/vinylester composites.

The present chapter examines the previous experimental data on compressive failure reported in the literature, with a focus on understanding the effect of three different parameters viz. fiber geometry (ie. diameter), matrix elastic properties and type of loading (uniaxial or axial-shear loading) on compressive failure. These experimental data are then examined in the light of a new non-dimensional number that is used to classify the failure mechanism. The results from an experimental study that examined glass fiber/vinylester composites reinforced with different fiber diameters are also reported. These experiments were conducted to generate results that reinforced the conlusions reached in the chapter.

7.2 Experimental Work

Circular cylindrical specimens of 6.8 mm diameter and 12.5 mm gage length were used to study the behavior of glass and carbon unidirectional FRPC under pure compression and combined compression-torsion loading. For understanding the effect of fiber diameter, glass composites were manufactured using glass fibers of two different diameters ($13.5\mu m$ and $24\mu m$). The material properties and the fiber volume fractions V_f, examined are given in Table 7.1 and Table 7.2. The E-glass fibers were obtained from Vetrotex Certainteed and the carbon fibers from Hexcel corporation. Vinylester (Dow Derakane 411-C50) resin was used as the matrix material for both type of reinforcing fibers. For the pure compression tests, a special test fixture made of hardened steel with four guide rods and a thick base was used. The four guide rods and the thick base was needed to prevent any macroscopic buckling of the specimens. A schematic of the test fixture is shown in Figure 7.1. In the case of compression-torsion loading, collet grips were used since they can provide resistance to slipping of the specimen in torsion and also in compression loading.

Further details of this experimental setup and the experimental investigation are provided in Yerramalli and Waas (2001).

	E_f(MPa)	G_f(MPa)	r_0(mm)
Glass fiber	72000	29508	0.012
Vinylester	3585	1318	

Table 7.1: Properties of glass fiber and vinylester resin

	E_f(MPa)	r_0(mm)
carbon fiber	276000	0.0025

Table 7.2: Properties of carbon fiber

7.3 Failure Mechanisms

Failure mechanisms that dominate the compressive behavior of polymer matrix composites are kinking and splitting. However, the forces triggering these failure mechanisms are entirely different. Kinking is a geometric instability induced failure mechanism whereas splitting is governed by the propensity to fracture, where crack growth is initiated from pre-existing flaws. Splitting in FRPC is dictated by the magnitude of the fiber/matrix interfacial fracture energy. Thus, a mechanism based approach to studying failure should ideally include the effect of each of the important parameters like fiber diameter, fiber misalignment, fiber and matrix properties and type of loading on the resulting analysis. The expression for splitting compressive stress as derived in Lee (1998), Lee and Waas (1999) and given in Yerramalli and Waas (2002b) is as follows

$$\sigma_{cr}^{sp} = \sqrt{\frac{8V_f^2\gamma_f}{r_o(1/\delta - \beta)}}, \tag{7.1}$$

where δ and β are constants dependent on the elastic properties of the matrix and the fiber. For a unidirectional composite with initial misalignment ϕ, the kinking compressive stress as given by the Argon-Budianksy-Fleck prediction is

$$\sigma_{cr}^{k} = \frac{\tau_y}{\phi + \gamma_y}, \tag{7.2}$$

where τ_y is the composite shear yield strength and γ_y is the corresponding shear strain. In the following sections, a discussion on the three important parameters affecting the compressive strength is presented.

Effect of fiber diameter

As can be seen from equation 7.1, the compressive splitting stress is inversely proportional to radius of fiber and directly proportional to the fracture energy γ_f. Thus, one would expect that, if the fracture energy γ_f, fiber volume fraction, V_f, and the elastic properties of fiber and matrix are kept the same, reducing the fiber diameter should result in an increase in compressive splitting strength. Based on the above model, it was decided to conduct pure compression tests on glass fiber composites reinforced with glass fibers of $13.5\mu m$ and $24\mu m$ diameter. For this purpose glass composite cylindrical rods having dimensions mentioned earlier, that have a range of fiber volume fractions (10 % $-$60 %) were manufactured. Under pure compression loading it was observed that instead of an increase in failure strength the failure mechanism was seen to change from splitting to kinking. Even at a low fiber volume fraction of 10%, where splitting was observed in case of glass composites reinforced with $24\mu m$ diameter specimens, the composite specimens reinforced with

fibers of $13.5\mu m$ diameter failed by kinking for all the fiber volume fractions tested. The various failure mechanims observed in glass composites of $24\mu m$ and $13.5\mu m$ specimens are shown in Figure 7.2 through Figure 7.4. A plot of the failure compressive strength as a function of fiber volume fraction, V_f, for both glass composites (reinforced with two different fiber diameters) is presented in Figure 7.5.

Effect of fiber properties

The effect of fiber properties was studied by changing the type of reinforcing fiber. With different types of fibers viz. glass and carbon it was found that the compressive stress as well as the failure mechanism changed. A comparison of the compressive failure stress as observed in the experiments by Lee and Waas (1999) for carbon and glass fiber reinforced composites is shown in Figure 7.6. The variation of compressive strength as a function of fiber volume fraction, V_f, shows that both glass and carbon fiber reinforced composites have a similar trend.

Effect of Loading

Research into the compressive strength behavior of fiber reinforced composites has shown that fiber misalignments cause a reduction in failure stress of the composites under pure compressive loading. In case of multiaxial loading (compression-compression or compression-torsion) the compressive failure strength and the failure mechanism are both affected. Oguni et al. (2000) looked into the failure mode transition due to confining pressure in E-glass/vinylester composites (with reinforcing fiber diameter of $24\mu m$). In the present work multiaxial loading in the context of compression-torsion loading of cylindrical specimens of glass/vinylester composites

(fiber diameters of $24\mu m$) will be presented. The failure mechanism observed in the glass composite specimens under compression-torsion loading is shown in Figures 7.4 through Figure 7.7. It was observed that at high compression to low rotation loading ratios, the specimens were failing in a combined splitting-kinking failure mode. Whereas at high rotation loading the failure was dominated by matrix cracking and splitting. At intermediate loading ratios, kinking was observed to be the failure mechanism. In case of carbon/vinylester composites, the failure mechanism was observed to be kinking throughout the range of loading ratios tested. An interesting observation is that the same type of glass composite changes it's failure mode when tested under different loading ratios. This observation was also made by Piggott (1981) who found that the failure mode changed when the composites were tested under pure compression with partially cured matrix. The reason for the change in failure mechanism can be attributed to the magnitude of the shear modulus of the matrix and hence the composite. As evident from equation (7.2), the kinking stress is dependent on the shear properties of the composite. Hence, when the torsional load is sufficiently high, beyond the magnitude required to cause shear yielding of the composite and the matrix, glass composites tend to fail by kinking instead of splitting. Similarly, when a resin is partially cured (as was the case with the experiments conducted by Piggott (1981)), it results in a matrix with a lower shear yield stress, inducing the glass fiber reinforced composites to fail by kinking instead of splitting, since, splitting would have required higher compressive stresses to cause failure.

7.4 Dimensional Analysis

The experimental and analytical work in understanding the compressive behavior of fiber reinforced composites, as outlined in the previous sections, have revealed

that the geometric (fiber diameter, V_f, misalignment angle, ϕ) parameters and the fiber and matrix mechanical and fracture properties (E_f, E_m, G_m and γ_f) are some of the most important parameters controlling the failure mechanisms in fiber reinforced composites. Based on this observation, it was decided to derive a suitable dimensionless number which can be used to classify fiber reinforced composites based on their failure mechanism and is given below.

The first step in determining the non-dimensional number is to write a general functional relationship including all the terms relevant to the physical phenonmenon, which in this case is the failure mechanism in the composite.

$$f(\gamma_f, 2r_0, G_c)$$

Here, we consider only the basic material and geometric parameters effecting the failure mechanism. Here, γ_f represents the fracture energy, G_c is the shear modulus of the composite which can be calculated from the matrix (G_m) and fiber (G_f) shear modulus values and the fiber volume fraction, V_f or determined experimentally. $2r_0$ is the fiber diameter which represents the geometric parameter. These parameters are then written down in terms of their fundamental dimensions (M, L, T). The units of γ_f are J/m^2 which is $M^1L^0T^{-2}$. Similarly, the variables r_0 and G_c can be expressed as $M^0L^1T^0$ and $M^1L^{-1}T^{-2}$ respectively. We can write the above dimensions and the variables in a dimensional matrix form (Table 7.3) as explained by Langhaar (1980).

The total number of variables n is 3 and the total number of fundamental units, $j = 3$. Thus, applying Buckingham's-Π theorem we get zero Π terms. But, we observe that row-1 and row-3 are linearly dependent and thus only one of the rows needs to be considered. Similarly, using the concept of rank of the dimensional matrix instead of using the number of fundamental units ($j = 3$), we get $j = 2$. Thus, the

	γ_f	G_c	r_0
M:	1	1	0
L:	0	-1	1
T:	-2	-2	0

Table 7.3: Dimensional matrix

total number of Π terms will be $n - j = 1$. We choose the variables G_c and r_0 as the repeating variables and the variable γ_f as the non-recurring variable. The expression for Π_1 is written as

$$\Pi_1 = \gamma_f G_c^a r_0^b$$

$$\{M^0 L^0 T^0\} = \{M^1 L^0 T^{-2}\} \{M^a L^{-a} T^{-2a}\} \{M^0 L^b T^0\} \tag{7.3}$$

By equating the exponents of like terms in equation (7.3) and considering only the first two equations as explained previously, we get

$$1 + a + 0 = 0$$

$$0 - a + b = 0 \tag{7.4}$$

From equation (7.4) we get $a = -1$ and $b = -1$. Thus, the functional relation can be written as

$$\Pi_1 = \frac{\gamma_f}{G_c r_0} = \eta_c \tag{7.5}$$

The right hand side of equation (7.5) represents a non-dimensional number which can be used to predict the failure mechanism in fiber composites and henceforth called

η_c. This number can be looked upon as a ratio of surface modulus ($\gamma_f/r_0 \rightarrow$ units of N/m^2) to composite shear modulus. It can be seen that this non-dimensional number incorporates V_f implicitly since the value of composite shear modulus G_c is dependent on the fiber volume fraction, V_f.

A progressive reduction in η_c indicates that the shear modulus is increasing relative to the fracture energy, γ_f. A higher shear modulus will make it less conducive to fail by kinking and causes the composite to split. Similarly, a larger η_c implies that it is less likely for the composite to split and hence fail by kinking. Thus, using η_c, an apriori prediction of the failure mechanism can be made for a given fiber and matrix combination. Figure 7.8 shows the variation of $log(1/\eta_c)$ against fiber volume fraction, V_f, plotted for a glass/vinylester composite with $r_0 = 6.75\mu m$ and $r_0 = 12\mu m$ and $\gamma_f = 0.1224KJ/m^2$. G_c, the shear modulus of the composite depends on matrix properties and fiber volume fraction. This universal band splits the plot in figure 7.8 into two regions. Points located in the shaded area correspond to composites that fail by splitting. Points located in the unshaded area correspond to kinking failure. Points located in the band correspond to transition between kinking and splitting. Thus, for any given composite, once η is calculated, figure 7.8 can be used to a priori establish what compressive failure mechanism is operative and thus an appropriate mechanism based compressive strength model can be used to predict the compressive failure strength. From the experimental observations, it is known that composites reinforced with glass fibers of $13.5\mu m$ diameter failed by kinking throughout the range of V_f tested. In contrast, composites reinforced with glass fibers of $24\mu m$ diameter failed by splitting at lower V_f and splitting/kinking at higher V_f. Thus, the curve for $13.5\mu m$ glass specimens can be used as a limiting curve for kinking and the curve for $24\mu m$ glass composites can be used as a limiting curve for splitting. The zone in

between these two bounds is a transition zone. If for any material the value of η_c is lying between these two bounds, then based on the V_f value, the failure mechanism could be kinking, splitting or a combination of both.

Calculating the value of η_c for carbon fiber composites, we see that the curve of $log(1/\eta_c)$ lies in the bottom half below the $13.5\mu m$ glass curve. This is the kinking region and is consistent with the experimental observation that carbon composites fail by kinking for all the fiber volume fractions tested. Further, for comparison, the value of η_c has been calculated for a ceramic matrix composite and it is found that the curve of $log(1/\eta_c)$ lies in the top part of the plot. This indicates that the ceramic matrix composite fails by splitting as observed in the experiments by Budiansky et al. (1986).

7.5 Results and Discussion

As seen in Figure 7.9, η_c has been calculated as a function of V_f. The values of γ_f chosen for glass fiber is $0.1224 KJ/m^2$ and for carbon fibers it was taken as $0.06 KJ/m^2$. In case of Silicon carbide fibers the value of $\gamma_f = 0.022 KJ/m^2$ was taken from the paper by Budiansky et al. (1986). Using these values, it has been shown in the previous section that the curves of carbon/vinylester and Sic/LiAlSi lie in two extreme corners of the plot, while, the curves for glass/vinylester composites lie in the center of the plot. It can therefore be inferred that the glass composites tested lie in a transition zone where the failure mechanism changes from kinking to splitting or vice-versa. This shows the importance of η_c. Based on the magnitude of η_c, a suitable fiber-matrix combination could be chosen so as to have a particular failure mechanism. Based on this number, one can explain the reason why a glass composite of smaller diameter fails by kinking while a glass composite reinforced with larger

diameter fibers ($24\mu m$) fails by splitting. With the reduction in the fiber diameter the value of surface modulus ($\gamma_f/2r_0$) increases for the same material system. This makes the splitting failure stress larger causing it to fail by kinking. Similarly, when the glass composites of $24\mu m$ diameter fibers are subjected to compression-torsion loading they tend to have a failure mode transition from splitting to kinking. This can be explained by looking at the value of η_c as a function of applied shear stress. Once the value of remotely applied shear stress exceeds the value of shear yield stress, τ_y then the instantaneous shear modulus of the composite starts to reduce and leads to a higher value of η_c. A higher value of η_c indicates that the shear modulus is very low which makes it easier for the composite to fail by local buckling of fibers leading to kinking. The value of η_c for experimental data obtained from Piggott (1981) and Yerramalli and Waas (2002b) are presented in Figure 7.10. The data obtained from Piggott (1981) was for a $V_f = 30\%$ glass composite with a partially cured matrix. The test data from Yerramalli and Waas (2002b) was obtained from testing glass composites ($V_f = 50\%$) under combined compression-torsion loading. As can be seen, at a given fiber volume fraction, as the shear modulus decreased, $log(1/\eta_c)$ decreases. Once this number approaches the threshold for kinking, which is defined by the curve corresponding to the $13.5\mu m$ glass fiber composites, the specimens start to fail by kinking. This corroborates with the experimental observations made by Piggott (1981) and Yerramalli and Waas (2002b). In figure 7.11, a band of values that account for parameter uncertainties is presented. A sensitivity analysis of η is in order to explain, how the band of values were computed. Since, $\eta = \gamma_f/G_c r_0^2$ it follows that

$$d\eta = \frac{d\gamma_f}{G_c r_0} - \frac{-\gamma_f dG_c}{G_c^2 r_0} - \frac{-\gamma_f dr_0}{G_c r_0^2} \tag{7.6}$$

Thus, for fixed G_c and r_0, $d\eta = d\gamma_f/G_c r_0$. Consequently, a 10% uncertainity in γ_f, translates to a 10% uncertainity in η. Similarly, the uncertainities in G_c and r_0 can be used to calculate the uncertainities in η. Therefore, instead of providing a single line in the η vs V_f space, we have shown a band of values that relate η to V_f.

The implications of η_c for the design of elevated compressive strength composites is also now evident. As shown through the experimental results, carbon composites failed by kinking throughout the V_f examined. Yet, as indicated by equation (7.1), the splitting compressive strength of carbon composites is several times larger than the kinking strength (equation (7.2)). Thus it is desirable to *design* carbon composites such that they will fail by splitting. This implies a need to reduce η_c for carbon composites. A reduction is possible by either increasing the value of G_c or reducing the value of surface modulus γ_f/r_0.

7.6 Conclusions

A new non-dimensional number η_c has been derived to classify the compression failure mechanism of continuous fiber reinforced composites. This number was used to explain some of the causes behind the various failure mechanisms observed during the compression testing of polymer matrix composites. Results from an experimental program into studying the effect of fiber diameter, fiber properties and the type of loading were used to verify the prediction made by using η_c. It can be concluded from this study that the fiber diameter, the matrix (and hence the composite) shear response and the fiber-matrix interface fracture energy all play an important role in influencing the failure mechanism and hence the compressive strength. For the same material system (fiber-matrix) a change in failure mode can be obtained for example by changing the fiber diameter or the interface fracture energy. In a similar vein, the

matrix shear properties are also significant in controlling the failure mechanism.

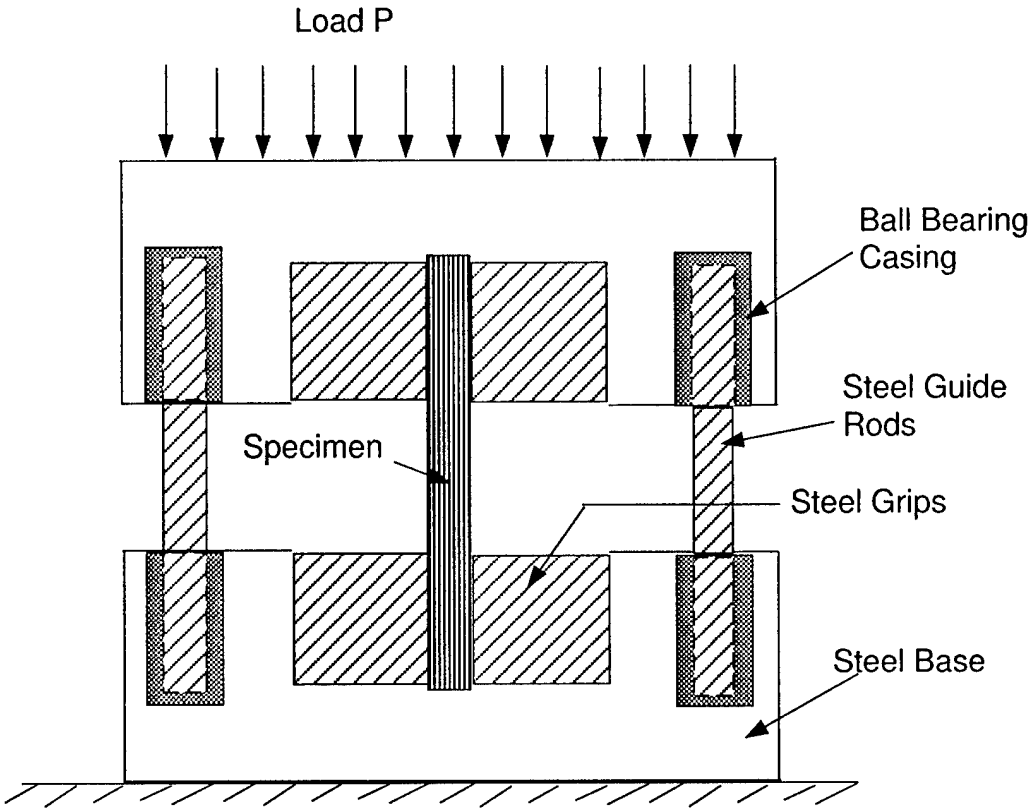

Figure 7.1: A cross sectional view of pure compression grips

Figure 7.2: Kink band in glass composites of fiber diameter $13.5\mu m$ and $V_f = 10\%$

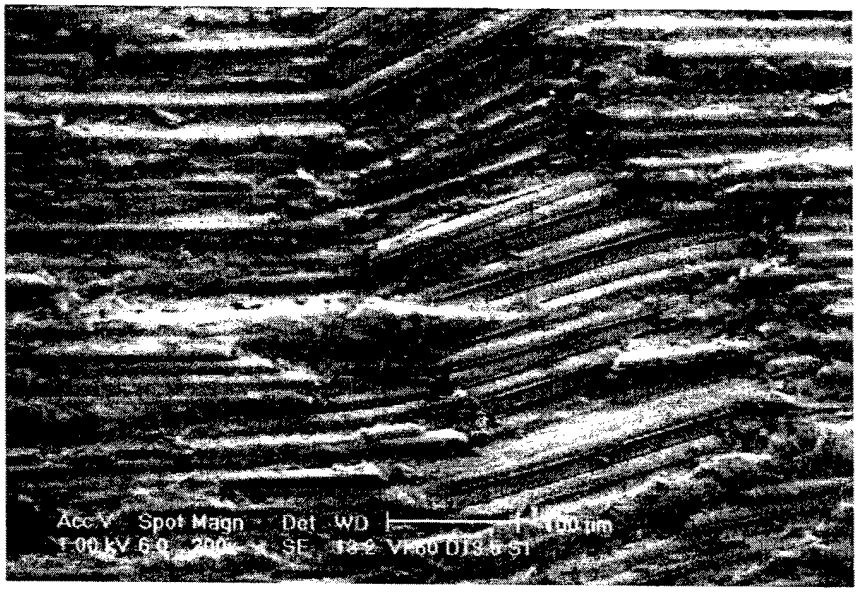

Figure 7.3: Kink bands in glass composites of fiber diameter $13.5\mu m$ and $V_f = 60\%$

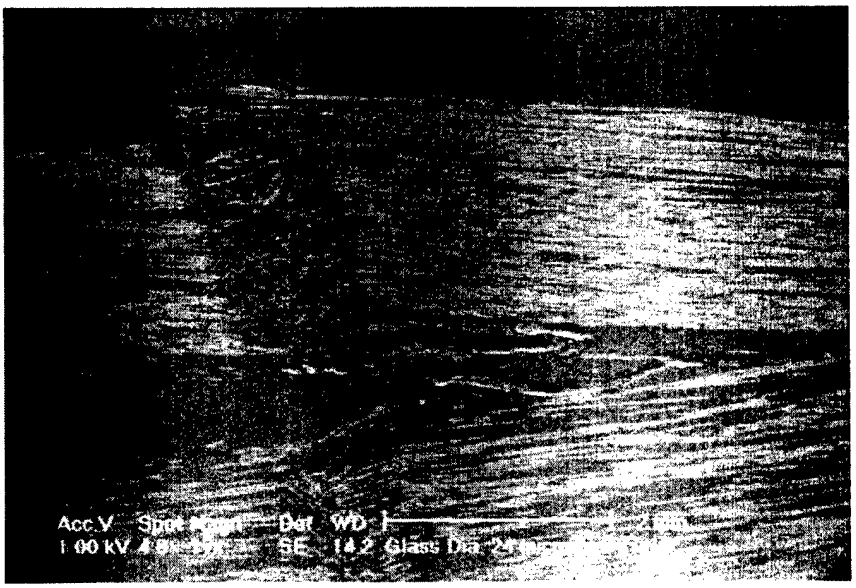

Figure 7.4: Combined splitting and kinking in glass composites of fiber diameter $24\mu m$ and $V_f = 50\%$

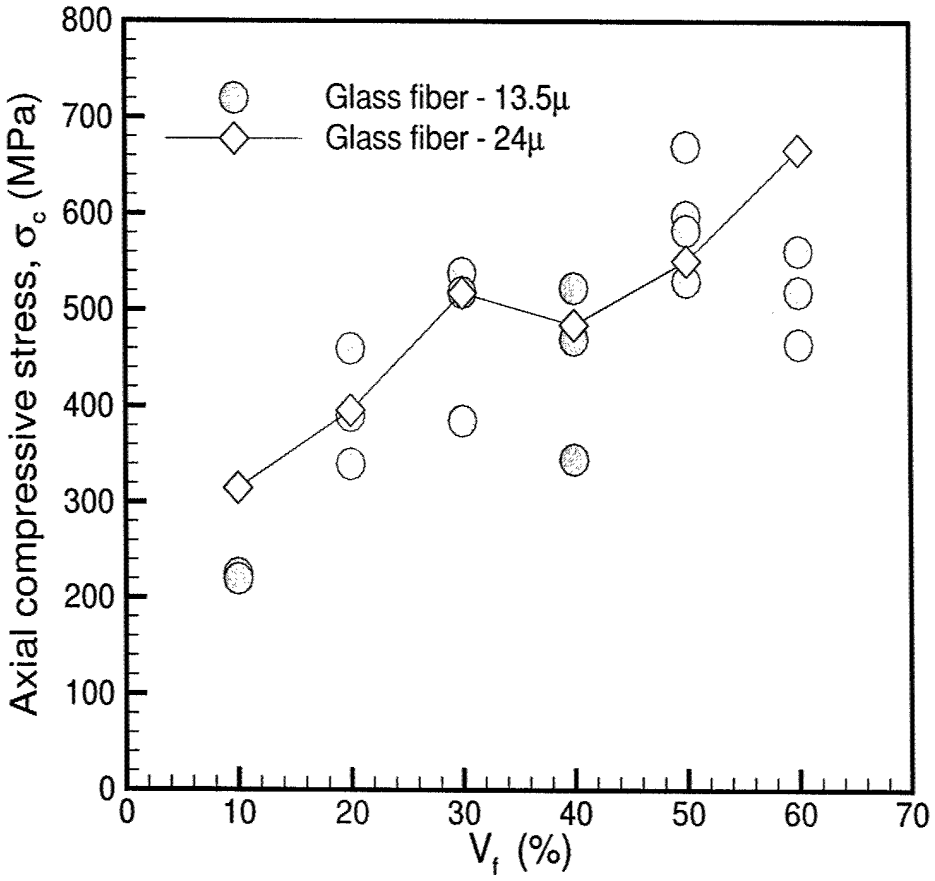

Figure 7.5: Comparison of compressive strengths between glass $24\mu m$ and $13.5\mu m$ diameter specimens

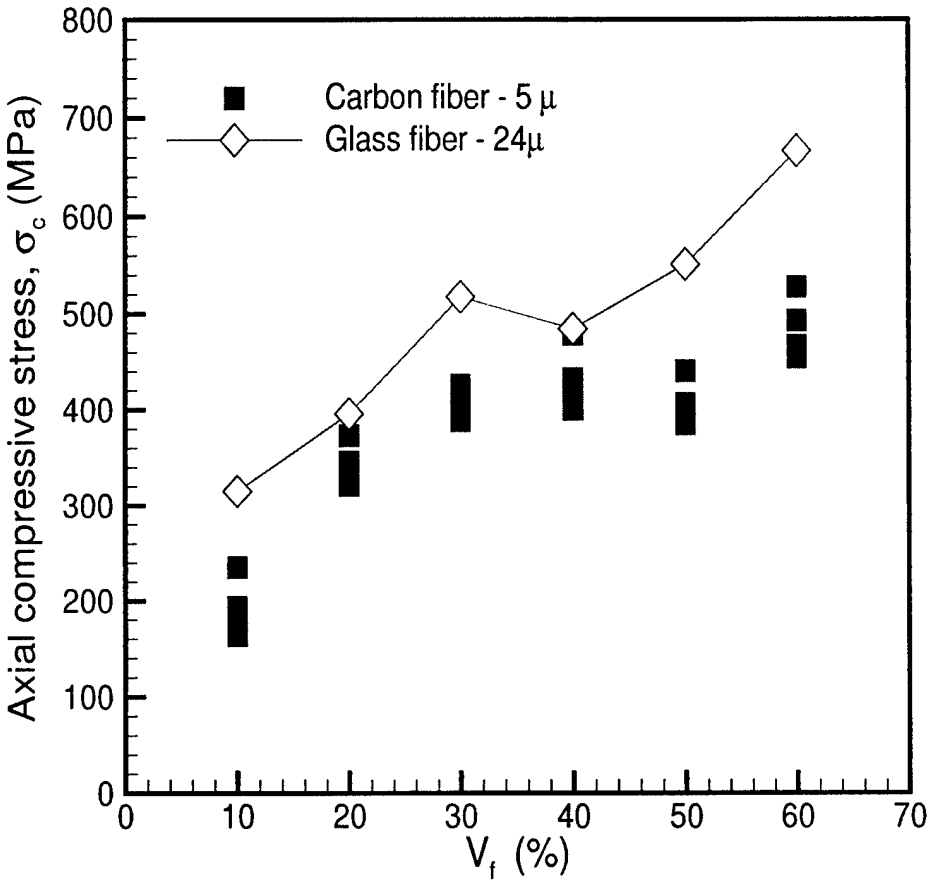

Figure 7.6: Comparison of compressive stress of glass and carbon composites as function of V_f

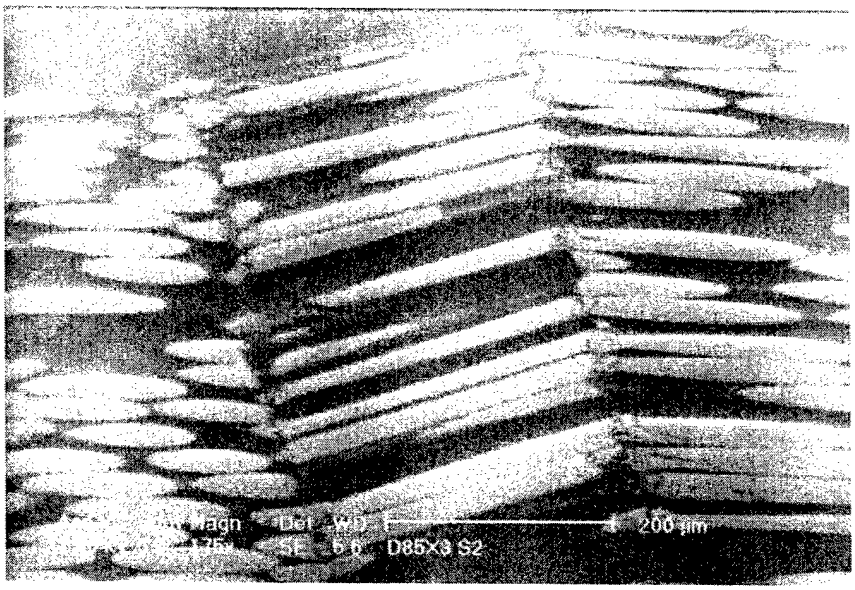

Figure 7.7: Kink band in glass composite reinforced with $24\mu m$ fiber diameter at $\Delta/R\theta = 0.52$

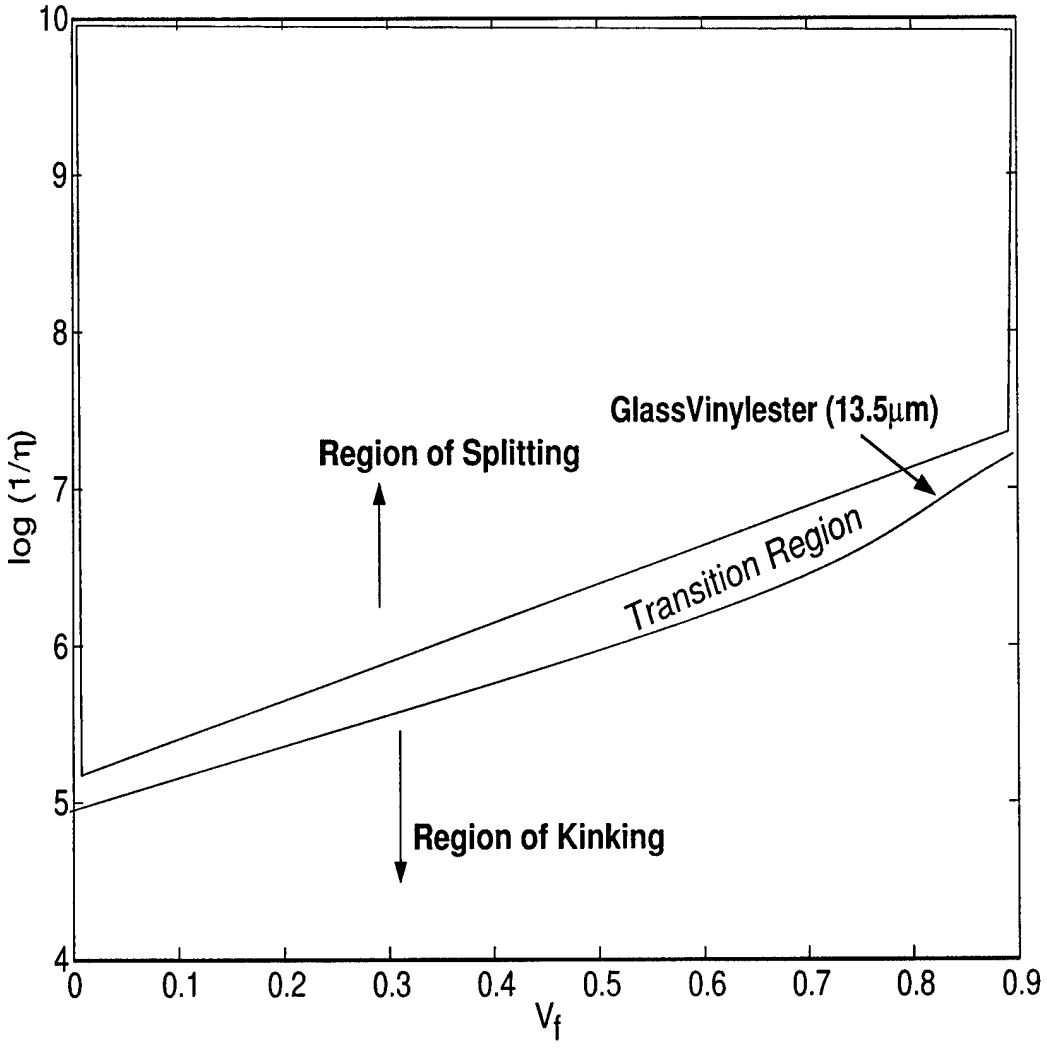

Figure 7.8: Variation of the non-dimensional number, η with V_f

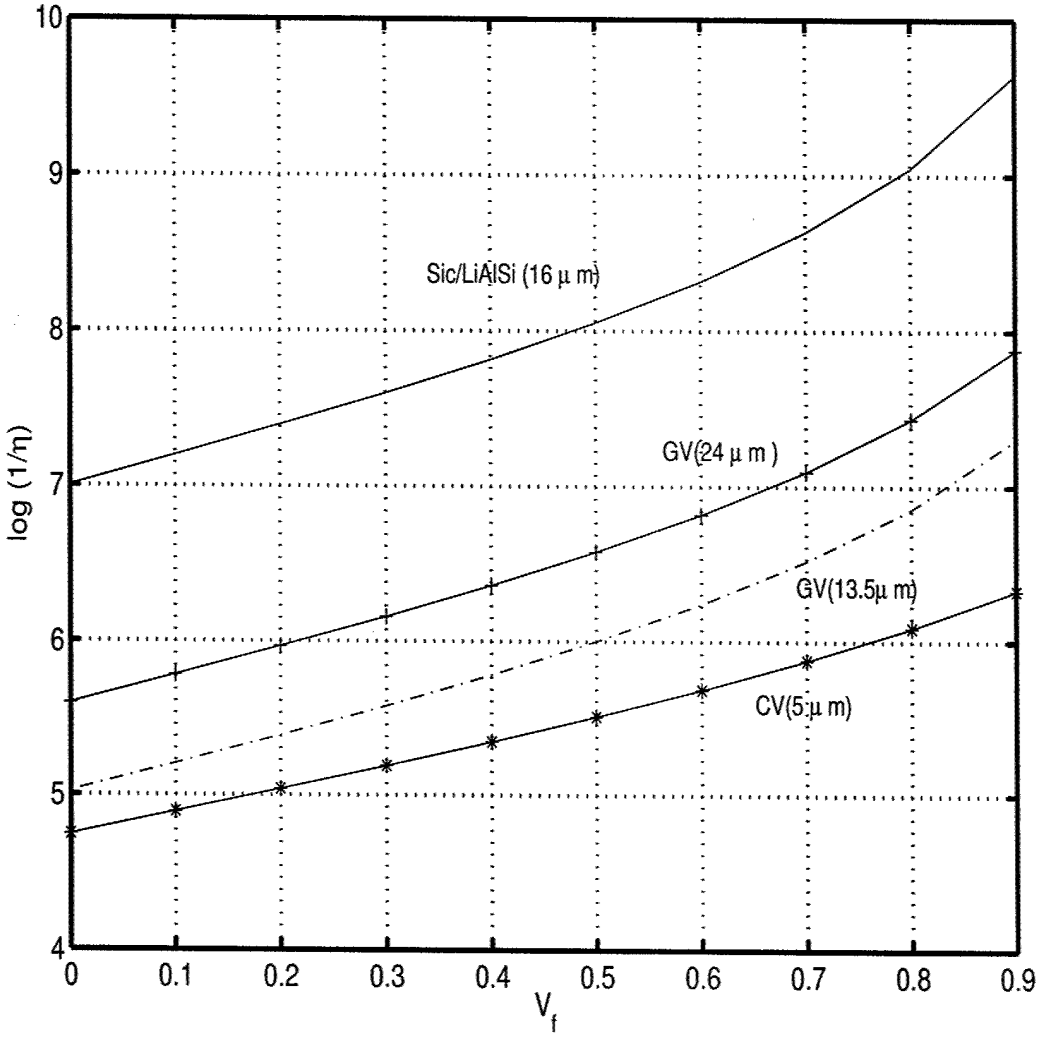

Figure 7.9: Variation of the non-dimensional number with V_f

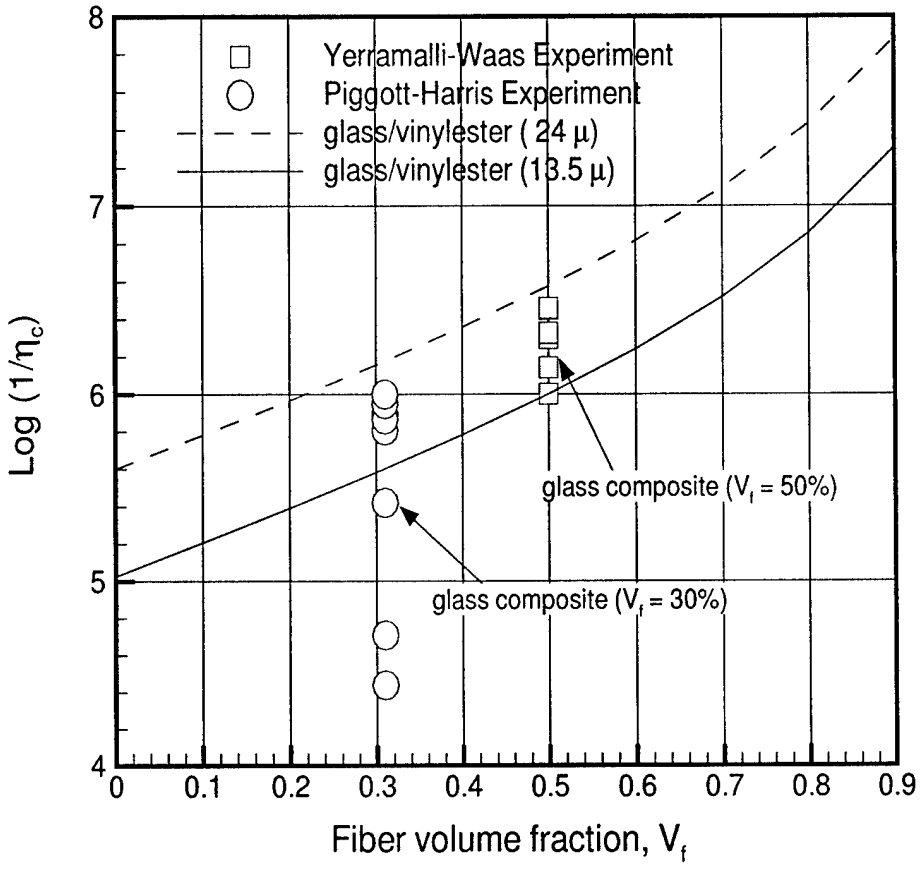

Figure 7.10: Variation of non-dimensional number for glass composites as a function of shear modulus at fixed V_f

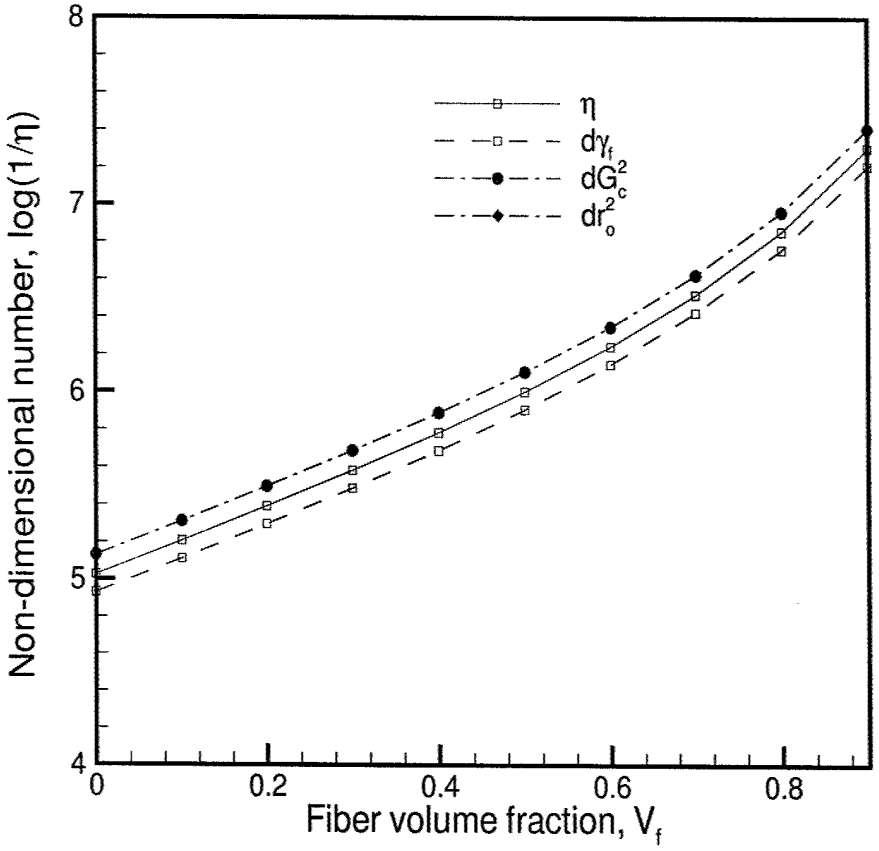

Figure 7.11: Variation of the non-dimensional number, η due to uncertainities (10%) associated with the values of γ_f, G_c and r_0 with V_f

CHAPTER VIII

CONCLUSIONS AND SUGGESTIONS FOR FUTURE WORK

8.1 Conclusions

This thesis was focussed on examining the failure behavior of unidirectional fiber reinforced composites under pure compression and combined compression/torsion loading. A combined experimental and analytical (both analysis and numerics) approach was adopted in order to fill the lacunae in the existing knowledge base on composite compressive behavior. Two different systems of unidirectional FRPC were examined to obtain a clearer understanding and to develop ideas applicable over a broad range of parameters that influence compressive response, instead of being limited to a particular set of material systems.

The important conclusions that can be drawn from the current work are as follows; composite compressive failure strength and failure mechanism are strongly influenced by the fiber/matrix system being used. As such, it is not possible to discuss the compressive strength in isolation without recourse to the particular failure mechanism. This conclusion has been verified by the use of a non-dimensional number that classifies the FRPC according to the failure mechanism prevalent in that particular fiber/matrix system. The role of various material and geometric param-

eters influencing the composite splitting compressive strength has been highlighted by the development of a fracture mechanics based failure strength model. The effect of fiber radius on the predicted compressive strength has been studied experimentally and modeled numerically via the finite element method. It was observed that the reduction in fiber radius led to a change in failure mechanism without a significant increase in the observed compressive strength as mentioned in chapter VII. The analytical splitting model of Lee and Waas (1999), was extended to the case of non-steady crack propagation by using a modified shear lag theory. A closed form expression for compliance change as a function of crack length was obtained. The results obtained from this expression were compared to those obtained from finite element analysis from Lee and Waas (1999).

The combined compression-torsion loading of glass fiber(dia=24μm) composites indicated that the failure envelope for these composites was different from that of carbon fiber composites. The glass composites tested showed an initial insensitivity to the applied remote torsional loading and only after the remotely applied shear stresses exceeded a critical value did the compressive strength drop rapidly. The glass composites also exhibited a change in failure mechanism as the remotely applied torque was increased in magnitude. This change in failure mechanism was captured through the non-dimensional number presented in chapter VII.

In case of combined compression-torsion loading, the conventional Budiansky-Fleck expression for kinking stress was extended to the case of a solid cylindrical specimen. This expression, however, does not have a explicit dependance on geometric parameters like fiber radius or V_f. Thus, to understand the role of fiber radius on the predicted kinking stress, a 3D FE analysis was conducted. The results from the FE analysis indicate that the fiber radius is inversely proportional to the kinking

compressive strength for a given fiber/matrix system. It was also observed from the FE analysis that for small fiber diameter composites the fiber strain could exceed the maximum fiber strain before the limit load due to the kinking instability is reached. This, indicates that the kinking process could initiate from a fiber break, as has been reported in the literature by other researchers.

Hybrid composites were studied under both static and dynamic loading to understand the effect of fiber type on the composite compressive failure strength and failure mechanism. It was observed that the compressive strength has a non-monotonic relation with the hybrid ratio, with the strength first decreasing from either end (ie. pure glass or pure carbon) and then increasing. However, the elastic modulus was found to increase monotonically with hybrid ratio (as we start adding carbon fibers to pure glass). It was observed that the experimental results obtained from the glass dominated hybrid composites could be better explained by a iso-stress model, while the experimental results obtained from the carbon dominated composites was better explained by a iso-strain model. The high strain rate tests showed a definite increase in the compressive strength. However, a definite relation between the strength and strain rate could not be drawn at this stage due to the scatter in the data.

8.2 Suggestions for Future Work

Some of the work that can be done to extend the findings in this thesis on failure mechanics in fiber composites, not just for compressive failure but failure in general, are to study the role of the fiber diameter on failure mechanism. The effect of fiber diameter on compressive failure has been studied in this work, and preliminary work has been done to understand the role of fiber diameter on the shear response of composites (not presented in this thesis). However, a comprehensive study into the

role of fiber diameter on all the mechanical properties and throughout the entire loading range ie. linear and non-linear, should be undertaken. This would clearly indicate if a so-called size effect exists in fiber reinforced polymer matrix composites as has been indicated by researchers in metal-matrix composites (see Xue et al. (2002)). Also, thermal effects imparted on account of residual stresses can play an important role in the case of FRPC due to the large mismatch in the thermal coefficient. This is not the case in metal matrix composites. Another, important factor is the interphase, as has been pointed out in chapter II. The interphase could play a key role in the failure behavior of FRPC. Work has been done in each of these areas independently, however a comprehensive work covering all the above aspects with the intention of understanding the failure behavior of composites has not been done.

The finite element modeling work in this thesis has shown the necessity to model the composite in 3D. However, the use of 3D elements to model an elastic fiber is computationally expensive. An approach to combine structural elements with elasticity elements could lead to a cost effective solution. Work into developing such elements, which could then be implemented in a commercial package like ABAQUS, would be useful for modeling intricate composite micro-structure.

High strain rate behavior of fiber composites is another area in which there is very little data available. The pure compressive properties of glass and carbon uni-directional FRP are available and that of hybrid composites has been presented in this thesis. However, high strain rate properties under tensile and torsional loading are not available. Similarly, there is no experimental data on the high strain rate behavior of FRPC under combined compression-torsion loading. In fact, the use of SHPB under a combined compression-torsion loading is itself not well established.

Thus, high strain rate multi-axial behavior of FRPC could be a potentially interesting area to pursue. The increasing use of FRPC in military applications would increase the demand for such an investigation.

APPENDICES

APPENDIX A

Manufacturing of Composite Specimens for Compression Testing

The method of preparation of unidirectional composites for compression testing is described below.The composite specimens are cylindrical in shape and are made of vinyl ester resin and E- glass or carbon fibers.The setup consists of a pressurizing unit and a reservoir of resin. The composite specimens are manufactured by pressurizing resin into glass tubes filled with fibers. Air pressure is used to force the resin in the reservoir into the glass tube. Air pressure is varied by a control unit which regulates the input air pressure. The resin is cylced through the glass tubes filled with fibers once or twice until the fibers are properly wetted. This is to avoid the possibility of formation of air bubbles in the specimen. Once the glass tubes are filled with resin they are placed in a oven and heated upto 80^0C for two hours. Afterwards they are allowed to cool and then taken out. The specimens are cut into appropriate lengths and then subjected to compression testing.

A.1 Materials and Chemicals

1. Matrix - Vinly-ester resin (Dow-Derakane 411- C50)

2. Fibers - E-glass 24μm dia.(Certainteed R099-625)

3. Fibers - Carbon $5\mu m$ dia.(Hercules 1M 7-12K)

4. Initiator - Benzoyl peroxide and cleaner - Acetone

5. Glass tubes internal diameter - 6.8 mm and length of 300 mm.

A.2 Procedure

A step-by-step description of the various steps to manufacture the specimens is given below.

1. Matrix preparation; Take about $300gm$ of vinylester resin into a container. Add initiator to the extent of 1% by weight of the resin. Mix the resin and initiator till all the particles of the initiator are dissolved in the resin. Pour the resin into the reservoirs of the setup.

2. Fiber preparation; Clean the glass tubes to be used for specimen making with high pressure air. Based upon the volume fiber fraction required count the number of fibers and pull them into the glass tube.

3. Filling the glass tube with resin; Once the fibers are inserted into the glass tube attach them to the tubes connected to the resin reservoir by metal clips. Open the valves of the reservoir and then apply air pressure to force the resin into the tube. Recycle the resin through the glass tube once or twice and then close the valve of the reservoir to cut off the supply of resin and then seal the bottom end of the tube with a cork. When manufacturing composites of low volume fiber fraction make the resin flow from bottom to top so that air bubbles trapped inside can be more easily removed.

4. Curing; Remove the glass tube from the setup Place the glass tube into the

oven and set the temperature of oven to 800 C. Allow the specimen to cure for two hours and then switch off the oven. Take the specimen out of the oven once it is cooled and then cut it to appropriate length for compression testing.

Calculation of the number of fibers required for a given volume fiber fraction

1. E-glass fibers

   - Fiber diameter = 24.1 μm = 0.024 mm
   - Radius r_f = 0.01205 mm
   - Area of fibers, $A_f = \pi r_f^2 = 0.00015625\ \pi\ mm^2$
   - One strand of fiber contains = 3580 fibers = $0.575\ \pi\ mm^2$
   - Inner dia. of glass tube = 6.8 mm
   - Inner radiusrg = 3.175 mm
   - Area of glass tube, $A_g = 10.080625\ \pi\ mm^2$

If we take the glass fibers to be of the same length as that of the glass tube then 10% of fiber volume fraction = 0.1, $A_g = 1.0080625\pi\ mm^2$; number of strands = 1.0080625/0.575

For V_f = 10% number of glass fiber strands required = 2

APPENDIX B

Axial Compliance of a Misaligned Fiber

Consider the response of an axially loaded misaligned fiber of uniform cross sectional area, A_f, length $2l$ and elastic modulus E_f within the context of geometrically non-linear Euler-Bernoulii beam theory in the X-Z plane. Let a set of cartesian coordinate axes be chosen such that the X axis is pointing along the center line of the fiber and Z axis is pointing in a direction transverse to the X axis. Let the origin of the axes be such that $x = 0$ is at the center and $x = \pm l$ signify the abcissae of the crack tips. Let the initial misalignment, total deflection in the z-direction measured from the fiber centerline and the additional deflection be denoted by $w_0(x), w(x)$ and $w_1(x)$, respectively. Then, the deflection, $w(x) = w_0(x) + w_1(x)$, is governed by,

$$\frac{d^4w}{dx^4} - \frac{d^4w_0}{dx^4} + \lambda^2 \frac{d^2w}{dx^2} = 0$$

where, $\lambda^2 = \frac{P_f}{E_f I_f}$. Assuming an initial misalignment distribution of $w_0(x) = A_0(1+cos\frac{\pi x}{l})$, solving the above equation for clamped boundary conditions at $x = \pm l$, and, adopting the definition of axial strain $\epsilon_x = \frac{du}{dx} + \frac{1}{2}(\frac{dw}{dx})^2 - \frac{1}{2}(\frac{dw_0}{dx})^2$, in conjunction with the one dimensional stress-strain relation $\sigma_x = E_f \epsilon_x$, we obtain the relation,

$$(EA)_{eff} = \frac{E_f A_f}{1 + \frac{A_0^2 A_f}{2I_f}},$$

APPENDIX C

Interaction between the Axial stress and Torsional stress

In this section the effect of axial stress on the non-linear behavior of the matrix and composite under shear stress is studied. For this purpose we use a $J2$ deformation theory of plasticity to model the matrix and the composite material. The general method is described as follows. We first model the material as a non-linear material and use a Ramberg-Osgood fit of the form $\gamma = (\tau/G) + (\tau/A)^n$ to describe the behavior of the material in shear. Then using the definition of equivalent stress and equivalent strain, we can get the stress-strain curve of the material under uniaxial load. The uniaxial stress-strain relation is obtained in the form $\epsilon = (\sigma/\epsilon) + (\sigma/B)^n$ where $B = A\ 3^(1/2 + 1/2n)$. Once the uniaxial stress- strain curve is determined we can determine the plastic secant modulus, E_s^p and the poisson's ratio as follows

$$E_s^p = \frac{B^n E}{B^n + E\sigma^{n-1}}$$
$$\nu_s = \frac{1}{2} + \frac{E_s^p\ (\nu - 1/2)}{E}$$

Once the secant modulus and poisson's ratio are determined, then the corresponding shear stress and the shear strain can be determined. Figure C.1 shows a comparison

between the failure envelope predicted by considering the material as a deformation theory of plasticity solid and the one obtained by not assuming it to be a deformation theory of plasticity solid. It can be seen that there is not much of a difference between the two curves except in the range where the compressive stress is low and shear stress is high.

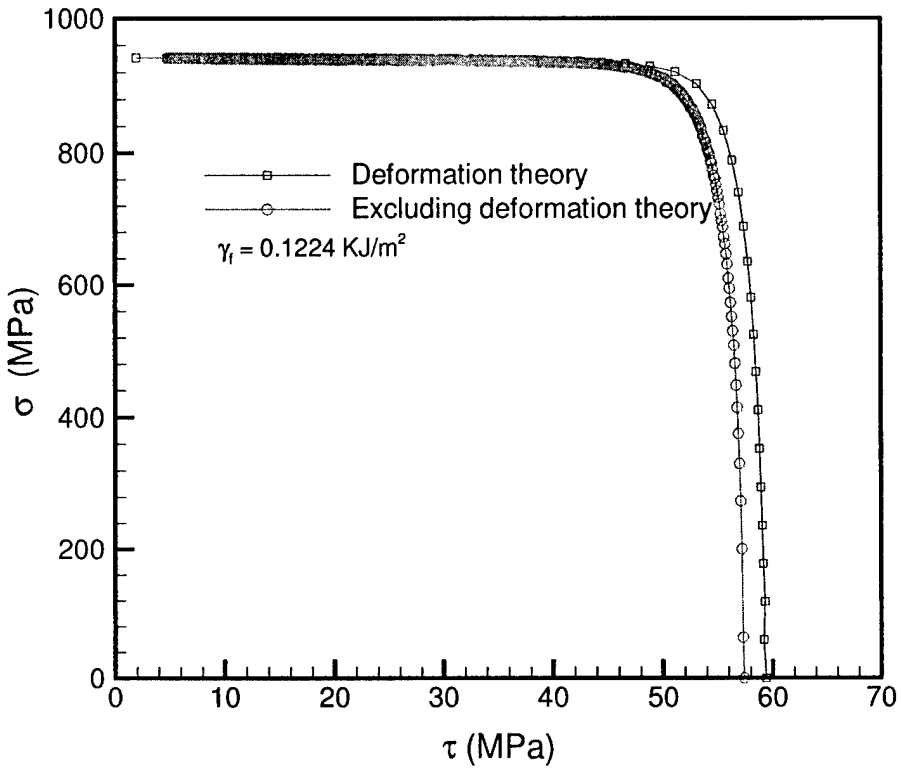

Figure C.1: Comparison of failure envelopes considering the composite as a deformation theory solid and as a nonlinear elastic solid

APPENDIX D

Split Hopkinson Pressure Bar Setup (SHPB)

At the beginning of the twentieth century, with the increasing use of these metals in structures exposed to shock and explosive loadings, high strain rate properties of commonly used metals were increasingly becoming a necessity for the designer. English physicist, Hopkinson (1914), is credited with developing a experimental methodology to determine the high strain rate properties of metals. However, the method was later modified and improved by Kolsky (1949, 1953). The current split Hopkinson pressure bar setup which is widely used can be attributed to Kolsky and is also referred to as Kosky bar in the literature. Bancroft (1941), solved the Pocchammer-Love equation for the velocity of logitudinal waves in cylindrical bars. His results led to a better understanding of the dispersion effects in cylindrical bars and also methods to correct the dispersion effects. Other important contributions that have enhanced the understanding of the split Hopkinson pressure bar test setup are given in Davies (1948), who presents a detailed discussion of the split Hopkinson pressure bar setup. It should be noted that the split Hopkinson pressure bar test apparatus is a "load cell". Just as the sensitivity of the load cell is determined by the dimensions of the load cell and the material used to construct the load cell, the SHPB setup can also be made more sensitive for the particular type of material being tested by

choosing the bars to be of appropriate length and diameter. In the following sections, a description of the SHPB setup at the Aerospace engineering department is presented.

D.1 Experimental Setup

As can be seen in figure D.1, the SHPB setup consists of a gun (in this case a gas gun) to propel the impactor at the required velocity, a incident bar and a transmission bar. The specimen is sandwiched between the incident bar and the transmission bar as shown in figure D.1. The various dimensions and the material used for the SHPB setup are mentioned below.

D.1.1 Material and Equipment

The shafts were manufactured by Thomson Industries and are made of 440C Stainless steel. The lengths of the incident bar and the transmission bar were kept the same and are equal to $914.4mm$. The diameter of the incident bar, the transmission bar and the striker is $12.7mm$. The physical properties of these shafts are mentioned in Table D.1. The pressure tank is a DOT 3A 5000 class high pressure cylinder and is rated upto 4000 psi. The barrel of the gas gun was $0.61m$ long and has a wall thickness of $31.75mm$. The tip of the barrel was machined with holes to relieve the gas pressure behind the projectile at exit. A solenoid valve is used to control the outflow of the gas from the reservoir. The solenoid valve is rated upto 4000 psi and is attached to a electrical trigger switch, which opens the valve instantaneously to release the gas into the barrel and thus propel the striker bar.

Sp.gravity	7.62
Density	7620 Kg/m^3
Mod. of Elasticity	220 GPa
0.2% σ_y	1896 MPa
Ult. tensile strength	1965 MPa
Brinell Hardness	580

Table D.1: Physical properties of the SHPB shafts

D.1.2 Details of SHPB design

The first step in deciding the dimensions for the various bars in the SHPB setup would be to determine the range of velocities at which the gas gun can be operated and the type of material to be tested. For determining the velocity of the projectile at a given gas pressure in the tank, some simplifying assumptions are made; It is assumed that the pressure acting on the face of the striker bar is uniform and constant throughout the length of the barrel and that friction between the bar surface and the inner surface of the barrel is negligible. Then, using Newton's law we can obtain a relation for the acceleration in the bar to be $a = F/m$, where a is the acceleration of the striker bar, F is the force acting on the end of the striker bar and m is the mass of the striker bar. Assuming the cross-sectional area of the striker bar to be A_{st}, length to be L_{st}, density to be ρ_{st}, and pressure in the tank to be P_g, we can obtain the relation for acceleration of the striker bar to be $a = P_g/L_{st}\rho_{st}$. Then, using the equations of motion for a rigid body initially at rest we get the velocity of the striker bar to be $v_{st} = \sqrt{2P_gL_b/L_{st}\rho_{st}}$. Thus, the striker velocity is inversely proportional to the length of the striker bar and directly proportional to the distance over which the pressure is acting ie. L_b the length of the barrel. Hence, for a given gas tank pressure with the barrel length and density fixed, we can only change the striker

bar length to obtain different exit velocities of the striker. In the current setup, the length of striker bar was kept constant and the pressure changed to obtain different velocities of impact since the striker bar length is directly responsible for the duration of the incident pulse as described in the following section. The striker bar velocity is obtained using two infrared photosensors, the output of which is connected to a high speed data acquisition system. The gun barrel is drilled with lateral holes at the end where the striker bar exits so as to make the pressure equal to atmosphere at the tip of the barrel. The predicted velocity from the equation above and the actual velocities obtained from the sensor are shown in figure D.2. It can be seen that there is a wide disparity between the measure velocities and the predicted velocities. Hence, the sensors were always placed to record the velocities during the impact and they also acted as a source of triggering for the high speed data acquisition system.

In choosing the dimensions of the incident bar and the transmission bar the effects of wave dispersion and the material being tested should be taken into account. Dispersion in cylindrical bars is a result of the dependancy of the bar's phase velocity on frequency, which in effect distorts the wave shape as it travels along the length of the bar. The dispersive properties of the incident and transmission bar should be known to provide a correction to shape of the pulse. This is necessary because the shape of the pulse observed and recorded at the strain gage position will be different than the one at the specimen/bar interface and we are interested in the shape of the pulse at the specimen/bar interface. The dispersion correction can be found from the solutions presented by Bancroft (1941). For the present setup, the ratio of the wave length of the pulse, λ, which is equal to twice the length of the striker bar, to the diameter of the bar, d is 0.02. It can be seen from the results presented by Bancroft (1941) and also in Meyers (1994) that the effects of dispersion are negligible for this

ratio of d/λ and for the poisson's ratio of 0.25. Thus, the obtained wave form need not be corrected for dispersion effects.

The duration of the incident pulse is determined by the length of the striker bar. It can be seen from figure D.3 that as the compressive wave referred to as "incident wave" starts to travel in the incident bar away from the striker bar/incident bar interface, another compressive wave referred to as "impactor wave" travels in the opposite direction in the striker bar. Once the impactor wave reaches the free end of the striker bar it reflects back and returns as a tensile wave. On reaching the striker bar/incident bar interface the tensile wave causes the separation of the striker bar from the incident bar. For a striker bar of $304.8mm$ and made of 440C stainless steel with a longitudinal wave velocity of $5416m/s$ the duration of the impact pulse comes to be $112\mu sec$. The incident wave reaches the specimen/incident bar interface and gets partially reflected depending upon the impedance mismatch between the specimen and the incident bar. The higher the mismatch, the stronger is the reflected pulse and weaker is the transmission pulse. This has implications in the choice of materials being used for the incident and the transmission bar. Thus, for very soft specimens, a very stiff incident bar would mean a low amount of transmission of the stress pulse through the specimen into the transmission bar. This would lead to difficulties in the measurement of strains in the transmission gage. This has led to the development of polymer based SHPB setups for testing soft materials (Chen et al. (2002)). The reflected pulse which is tensile in nature reaches the interface of striker/incident bar. However, by keeping the striker bar to be sufficiently shorter than the incident bar ($2L_{st} < L_{incd}$) one can ensure the separation to happen when the tensile wave in the striker bar reaches the striker bar/incident bar interface.

Once, the incident wave reaches the specimen/incident bar interface, some part of

it is reflected and a part of it is transmitted into the specimen. This transmitted wave reaches the other end of the specimen ie. specimen/transmission bar interface and again undergoes partial reflection and partial transmission. By keeping the specimen length to be very short and ensuring the duration of incident pulse to be sufficiently long, one can ensure that the specimen attains a uniform state of stress. For brittle materials, where the specimen might break even before a uniform state of stress is reached, pulse shapers are used. Pulse shapers are soft ductile materials like copper or brass which increase the rise time of the incident pulse and thus ensure that the specimen attains a stress equilibrium before the failure stress in the specimen is reached (Follansbee and Franz (1983); Frew et al. (2002)). In the present setup, a small piece of brass was used at the striker/incident bar interface to act as a pulse shaper while testing the composites. The use of a pulse shaper results in a lower strain rate at a given velocity of impact since the duration of the impact pulse is increased and the shape of the pulse acquires a trapezoidal form. The pulse shaper also acts as a dispersion correction device since it increase the wave length of the incident pulse thus causing the ratio, d/λ to decrease further.

At the specimen/transmission bar interface, there is a partial transmission of the stress wave. This transmission wave propagates through the transmission bar and reaches the free end of the transmission bar and reflects back as a tensile wave. Once this wave reaches the specimen/transmission bar interface the contact between the specimen and the transmission bar is lost. Depending on the length of this bar, one can adjust the number of pulses that are transmitted through the specimen. In the current setup all the experiments were performed by keeping the transmission bar and the incident bar to be of equal length. A third bar known as a throw-off bar was added to the assembly. This bar is shorter in length as compared to a transmission

bar and acts as a momentum trap reducing the motion of the transmission and incident bars.

In the experimental setup, strain gages are attached to the incident bar and transmission bar surfaces for recording the voltages. The strain gages are located such that they can record the complete compressive stress wave without the refleted tensile wave being superposed on the incident wave. Also, the strain gage is attached at a sufficient distance from the specimen/bar interfaces to avoid end effects. In the current setup, a full Wheatstone bridge circuit was used to measure the strains in both incident and the transmission bars. 350Ω resistance strain gages of $1mm$ gage length were used to obtain the strain data. High resistance and the use of a full bridge makes it easier to record the voltages. The amplification was kept at 100 and the input voltage to the bridge was $10V$. In the following section, the analysis for obtaining the stress-strain curve from the information acquired from the incident and transmission bar strain gages is presented.

D.2 Wave Analysis

The analysis for SHPB setup is well established and is given in many sources but Graff (1975) and Meyers (1994) provide a detailed description of the wave analysis in solids. In the following paragraphs, a brief description of the steps required to obtain the stress-strain response of the specimen is presented. The three strains that are measured from the incident and the transmission bar strain gages are referred to as the direct incident strain, ϵ_i, the reflected strain, ϵ_r, and the transmitted strain, ϵ_t. From these three strain recordings, one can obtain the complete stress-strain response of the specimen using the one dimensional wave theory. Following the terminology given in Meyers (1994), we first assume the impedance of the incident

and transmission bars to be same and given by the expression ρAC, where ρ is the density, A is cross-sectional area and C is the wave speed in the bars. Also, we assume that the specimen impedance is smaller than the incident and transmission bars and is given by $\rho_s A_s C_s$. Let the interface velocity at the incident bar/specimen interface be V_1 and that at the specimen/transmission bar interface be V_2. If L is the length of the specimen and since $V_1(t) > V_2(t)$, the length L decreasses with time and the specimen undergoes plastic deformation. The strain rate $\dot{\epsilon}$ can be calculated as

$$\dot{\epsilon} = \frac{V_1(t) - V_2(t)}{L} \tag{D.1}$$

Now to express the velocities in terms of the strains, we make use of the relation between the stress in a bar and the interface velocity (obtained using impulse-momentum equations and one dimensional Hooke's law) and obtain $V_1 = C_s\epsilon_i$ ($at\ t = 0$) and $V_2 = C_s\epsilon_t$. At $t > 0$, V_1 decreases because of the reflected wave. Thus, $V_1 = C_s(\epsilon_i - \epsilon_r)$. By substituting the above expressions for the velocities into equations (D.1) we obtain

$$\frac{d\epsilon}{dt} = \frac{C_s(\epsilon_i - \epsilon_r) - C_s\epsilon_t}{L} \tag{D.2}$$

From equations (D.2), we can obtain the strain by integrating the strain rate from 0 to t:

$$\epsilon(t) = \frac{C_s}{L}\int_0^t (\epsilon_i(t) - \epsilon_r(t) - \epsilon_t(t)) \tag{D.3}$$

In order to obtain the stress in the specimen, we assume equilibrium with $P_1(t)$ being the force acting on interface-1(incident/specimen) and $P_2(t)$ being the force acting on interface-2(specimen/transmission):

$$\sigma = \frac{P_1(t) + P_2(t)}{2A_s}$$

$$
\begin{aligned}
P_1(t) &= AE(\epsilon_i + \epsilon_r) \\
P_2(t) &= AE\epsilon_t \\
\sigma &= \frac{AE}{2A_s}(\epsilon_i(t) + \epsilon_r(t) + \epsilon_t(t))
\end{aligned} \tag{D.4}
$$

Where E is the elastic modulus of the bars and A is cross-sectional area of the bars. For equilibrium, $P_1(t) = P_2(t)$ and $\epsilon_i + \epsilon_r = \epsilon_t$:

$$\sigma = E\frac{A}{A_s}\epsilon_t(t) \tag{D.5}$$

$$\dot{\epsilon} = -\frac{2C}{L}\int_0^t \epsilon_r dt \tag{D.6}$$

Using equations (D.5-D.6) we can caculate the specimen stress-strain response from the strain gage data obtained from the strain gages attached to the incident and transmission bar surfaces. Results obtained from the testing of hybrid composites using the SHPB setup are presented in chapter VI.

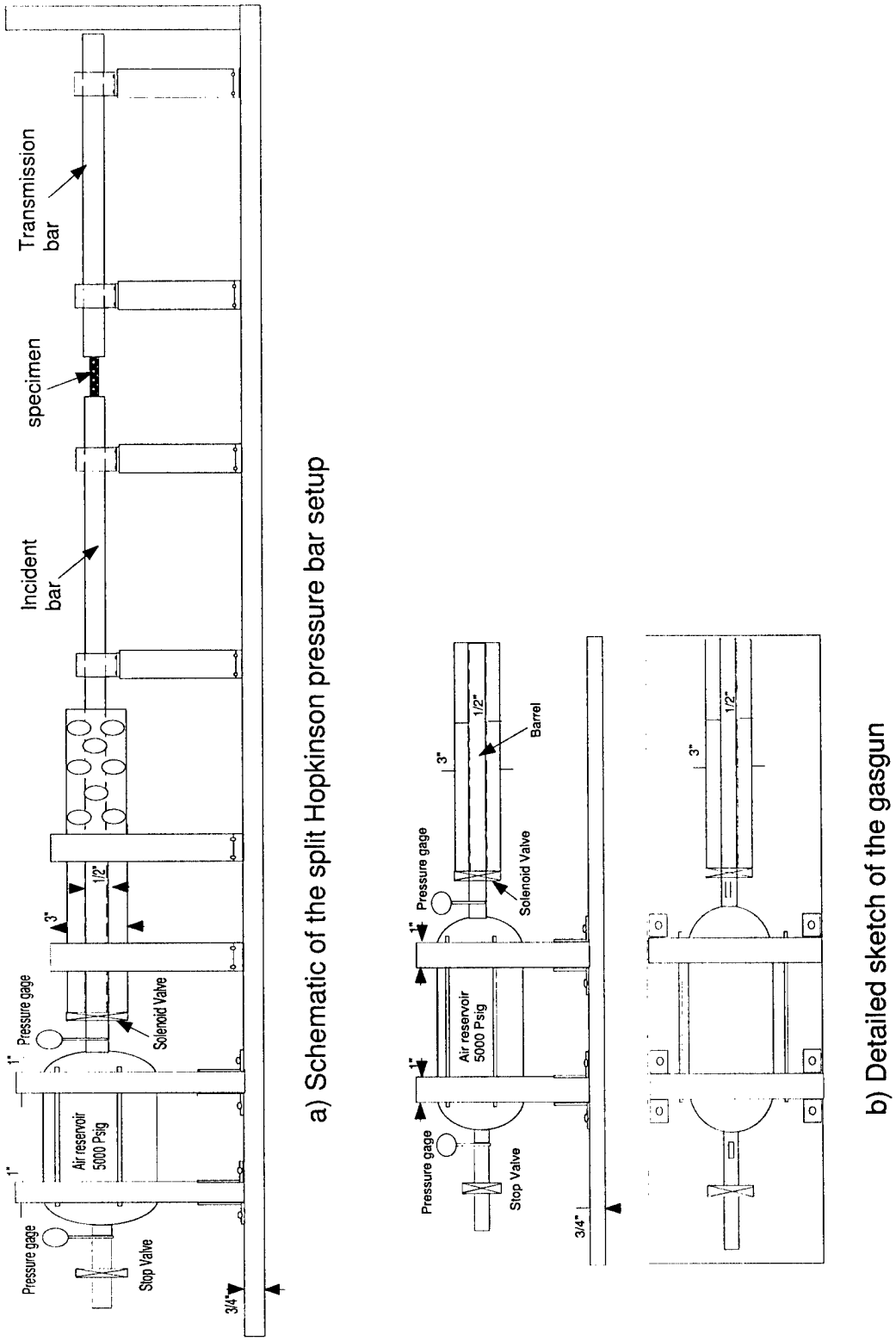
Transmission bar
specimen
Incident bar
3"
1/2"
Pressure gage
Solenoid Valve
1"
Air reservoir 5000 Psig
1"
Pressure gage
Stop Valve
3/4"
a) Schematic of the split Hopkinson pressure bar setup
Barrel
3"
1/2"
Pressure gage
Solenoid Valve
1"
Air reservoir 5000 Psig
1"
Pressure gage
Stop Valve
3/4"
3"
1/2"
b) Detailed sketch of the gasgun

Figure D.1:

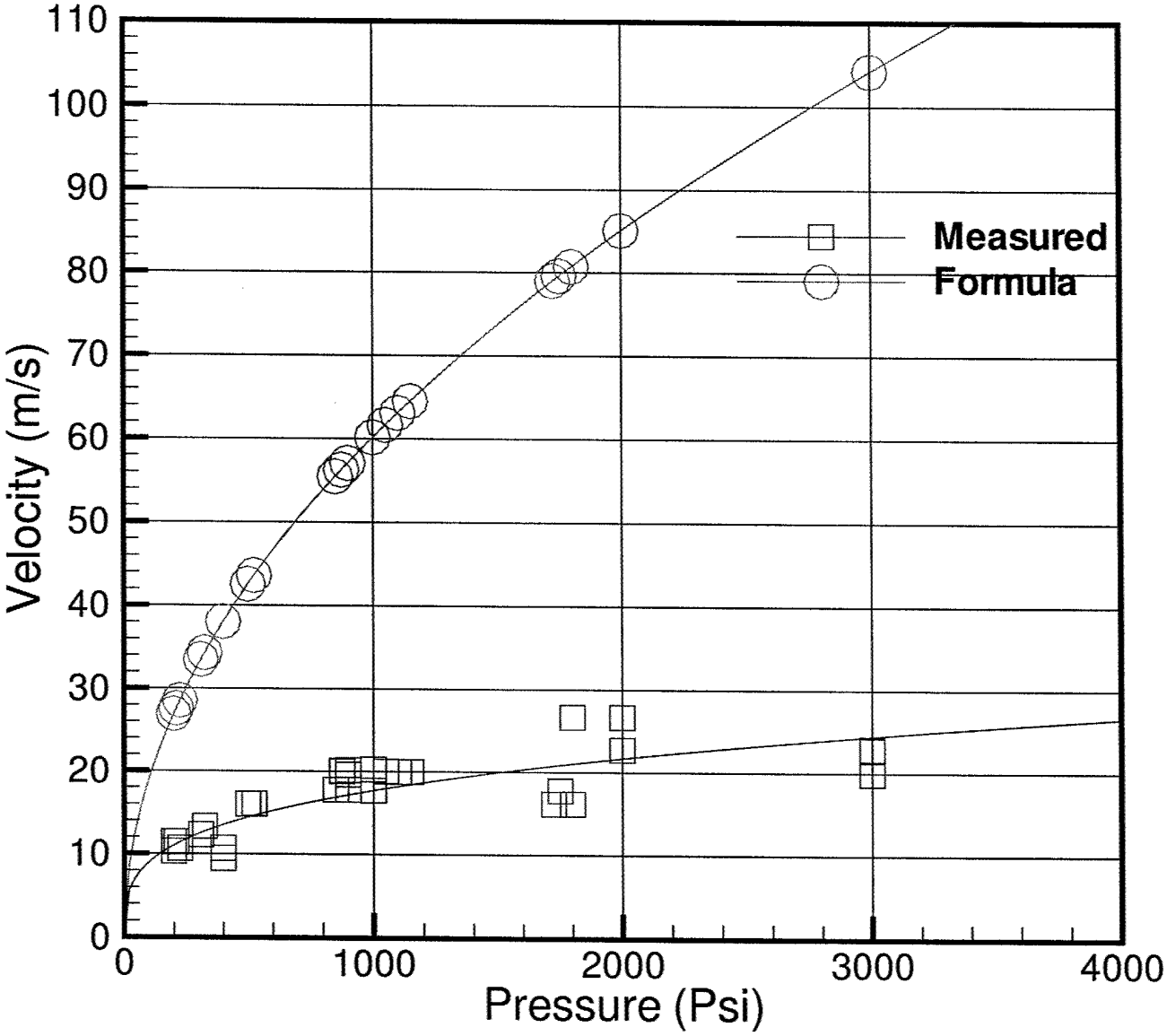

Figure D.2: Comparison of the measured striker velocity and the predicted velocity

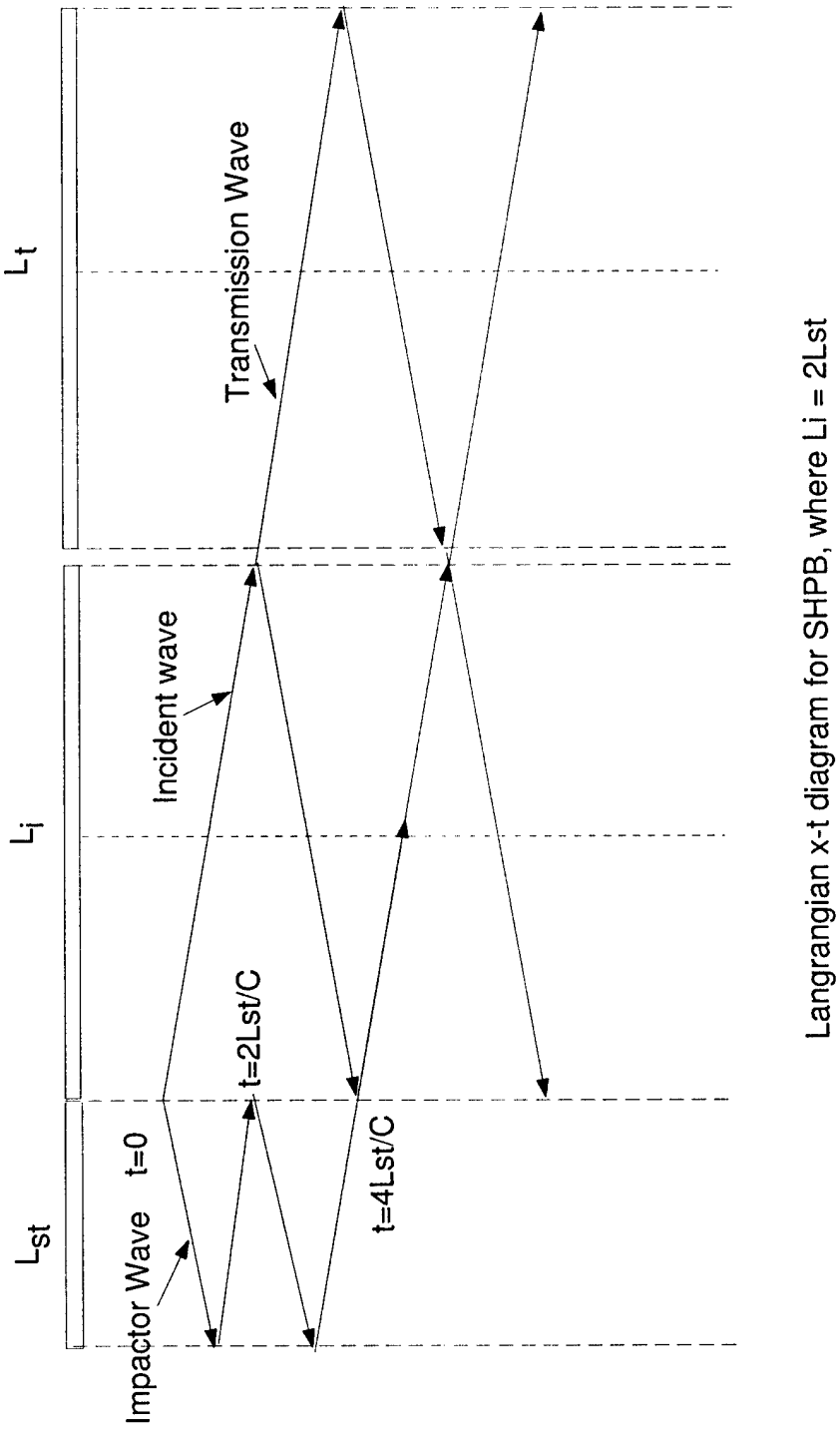
Langrangian x-t diagram for SHPB, where Li = 2Lst
Lt
Li
Lst
Transmission Wave
Incident wave
Impactor Wave
t=0
t=2Lst/C
t=4Lst/C

Figure D.3:

BIBLIOGRAPHY

BIBLIOGRAPHY

Agarwal, B. D., Broutman, L. J., 1983. Analysis and Performance of Fiber Composites, 2nd Edition. John Wiley and Sons.

Ahn, J. H., Waas, A. M., July 1999. A micromechanics-based finite element model for compressive failure of notched uniply composite laminates under remote biaxial loads. ASME Trans. J. of Eng. Materials and Technology 121, 360–366.

Alwan, J., Naaman, A. E., 1994. New formulation for the elastic modulus of fiber reinforced quasi brittle matrices. ASCE Journal of Engineering Mechanics 120 (11), 2443–2460.

Argon, A. S., 1972. Fracture of composites. In: Herman, H. (Ed.), Treatise on Materials Science and Technology. Vol. 1. Academic Press, New York, pp. 79–114.

Aveston, J., Sillwood, J. M., 1976. Synergistic fiber strengthening in hybrid composites. Journal of Materials Science 11, 1877–83.

Bancroft, D., April 1941. The velocity of longitidinal waves in cylindrical bars. Physical Review 59, 588–593.

Batdorf, S. B., Ko, R. W. C., 1986. Shear plastic stress-strain relation obtained from torque-twist data. Journal of Engineering Materials and Technology, Trans. ASME 108 (4), 354–357.

Bazhenov, S. L., Kuperman, A. M., Zelenskii, E. S., Berlin, A. A., 1992. Compressive failure of unidirectional glass-fiber-reinforced plastics. Composite Science and Technology 45, 201–208.

Berbinau, P., Soutis, C., Goutas, P., Curtis, P. T., 1999. Effect of off-axis ply orientation on 0^0-fibre microbuckling. Composites: Part A 30, 1197–1207.

Brush, D. O., Almroth, B. O. ., 1975. Buckling of bars, plates and shells. McGraw-Hill, New York.

Budiansky, B., 1983. Micromechanics. Computers and Structures 16, 3–12.

Budiansky, B., Fleck, N. A., 1993. Compressive failure of fibre composites. Journal of the Mechanics and Physics of Solids 41 (1), 183–211.

Budiansky, B., Fleck, N. A., Amazigo, J. C., 1998. On kink band propagation in fiber composites. Journal of the Mechanics and Physics of Solids 46, 1637–1653.

Budiansky, B., Hutchinson, J. W., Evans, A. G., 1986. Matrix fracture in fiber-reinforced ceramics. Journal of the Mechanics and Physics of Solids 34 (2), 167–189.

Camponeschi, E. T., 1991. Composite materials fatigue and fracture. Vol. 3 of STP 1110. ASTM, Philadelphia, pp. 550–578.

Chen, W., Lu, F., Frew, D. J., Forrestal, M. J., May 2002. Dynamic compression testing of soft materials. ASME Trans. Journal of Applied Mechanics 69.

Christensen, R. M., 1991. Mechanics of Composite Materials, 1st Edition. Krieger Publishing Company, Malabar, Florida.

Cox, H. L., 1952. The elasticity and strength of paper on other fibrous materials. Br.J.Appl.Phys 3, 72.

Daniel, I. M., Hao-Ming, H., Shi-Chang, W., 1996. Failure mechanisms in thick composites under compression loading. Composites: Part B: Engineering 52, 577–552.

Daniel, I. M., Isahi, O., 1994. Engineering Mechanics of Composite Materials. Oxford Univ. Press.

Davies, E. D. H., Hunter, S. C., 1963. The dynamic compression testing of solids by the method of the split hopkinson pressure bar. Journal of the Mechanics and the Physics of Solids 11, 155–179.

Davies, R. M., 1948. A critical study of hopkinson pressure bar. Philosophical Transactions of Royal Society A240, 375–457.

Dorey, G., Sidey, G. R., Hutchings, J., 1978. Impact properties of carbon fiber-kevlar49 fiber hybrid composites. Composites 9, 25–30.

Dow, J. F., Gruntfest, I. J., 1960. Determination of most needed, potentially possible improvements in materials for ballistic and space vehicles. Tech. Rep. TIS R60SD389, General Electric Corporation.

Drapier, S., Grandidier, J.-C., Potier-Ferry, M., 1999. Towards a numerical model of the compressive strength for long fiber composites. European Journal of Mechanics, A/Solids 18 (1), 69–92.

Drapier, S., Grandidier, J.-C., Potier-Ferry, M., 2001. A structural approach of plastic microbuckling in long fibre composites: Comparison with theoretical and experimental results. International Journal of Solids and Structures 38 (22-23), 3877–3904.

Drzal, L. T., Rich, M. J., Koenig, M. F., Llyod, P. M., 1982a. Adhesion of graphite fibers to epoxy matrices : I. the effect of fiber finish. J.Adhesion 16, 133–152.

Drzal, L. T., Rich, M. J., Llyod, P. M., 1982b. Adhesion of graphite fibers to epoxy matrices : I. the role of fiber surface treatment. J.Adhesion 16, 1–30.

Fan, J., Slaughter, W. S., 1997. High strain rate compression of fiber composites. Journal of the Mechanics and Physics of Solids 45 (5), 731–751.

Fleck, N. A., 1997. Compressive failure of fiber composites. In: Advances in applied mechanics. Vol. 33. Academic Press, New York, pp. 43–117.

Fleck, N. A., Deng, L., Budiansky, B., 1995. Prediction of kink width in compressed fiber composites. ASME Journal of Applied Mechanics 62, 329–337.

Fleck, N. A., Shu, J. Y., 1995. Microbuckle initiation in fibre composites: A finite elemen study. Journal of the Mechanics and Physics of Solids 43 (12), 1887–1918.

Follansbee, P. S., Franz, C., 1983. Wave propagation in the split hopkinson pressure bar. Journal of Engineering and Materials Technology 105, 61–66.

Frew, D. J., Forrestal, M. J., Chen, W., March 2002. Pulse shaping techniques for testing brittle materials with a split hopkinson pressure bar. Experimental Mechanics 42 (1), 93–106.

Garland, B. D., Beyerlein, I. J., Schadler, L. S., 2001. Development of compression damage zones in fibrous composites. Composites Science and Technology 61 (16), 2461–2480.

Graff, K. F., 1975. Wave Motion in Elastic Solids. Dover Publications, Inc. New York.

Haberle, J. G., Matthews, F. L., October 1993. The influence of test method on the compressive strength of several fiber-reinforced plastics. Journal of Advanced Materials , 35–45.

Hallett, S. R., Ruiz, C., Harding, J., 1999. The effect of strain rate on the interlaminar shear strength of a carbon/epoxy cross-ply laminate: comparison between experiment and numerical prediction. Composites Science and Technology 59, 749–758.

Hashin, Z., 1966. Viscoelastic fiber reinforced materials. J. AIAA 4.

Hashin, Z., Rosen, B. W., 1964. The elastic moduli of fiber reinforced materials. Journal of Applied Mechanics , 275–306.

Hayashi, T., Nov. 1965. On the shear instability of structures caused by compressive load. In: AIAA/RAeS/JSASS Aircraft Design and Technology Meeting. Vol. AIAA Paper No. 65-770. AIAA, Los Angeles, CA.

Herakovich, C. T., 1998. Mechanics of Fibrous Composites. John Wiley and Sons.

Hopkinson, B., 1914. A method of measuring the pressure in the deformation of high explosives by the impact of bullets. Philosophical Transactions of Royal Society A213, 437–452.

Horii, H., Nemat-Nasser, S., 1985. Compression-induced microcrack growth in brittle solids: Axial splitting and shear failure. Journal of Geophysical Research 90 (B4), 3105–3125.

Horii, H., Nemat-Nasser, S., 1986. Brittle failure in compression: splitting, faulting, and brittle-ductile transition. Philosophical Transactions of the Royal Society of London, Series-A:Physical Sciences and Engineering 319, 337–374.

Hsu, S. Y., Vogler, T. J., Kyriakides, S., 1998. Compressive strength predictions for fiber composites. ASME Journal of Applied Mechanics 65, 7–16.

Hsu, S. Y., Vogler, T. J., Kyriakides, S., 1999. Inelastic behavior of an as4/peek composite under combined transverse compression and shear. part II: modeling. International Journal of Plasticity 15, 807–836.

Hyer, M. W., Waas, A. M., 2000. Mircomechanics of linear elastic continuous fiber composites. In: Chou, T. W. (Ed.), Comprehensive Composite Materials. Vol. 1. Elsevier Science, Ch. 12.

Jelf, P. M., Fleck, N. A., 1994a. The failure of composite tubes due to combined compression and torsion. Journal of Materials Science 29, 3080–3084.

Jelf, P. M., Fleck, N. A., 1994b. The failure of composite tubes due to combined compression and torsion. Journal of Materials Science 29, 3080–3084.

Khamseh, A., Waas, A. M., July 1992. Failure of uniply model composites under compression. ASME Trans. J. of Eng. Materials and Technology 114, 304–310.

Kolsky, H., 1949. An investigation of the mechanical properties of materials at very high rates of loading. Proc. R. Soc. London, Ser.B B62, 676–700.

Kolsky, H., 1953. Stress Waves in Solids. Oxford University Press, London.

Kozey, V. V., 1993. Splitting-related kinking failure mode in unidirectional composites under compressive loading. Journal of Materials Science Letters 12, 43–47.

Kumar, P., Garg, A., 1988. Failure moeds and fractographic study of glass-epoxy composite under dynamic compression. Journal of Materials Science 23, 2305–2309.

Kyriakides, S., Arseculeratne, R., Perry, E. J., Liechti, K. M., 1995. On the compressive failure of fiber reinforced composites. In: Proceedings of the sixtieth birthday celebration of Prof. W. G. Knauss. International Journal of Solids and Structures. Vol. 32. pp. 689–738.

Lager, J. R., June, R. R., 1969. Compressive strength of boron-epoxy composites. Journal of Composite Materials 3 (1), 1–9.

Lagoudas, D. C., Tadjbakhsh, I., Fares, N., 1991. A new approach to microbuckling of fibrous composites. Journal of Applied Mechanics 58 (2), 473–479.

Langhaar, H. L., 1980. Dimensional Analysis and Theory of Models. Robert E. Krieger Publishing Company, Inc., Malabar, Florida.

Lanir, Y., Fung, Y. C. B., 1972. Fiber columns under compression. Journal of Composite Materials 6, 387–401.

Lee, C. S., Hwang, W., Park, H. C., Han, K. S., 1999. Failure of carbon/epoxy composite tubes under combined axial and torsional loading 1. experimental results and predictions of biaxial strength by the use of neural networks. Composites Science and Technology 59, 1779–1788.

Lee, S. H., 1998. Compressive behavior of fiber reinforced unidirectional composites. Ph.D. thesis, Aerospace Engineering Department, University of Michigan, Ann Arbor.

Lee, S. H., Waas, A. M., 1999. Compressive response and failure of fiber reinforced unidirectional composites. International Journal of Fracture 100, 275–306.

Lee, S. H., Yerramalli, C., Waas, A. M., 2000. Compressive splitting response of glass-fiber reinforced unidirectional composites. Composites Science and Technology 60, 2957–2966.

Lyon, R. E., 1991. Shear strength of a ductile material from torsion test of solid cylinders. Journal of Testing and Evaluation 19 (3), 240–243.

Martinez, G. M., Piggott, M. R., Bainbridge, D. M. R., Harris, B., 1981. The compression strength of composites with kinked, misaligned and poorly adhering fibres. Journal of Materials Science 16, 2831–2836.

Mendelson, A., 1983. Plasticity: Theory and Application. Krieger Publishing Company, Malabar, Florida.

Meyers, M. A., 1994. Dynamic Behavior of Materials. John Wiley and Sons, Inc.

Moran, P. M., Liu, X. H., Shih, C. F., 1995. Kink band formation and band broadening in fiber composites under compressive loading. Acta metall. Mater. 43, 2943–2958.

Nadai, A., 1950. Theory of Flow and Fracture of Solids. Vol. 1. Mc-Graw Hill, New York.

Naik, N. K., Kumar, R. S., 1999. Compressive strength of unidirectional composites: evaluation and comparison of prediction models. Composite structures 46, 299–308.

Narayanan, S., Schadler, L. S., 1999. Mechanisms of kink-band formation in graphite/epoxy composites: a micromechanical experimental study. Composite Science and Technology 59, 2201–2213.

Nemat-Nasser, S., Deng, H., 1994. Strain rate effect on brittle failure in compression. Acta Metallurgica Materialia 42 (3), 1013–1024.

Nemat-Nasser, S., Horii, H., 1982. Compression-induced nonplanar crack extension with application to splitting, exfoliation, and rockburst. Journal of Geophysical Research 87 (B8), 6805–6821.

Oguni, K., 2000. Micromechanical aspects of failure in unidirectional fiber reinforced composites. Ph.D. thesis, Graduate Aeronautical Laboratories, California Institute of Technology, Pasadena, CA.

Oguni, K., Ravichandran, G., 2000. An energy-based model of longitudinal splitting in unidirectional fiber-reinforced composites. Journal of Applied Mechanics 67, 437–443.

Oguni, K., Tan, C. Y., Ravichandran, G., 2000. Failure mode transition in unidirectional E-glass/vinylester composites under multiaxial compression. Journal of Composite Materials 34 (24), 2081–2097.

Parry, T. V., Wronski, A. S., 1981. Kinking and tensile, compressive and interlaminar shear failure in carbon-fibre-reinforced plastic beams tested in flexure. Journal of Materials Science 16, 439–450.

Piggot, M. R., Sandai, A., Chua, P. S., Anderson, D., 1986. Mechanical interactions in the interphasial region of fibre reinforced thermosets. In: Composite Interfaces. North-Holland, Amsterdam.

Piggott, M. R., 1981. A theoretical framework for the compressive properties of aligned fibre composites. Journal of Materials Science 16, 2837–2845.

Piggott, M. R., Harris, B., 1980. Compression strength of carbon, glass and kevlar-49 fibre reinforced polyester resins. Journal of Materials Science 15, 2523–2538.

Piggott, M. R., Harris, B., 1981. Compression strength of hybrid fibre-reinforced plastics. Journal of Materials Science 16, 687–693.

Pompe, G., Mader, E., 2000. Experimental detection of a transcrystalline interphase in glass-fibre/ polypropelene composite. Composite Science and Technology 60, 2159–2167.

Quek, S. C., 2002. Compressive response and failure of braided textile composites : experiments and analysis. Ph.D. thesis, University of Michigan, Ann Arbor, MI.

Rosen, B. W., 1965. Mechanics of composite strengthening. In: Bush, S. H. (Ed.), Composite Materials. American Society of Metals, Metals Park, OH, pp. 37–75.

Sadowsky, M. A., Pu, S. L., Hussain, M. A., 1967. Buckling of microfibers. ASME Journal of Applied Mechanics 34, 1011–1016.

Schapery, R. A., 1995. Prediction of compressive strength and kink bands in composites using a work potential. International Journal of Solids and Structures 32 (6/7), 739–765.

Schapery, R. A., Sicking, D. L., 1995. On nonlinear constitutive equations for elastic and viscoelastic composites with growing damage. In: Bakker, A. (Ed.), Mechanical Behavior of Materials. Delft University Press, Delft, The Netherlands, pp. 45–76.

Schutz, J. B., 1994. Properties of composite materials for cryogenic applications. Cryogenics 38 (1), 3–12.

Sierakowski, R. L., Nevil, G. E., A., R. C., R., J. E., 1971. Dynamic compressive strength and failure of steel reinforced epoxy composites. Journal of Composite Materials 5 (3), 362–377.

Steif, P. S., 1988. A simple model for the compressive failure of weakly bonded fiber-reinforced composites. Journal of Composite Materials 22, 818–828.

Sun, C. T., Jun, A. W., 1994. Compressive strength of unidirectional fiber composites with matrix nonlinearity. Composite Science and Technology 52, 577–587.

Sutcliffe, M. P. F., Fleck, N. A., 1997. Microbuckle propagation in fibre composites. Acta materialia 45, 921–932.

Vogler, T. J., Hsu, S. Y., Kyriakides, S., 2000. Composite failure under combined compression and shear. International Journal of Solids and Structures 37, 1765–1791.

Vogler, T. J., Hsu, S. Y., Kyriakides, S., 2001. On the initiation and growth of kink bands in fiber composites. part II: analysis. International Journal of Solids and Structures 38, 2653–2682.

Vogler, T. J., Kyriakides, S., 1998. On the effect of loading rate on the compressive strength of an as4/peek composite. ASME Journal of Applied Mechanics 65, 1056–1058.

Vogler, T. J., Kyriakides, S., 1999. Inelastic behavior of an as4/peek composite under combined transverse compression and shear. part I: experiments. International Journal of Plasticity 15, 783–806.

Vogler, T. J., Kyriakides, S., 2001. On the initiation and growth of kink bands in fiber composites. part I: experiments. International Journal of Solids and Structures 38, 2639–2651.

Waas, A. M., 1992. Effect of interphase on the compressive strength of unidirectional composites. Journal of Applied Mechanics 59 (2).

Waas, A. M., C. D. Babcock, J., Knauss, W. G., March 1990. A micromechanical model for elastic fiber microbuckling. ASME Transactions Journal of Applied Mechanics 57, 138–149.

Waas, A. M., Schultheisz, C. R., 1996. Compressive failure of composites parts I and II. Progress in Aerospace Sciences 32 (1), 1–78.

Wan, L., Takeda, N., Dec 1993. Characterization of impact compression damage progress in composite laminates by improved shpb techniques. In: Kishi, T., Takeda, N., Kagawa, Y. (Eds.), Advanced Materials - New Processes and Reliability. Vol. 1. Society for the advancement of material and process engineering, SAMPE, Nippon Convention Center, Chiba, Japan.

Weaver, C. W., Williams, J. G., 1975. Deformation of a carbon-epoxy composite under hydrostatic pressure. Journal of Materials Science 10, 1323–1333.

Williams, J. L., Donellan, M. E., James, M. R., Morris, W. L., 1990. Elastic modulus of the interphase in organic matrix composites composites. Mat.Res.Soc.Symp.Proc. 170, 285–289.

Wisnom, M. R., Atkinson, J. W., 1997. Constrained buckling tests show increasing compressive strain to failure with increasing strain gradient. Composites-Part A: Applied Science and Manufacturing 28 (11), 959–964.

Wisnom, M. R., Atkinson, J. W., Jones, M. I., 1997. Reduction in compressive strain to failure with increasing specimen size in pin-ended buckling tests. Composites Science and Technology 57 (9-10), 1303–1308.

Xue, Z., Huang, Y., Li, M., 2002. Particle size effect in metallic materials: a study by the theory of mechanism-based strain gradient plasticity. Acta Materialia 50, 149–160.

Yao, L. N., Chou, T.-W., 1989. Analysis of hybrid effect in unidirectional composites under longitudinal compression. Composite Structures 12, 27–37.

Yerramalli, C. S., Waas, A. M., November 11-16 2001. Failure of composites under combined loading. In: Proceedings of 2001 ASME International Mechanical Engineering Congress and Exposition, New York.

Yerramalli, C. S., Waas, A. M., May 2002a. Compressive splitting failure of composites using modified shear lag theory. International Journal of Fracture 115, 27–40.

Yerramalli, C. S., Waas, A. M., 2002b. A failure criterion for fiber reinforced polymer composites under combined compression-torsion loading. Accepted in International Journal of Solids and Structures .

Yerramalli, C. S., Waas, A. M., April 2002c. In-situ matrix shear response using torsional test data of fiber reinforced unidirectional polymer composites. ASME Trans. J. of Eng. Materials and Technology 124, 152–159.

Yuan, J., Takeda, N., 2000. Impact compressive failure of gfrp unidirectional composites. Science and Engineering of Composite Materials 9 (1), 1–9.

Yuan, J., Takeda, N., Waas, A. M., 1998. A note on the data processing in split hopkinson pressure bar test. Experimental Techniques 22 (5), 31–24.